SPACECRAFT DEPARTMENT

MISSILE AND SPACE DIVISION

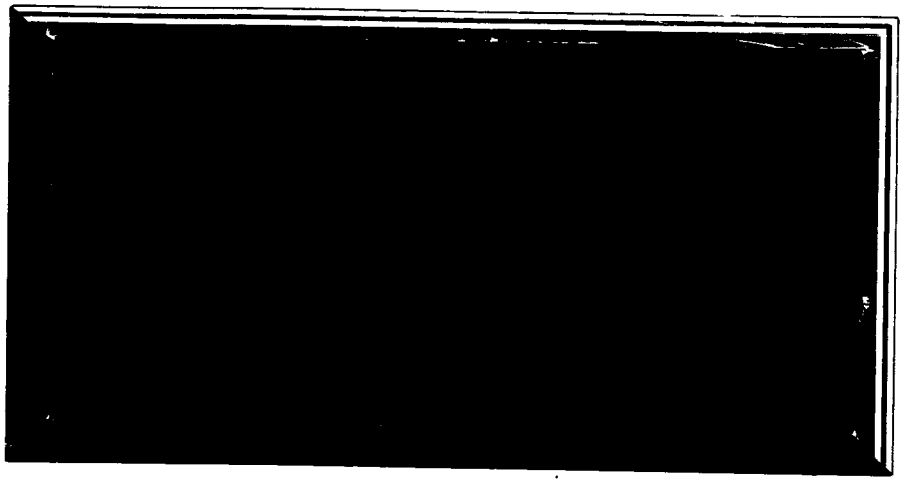

GENERAL ELECTRIC

RE-ORDER NO. 65-323

DOCUMENT NO. 65SD4286
1 May 1965

SOLAR THERMIONIC FLIGHT EXPERIMENT STUDY FINAL REPORT

VOLUME III — SPACECRAFT DESIGN (PHASE II)

PREPARED UNDER
CONTRACT NO. 950852 under NAS 7-100

FOR

JET PROPULSION LABORATORY
CALIFORNIA INSTITUTE OF TECHNOLOGY
4800 OAK GROVE DRIVE
PASADENA, CALIFORNIA 91103

GENERAL ELECTRIC
SPACECRAFT DEPARTMENT
A Department of the Missile and Space Division
Valley Forge Space Technology Center
P.O. Box 8555 • Philadelphia 1, Penna.

TABLE OF CONTENTS

TABLE OF CONTENTS (Continued)

TABLE OF CONTENTS (Continued)

TABLE OF CONTENTS (Continued)

TABLE OF CONTENTS (Continued)

LIST OF ILLUSTRATIONS

LIST OF ILLUSTRATIONS (Continued)

LIST OF ILLUSTRATIONS (Continued)

LIST OF TABLES

LIST OF TABLES (Continued)

SECTION 7

INTRODUCTION TO SPACECRAFT DESIGN

SECTION 7.

INTRODUCTION TO SPACECRAFT DESIGN

7.1 OBJECTIVE

The objective of this second phase of the study is to develop spacecraft designs for the three missions selected in Phase I. In establishing the spacecraft designs, consideration will be given to the following principal areas.

a. Solar Thermionic Experiment Design

b. Secondary Experiments

c. Telemetry, Tracking and Command Subsystem

d. Attitude Control Subsystem

e. Power Subsystem

f. Spacecraft Structure and Thermal Control

The spacecraft designs will be conceptual in depth and establish the general configuration, performance and weight of the vehicles.

7.2 SELECTED MISSIONS

The pertinent information on the three missions selected in Phase I (see Section 6-Volume II) is summarized in Table 7-1. The missions are listed in order of attractiveness and in subsequent sections will be referred to as Missions A, B and C.

The conclusions drawn in the Mission Analysis Phase of the study were based on a spacecraft weight of 350 pounds. When the spacecraft designs are formulated, their weights will be calculated and compared with this figure; the effect of any deviations will be determined.

Table 7-1. Summary of Selected Missions

Mission	Orbit	Orbit Altitude NM	Orbit Inclination Degrees	Orbit Period Hours	Orbit Maximum Dark Period Hours	Launch Vehicle	Launch Site	Thermionic System Concentrator Diameter, Inches	Thermionic Generator Power Output Watts	Secondary Experiments
A	Modified Sun-Synchronous	1,000	101.84	2.07	0.4	Improved Delta DSV-3E	WTR	50	144	See Table 6-5 Volume II
B	Highly Elliptical	25,000 Apogee 200 Perigee	45	14.0	2.09	Improved Delta DSV-3E	ETR	50	144	See Table 6-5 Volume II
C	Low Altitude Circular	325	30	1.61	0.617	Improved Delta DSV-3H	ETR	50	144	See Table 6-5 Volume II

In formulating the spacecraft designs, a 1967 to 1969 flight period is assumed. This period is believed to be in keeping with a reasonable development program for solar thermionics.

The spacecraft are designed for a useful life in space of one year. This value of design life was selected because in addition to the primary experiment, it is highly desirable to obtain performance information on many of the secondary experiments over extended periods of space operation.

SECTION 8

SOLAR THERMIONIC EXPERIMENT DESIGN

PRINCIPAL CONTRIBUTORS:

Dr. P. Brosens
E. W. Williams
J. H. Paul
M. J. Concannon

SECTION 8
SOLAR THERMIONIC EXPERIMENT DESIGN

8.1 INTRODUCTION

This section presents the proposed design for the solar thermionic primary experiment. The systems calculations establishing the expected performance of the solar thermionic system were performed in the Mission Analysis phase of the study and are presented in Section 4. The major results of these calculations are summarized in Table 8-1. These performance parameters served as the starting point for establishing the solar thermionic experiment design.

Since the selected missions all employ a version of the IMPROVED DELTA launch vehicle the allowable payload diameter (57 inches) is identical in all three cases. This allows the basic solar thermionic system design to be the same for the three missions.

The study ground rules placed two restrictions on the thermionic system: (1) that the generator contain four thermionic converters, and (2) that the generator power output be a minimum of 100 watts.

8.2 DESIGN PHILOSOPHY

The thermionic system design is based on present state-of-the-art performance and fabrication techniques. The emphasis was placed on designing a thermionic system that could be developed with existing technology and would deliver the estimated performance. Low weight and extremely high performance were not major design criteria. As a result of this conservative approach it is very likely that the estimated system performance and weight could be improved upon by the time a system is actually developed for this application.

Table 8-1 Thermionic System Performance Parameters

PERFORMANCE PARAMETERS	
Converter Emitter Temperature	2000°K
Converter Electrode Spacing	2 Mils
Converter Emitter Material	Rhenium
Converter Sleeve Thickness	0.0025 Inches [a]
Converter Emitter Area	2 cm^2
Converter Operating Point	Peak Efficiency
Converter Power Density	18 Watts/cm^2
Converter Voltage Output	0.85 Volts
Converter Efficiency	17.4 Percent
Concentrator Diameter	50 Inches
Concentrator Rim Angle	60 Degrees
Concentrator Geometric Error, 3 σ	12 Minutes
Concentrator Reflectivity	90 Percent
Concentrator Blockage Factor	5 Percent
Concentrator-Absorber Efficiency	67 Percent
Thermionic Generator Aperture Diameter	0.71 Inches
Thermionic Generator Efficiency	12.2 Percent
Thermionic Generator Power Output	144 Watts
Thermionic Generator Voltage (Four Converters in Series)	3.4 Volts
Thermionic System Efficiency	8.2 Percent

Note

a. In the final converter design, shown in Figure 8-2, the use of a re-entrant emitter sleeve design allows this thickness to be increased to 0.007 inches with no decrease in converter performance.

8.3 DESCRIPTION OF COMPONENTS

The solar thermionic system is composed of three major components: (1) solar concentrator, (2) thermionic generator, and (3) generator-concentrator support structure. The basic design of these three components is described in this section.

8.3.1 SOLAR CONCENTRATOR

Figure 8-1 shows the proposed concentrator design. The concentrator parabolic surface would be electroformed nickel, 15 mils in thickness. This surface would be bonded near the outside edge to a torus which would serve as the main structural member. A bonding material such as RTV-60 (room temperature vulcanizing rubber) would be used. The torus material would be nickel also to eliminate thermal expansion mismatch between the concentrator surface and the torus. The torus would be 2 inches in diameter with a 15-mil wall. The parabolic surface would be covered with a highly reflective multilayer coating such as Liberty Mirror Coating No. 747. This is a vapor deposited aluminum coating with an enhancing vapor deposited undercoat and overcoat*. A four-inch diameter hole would be provided in the center of the concentrator to aid in reflectance measurements of the concentrator surface (see Section 8.6.1). The edge of the concentrator surface would be notched at three locations (120 degrees apart) to provide attachment points for the generator support arms.

Nickel was selected for the electroformed surface because most of the existing experience in electroformed concentrators is with nickel. However, work is being conducted on electroforming aluminum (Reference 8-1) and should this work progress to the point where nickel concentrator performance could be matched with aluminum, then aluminum would definitely be preferred. The capability to fabricate a high performance stretch-formed aluminum concentrator should also be investigated since this offers a potential means of eliminating the nickel concentrator. Aluminum has two major advantages over nickel for this application: (1) it would reduce the concentrator weight by approximately two thirds, and (2) it would

*The exact details of the Liberty Mirror coatings are company proprietary.

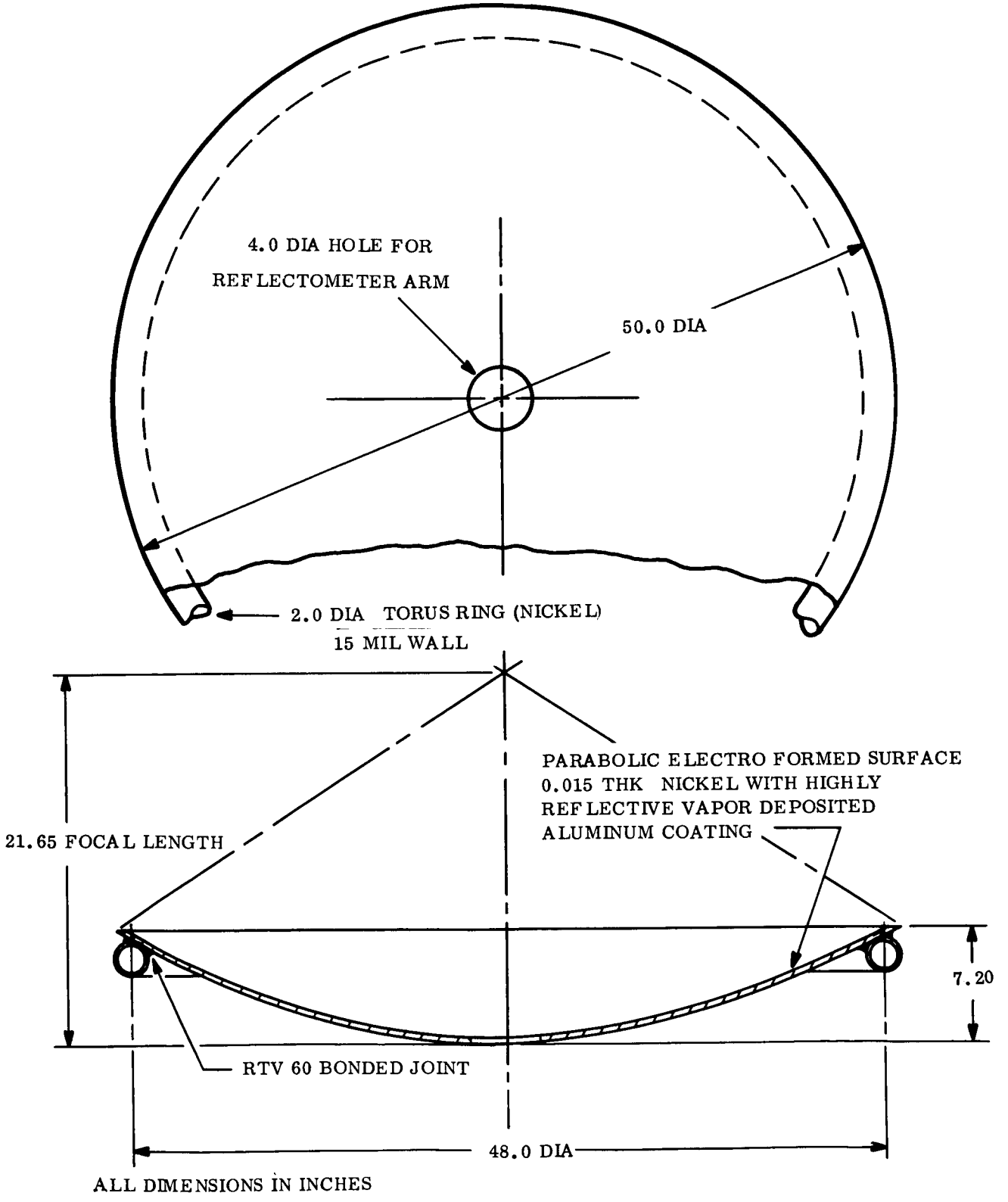

Figure 8-1. Solar Concentrator

eliminate the large disturbance torques resulting from the interaction between the magnetic nickel concentrator and the earth's magnetic field (see Section 11.3.7).

The concentrator skin thickness could probably be made smaller than 15 mils. Concentrators in this size range have been built with 8 to 10-mil skins (References 8-1 and 8-2). Calculations performed in Reference 8-1 indicate that for concentrators of this size a skin thickness of less than 10 mils is adequate to withstand launch loads. However, a 50-inch diameter concentrator, with a 10-mil skin, would have to be handled with extreme care. Also, some difficulty has been experienced in the past with separating 10-mil concentrator surfaces from the male master during the electroforming process. These separation difficulties have resulted in some of the concentrator geometric accuracy being lost. Therefore, since weight is not a major problem in this application, a skin thickness of 15 mils was chosen in an attempt to minimize handling difficulties and achieve a more accurate concentrator.

The particular scheme shown for attaching the parabolic surface to the torus is only one of several which might be employed. This particular approach was chosen because it allows the "effective" concentrator diameter to equal the outside diameter of the torus. This simplifies the packaging problem since the overall concentrator diameter is minimized (no overhanging torus). This scheme was used successfully on a recent solar concentrator fabricated by the General Electric Re-entry Systems Department for NASA-Langley (Reference 8-1).

The center hold and the three notched areas at the outside diameter of the concentrator would be formed during the electroforming process. This would be accomplished by masking the male master so that no nickel was plated in those areas. This procedure has been used successfully in fabricating concentrators in the past (References 8-2 and 8-3) and is considered state of the art.

Liberty Mirror Coating No. 747 was selected for the concentrator surface because of its measured high reflectivity (see Section 4.4.1.1-Volume II) on electroformed nickel. Also this coating has been used with good results on solar concentrators in the past.

The manufacturer of this coating states it will meet the following specifications (Reference 8-4):

a. Reflectivity - The coating* shall not have less than 88 percent total reflectivity for light in the visible region as measured with a Weston Photronic cell with a viscor filter and a tungsten lamp supplying light at an angle of incidence of 22.5 degrees.

b. Adherence - No visible part of the coating shall be removed by the cellulose tape test described below: The tacky surface of cellulose tape shall be carefully placed in contact with a portion of the reflective surface and firmly rubbed against that surface. It shall then be quickly removed with a snap action which exerts the greatest possible stripping action of the reflective film.

c. Hardness - No evidence of film removal or film abrasion shall be visible to the eye when the following test is applied: A pad of clean dry cheese cloth (previously laundered) 3/8-inch in diameter, 1/2-inch thick, bearing with a force of one pound on the coating shall be rubbed across the coated element in any direction 25 times.

d. Corrosion Resistance - There shall be no noticeable deterioration of the finished surface when given the salt atmosphere test described here: The coating shall be placed in a thermostatically controlled cabinet with a salt atmosphere for 24 continuous hours at a temperature of 95°F. The salt atmosphere shall be obtained by allowing a stream of air to bubble through a salt solution containing 1 1/2 pounds of sodium chloride per cubic foot of water.

---

*In the manufacturer's specification the reflectivity sample is deposited on a glass substrate. Past experience indicates that the measured reflectivity of a coating on an electroformed nickel substrate is essentially the same as that on a glass substrate (Reference 8-2).

e. Temperature - The coating shall function satisfactorily and shall not be damaged by exposure to an ambient temperature of minus 60^{o}F and plus 500^{o}F.

Of course these tests are not sufficient to qualify the coating for use in a space application but they do indicate that it has some of the required properties. Final selection of a coating for the concentrator surface would require a test and evaluation program that considered, among others, the effects of the following factors:

a. Temperature
b. Pressure
c. Low energy protons
d. Ultraviolet radiation
e. Micrometeoroids

If prior to a solar thermionic flight experiment a space experiment was conducted, such as the one described in Reference 8-5 and Section 5.2.6 (Volume II) of this report, evaluating the effects of the space environment on reflective surfaces this information would be extremely valuable in selecting a coating for this application.

8.3.2 THERMIONIC GENERATOR

The design of the generator is presented in Figures 8-2 (sheets 1 and 2) and 8-3. The parts description and the corresponding materials are listed in Table 8-2. The generator consists of four identical thermionic converters spaced at 90-degree intervals around the axis of the generator cavity. The emitter pieces of the converter are so shaped as to cover almost completely the interior wall of the cavity absorber. The structural details of the thermionic converters are very similar to those of the Advanced Solar Energy Thermionic converter developed for JPL in a current program at Thermo Electron Engineering Corporation, except that the inter-electrode spacing is two-mils as opposed to the value of one-mil used in the advanced converter. The most important design features are as follows:

a. To reduce the danger of electrical shorting due to high temperature creep under ground test conditions a re-entrant emitter sleeve is used to support the relatively heavy emitter. The re-entrant emitter support also enables optimization of the heat losses in the emitter support without having to use an excessively small wall thickness in that member. A further advantage is that this structure permits a reduction in radiation losses by a self-shielding effect.

b. The use of a concealed ceramic seal, well isolated from thermal expansion stresses, and shielded by other converter components from accidental meteorite impact.

c. A one-piece collector structure from which the converter is attached to the thermionic generator. Attachment at the point shown has the advantage that the heaviest converter component is supported directly, at a point close to the converter center of gravity.

d. A finned radiator structure consisting of four fins so oriented that they have a minimum look angle at the cesium tube of the converter. This is an important feature to reduce both cesium reservoir tube dimensions and generator radiator warm up time. The radiator fins can also be used to provide support at the end of the cesium tubes by means of a thin metal washer, thus avoiding cantilever movements on the cesium tubes resulting from vibration during the launch phase.

Figure 8-4 is a photograph of the Advanced Solar Energy Thermionic converter structure which shows some of the features outlined here.

The converters are provided with a rectangular, beveled, flange around the cavity-emitter pieces (Part 30) which helps to reduce interstitial radiation losses from the cavity absorber.

The common support for the four converters is a single block of niobium (Part 53), appropriately machined to accommodate the converter structures. The back plate (Part 62) helps to protect the internal shielding of the generator from damage during handling.

Table 8-2. Generator Parts List

Part Number	Description	Material	Number Required
1	Cavity piece	Ta	1
2	Emitter	Re	4
3	Collector	Mo	4
4	Emitter support	Ta	4
5	Intermediate support	Nb	4
6	Outer seal flange	Nb	4
7	Seal	Al_2O_3	4
8	Inner seal flange	Nb	4
9	Cesium tube	Ni	4
10	Cesium reservoir	Cu	4
11	Radiator fins	Cu	16
12	Cesium reservoir ring	Ni	4
13	Cesium reservoir heater	-	4
14	Terminal post	Nb	4
15	Lead clamp	Nb	4
16	Lead connector	Cu	4
17	Stranded lead	Cu	4
18	Emitter terminal screw	Ti	4
19	Emitter terminal nut	S S	4
20	Collector terminal	S S	4
21	Collector terminal screw	S S	4
22	Collector terminal nut	S S	4
23	Ceramic stand off	Al_2O_3	16
24	Support insulator	Al_2O_3	16
25	Washer	S S	16
26	Mounting screw	S S	16
27	Emitter shield #1	Ta	20
28	Emitter shield #2	Ta	80
29	Emitter shield #3	Ta	80
30	Cavity support piece	Ta	4
31	Insulator washer #1	ThO_2	16
32	Insulating washer #2	ThO_2	32
33	Cavity screw	Ta-W[a]	16
34	Cavity nut	Ta-W	16
51	Rear cavity piece	Ta	1
52	Rear cavity shield	Ta	20
53	Generator block	Nb	1
54	Aperture cone	W	1
55	Shield cone	Ta	1
56	Generator support ring	S S	1
57	Generator block support	S S	4
58	Cone screws	Ta-W	8
59	Shield screw washer	S S	8
60	Shield screw	S S	8
61	Shield nut	S S	8
62	Block cover	Nb	1
63	Block screws	S S	4

Note:

a. Ta-W = Tantalloy 10 percent W.

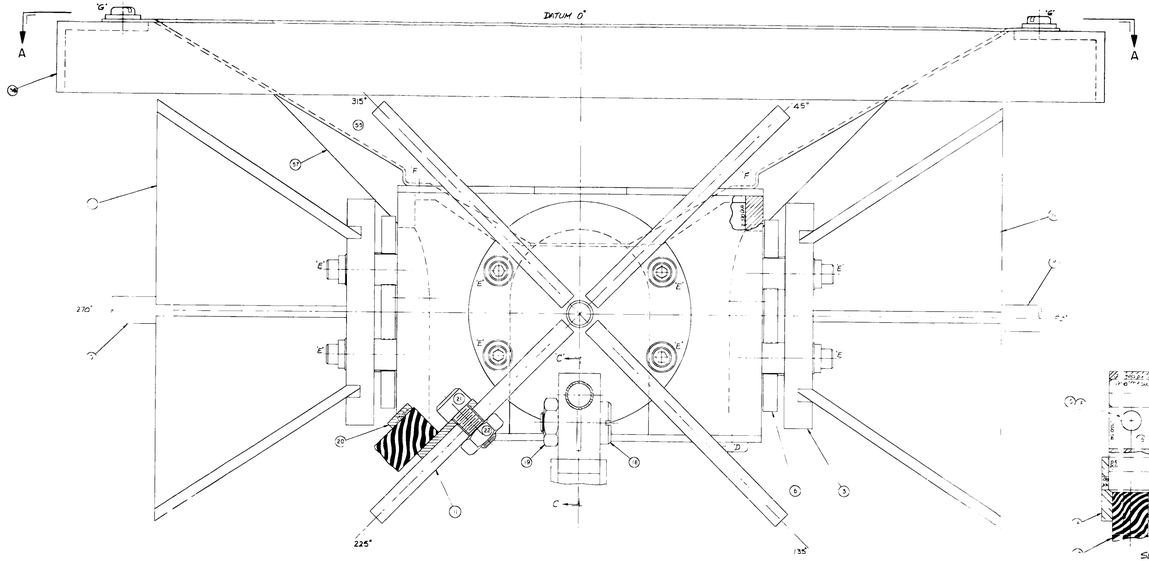

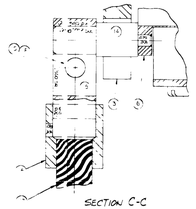

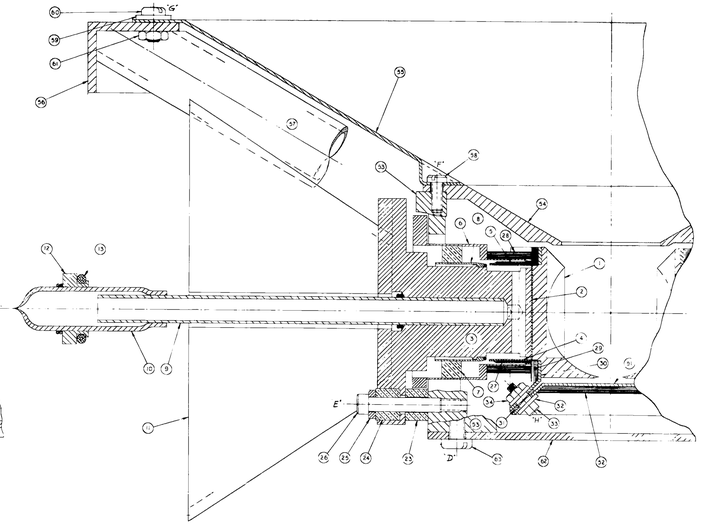

Figure 8-2. Thermionic Generator
(Sheet 1 of 2)

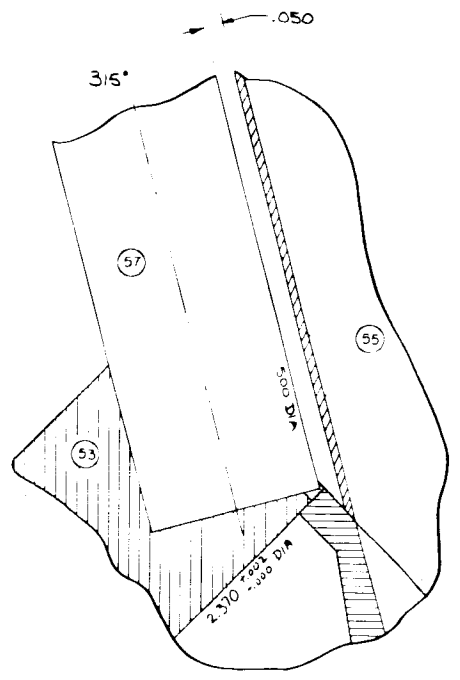

SECTION B-B

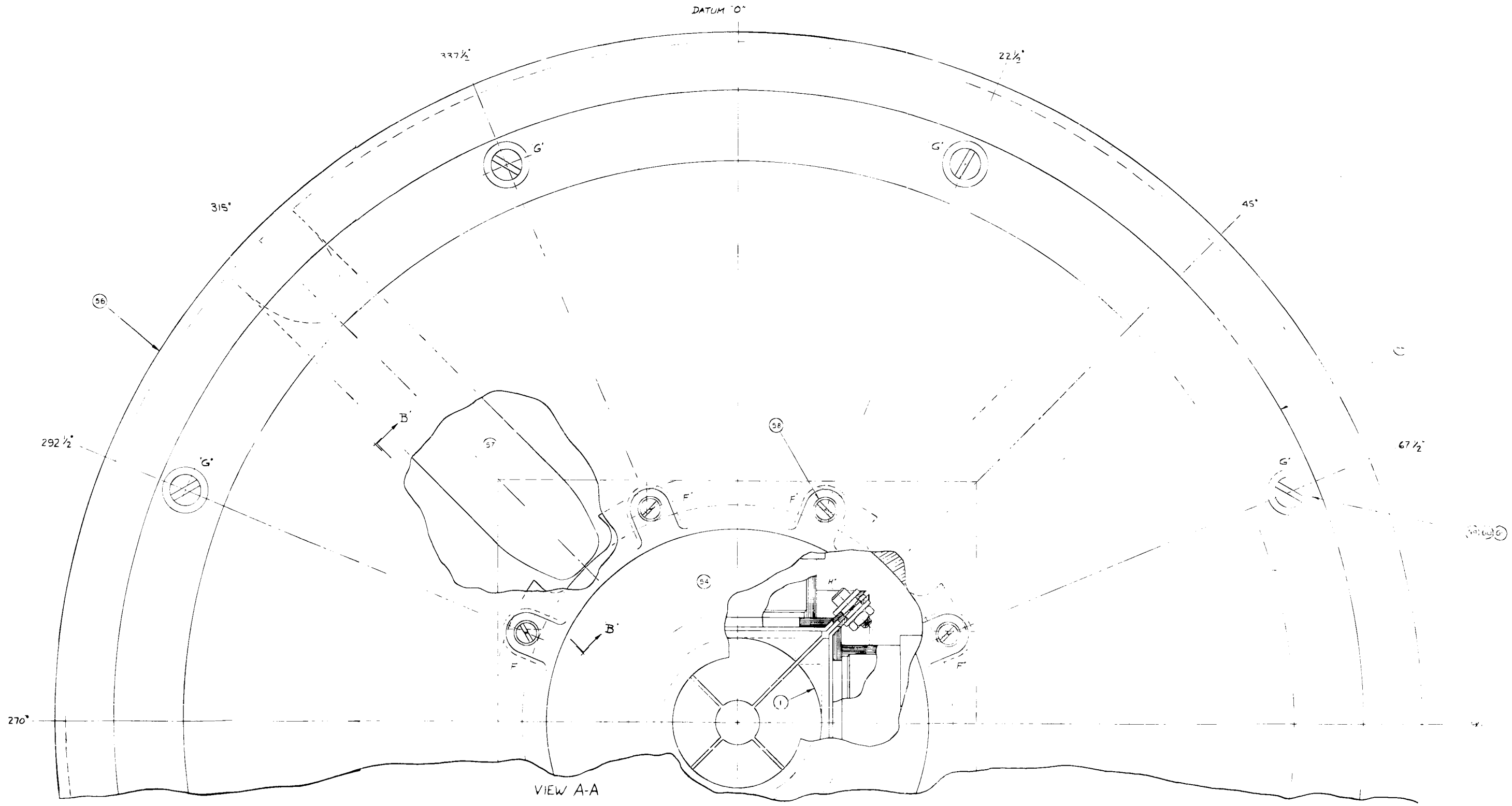

Figure 8-2. Thermionic Generator
(Sheet 2 of 2)

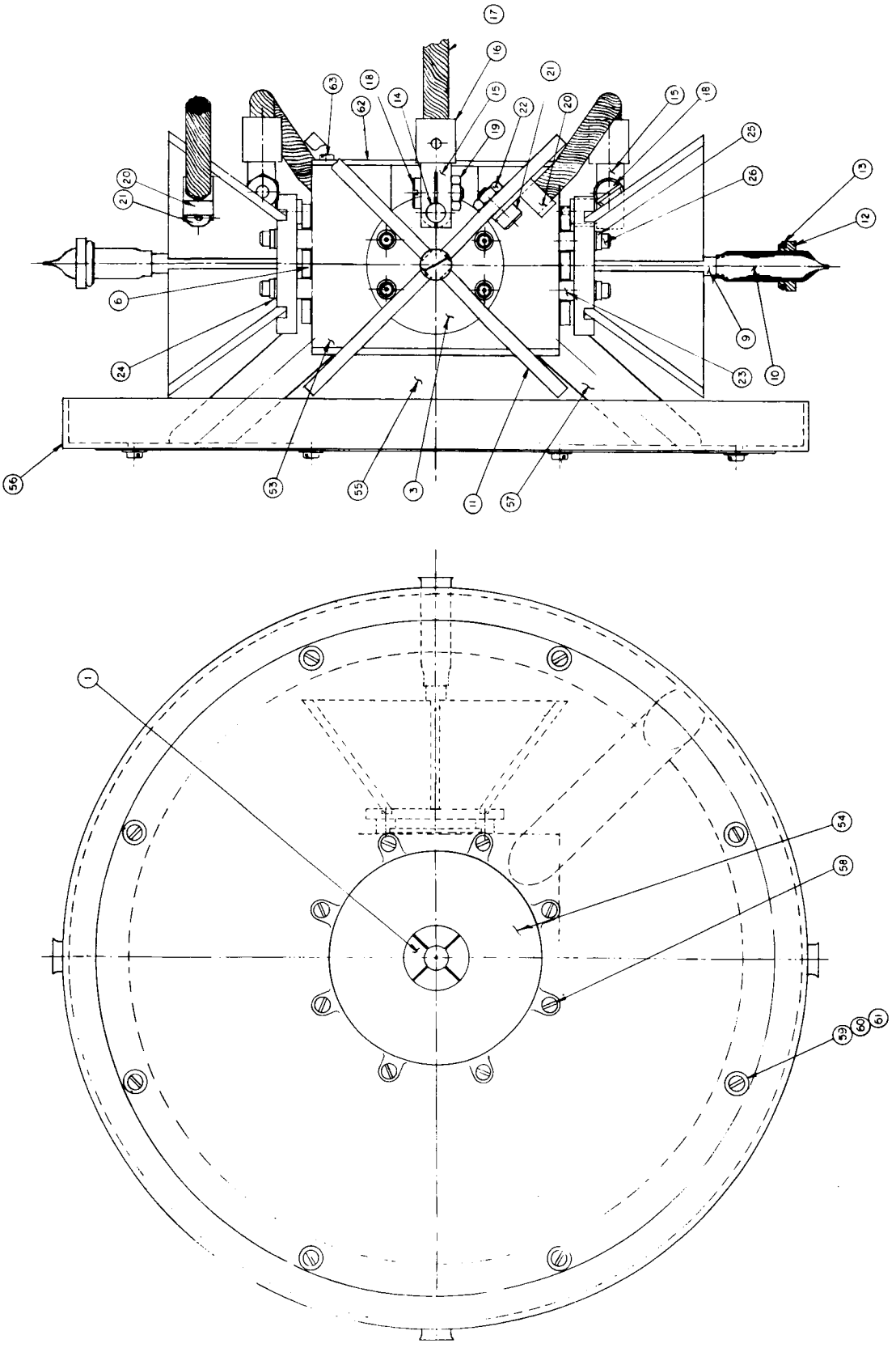

Figure 8-3. Thermionic Generator Assembly Drawing

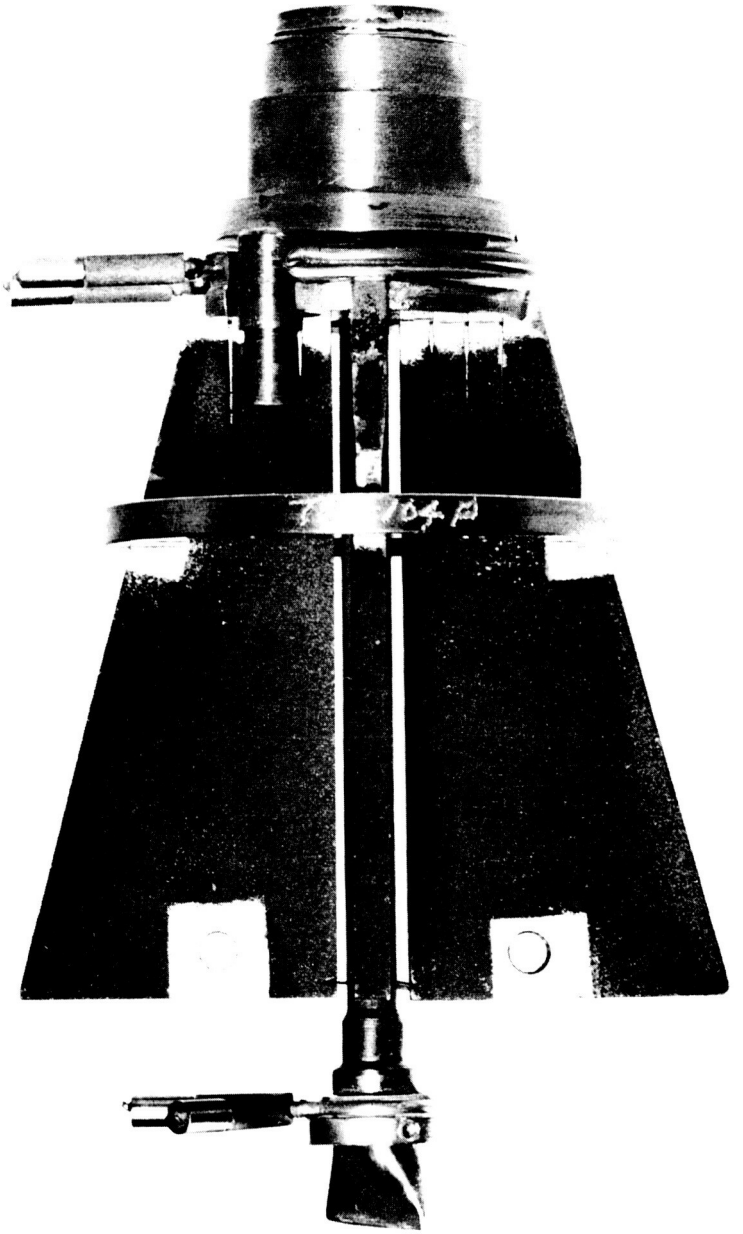

Figure 8-4. Advanced Solar Energy Thermonic Converter Structure

The front cone of the generator consists of two pieces: (1) an inner tungsten cone capable of withstanding highly concentrated misdirected solar energy, and (2) an outer tantalum shield (Part 55) designed to prevent impingement of concentrated solar energy on the converter radiators.

The generator support block is connected to a support ring (Part 56) by means of four tubes (Part 57) welded into the generator block and to the support ring.

8.3.3 GENERATOR-CONCENTRATOR SUPPORT STRUCTURE

The proposed approach for mounting the solar thermionic generator and concentrator is shown in Figure 8-5.

The generator mounting ring (see Figure 8-3) would be supported from the parabolic concentrator torus by three truss tubes 120 degrees apart. The torus support ring would be attached to the spacecraft body at the three points formed by the intersection of the three truss tubes with the torus ring. As mentioned in Section 8.3.1, three small slots must be formed in the parabolic concentrator surface to accommodate the truss tubes.

This design allows loads from the generator to be passed directly into the spacecraft body without loading the parabolic concentrator. The RTV-60 bond between the parabolic surface and the torus would minimize deformations resulting from loads transferred from the torus to the parabolic surface.

8.3.3.1 Method of Attaching Concentrator Torus to Spacecraft

The attachment of the torus to the spacecraft body is shown in detail in Figure 8-5. The attachment is designed to provide complete structural support of the torus during launch acceleration and vibration loading, as well as allow the torus to thermally expand or contract with respect to the spacecraft body without causing induced stresses.

The support at point A consists of a single self-aligning, mono ball type, bearing. This point supplies support loads in three orthogonal directions but has no moment capability. This allows rotation to take place at point A, but no relative motion between the torus and the spacecraft.

The support at point B consists of a short swinging link hinged at each end. The hinge-lines at each end of the link are parallel and are both normal to a line joining points A and B. This allows point B to move relative to point A along a line joining points A and B, but does not allow motion in any other direction.

The support at point C consists of a short link with a self-aligning, mono ball type bearing at each end. At this point the torus can move with respect to the spacecraft in any direction in the plane defined by points A, B and C, but is restrained from moving in a direction normal to the ABC plane.

If, for example, the torus were to increase in diameter with respect to the spacecraft body, point B would move away from point A along the line AB. Point C, however, would move both radially outward and tangentially in a clockwise direction (looking down on the torus). Due to rotations of the links, the torus would also move slightly out of plane from its original position, but this angle would be extremely small and of no consequence with the type of attitude control system proposed (see Section 11.1).

8.3.3.2 Thermionic Generator Alignment

Locating the generator support ring on the generator mounting surface would be achieved by accurately locating the four holes in the generator mounting ring. It is expected that matched tooling would be used for this purpose, and that the operation would be performed after assembly of the parabola, torus, and support structure was completed, and the optical axis of the concentrator determined. Location of the generator axis to within 0.01 inches of the desired location could be readily achieved by this means.

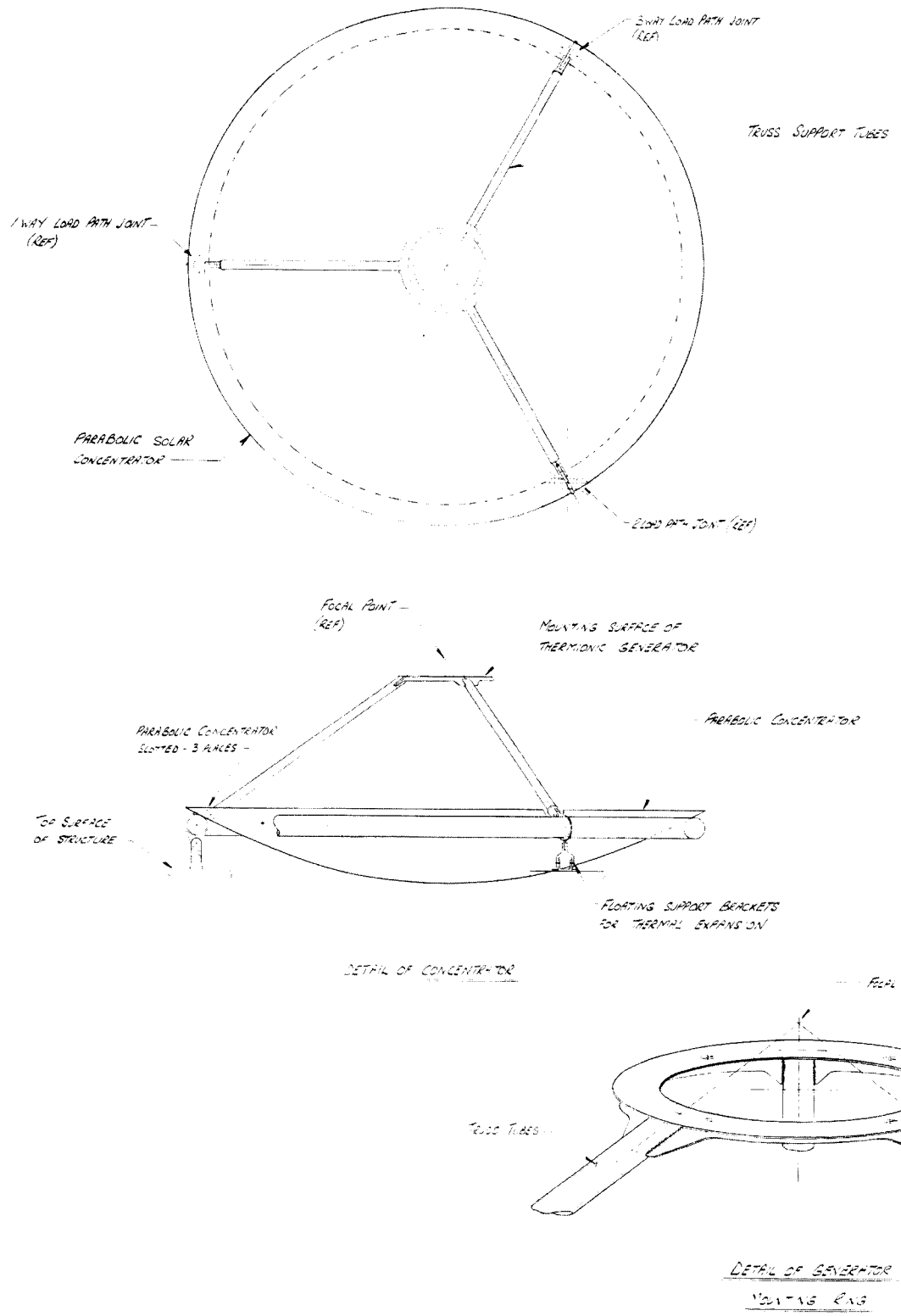

Figure 8-5. Proposed Construction of Solar Concentrator - Generator Support Structure

Angular alignment of the generator axis to the optical axis of the concentrator, and accurate location of the generator along the optical axis would then be accomplished by shimming at the four generator mounting holes against an optical reference.

It would be necessary to establish the optical axis and focal length of the concentrator under solar and thermal conditions simulating those expected in space, since these quantities can be significantly effected by the operating environment.

8.4 THERMIONIC GENERATOR DESIGN ANALYSIS

In Section 4 (Volume II) the solar concentrator and thermionic converter performance was analyzed in detail and these performance estimates are considered to apply in this section. However, the performance of the total generator (thermionic converters plus generator structure) could only be estimated from past experience (see Section 4.3-Volume II) because the generator design was not available to be analyzed. Now that the design has been established its performance must be analyzed and compared with the assumptions made in Section 4.3.

8.4.1 CAVITY FLUX ANALYSIS

A cavity flux analysis was conducted to determine the distribution of the solar and thermal radiation within the generator cavity, and the cavity reradiation loss. For the purpose of this analysis, the geometry of the generator cavity, which is shown in Figure 8-6, was simplified to that shown in Figure 8-7. The simplification consists primarily of approximating the nearly hemispherical bottom of the generator cavity by a flat bottomed cylinder. The cavity was then divided into three principal areas which are shown in Figure 8-7 and are defined as follows:

a. Area No. 1 consisting of the heated faces of the thermionic converters and the interstitial spaces between them.

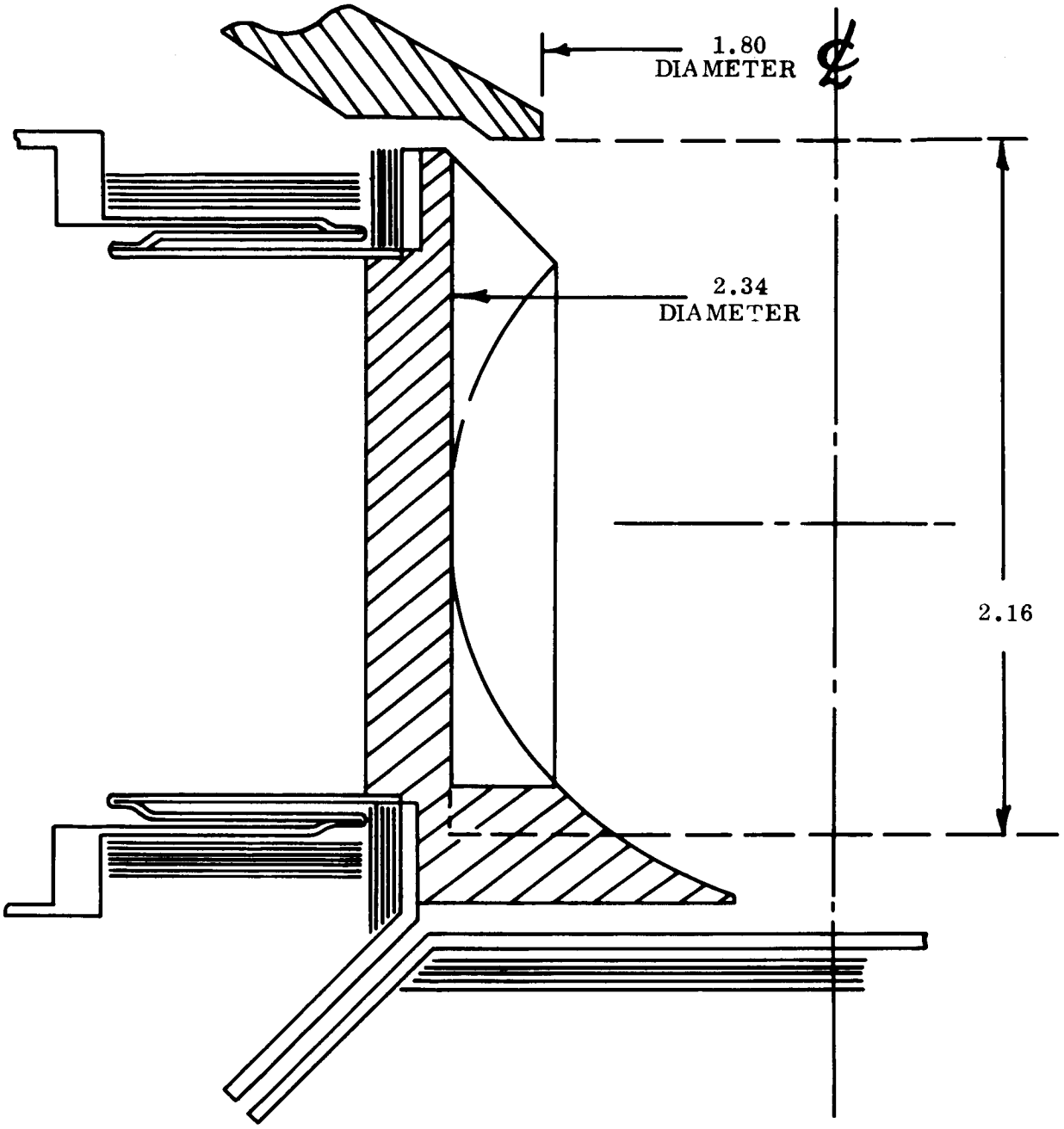

ALL DIMENSIONS IN CENTIMETERS

Figure 8-6. Generator Cavity Geometry

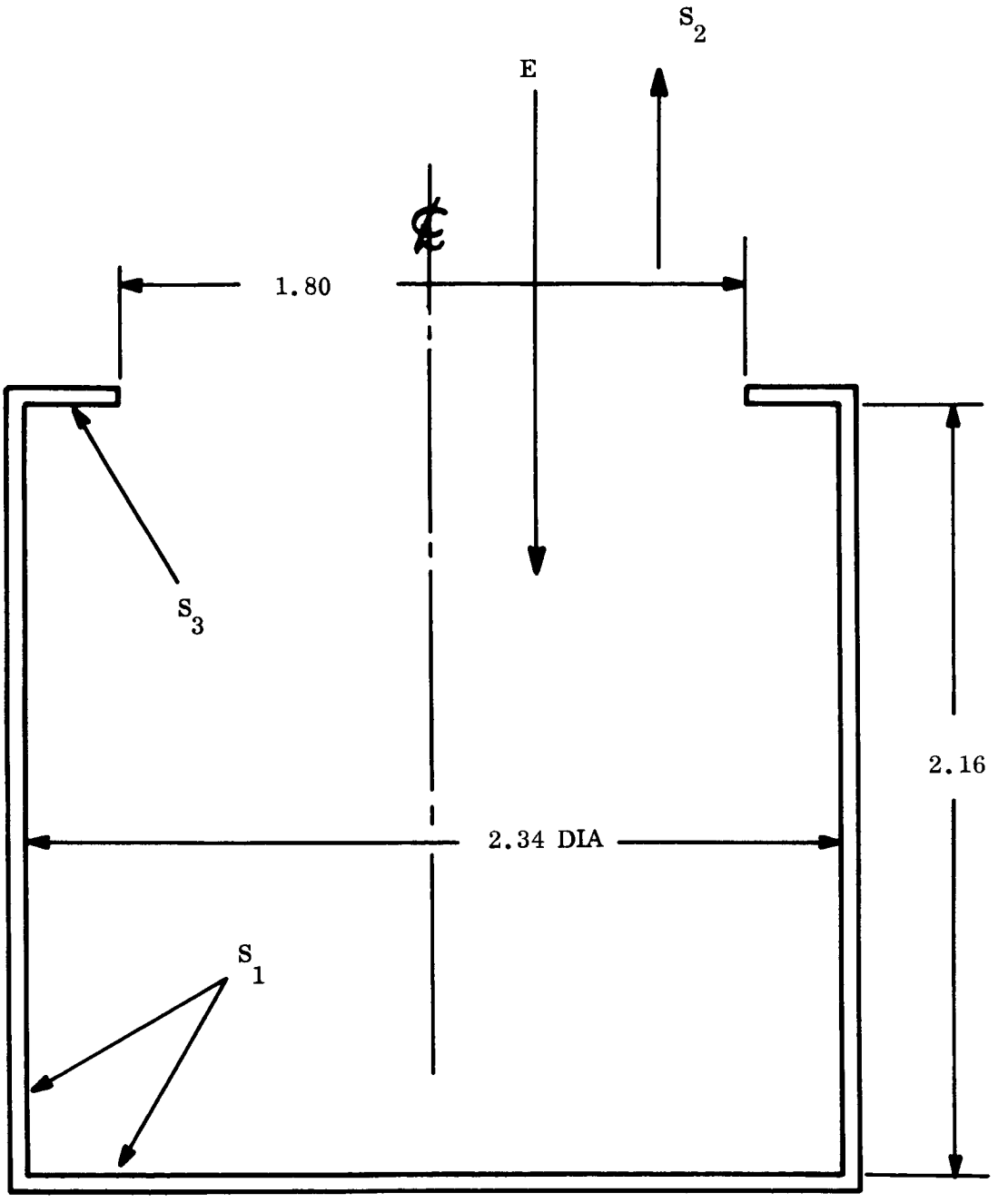

ALL DIMENSIONS IN CENTIMETERS

Figure 8-7. Idealized Generator Cavity Geometry

b. Area No. 2 equal to the cavity aperture.

c. Area No. 3 consisting of the portion of the front cone exposed to the interior of the cavity.

The numerical values of these areas and the corresponding radiation view factors are calculated in Appendix B. Assuming that the cavity surfaces radiate like perfect diffused surfaces, and that they are each at a uniform temperature, it is possible to write simple equations describing the distribution of radiant flux within the cavity. These equations are presented in Appendix B for both the solar and the thermal components of the cavity radiation. To obtain numerical solutions, the absorptivity of the heated faces of the thermionic converters to the incident solar radiation was assumed to be 0.80. This relatively high value would be achieved by means of fine grooving of the surfaces. In Appendix B it is shown that the corresponding thermal emissivity of these surfaces is approximately 0.56. The solar absorptivity and the thermal emissivity of the cone surface exposed to the interior of the cavity were assumed to equal 0.50 and 0.25 respectively. The cavity flux distribution was then calculated for different values of incident solar flux and different emitter temperatures. The results of these calculations are presented in Table B-1 of Appendix B, and are shown graphically in Figures 8-8 and 8-9. The 1412 watts curve, shown in Figure 8-8, represents the energy entering the generator cavity at the design point (see Section 4.4.2-Volume II). The value of 1271 watts represents a 10 percent decrease with respect to the design point value. The energy available to the thermionic converters, Q_E, plotted in Figures 8-8 and 8-9, was obtained by subtracting the interstitial and shielding radiation losses from the values of Q_1 listed in Table B-1 (Appendix B). The interstitial and shielding radiation losses were determined in the following manner. Of the two types of interstitial spaces between converters, represented by A_1 and A_2 in Figure 8-10, only the A_1 gap was considered to contribute significantly to the cavity losses. Any radiation penetrating the interstitial spaces represented by A_2 has such a large chance of striking the converter emitter pieces that this radiation was not considered as a loss. The loss through area A_1 is calculated in Appendix C and was assumed to take place with an effective absorptivity of 0.5. The cavity shielding losses were estimated by assuming that

they would equal five percent of the black body radiation loss that would take place through an area equal to that of the shielding. These calculations are also shown in Appendix C.

It is interesting to note in Table B-1 (Appendix B) that the reradiation from the cavity for the various conditions studied is always very close to black body radiation. At the design point input of 1412 watts and a 2000^{o}K emitter temperature, the cavity reradiation exceeds black body radiation by eight percent.

8.4.2 CONVERTER HEAT TRANSFER AND GENERATOR ENERGY BALANCE

Now that the energy available for operating the thermionic converters has been established as a function of emitter temperature and energy entering the generator cavity (Figures 8-8 and 8-9), the generator energy balance can be checked by computing the converter energy requirements and comparing this with the energy available. This is the analytical procedure for establishing the generator energy balance presented in Reference 8-6. An understanding of the thermionic converter heat transfer is also useful in sizing the converter radiator structure. The magnitudes of the various converter heat transfer components are presented in Section 4.2.2 (Volume II) and are assumed to be valid for the converter design presented in Figure 8-2. Some of the assumptions made in the converter heat transfer calculations are reviewed in Appendix D. Table D-1 shows the calculated values of the energy required by one converter at various values of emitter temperature and output current. Table D-2 (Appendix D) shows corresponding values of energy rejected to the collector-radiator structure for the same range of emitter temperatures and output currents. These values are plotted in Figures 8-11 and 8-12.

In addition to showing the energy required per converter, the dashed line on Figures 8-11 and 8-12 indicates how much energy is actually available to each converter for a solar input of 1412 watts. From Figure 8-11 it is apparent that there is approximately five percent (11 watts) more energy available to each converter than is required to operate at the design point. A number of alternatives could be proposed such as:

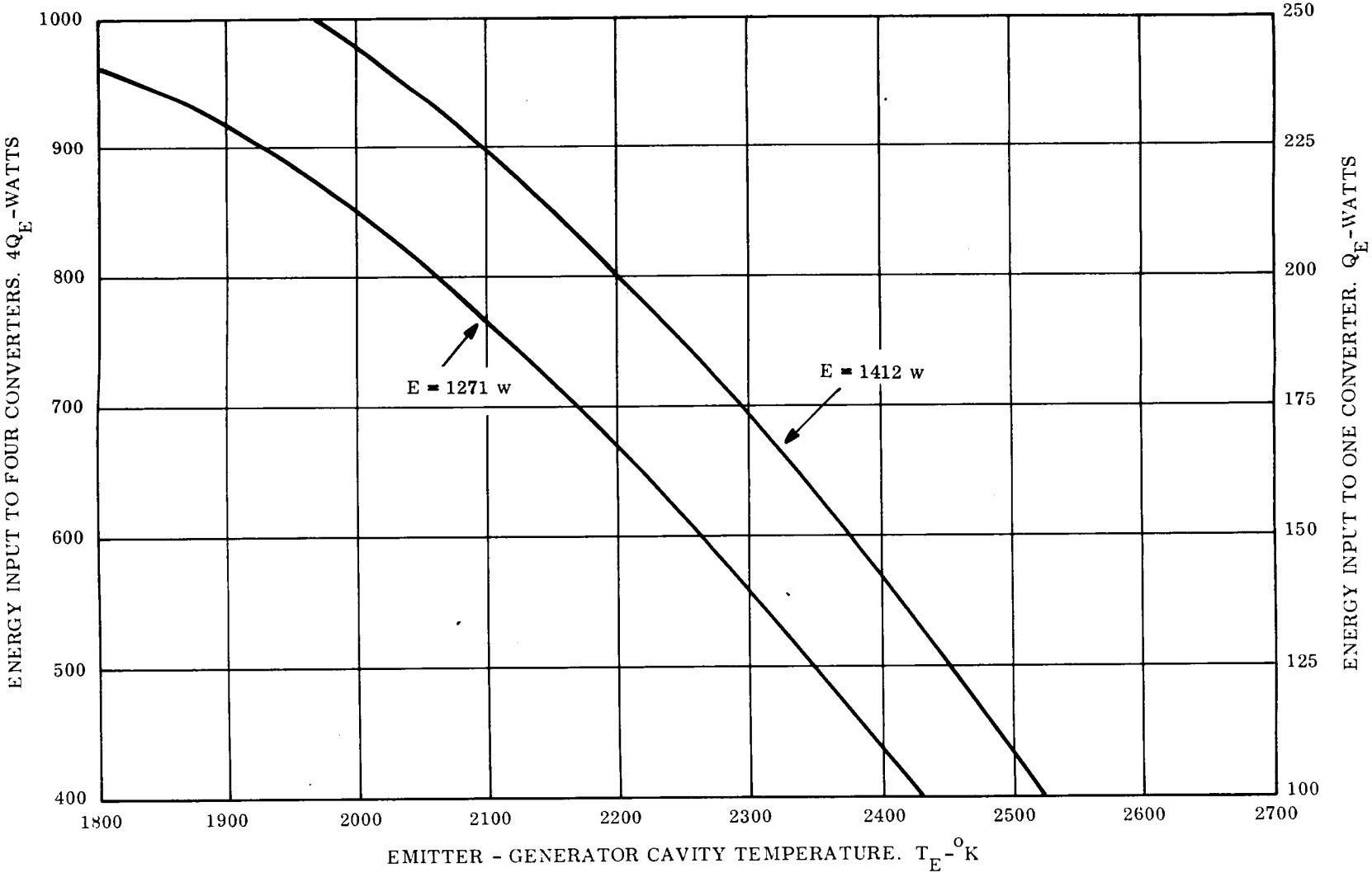

Figure 8-8. Energy Available to Converters vs. Emitter-Generator Cavity Temperature

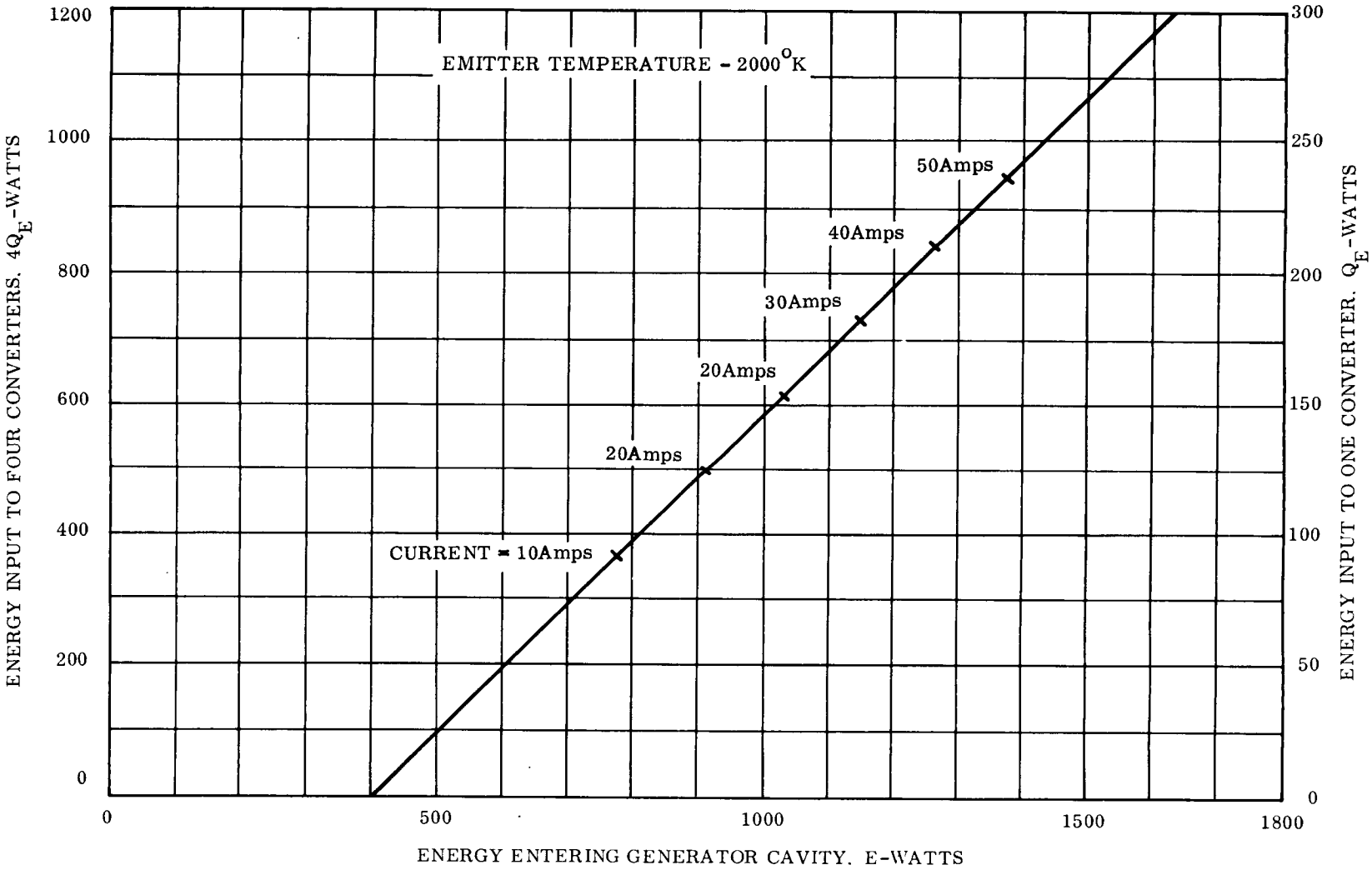

Figure 8-9. Energy Available to Converters vs. Energy Entering Generator Cavity

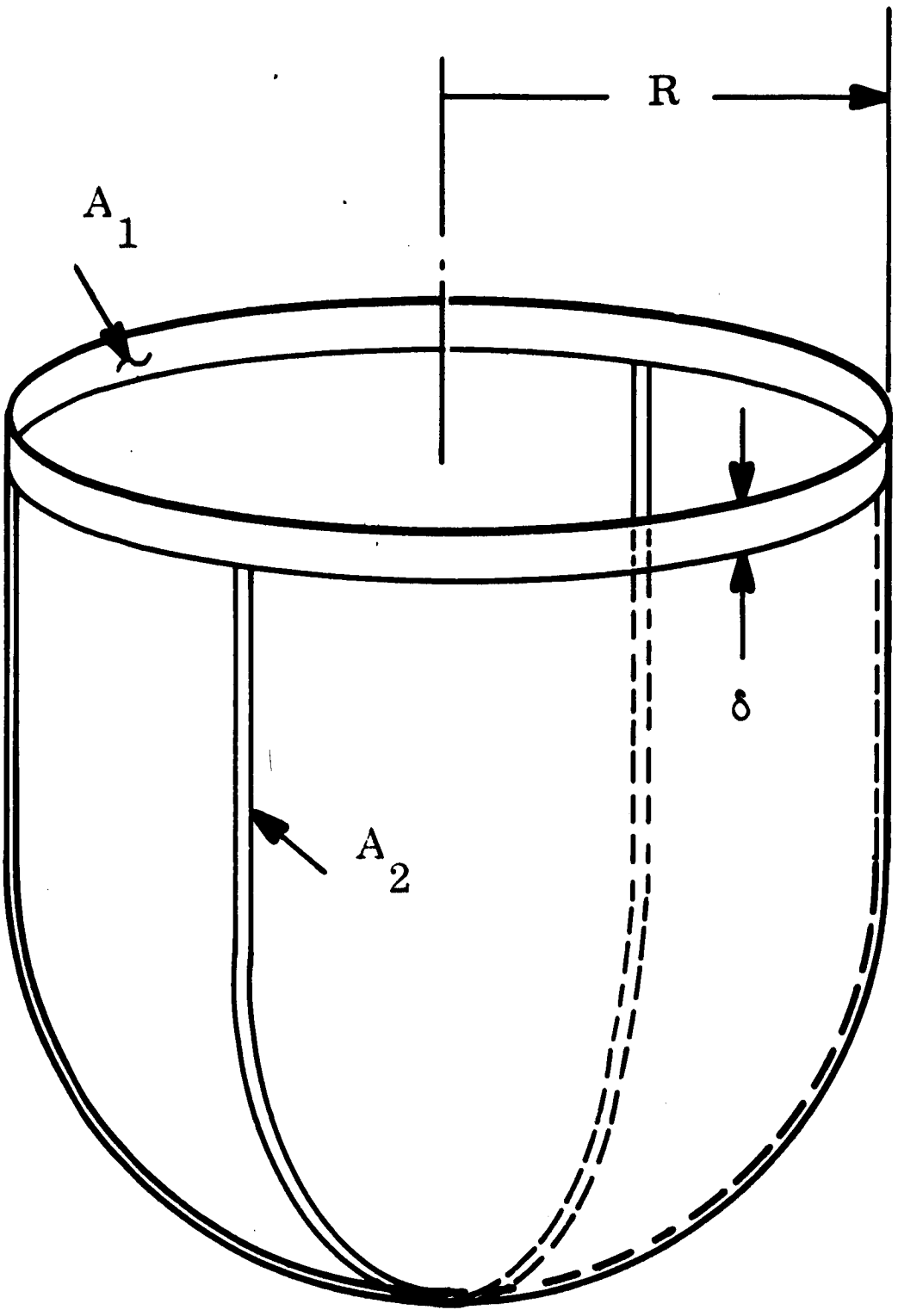

Figure 8-10. Geometry of Cavity Interstices

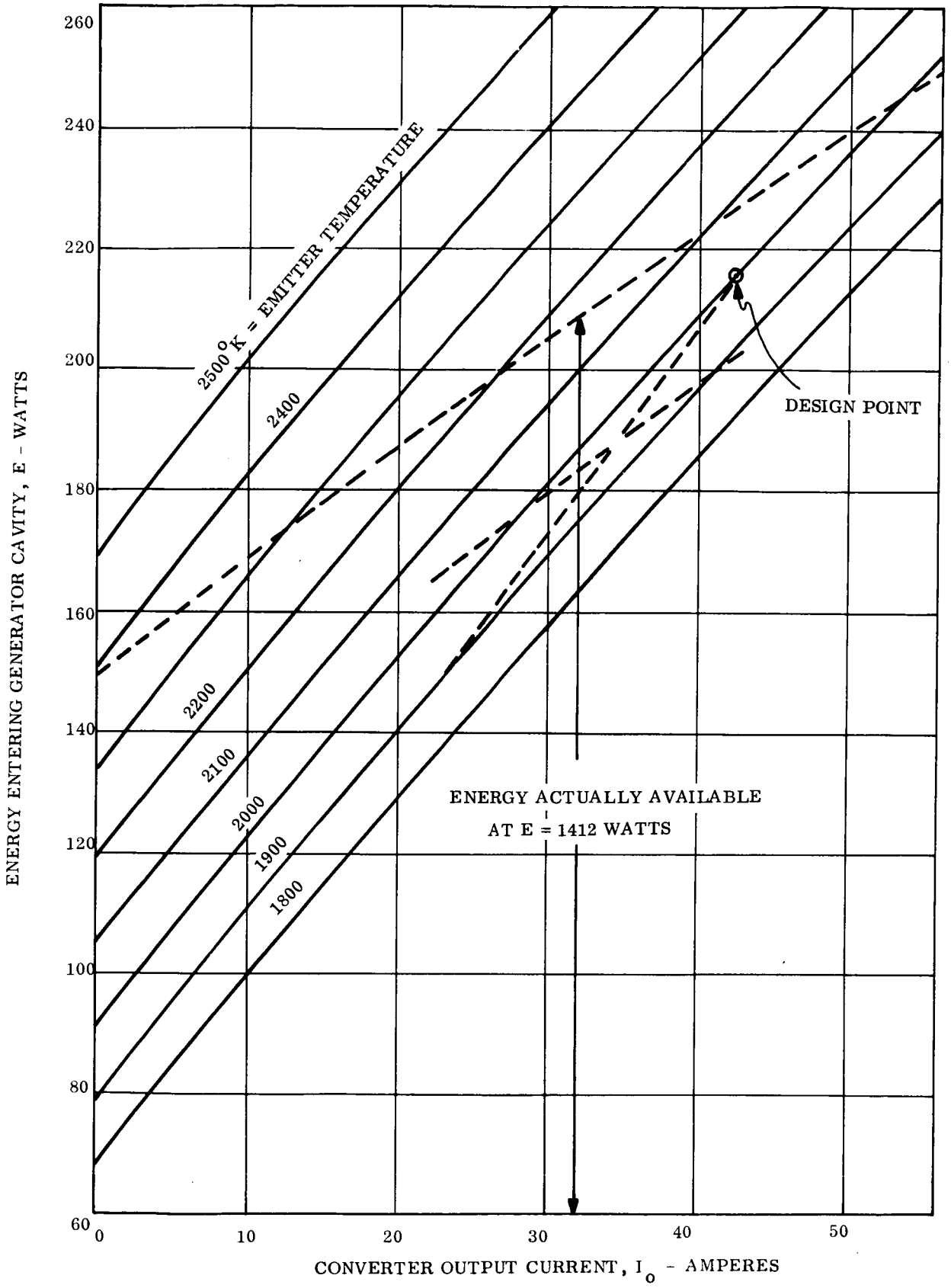

Figure 8-11. Energy Required by Converters

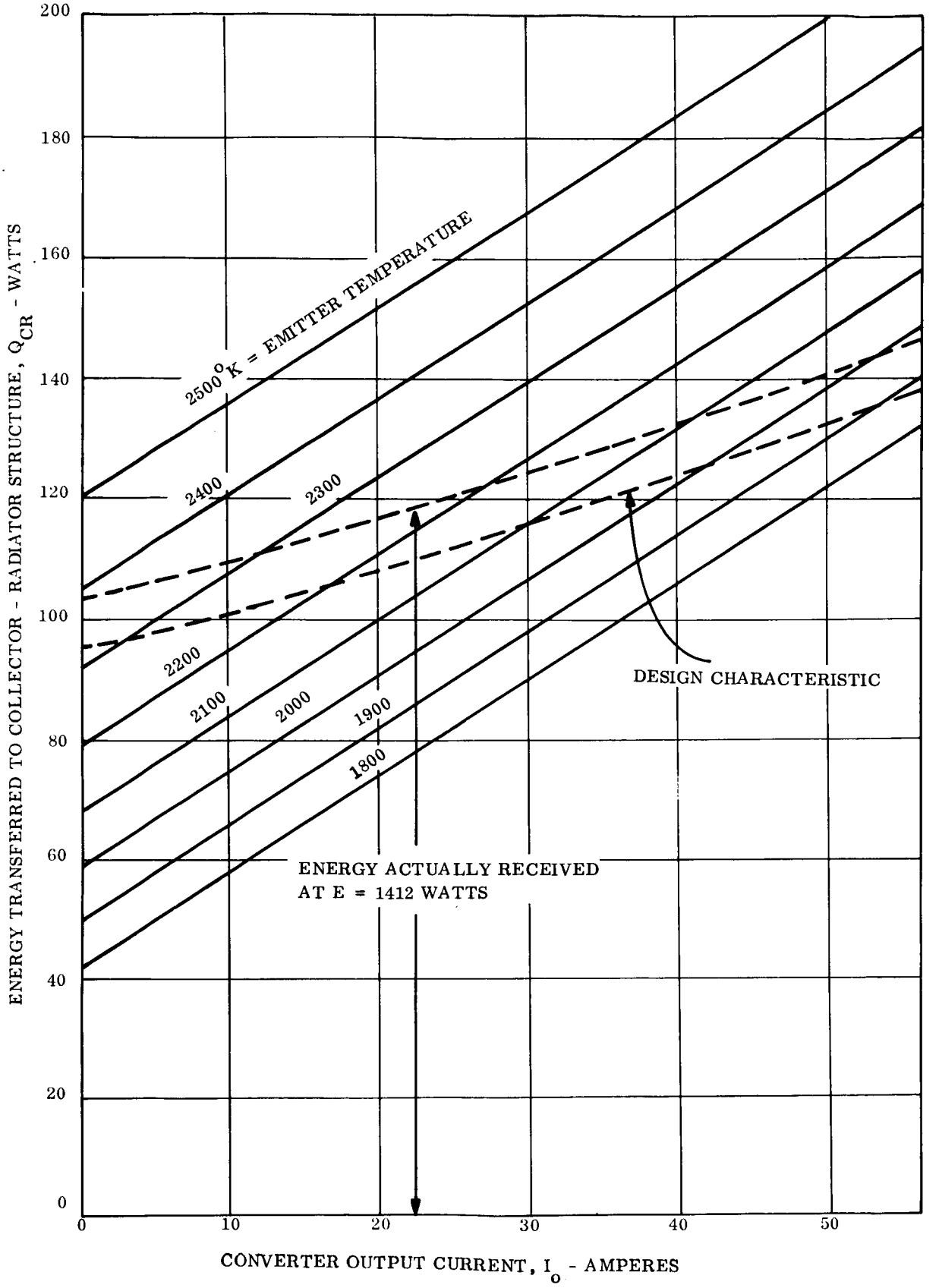

Figure 8-12. Energy Received by Collector-Radiator Structure vs. Output Current and Emitter Temperature

a. It would be possible to operate the converters at the selected design point with a slightly smaller solar concentrator.

b. With the specified value of input solar energy (1412 watts) the converters could be operated at the same output current density at an emitter temperature of approximately 2090^{o}K.

c. The converters could be operated at an emitter temperature of 2000^{o}K and at an output of 66 instead of 42.4 amperes.

d. For the specified value of input energy (1412 watts), the converter emitter area could be increased from 2 to 2.2 square centimeters and the converters operated at an emitter temperature of 2000^{o}K. This, of course, would increase the generator power output by 10 percent.

Anyone of these approaches would further enhance the thermionic system performance; but based on past hardware experience the recommendation is made that the five percent energy factor be held in reserve as a safety factor. It is impossible to calculate, with a high-degree of accuracy, the thermal losses from the thermionic generator. Therefore, any attempt to account for an apparent five percent excess in energy is felt to be unrealistic. As a result the energy available to the converters was assumed to be represented by a lower curve, than the dashed line shown in Figure 8-11, that would pass through the design point. The effect of this shift in the value of available energy to the thermionic converters is shown in Figure 8-12, where a new dashed curve has been drawn and is labeled "Design Characteristic."

8.4.3 RADIATOR DESIGN

In Section 4.2.2 (Volume II), the optimum collector temperature was estimated to be 998^{o}K. Figure 8-13 presents the collector dimensions corresponding to the thermionic converter design shown in Figure 8-2. The calculations performed in Appendix E indicate that at the design point, the collector structure must transfer 111.7 watts. Appendix E also presents

the calculations establishing the thermal resistance of the collector structure at 1.38°C per watt. Thus, for a heat transfer of 111.7 watts, a temperature drop in the collector of 154°C is expected, yielding a design point temperature at the base of the collector of 844°K. The radiator design problem then consists of determining the radiator structure of the lightest weight which, with an initial temperature of 844°K at the base of the collector, is capable of dissipating the expected radiator heat load. Because of conduction losses down the emitter support structure through the insulating seal into the midpoint of the collector structure, the actual heat load seen by the radiator is somewhat larger than 111.7 watts. For the radiator design, this heat load has been estimated at 128.1 watts. Figure 8-14 shows the basic radiator geometry which was adopted for the converter design shown in Figure 8-2. The converter support mechanism, the cesium tube, and the remainder of the generator structure tend to define values for the parameters, a, e, and ψ shown in Figure 8-14. Therefore, for the selected generator configuration, the value of a is 2.03 centimeters, the value of e is 0.32 centimeters and the value of ψ is $42^{\circ}50'$. The radiator design problem is then reduced to the determination of the radiator length, c, and the variation in fin thickness, h, which will yield the lowest radiator weight to dissipate the required amount of heat at the collector base temperature given. It was found in the design optimization that for this particular radiator requirement, variations in fin thickness do not result in significant decreases in radiator weight, and the numerical calculations were therefore conducted assuming a constant fin thickness. To minimize the radiator weight, various fin thicknesses were assumed, and for each fin thickness, the radiator height, c, required to dissipate the heat load of 128.1 watts was determined. The calculation procedure consisted of dividing the radiator into finite increments so that, for each increment, it was possible to determine the energy radiated by that element and the amount of heat transferred to the next element. Knowing the cross-sectional area of the fins, A_F, and the quantity of heat to be transferred, the temperature gradient at the interface with the succeeding elements, and therefore the change in element temperature, can be calculated. This in turn permits calculation of the radiation from the next element. Table E-1 (Appendix E) lists a series of twelve iterations made to determine the optimum radiator design and to find the temperature distribution corresponding to various radiator heat transfer loads. The results of these calculations are plotted in Figures 8-15, 8-16, and 8-17.

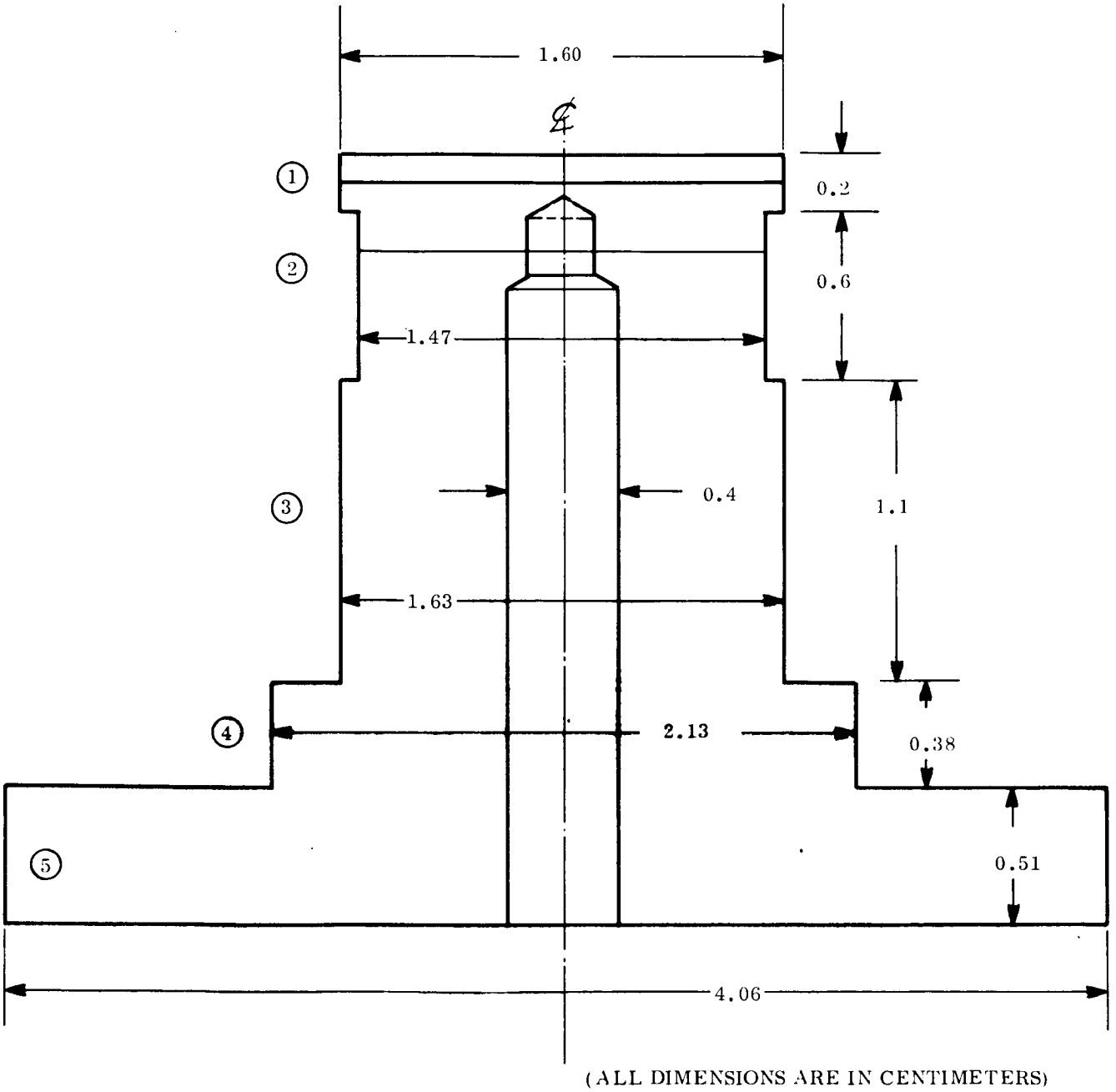

Figure 8-13. Collector Dimensions

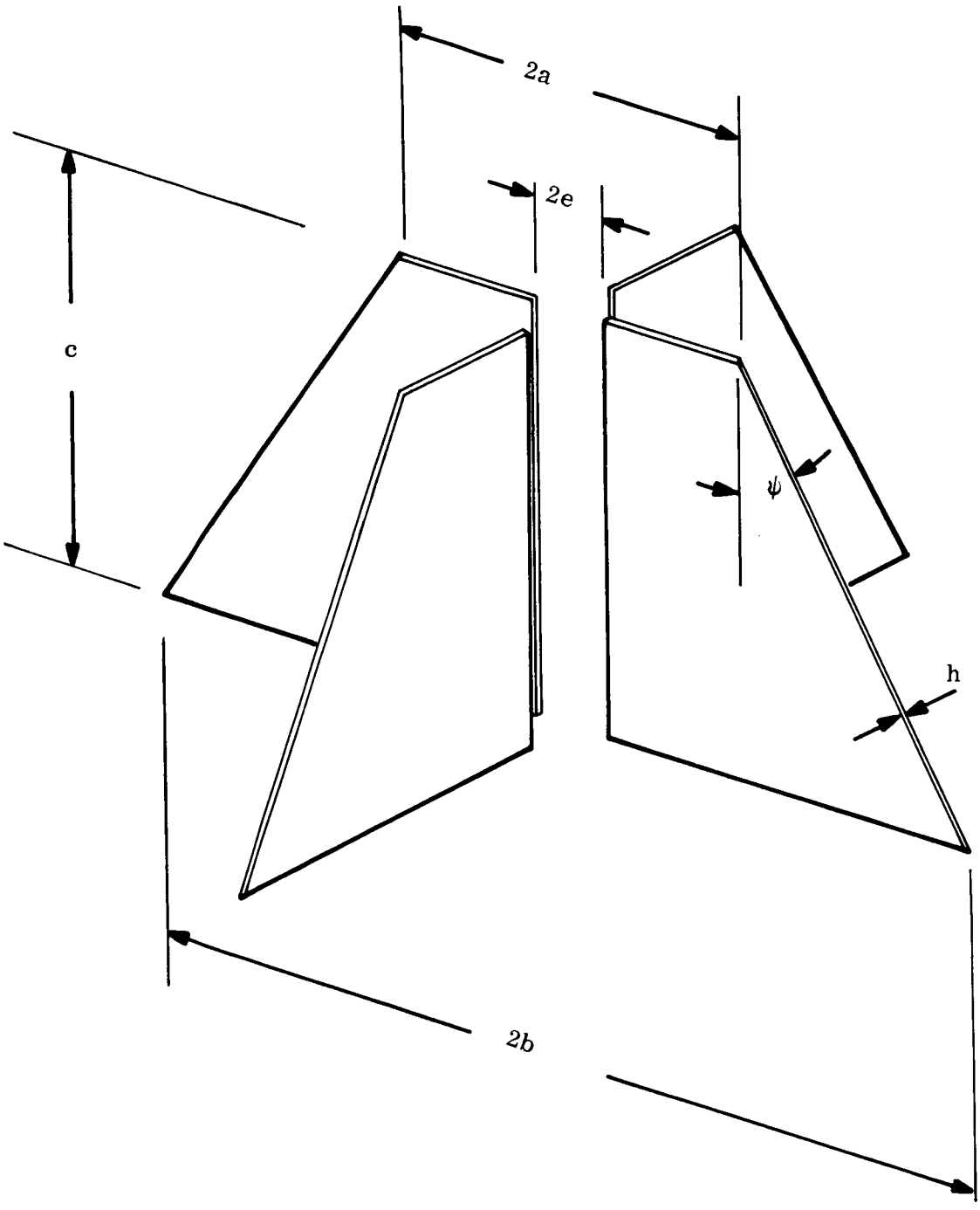

Figure 8-14. Converter Geometry

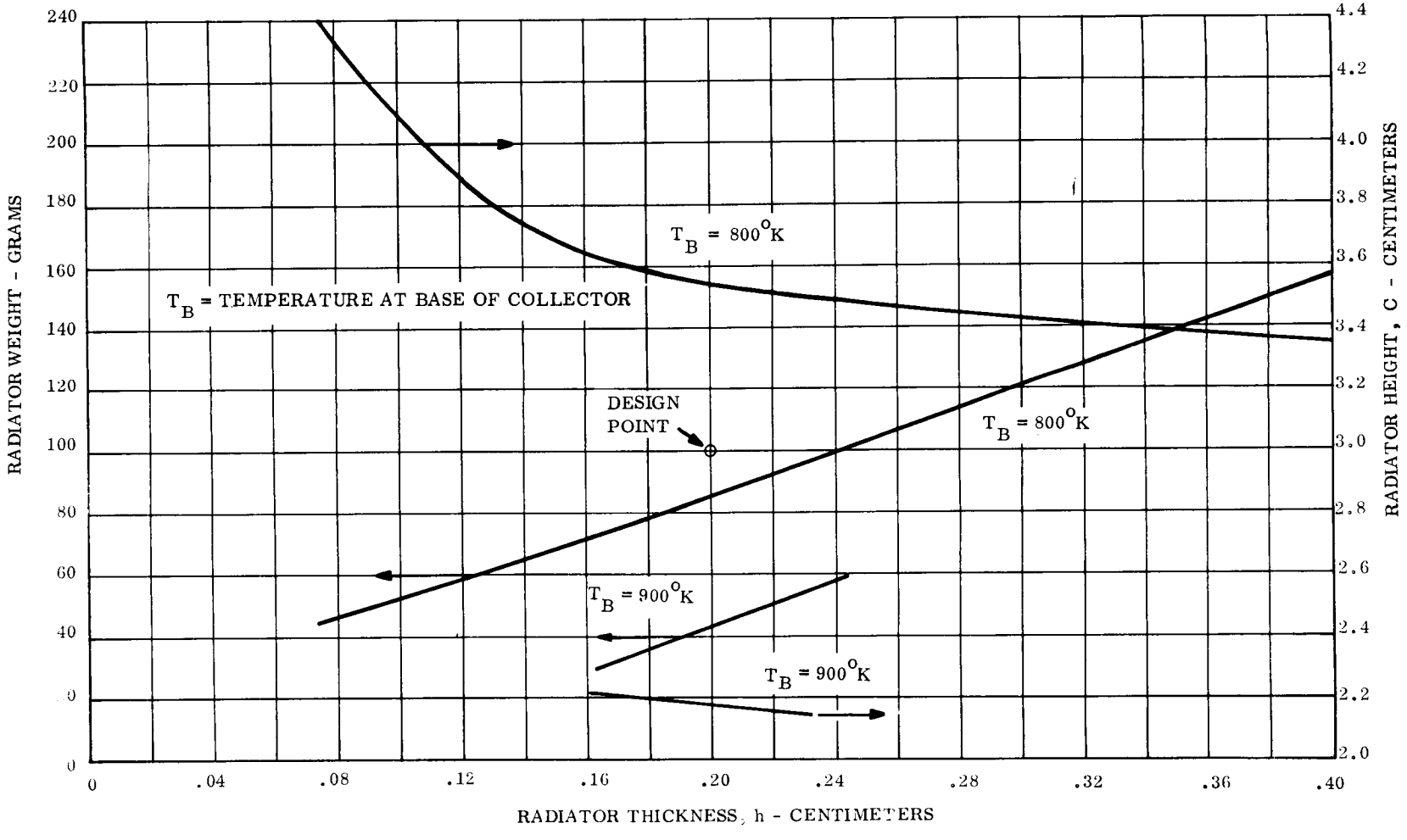

Figure 8-15. Radiator Dimensions and Weight Required to Radiate 128.1 Watts

Figure 8-15 shows the variation in fin height for a wide range of thicknesses and a collector base temperature of 800°K. It also shows the variation in radiator weight corresponding to this range of fin thicknesses. It is interesting to observe that even at the fin thickness of 0.08 centimeters (approximately 30 mils) the weight decreases as fin thickness is decreased. The saving in weight realized by decreasing the fin thickness to values below 0.20 centimeters was not considered to be worth the decrease in structural strength that occurs below that fin thickness. Therefore, a fin thickness of 0.20 centimeters was selected for the design. Figure 8-15 also shows partial plots corresponding to a collector base temperature of 900°K and the design fin thickness of 0.20 centimeters. Interpolating between the 800° and 900°K curves for a collector base temperature of 844°K the required radiator fin height is 3.0 centimeters. This point is shown in Figure 8-15 and labeled "Design Point." The radiator weight per converter corresponding to this fin height and a fin thickness of 0.20 centimeters is 66.6 grams.

Figure 8-16 shows the radiator temperature distributions in a fin 0.20 centimeter thick and 3.0 centimeters long for various values of heat transfer. It is apparent that the temperature gradients in the fin are very small, even at relatively high values of heat transfer.

Figure 8-17 is a replot of the data presented in Figure 8-16 and shows the heat handled by the converter radiator as a function of the collector base temperature. As will be seen later, Figure 8-17 is useful in studying the converter warm-up rate.

8.4.4 CESIUM RESERVOIR DESIGN

The cesium tube and the cesium reservoir of the thermionic converters must be designed so that, when the converter is at temperature, the cesium reservoir can maintain the designed value of reservoir temperature with a minimum addition of heat. Also, in order to achieve fast converter warm up, it is desirable to make the heat capacity of the cesium reservoir as small as possible, Moreover, in order to achieve the largest variation in reservoir temperature for a given increase in the amount of heat added to the reservoir, it is necessary to make the heat radiated by the reservoir at steady-state conditions as small as possible. Experience gained in the development of converters indicates that good strength and sufficient gas conductance for converter outgassing purposes is achieved with cesium tubes made of nickel, with a 3/16-inch

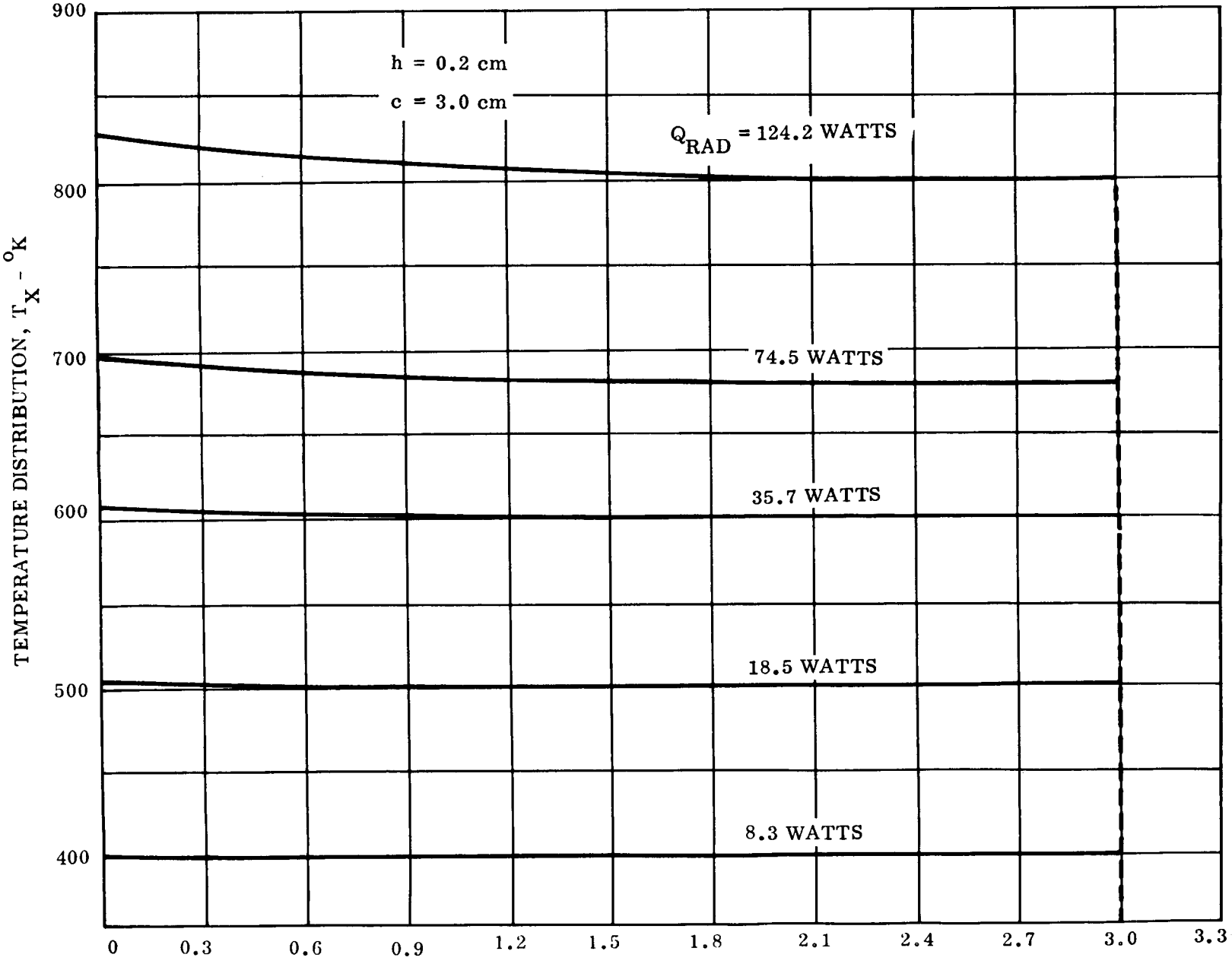

Figure 8-16. Radiator Temperature Distribution

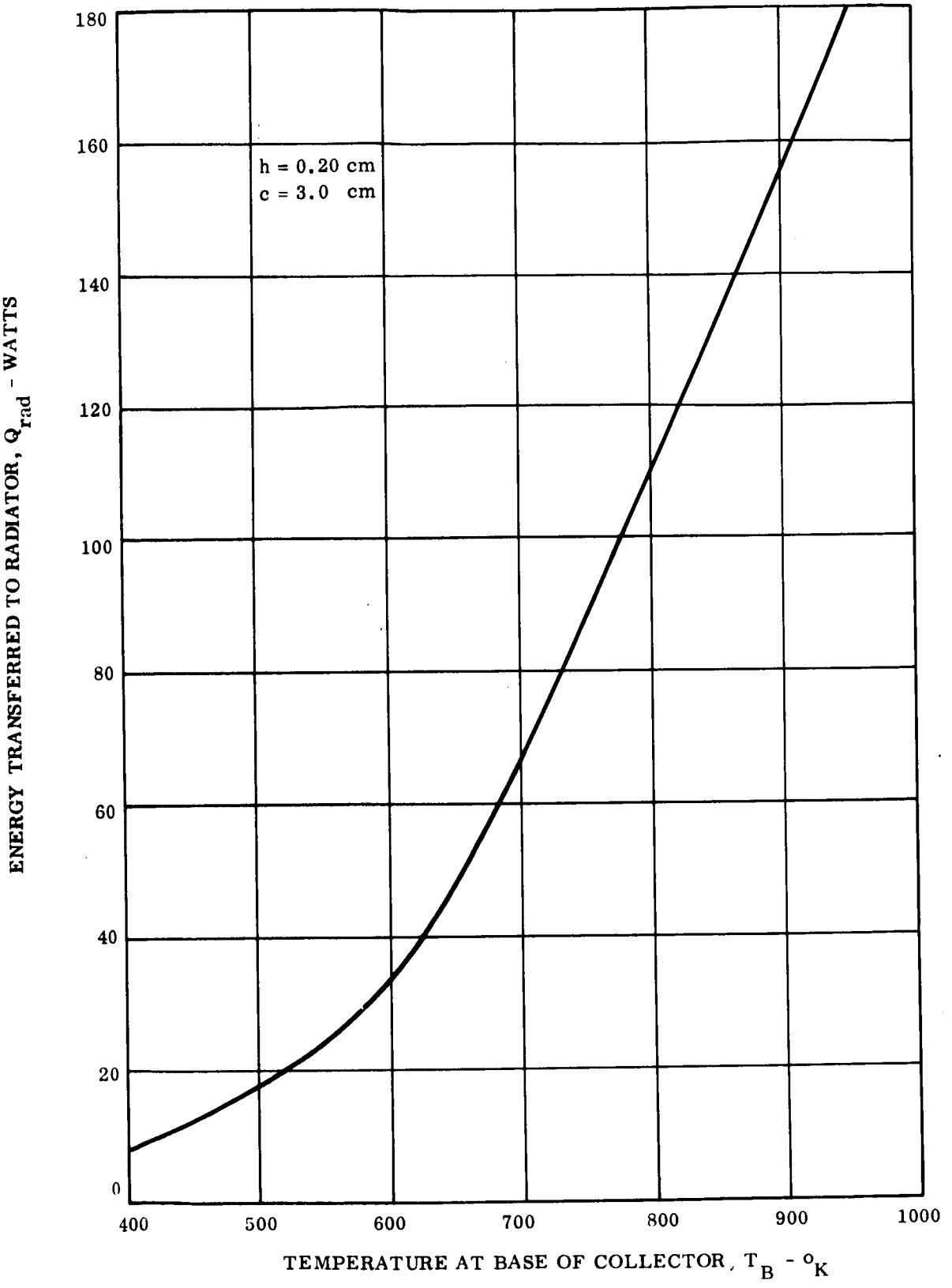

Figure 8-17. Radiator Heat Transfer vs. Temperature at Base of Collector

outside diameter and a wall thickness of 0.015 inches. This tube size, and material, were assumed for the purposes of this study. Figure 8-18 shows the cesium tube in relation to a radiator fin and Figure 8-19 shows a cross section of the cesium tube and radiator fins in the vicinity of the cesium tube. In order to calculate the cesium tube length required to achieve the desired design value of temperature, it is necessary to compute a heat balance for each element of the cesium tube along its length. Figure 8-19 shows that over the portion of the cesium tube which faces the radiator fins, radiant energy transfer takes place between the cesium tube, the radiator fins, and the space environment. The radiation view factors corresponding to the conditions of Figure 8-19 are derived in Appendix F which also includes expressions for the heat transfer to any finite element of the cesium tube. The radiation heat transfer characteristics of the cesium reservoir design are derived in the same appendix, and they are plotted in Figure 8-20. It is of interest to note in Figure 8-20 that the addition of 0.1 watt on the cesium reservoir can result in a considerable change of the reservoir temperature. For instance, Figure 8-20 indicates that if the reservoir is at $600^{o}K$, the addition of 0.1 watt will raise the temperature to $634^{o}K$.

Table F-1, (Appendix F) presents the numerical results of the cesium tube length calculations. The procedure was similar to that used in calculating the required height of the radiator fins. Knowing the collector base temperature to be $844^{o}K$, an arbitrary value of heat transfer at the origin of the cesium tube was assumed and then, element by element, (see Figure 8-21) the change in the heat transfer along the length of the tube and the corresponding changes in temperature were evaluated. This procedure was repeated until the arbitrary value of heat transfer assumed gave the design reservoir temperature of $639^{o}K$. The predicted reservoir radiation heat transfer given by Figure 8-20 was used in performing these calculations.

Three iterations were required to determine the necessary length of the cesium tube. (These calculations are given in Table F-1 of Appendix F.)

Table F-2 (Appendix F) shows the results of calculations made to determine the effect of collector base temperature on the equilibrium reservoir temperature for the chosen cesium tube design. The results of these calculations are plotted in Figure 8-22.

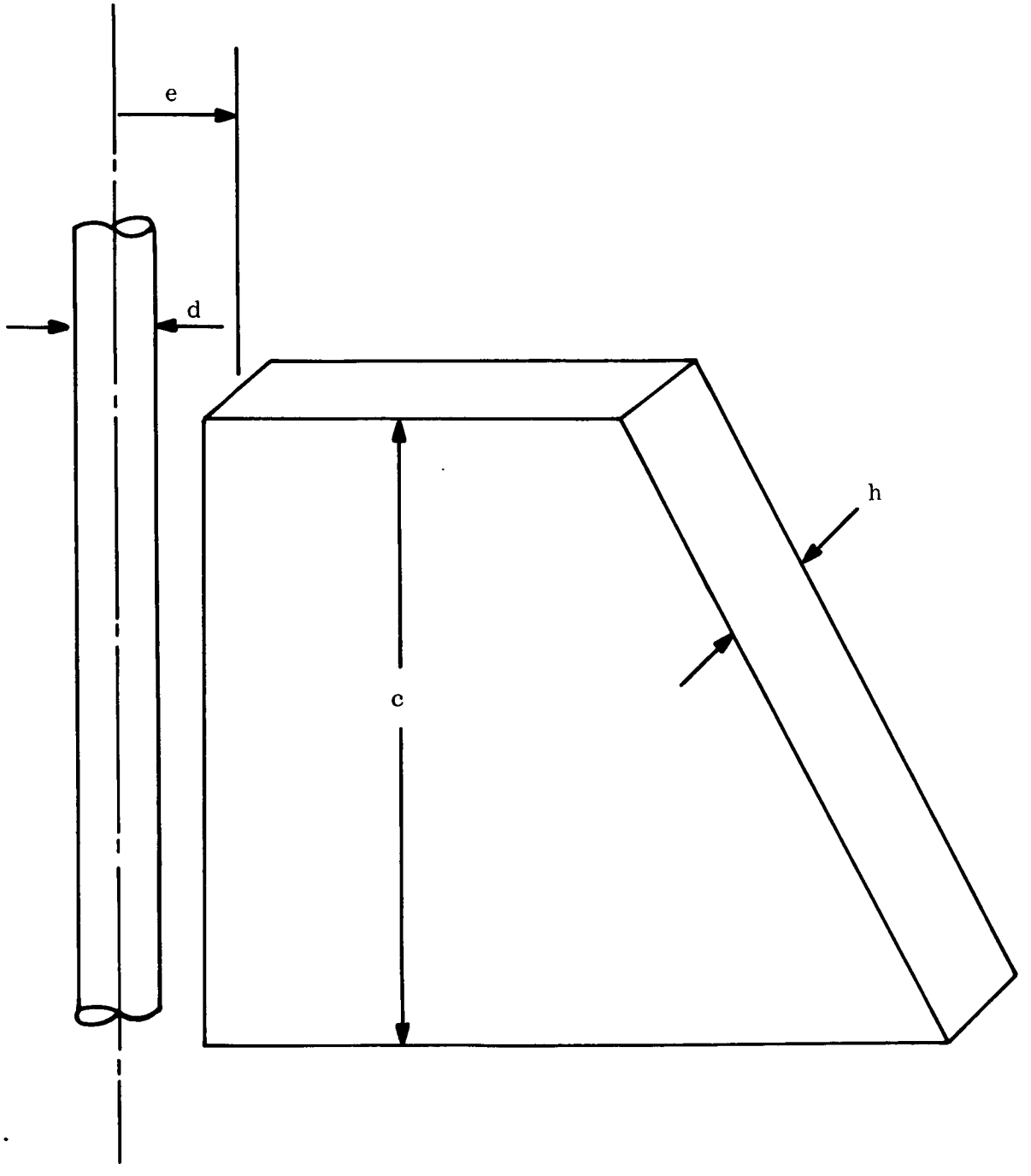

Figure 8-18. Cesium Tube and Radiator Fin Geometry

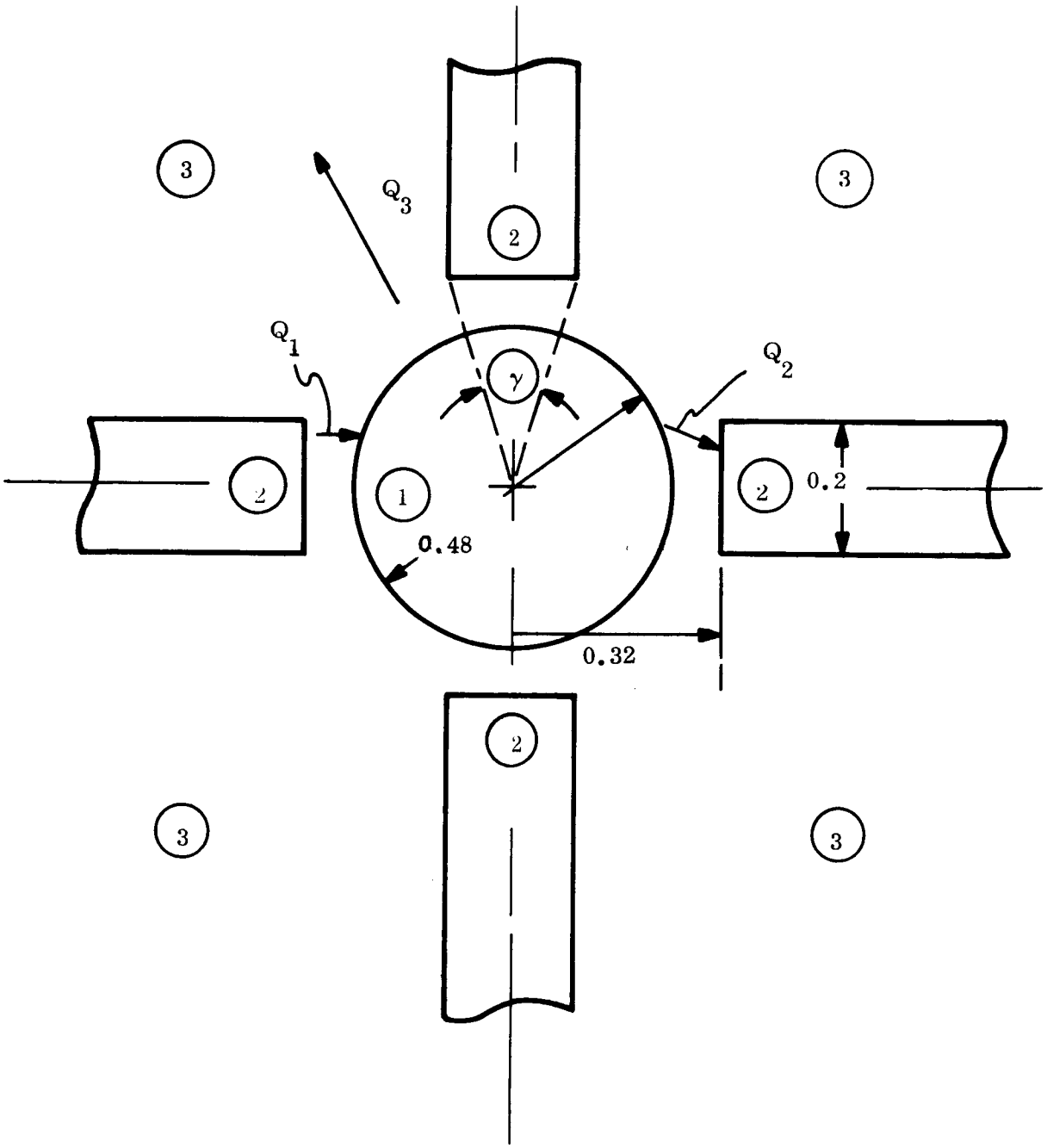

NOTE: ALL DIMENSIONS IN CENTIMETERS

Figure 8-19. Cesium Tube Radiation Heat Transfer

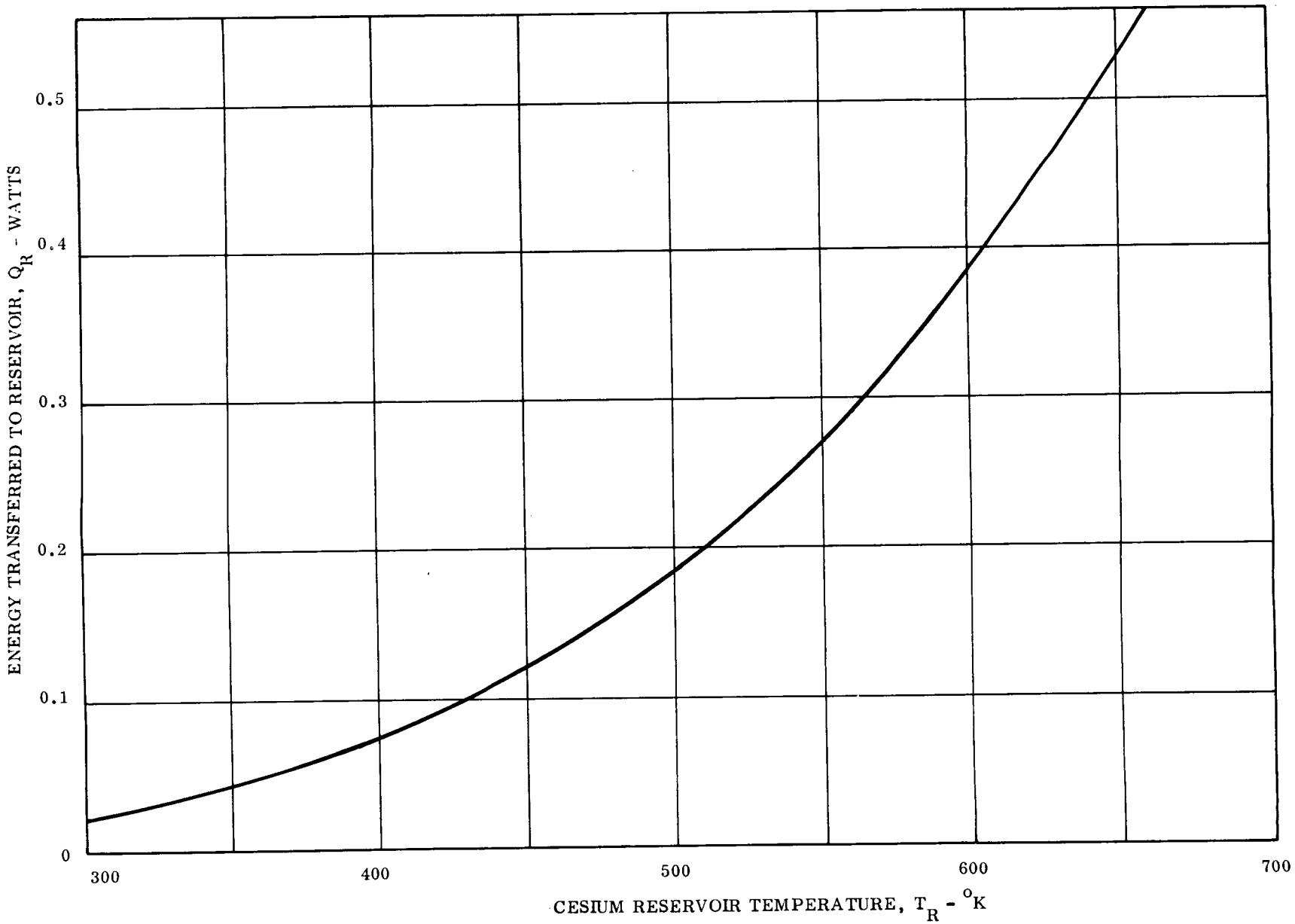

Figure 8-20. Radiation Energy Transfer From Cesium Reservoir

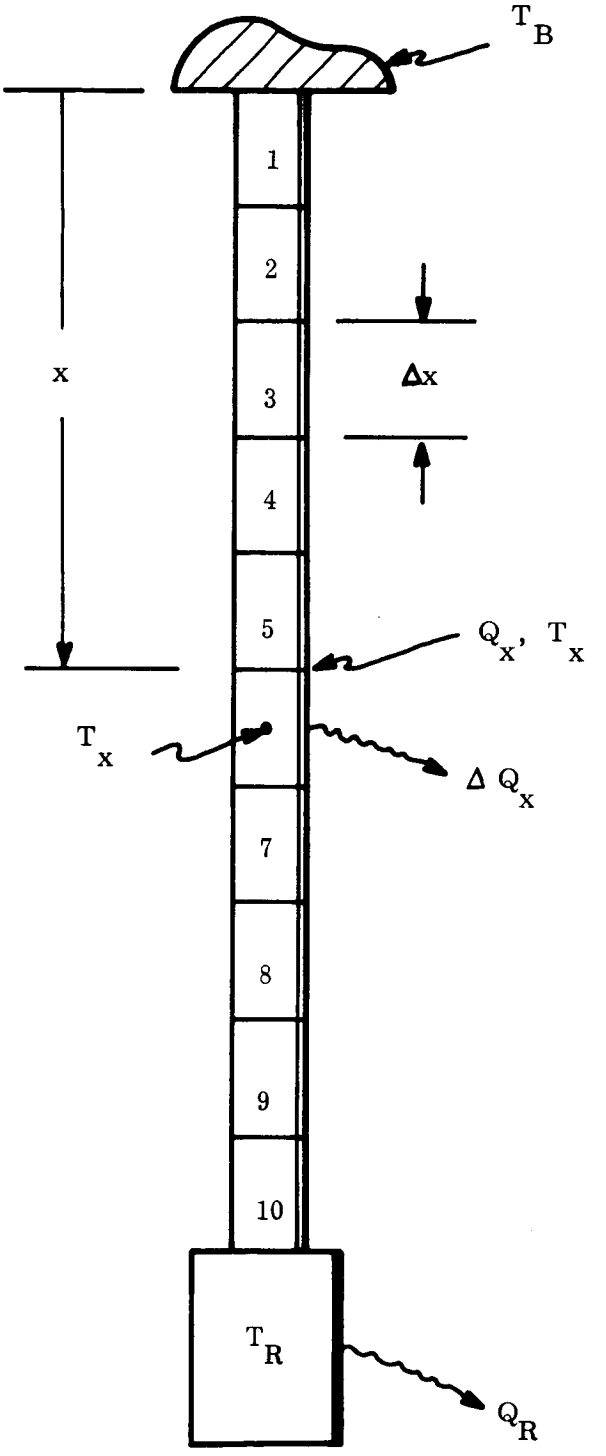

Figure 8-21. Cesium Tube Heat Transfer

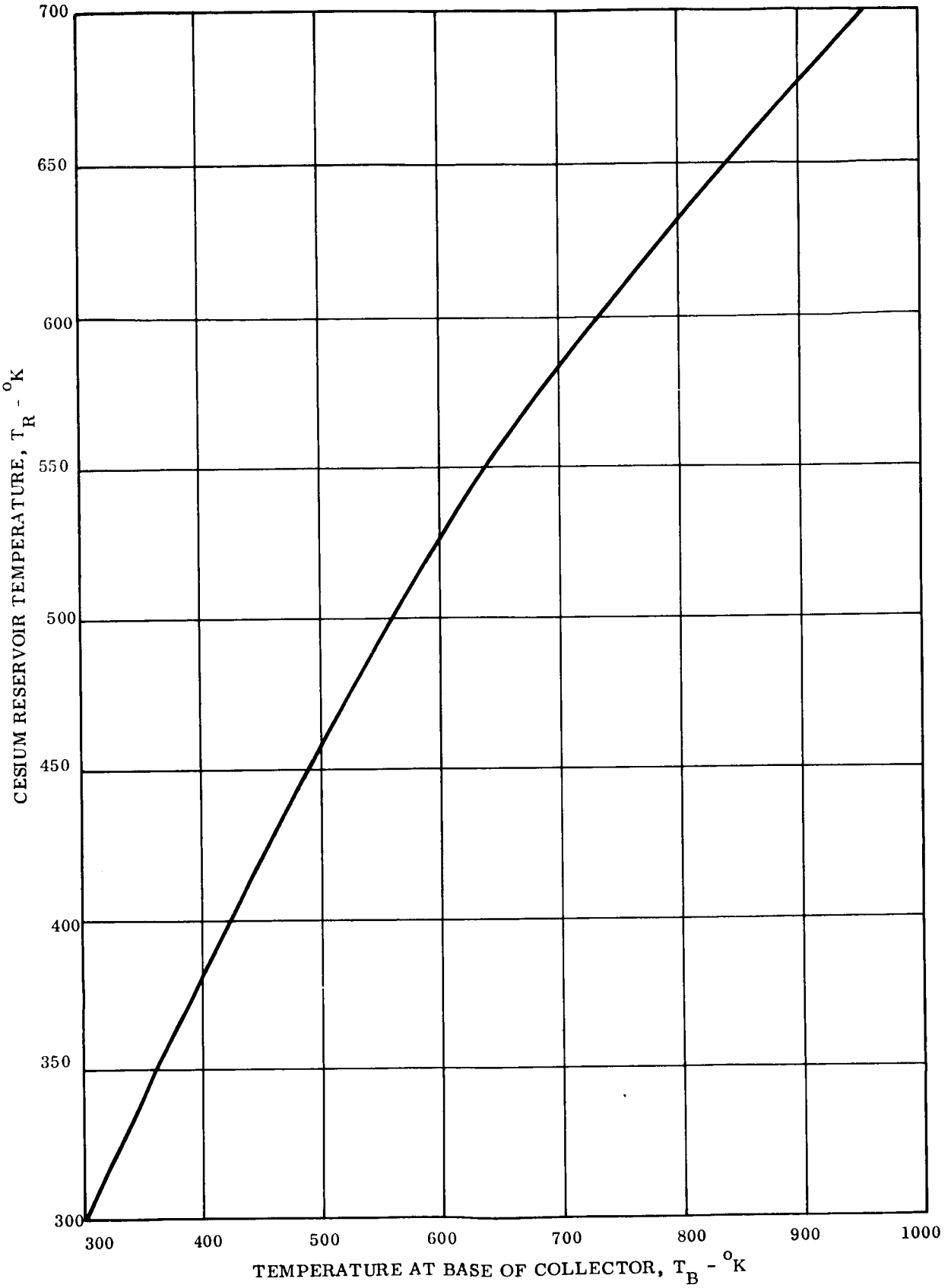

Figure 8-22. Equilibrium Reservoir Temperature vs. Temperature at Base of Collector

8.4.5 THERMAL CHARACTERISTICS OF COLLECTOR RADIATOR STRUCTURE

In this section the warm-up characteristics of the collector-radiator structure are determined. These are needed to calculate the overall thermal response of the generator. The collector-radiator structure may be visualized as a body of given specific heat which receives heat at a specified rate and which radiates part of it in proportion to the fourth power of its temperature. Appendix G gives the detailed analysis of this case and the expressions required to predict the corresponding rates of warm up.

Table G-1 (Appendix G) presents the specific heat calculations for the various components of the thermionic converter and gives the calculated values of the specific heat for both the collector-radiator subassembly and the cesium reservoir subassembly. Using the expressions derived in Appendix G, it was then possible to compute warm-up curves for the collector-radiator structure at various values of heat input. The results of these calculations are presented in Table G-2 (Appendix G) and are plotted in Figure 8-23. From these results it is apparent that in the typical heat transfer range of 110 to 130 watts, the time required for the collector to achieve full temperature is approximately 16 minutes.

8.4.6 THERMAL CHARACTERISTICS OF CESIUM RESERVOIR

The results of the cesium reservoir design calculations discussed in Section 8.4.4 are plotted in Figure 8-24 where the heat transfer received by the cesium reservoir is shown as a function of the temperature difference existing between the base of the collector structure and the reservoir. For the purpose of evaluating the generator warm-up characteristics, it is of interest to determine warm-up curves for the cesium reservoir in the same manner used for the collector-radiator structure.

Appendix H-1 summarizes the results of these calculations and the results are plotted in Figure 8-25. It can be seen that relatively modest values of auxiliary heat input will insure that the reservoir is up to temperature in a period of time consistent with the 16 minute collector-radiator structure warm-up time.

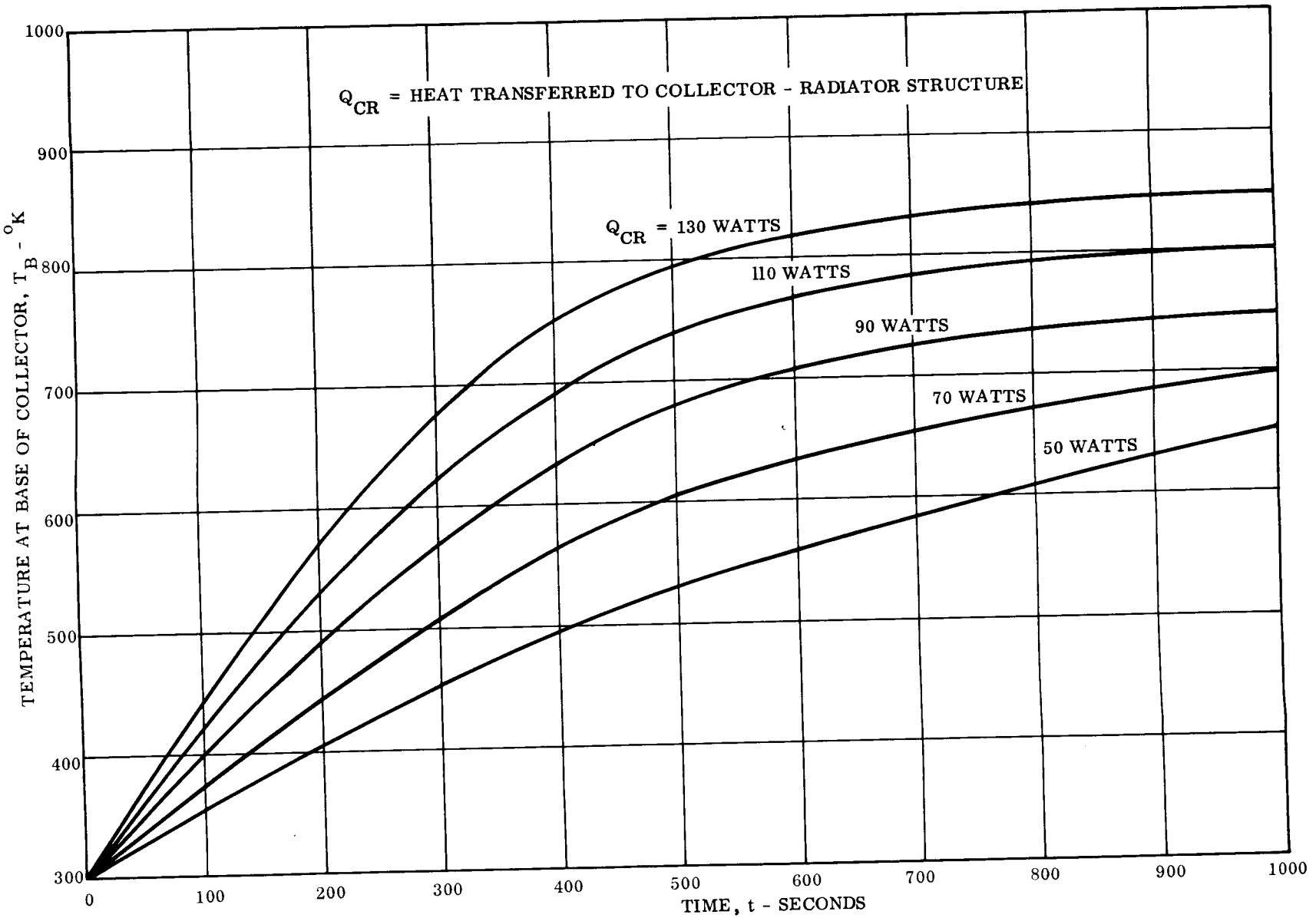

Figure 8-23. Collector Warm-Up Characteristics

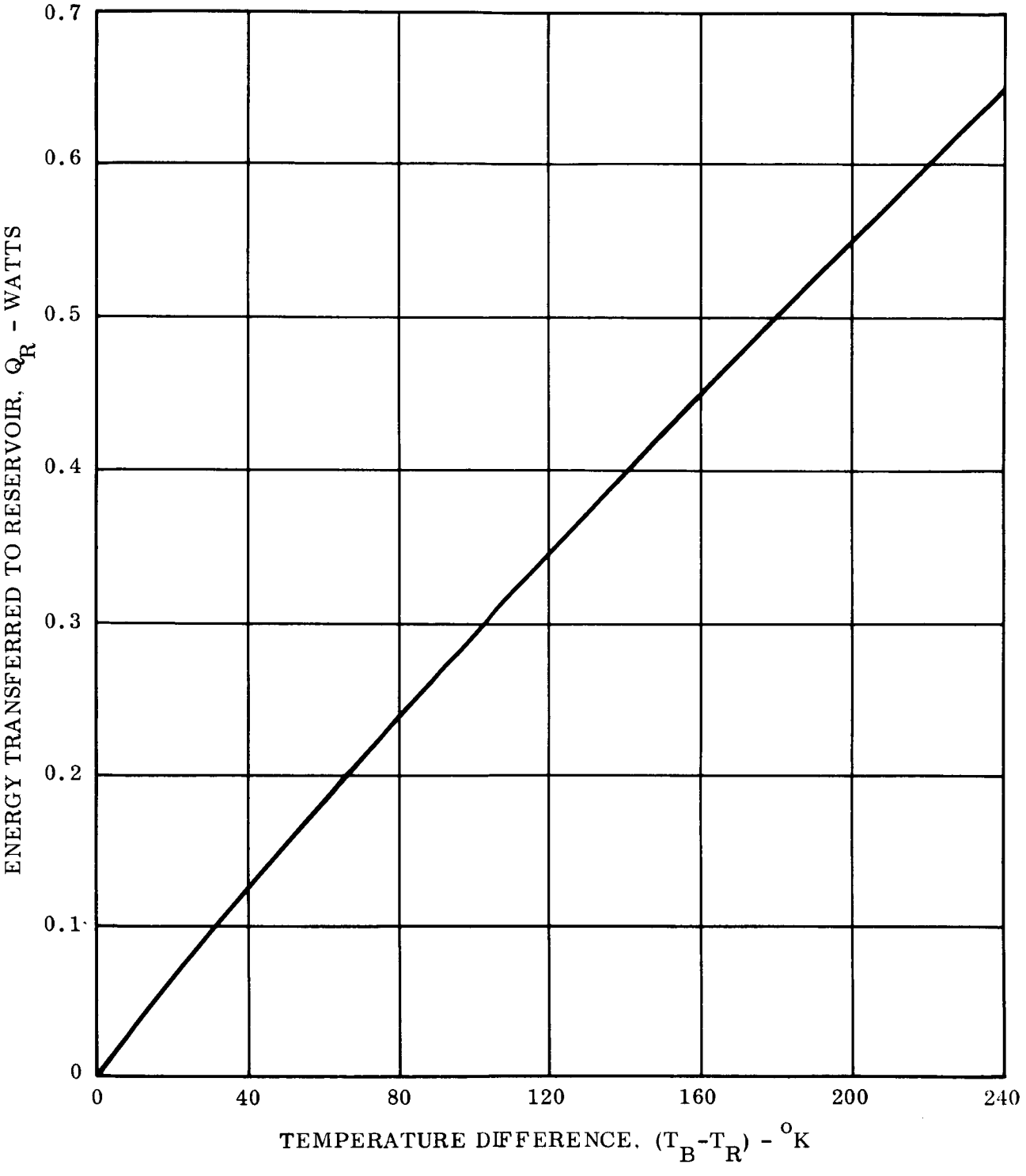

Figure 8-24. Cesium Reservoir Heat Transfer

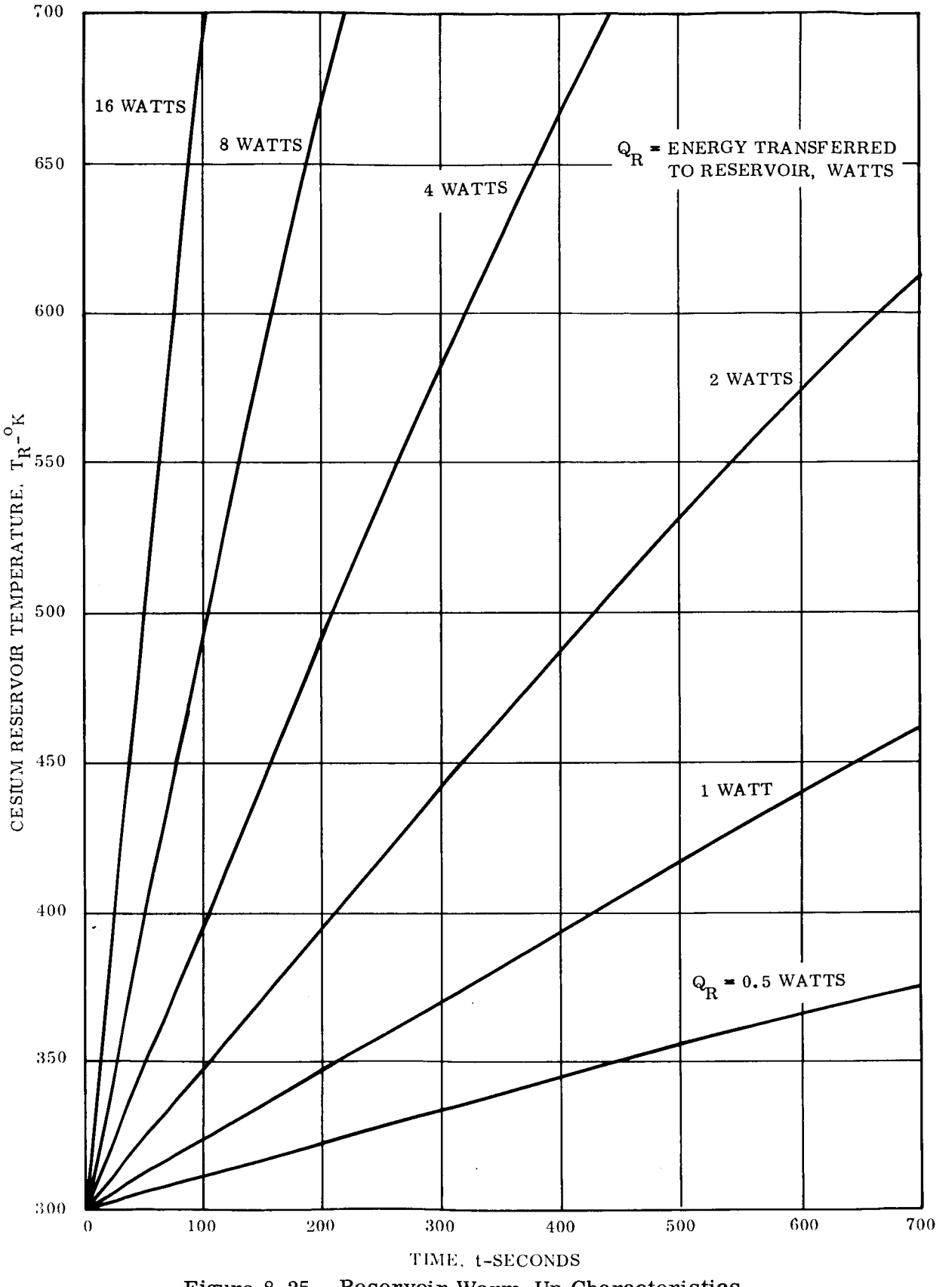

Figure 8-25. Reservoir Warm-Up Characteristics

8.4.7 GENERATOR WARM UP AND RECOMMENDED START-UP PROCEDURE

Although the problems associated with the start up of solar thermionic generators have been recognized they have been the subject of rather scanty analysis. The material presented in this section is the result of a preliminary effort to predict the generator warm-up transient under given conditions. The time available in this study did not permit a refined calculation of these transients, but it is felt the results arrived at are sufficient to warrant the conclusions drawn.

It has been assumed in this analysis that the generator load is such as to maintain an output voltage of 0.85 volts at each converter at all times. To apply this assumption, it was necessary to know what the output current of a thermionic converter would be as a function of cesium reservoir temperature when the output voltage was maintained at 0.85 volts and the emitter temperature at 2000^{o}K. Since this type of data was not available, a specific test was made on converter VIII-S-2* to determine the required output characteristics. The results of this test are presented in Table I-3 in Appendix I. The corresponding data points have been scaled up to the value of output current corresponding to the design point of this study in Figure 8-26.

With the help of Figure 8-26 and others, it was possible to predict the generator warm-up characteristics under a variety of conditions. If it is assumed that, for all practical purposes, the emitter structure of all converters reaches equilibrium temperature instantaneously, the following calculation procedure can be used. Initially, the output of the converters is nil, and Figure 8-12 predicts the amount of heat conducted to the radiator structure at whatever emitter temperature is established (the latter being a function of the amount of input energy control used during start-up). Knowing this amount of heat transfer, it is then possible to use Figure 8-23 to determine the temperature rise of the collector-radiator structure during the first 100 seconds of warm-up time. During this period of time, the cesium reservoir receives a quantity of heat determined by whatever auxiliary input is used during warm up and the amount conducted by the cesium tube, as given in Figure 8-24. Figure 8-25 can then

*Thermionic converter developed by Thermo Electron Engineering Corporation for JPL.

be used to find the temperature rise of the cesium reservoir during the next increment of time* Figure 8-26 tells whether the reservoir has increased in temperature to the point where an output current is obtained and whether the heat transferred to the collector-radiator structure must have changed accordingly. The procedure can thus be repeated for successive time intervals to generate a set of response temperature and output current curves for the collector and the cesium reservoir.

Figures 8-27 through 8-31 show the results obtained for special cases. The corresponding calculations are presented in Tables I-1 and I-2 of Appendix I. Figure 8-27 illustrates the case of generator warm up with the maximum flux (no flux control) and without the use of auxiliary reservoir heating. For this case it was assumed that the heat capacity of the cesium reservoir could be changed to approximately one-quarter of its calculated value in order to avoid undue warm-up time lags at the cesium reservoir. Figure 8-27 shows that under those conditions the warm up of the generator would take approximately 15 minutes. Figure 8-28 shows what happens when, under the same conditions, heat is added to the cesium reservoir in order to accelerate its warm up. It is assumed here that an automatic control system stops the cesium reservoir heating when the collector has reached a predetermined value of temperature which corresponds to a radiator fin temperature of $750^{o}K$. This assumption would correspond to the case where for example, the auxiliary heat was added to each cesium reservoir by means of a small solar concentrator supported from a radiator fin by a bi-metallic element. When the radiator fin reaches a given temperature, the bi-metallic element would deflect the solar concentrator and the addition of heat to the cesium reservoir would stop. It can be seen in Figure 8-28 that it is possible for a premature warm-up condition to exist with the net result that the warm-up time for the generator is barely reduced. Thus, in the case of Figure 8-28, the cesium reservoir heat is interrupted at a time when the base of the collector is not sufficiently hot to continue maintaining the cesium

*To accelerate the rate of warm up it is possible to study the use of thermionic converters that do not have a cesium reservoir. For such a design all the cesium would be vaporized to the correct vapor pressure when the converter envelope was at operating temperature. Such converters are not present state of the art, and therefore were not considered in this study.

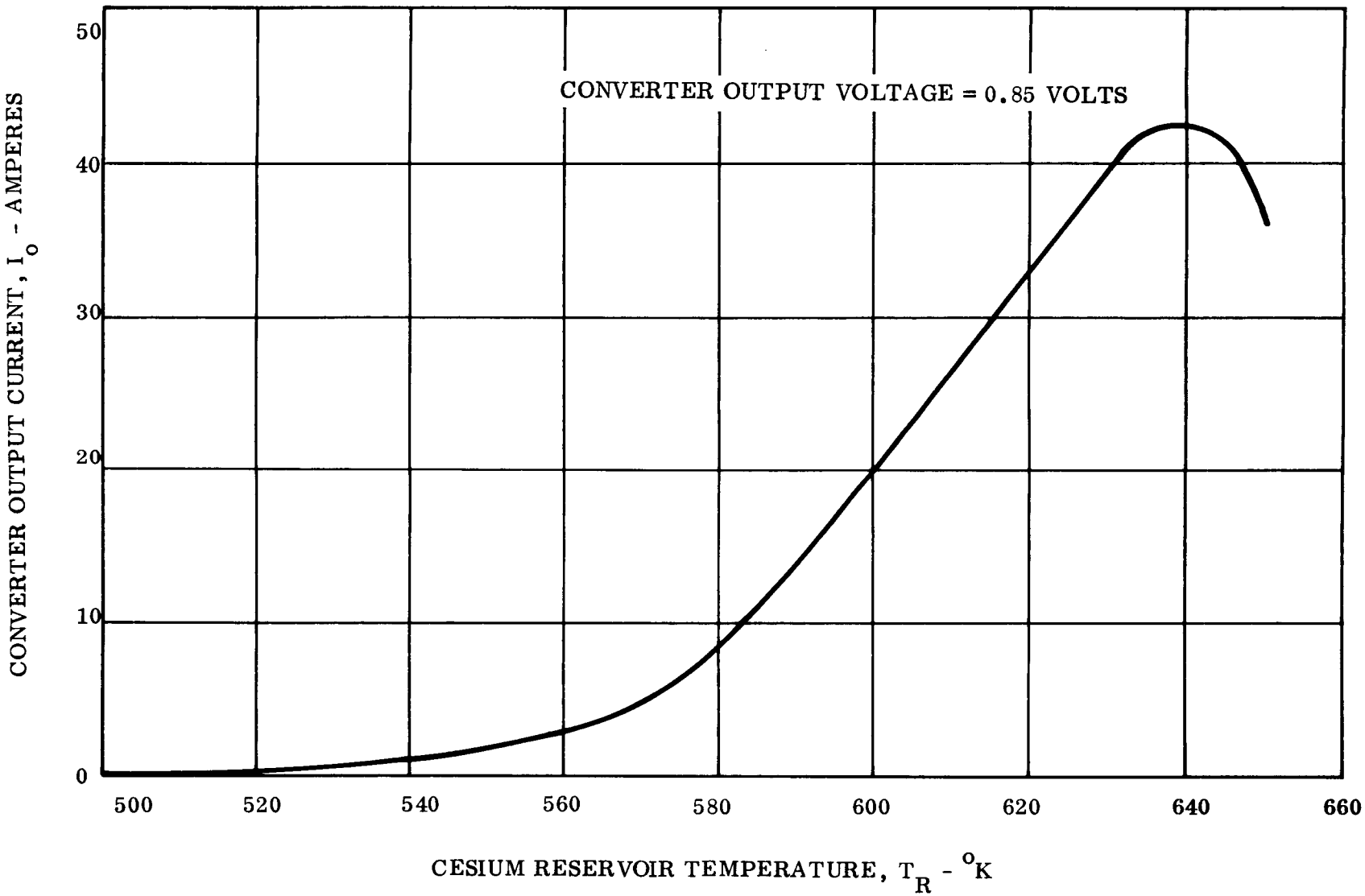

Figure 8-26. Converter Output vs. Cesium Reservoir Temperature

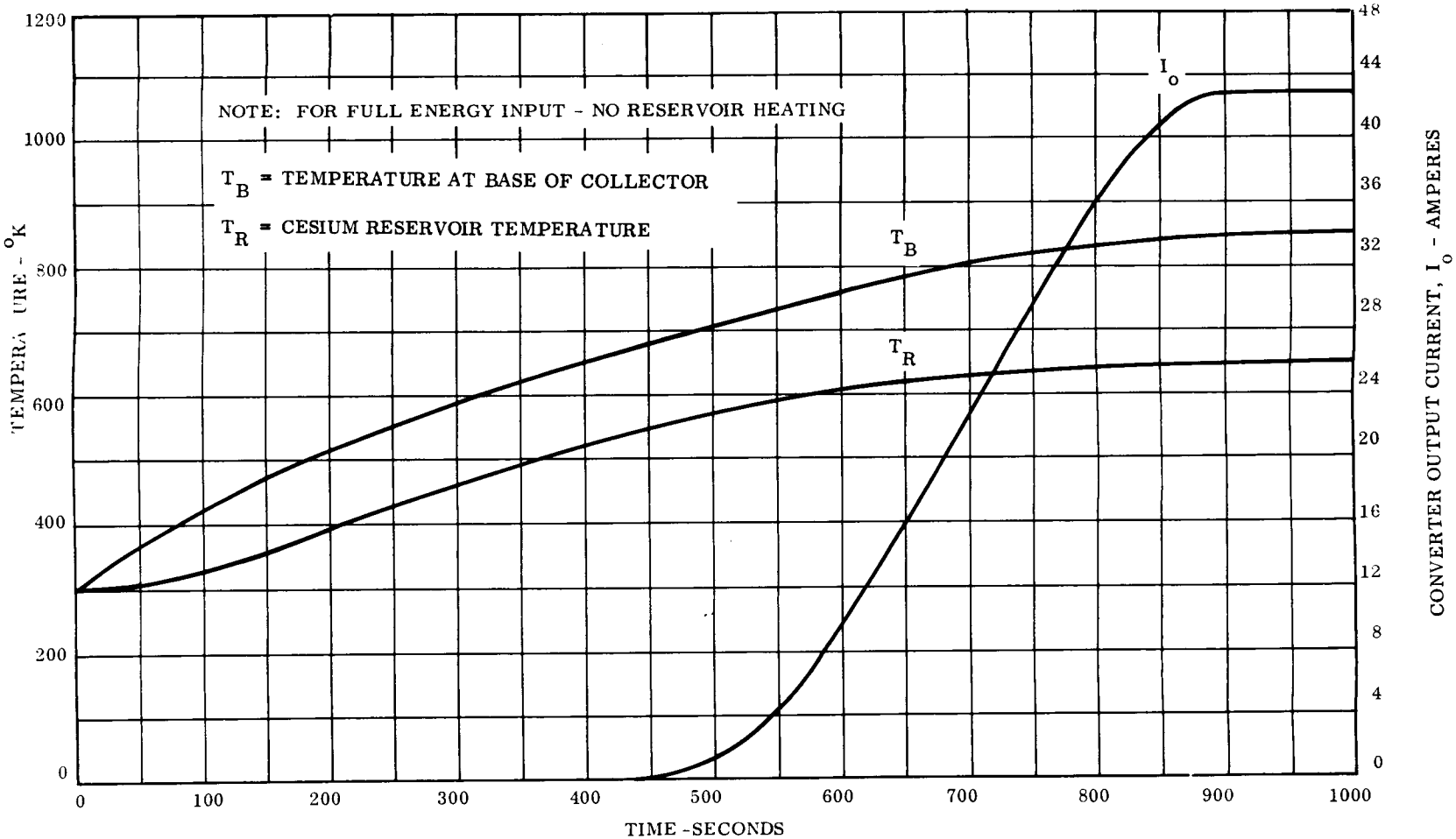

Figure 8-27. Converter Warm-Up Transient

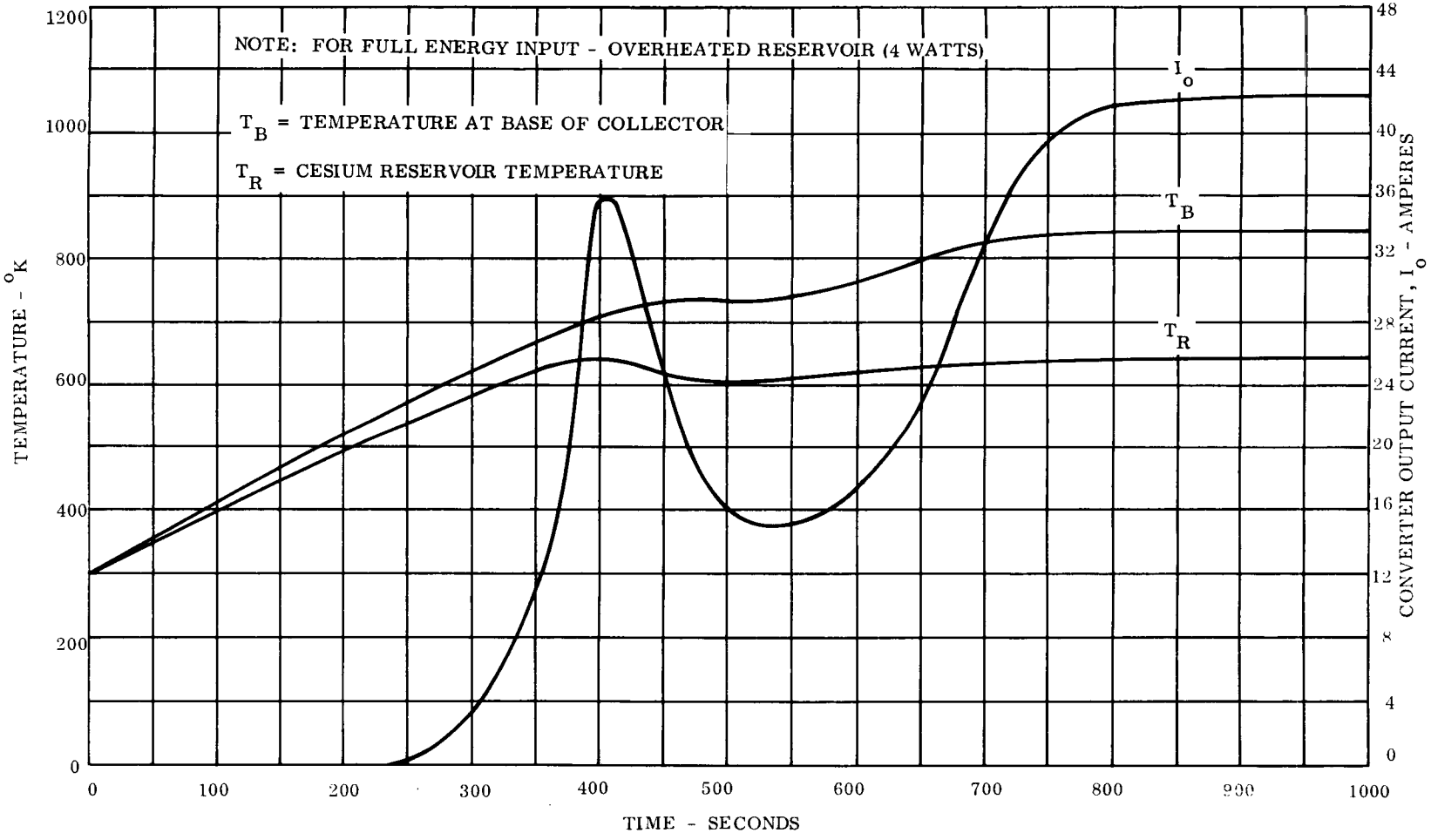

Figure 8-28. Converter Warm-Up Transient

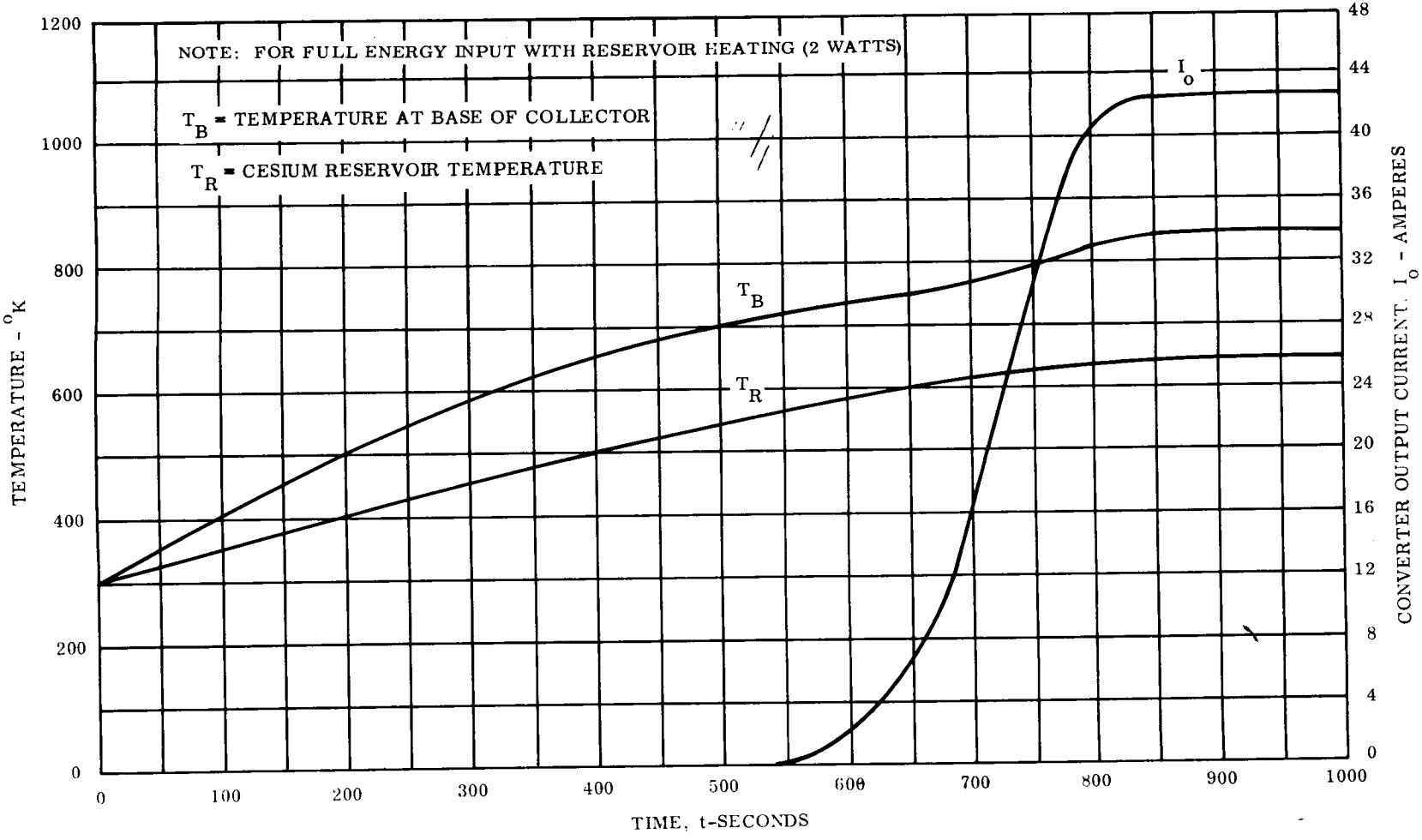

Figure 8-29. Converter Warm-Up Transient

reservoir temperature attained. Therefore, the cesium reservoir temperature drops, the output current drops, and the collector base temperature follows in such a manner that, in recovering from this condition, the overall warm-up time is just about equal to that achieved without the addition of reservoir heat. Figure 8-29 shows the same case, but with a reduced value of energy input to the cesium reservoir. In this case, the condition of premature heating of the cesium reservoir is avoided, but the overall generator warm-up time is still almost 15 minutes. It is possible that a more judicious selection of the amount of heat added to the cesium reservoir and of the cut-off point could result in a generator warm-up time of only ten minutes.

Figure 8-30 illustrates generator warm up with flux control adjusted so as to maintain a constant emitter temperature of $2000^{O}K$. No reservor heating is assumed and, again, the heat capacity of the cesium reservoir has been assumed equal to about one-quarter of the value calculated for the design given in Figure 8-2. The results for this case indicate that the generator will not fully warm up. Thus, at the end of 16 minutes, Figure 8-30 shows that the collector base temperature has stabilized at about $660^{O}K$ with a corresponding stable value of reservoir temperature of $580^{O}K$. This value of reservoir temperature is not able to produce an output current of sufficient magnitude to bring about a further warm up of the collector.

Figure 8-31 shows that the results obtained with a flux control maintaining a $2000^{O}K$ emitter temperature, and no reservoir heating, can also be avoided with the addition of about two watts to the cesium reservoir during generator warm up. However, the warm-up time, predicted by Figure 8-31, is still of the order of 15 minutes.

Selection of a generator warm-up method requires consideration of the mechanical complexity and reliability of available devices to control the cavity input energy and to provide temporary additions of heat to the cesium reservoirs; and on the ability of the thermionic converters to operate for short periods of time at emitter temperatures approximately $400^{O}K$ in excess of their design operating temperature. While the last item needs to be explored in the laboratory to a much greater extent it is felt that the experience to date indicates that thermionic converters will probably be capable of undergoing limited overheating without deleterious effects.

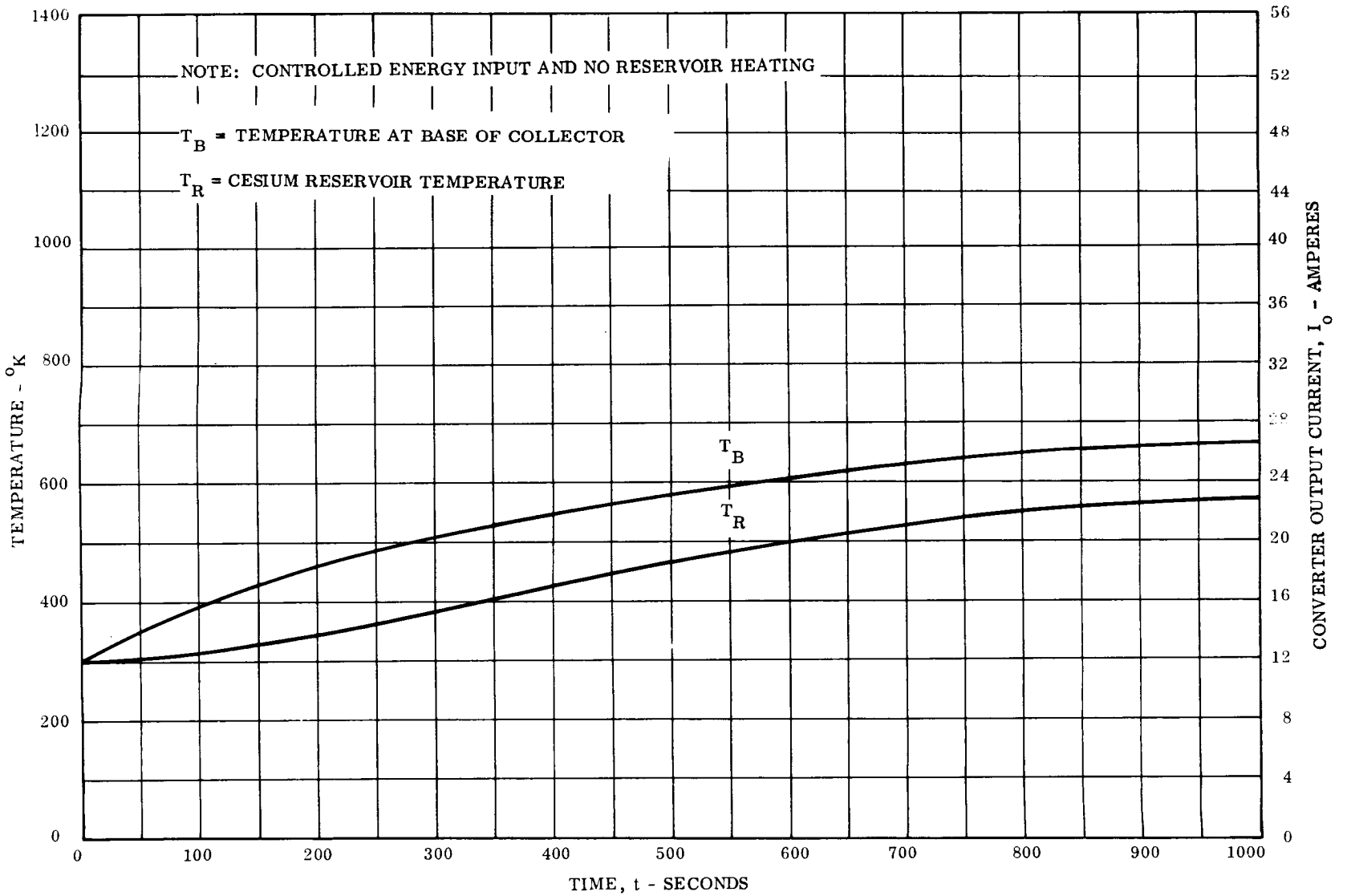

Figure 8-30. Converter Warm-Up Transient

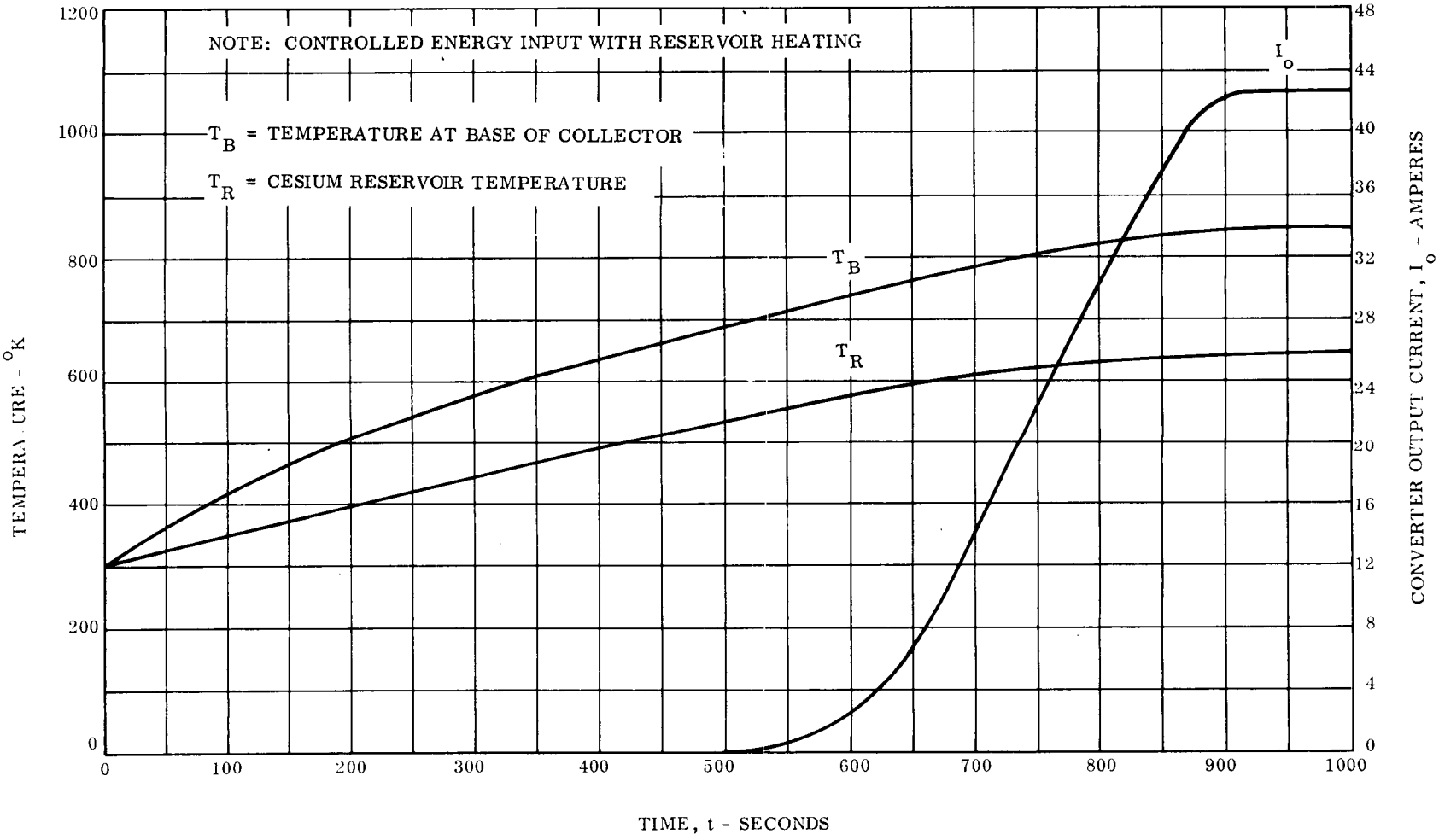

Figure 8-31. Converter Warm-Up (Controlled Power Input With Reservoir Heating)

If this proves to be the case then there is no advantage to controlling the cavity input energy or to using cesium reservoir heating during the warm-up phase, since the warm-up time is not significantly reduced by either of these approaches. However, the use of controls would tend to increase the system complexity, weight, and reduce the reliability. For these reasons the tentative conclusion is that generator warm up can best be accomplished without any form of control on the cavity input energy and without the use of auxiliary heat on the cesium reservoirs.

8.4.8 SUMMARY

The thermionic generator design presented in Figure 8-2 has been shown to be capable of producing an output of 144 watts when operated in space with a solar concentrator 50 inches in diameter. For a nominal generator energy input of 1180 watts this output corresponds to a generator efficiency of 12.2 percent. The total calculated generator weight (see Appendix K) is 5.68 pounds, corresponding to a specific power of 25.3 watts per pound, or a specific weight of 39.5 pounds per kilowatt.

The analysis indicates that a generator warm-up time of approximately 16 minutes is achievable either by controlling the input energy so that an emitter temperature of 2000^{o}K is always maintained and using auxiliary heat input to the cesium reservoir or by allowing the maximum energy input (no control on input energy) without reservoir heating. Of the two methods, the latter is favored because it is felt that thermionic converters will probably be capable of withstanding this sudden overheating for short periods of time and that the required flux control and auxiliary reservoir heaters would prove to be complicated and lower the system reliability.

The generator performance analysis substantiates the assumptions made regarding generator losses in Section 4.3 (Volume II) and the performance estimates and conclusions reached in Section 4 (Volume II) are valid for the generator design proposed.

8.5 GENERATOR ELECTRICAL CIRCUIT

To maximize the information obtained from the thermionic generator and the chances of conducting a successful experiment requires flexibility in the generator electrical circuit.

8.5.1 PROPOSED CIRCUIT DESIGN

The proposed circuit design is presented in Figure 8-32. The operation of this circuit is described below.

a. Switches K_1 and K_5 operate as a pair. When K_1 is closed K_5 is open and when K_5 is closed K_1 is open. Switches K_2 and K_6, K_3 and K_7, and K_4 and K_8 operate in this same manner.

b. The load resistor (R_5) can be varied by the stepping switch K_9 in five distinct steps - 0, 25, 50, 75 and 100 percent of full load.

c. Resistors R_1 through R_4 are fixed. The value of these resistors is chosen so that when in series with a converter the converter will operate at the design point.

d. To control all the switches then requires five command channels.

e. For series operation of all four converters switches K_1 through K_4 are closed, which, since they operate in pairs, requires switches K_5 through K_8 to be open.

f. For separate operation of each converter, switches K_1 through K_4 are open which means that switches K_5 through K_8 are closed.

g. To operate converters I, II and IV in series and place converter III in series with resistor R_3, switches K_1,K_2, K_4 and K_7 are closed and switches K_3,K_5, K_6 and K_8 are open.

NOTE: SWITCHES K_1 AND K_5, K_2 AND K_6, K_3 AND K_7, AND K_4 AND K_8 OPERATE AS PAIRS. FOR EXAMPLE WHEN K_1 IS CLOSED K_5 IS OPEN AND WHEN K_5 IS CLOSED K_1 IS OPEN.

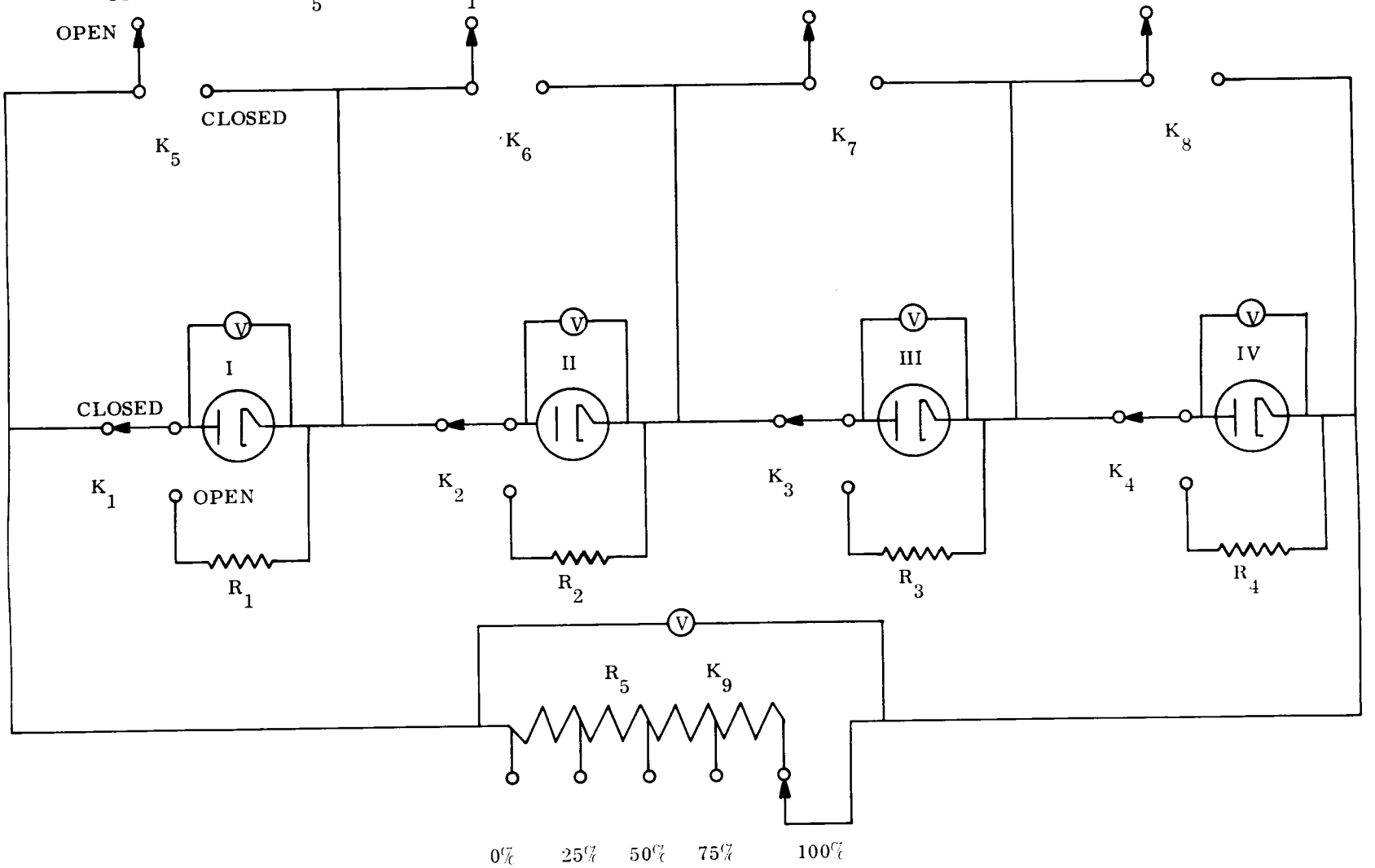

Figure 8-32. Thermionic Generator Electrical Circuit

Thus, through five command channels the capability exists to operate each converter separately or any combination in series as well as varying the generator load resistor in five increments from 0 to 100 percent of full load.

The advantages of this approach over wiring the four converters in a fixed series arrangement are significant. For example, assume that the four converters were operating in series and one of them experienced an open circuit failure. The thermionic generator output would immediately drop to zero. If the four converters were permanently wired in series with no flexibility in the electrical circuit nothing could be done and the generator performance aspects of the experiment would be ended. However, with the electrical circuit proposed here the faulty converter would be removed by command from the series string and the experiment continued with the remaining three converters in series.

The design of a circuit to perform the functions described here was discussed with the Kinetics Corporation. Based on a preliminary evaluation of the problem they suggested the use of motor actuated switches controlled by ground command. They estimated the entire control circuit could be flight packaged in a box smaller than four inches on a side and weighing less than six pounds. The voltage drop across the switch contacts was estimated to be less than 30 millivolts.

The details of the circuit design require further investigation to determine the impedance balance between the leads and the load resistors, the size of the load resistors, a method of dissipating the waste heat from the load resistors, etc.

8.5.2 GENERATOR LEAD LOSS

8.5.2.1 Proposed Design

The electronics associated with the electrical circuit would be located in the main spacecraft body behind the solar concentrator. This location was selected because it would provide shielding and a controlled thermal environment. Two electrical leads from each converter

would be routed from the generator down the inside of the generator support tubes to the main spacecraft body. Number 3 AWG stranded copper wire is recommended for the leads. The characteristics of this wire are summarized below (Reference 8-7):

Diameter (including insulation) - 0.3 inches
Number of strands - 7
Cross sectional area of conductor - 0.053 in^2
Resistivity (at 25°C) - 0.205×10^{-3} ohms/ft
Current carrying capacity - 80 to 105 amperes
Weight (including insulation) - 0.175 lb/ft .

Since there would be eight leads and only three support tubes one tube would have to handle two sets of leads. This would be accomplished by taking two leads down the inside of the tube and the other pair of leads would be strapped to the outside of the support tube, the outside pair of leads would be located on top of the support tube so they would not increase the concentrator blockage area or be exposed to direct concentrated solar energy during initial orientation periods.

At the design point the generator output would be 42.4 amperes at 3.4 volts (144 watts). The lead resistance for this mode of operation would be:

$$\begin{aligned} \text{Lead resistance} &= \text{resistivity} \times \text{length} \\ &= 0.205 \times 10^{-3} \times 8 \times 5 \\ &= 8.2 \times 10^{-3} \text{ ohms} . \end{aligned}$$

This results in an I^2R loss of

$$I^2R \text{ loss} = (42.2)^2 \times 8.2 \times 10^{-3} = 14.25 \text{ watts}$$

which represents approximately ten percent of the generator output. The corresponding voltage drop would be 0.34 volts. A loss of this magnitude is not considered prohibitive

particularly since the converter voltage output measurements would be made at the generator, thus allowing the generator output to be computed excluding the lead losses.

The weight of the generator leads would be 40 ft x 0.175 lb/ft = 7 pounds.

8.5.2.2 Alternate Approaches Considered

The following alternate approaches were considered for reducing the lead weight and I^2R losses:

a. Aluminum leads
b. Employ the generator support arms as leads
c. Use a d-c/d-c converter to increase the generator output voltage and decrease the current to be carried
d. Locate the control electronics near the generator.

Each of these approaches are discussed here.

Aluminum could be used instead of copper as the lead material. For the same size lead this would reduce the lead weight by a factor of 3.3 but because of aluminum's higher resistivity the I^2R loss would be increased by a factor of ten. Therefore aluminum leads would only be helpful if the lead diameter could be made significantly larger. Unfortunately it is difficult to increase the lead size above No. 3 AWG wire without increasing the solar concentrator blockage area.

Using the generator support arms as electrical leads offers the potential advantage of performing two functions with the same member, with a resulting saving in weight. For the proposed circuit design four rather than three support arms would be used with this approach. One support arm for each thermionic converter. Each arm would consist of two concentric tubes bonded together with an electrical insulator. One of the concentric tubes would serve as the collector lead from the converter and the other tube as the emitter lead. The tube wall

thicknesses would be adjusted to yield the same resistance in each tube*. To maintain the same concentrator blockage area that the three support arm approach gives would require that the outer tube in the four arm approach have an outside diameter of 0.563 inches. A minimum inside diameter on the inner tube of 0.375 inches would be required so that the voltage tap and thermocouple leads could be brought down from the generator inside the support arms. This leaves 0.563 - 0.375/2 = 0.094 inches for the tube walls and the insulating material. Assuming an insulation thickness of 0.04 inches the tube wall thicknesses could not exceed 0.054 inches. A cross section of the support arm is shown in Figure 8-33.

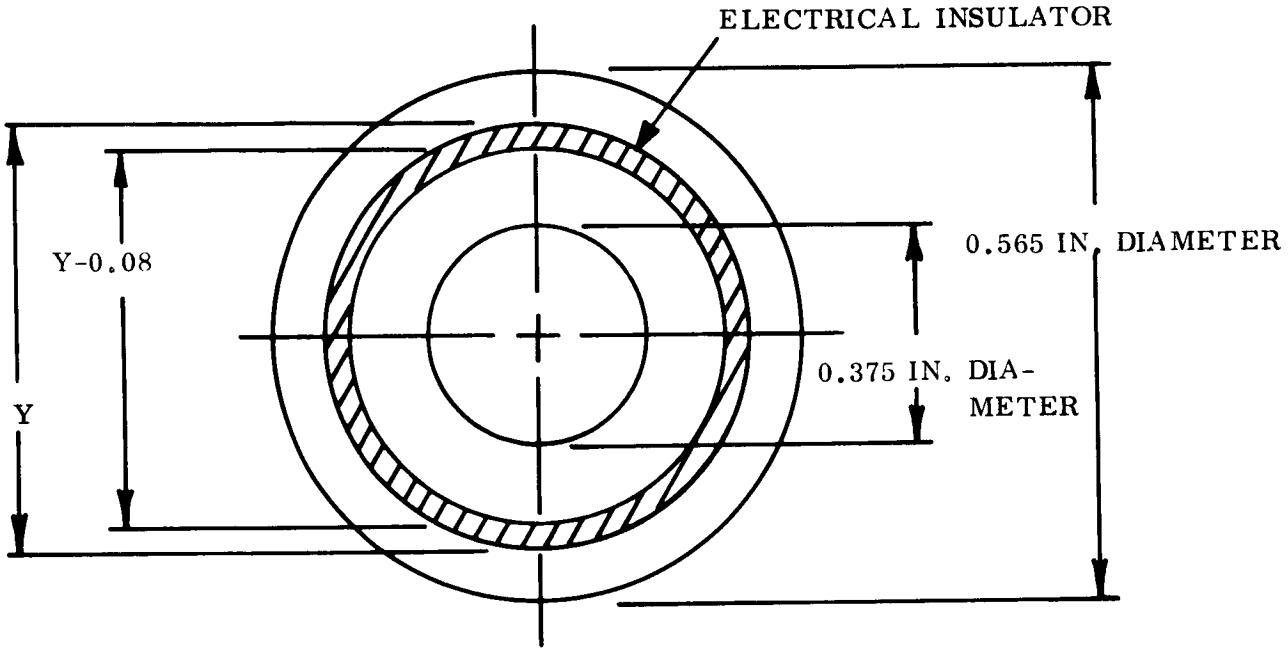

Figure 8-33. Cross Section of Support Arm

*This approach for using the generator support tubes as electrical leads has been studied by JPL. Hardware has been built for JPL by EOS and evaluation test conducted on this hardware at JPL. The results of these tests indicated that this is a feasible approach which in addition to saving weight also provides a convenient means for cancelling the magnetic fields produced in the high current carrying leads.

For equal resistivity in each tube (assuming the tubes are of equal length) the inside diameter, Y, of the outside tube is defined by the following equation:

$$A_1 = \frac{\pi}{4}(0.563^2 - Y^2) = A_2 = \frac{\pi}{4}\left[(Y-0.08)^2 - 0.375^2\right].$$

Solving for Y yields the following tube diameters and cross sectional areas.

Outer Tube - OD = 0.563 inches
ID = 0.516 inches
Wall thickness = 0.047 inches
Cross sectional area = 0.0397 square inches

Inner Tube - OD = 0.436 inches
ID = 0.375 inches
Wall thickness = 0.061 inches
Cross sectional area = 0.0397 square inches

The lead resistance is given by:

$$\text{Lead resistance} = \frac{\rho L}{A}$$

where

ρ = resistivity, ohm-inches
L = lead length, inches
A = cross sectional area, square inches.

Assuming aluminum for the support tubes the lead resistance of the support tubes alone (not including the lead lengths that would have to be added to each end of the support tube) would be

c. This approach requires adding another component to the experiment which adds inefficiency, weight, volume and most importantly reduces the experiment reliability.

The final approach considered was to mount the control electronics behind the generator. This would result in very short leads (approximately 8 inches per lead) and thus eliminate the I^2R loss problem. It also would greatly reduce the weight of the leads. This approach appears very attractive but must be investigated in greater depth before a definite recommendation can be made. Some of the points that must be considered are given below:

a. How small can the control electronics package be made?

b. Can the package be located near the generator without increasing the solar concentrator blockage area or interfering with the radiation heat transfer from the thermionic converter radiators?

c. Can the electronic package survive in this exposed location, or must it have a controlled environment similar to the one provided in the main spacecraft body?

These questions cannot be answered until the electrical circuit is designed in detail and this was beyond the scope of this study. If further investigation reveals that the control electronics can be located near the generator then this approach would be preferred to the one selected in this study.

8.5.3 MAGNETIC FIELD CONSIDERATIONS

When a current is passing through a conductor a magnetic field is produced. For large currents the resulting fields can be significant and may produce vehicle disturbance torques as well as interfere with the proper functioning of other spacecraft components. To avoid this potential problem each pair of thermionic generator leads would be twisted upon themselves. This allows the field produced in one lead to be cancelled by the opposing

$$\text{Lead resistance} = \frac{7.87 \times 10^{-6*} \times 26 \times 8}{0.0397} = 0.041 \text{ ohms.}$$

At the generator operating point the I^2R losses associated with the support arms alone would be

$$I^2R \text{ loss} = 42.2^2 \times 0.041 = 72.9 \text{ watts.}$$

This loss represents 50 percent of the generator output and is considered prohibitive. The I^2R losses could be reduced significantly by using copper in place of aluminum but copper is not a satisfactory structural material for the generator support arms. For this application it does not appear that the generator support arms could be used as leads unless the diameter of the tubes could be increased and this could not be done without increasing the solar concentrator blockage area which is undesirable. If the four converters were wired permanently in series and only two leads had to be brought down this approach would be more attractive.

A d-c/d-c converter could be located next to the generator to step up the generator output voltage and thus reduce the current that had to be carried by the leads. This approach was rejected for the following reasons:

a. The d-c/d-c converter must be located near the generator and therefore could not take advantage of the shielding and controlled thermal environment provided in the main spacecraft body.

b. Locating the d-c/d-c converter near the thermionic generator without increasing the solar concentrator blockage factor, or interfering with the view factors from the thermionic converter radiators, might be difficult.

---

* The resistivity of aluminum at $25^{\circ}C$ is 7.87×10^{-6} ohm-inches

field in the other lead. This is a common technique which is used effectively on spacecraft to minimize the magnetic effects of current loops.

8.6 INSTRUMENTATION

Adequate instrumentation is essential to a complete evaluation of the solar thermionic experiment. The proposed instrumentation is given in Table 8-3. On the basis of the information received from this instrumentation, coupled with the electrical circuit proposed in Section 8.5.1 and the supplementary data obtained from the priority "A" secondary experiments, the performance of the thermionic generator (including the individual converters), solar concentrator, and attitude control subsystem could be evaluated, any malfunctions detected, and in some cases corrective action taken to counter a malfunction.

8.6.1 QUANTITIES MEASURED

In order to evaluate the thermionic converter performance the voltage output of each converter (measured at the generator) and the voltage drop across the generator load would be measured (see Figure 8-32). In addition to the voltage measurements; the emitter, collector, fin, seal and cesium reservoir temperatures would be measured on each converter. These temperature measurements, because of the wide ranges and high levels involved, would have to be made with thermocouples. Thermocouples have the disadvantage of providing low voltage inputs to the telemetry subsystem but in this case it cannot be avoided. The recommended type of thermocouple for each of the temperature measurements is given in Table 8-3.

The thermionic converter temperature measurements coupled with several temperature measurements on the generator structure would provide sufficient information to analyze the generator thermal behavior. The temperature on the generator back cover and the outer edge of the shield cone, parts 62 and 55 respectively in Figure 8-2, would be measured. In addition the temperature drop on one of the generator block supports (Part 57 in Figure 8-2) would be measured. These generator structure temperatures would also be measured with thermocouples.

Table 8-3. Primary Experiment Instrumentation[a]

Measurement	Number of Measurements		Range of Output Signal	Comments
	Voltage	Temp		
A - Converter Performance				
Voltage Output Each Converter	4		0-1v	
Voltage Drop Across Load	1		0-4v	
Emitter Temperature Each Converter		4	0-35 mv	W-5 Re/W-25 Re Thermocouples
Collector Temperature Each Converter		4	0-35 mv	Chromel-Alumel Thermocouples
Fin Temperature Each Converter		4	0-30 mv	" " "
Seal Temperature Each Converter		4	0-35 mv	" " "
Cesium Reservoir Temperature Each Converter		4	0-15 mv	" " "
B - Generator Structure				
Temperature Generator Back Cover		2	0-30 mv	Cromel-Alumel Thermocouples
Temperature Outer Edge of Shield Cone		2	0-35 mv	W-5 Re/W-25 Re Thermocouples
Temperature Drop on One Generator Block Support		2	0-30 mv	Cromel-Alumel Thermocouples
C - Concentrator Performance				
Temperature Distribution on Concentrator Surface		10	0-3v	Measurements along two radial lines 90° apart made with resistance thermometers.
Concentrator Reflectivity	1		0-5v	
D - Orientation System Performance				
Thermocouples Located 90 degrees Apart Around the Aperature Opening		4	0-35 mv	W-5 Re/W-25 Re Thermocouples
Two Fine Sun Sensors (Pitch and Yaw)	2		0-5v	
Two Pair of Course Sun Sensors (Pitch and Yaw)	2		0-5v	

Notes.

a - A telemetry accuracy of one percent is adequate for all of the instrumentation in this table.

The solar concentrator surface temperature profile and reflectivity would be measured. The temperature profile would be measured along two radial lines 90 degrees apart. These temperature readings would provide a measure of the temperature extremes the concentrator was exposed to throughout the orbit and allow calculation of any deviations in the focal point location resulting from thermal distortion. Resistance thermometers would be used to make these temperature measurements. The reflectivity measurement would be made by a less sophisticated reflectometer than the one employed in the Solar Reflective Surfaces experiment described in Section 5.2.6 (Volume II). The major objective of this measurement would be to indicate any degradation by making a relative comparison between the reflectivity at a given time and the initial reflectivity value. The location of the reflectometer is shown in Figure 8-34.

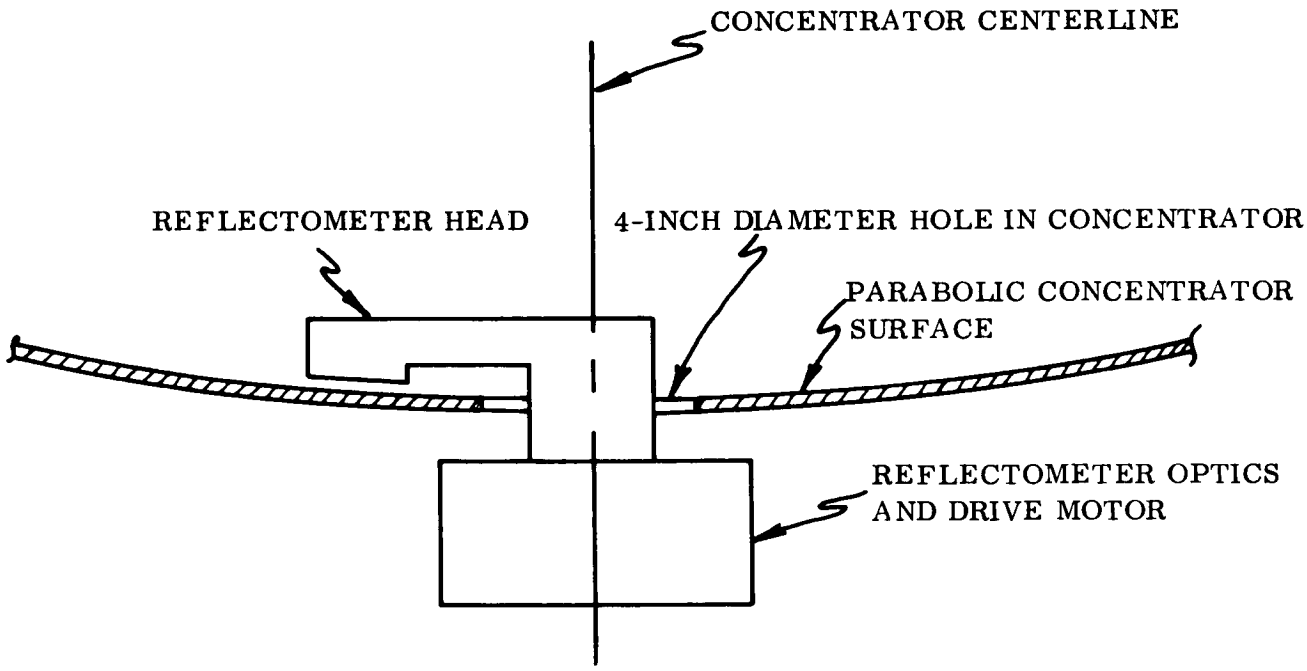

Figure 8-34. Reflectometer Location

The major reflectometer components and the drive motor would be located directiy below the center of the concentrator. The reflectometer head would be mounted in an arm which passed through the four-inch hole in the center of the concentrator. This arm would be motor driven so that the reflectometer head would be able to cover a circular band on the

concentrator surface. The length of the reflectometer arm would be sufficient (approximately five inches) to place the measuring head outside the shadow area of the thermionic generator so that the surface being measured would have received maximum exposure to sunlight. The reflectometer head would be rotated to a new location on a periodic basis*, so that a representative reflectivity, measured over more than one spot on the concentrator, could be obtained. Rotation of the head is also necessary because leaving it permanently in one place would shield the surface being measured from some of the environmental factors (micrometeoroids, ultraviolet radiation, etc.). The reflectometer would be supported by the main spacecraft structure and would not be in contact with any portion of the concentrator structure. The reflectivity of the solar concentrator surface is considered of sufficient importance to warrant this reflectance measurement in addition to those made in connection with the Solar Reflective Surfaces experiment (Section 5.2.6 - Volume II).

The orientation accuracy can be determined by monitoring the output signals from the sun sensors and the thermal sensors located around the aperture opening. There are two fine sun sensors (pitch and yaw) and two pairs of course sun sensors (pitch and yaw). This arrangement yields four signal outputs that must be monitored. There are four thermal sensors and measuring the output of each yields four additional voltages or eight total. Of course, measurement of these quantities would be made as part of the attitude control subsystem diagnostic instrumentation even if they were not needed to evaluate the primary experiment.

In addition to the data obtained from the instrumentation associated with the primary ment, the priority "A" secondary experiments would provide supplemental information on the micrometeoroid, ultraviolet radiation, and proton and electron environments encountered. This information would be beneficial in evaluating the solar concentrator performance since these factors are believed to be potential sources of reflectivity degradation. A further measure of the concentrator reflectivity performance would be obtained from the secondary Solar Reflective Surfaces experiment.

* This function would be executed upon stored or ground command.

8.6.2 FREQUENCY OF SAMPLING

To completely evaluate the primary experiment, including the transient phase, it would be necessary to read the quantities outlined in Table 8-3 every 15 seconds during 16-minute periods (approximate) at the beginning and end of the daylight portion of the orbit. In the intervals outside of these two 16-minute periods, readings would be made on a five minute basis throughout both the light and dark segments of the orbit. This scheme represents the most desirable arrangement but if it imposes too great a load on the telemetry subsystem an alternate procedure could be used. This alternate approach would follow the sampling cycle outlined above on a periodic rather than a continuous basis. For example this sampling cycle would be used during the initial phase of the experiment and at points where the transient data was needed to evaluate special circumstances which arise. When not operating on this sampling cycle each of the quantities would be recorded once every five minutes throughout the daylight portion of the orbit only. This latter approach, although not preferred, would provide a fairly complete picture while imposing a significantly smaller demand on the telemetry subsystem. This subject is discussed further in Section 9.3. The final decision on which approach to use is made in Section 10.

8.7 POWER REQUIREMENTS

The power required to operate the thermionic experiment is minimal. Approximately 1.4 watts would be required on a continuous basis for the temperature measurements. During the daylight portion of the orbit only, the cesium reservoir heaters and reflectometer would require a continuous 0.4 and 2.6 watts respectively. In total then the primary experiment would require 1.4 watts continuously with an additional 3.0 watts during the daylight phase of the orbit.

8.8 MODE OF OPERATION

Once the spacecraft was in orbit the solar thermionic experiment would operate as described below.

Under normal conditions the four thermionic converters would be connected in series and the load adjusted so at design temperatures the converters would operate at their peak efficiency point.

When the spacecraft emerged from the earth's shadow* the attitude control subsystem would orient the solar concentrator to the sun with the desired 0.1-degree accuracy. This would take approximately two minutes to accomplish (see Section 11). No auxiliary heat would be used to warm up the cesium reservoirs and no controls would be employed to limit the solar concentrator input to the generator cavity. As a result of this the emitter temperatures would reach approximately 2400^{o}K for a short period of time. The thermionic generator would reach the design operating point and steady state operation in approximately 16 minutes after acquiring the sun.

During steady state operation the cesium reservoir temperature would be adjusted to the optimum value by small electrical heaters (0.1 watt maximum). The heater control circuit would be designed so that it would attempt to maximize the converter power output for the given load and emitter temperature. During the daylight portion of the orbit the temperatures and voltages outlined in Table 8-3 would be monitored, the data stored, and telemetered back to earth when the spacecraft was over an appropriate ground station. The desired frequency of sampling the measured quantities calls for reading each quantity every 15 seconds during the transient warm-up phase (approximately 16 minutes) and then once every five minutes throughout the remainder of the daylight period. The steady-state mode of operation would continue until the spacecraft entered the earth's shadow.

Upon entering the earth's shadow the solar input to the generator would stop and the emitter temperature would start to drop. As the emitter temperature dropped, the generator power output would decrease until at an emitter temperature of approximately 1750^{o}K the generator power output would become zero (this assumes the cesium reservoir heaters are able to optimize the reservoir temperature as the emitter temperature decreases and that the

*In the Mission A case for the first four to six months of the experiment the spacecraft would not encounter any shadow periods.

design point load is maintained). The instrumentation outlined in Table 8-3 would be sampled every 15 seconds during the initial 16 minutes (approximate) of the shadow period and every five minutes through the remainder of the dark cycle.

At periodic intervals a generator EI curve would be measured by varying the generator load resistance. This would be accomplished by ground command. In order to check on the individual converters performance, they would periodically be commanded into series with their individual load resistors and the resulting performance recorded.

If a thermionic converter were to fail it would be removed from the series circuit by ground command and the experiment continued with the remaining good converters.

If the thermionic generator performance were to degrade, the operating point could be altered by changing the load resistance. This would also be achieved by ground command.

In general, commanded changes in the generator electrical circuit would be held to a minimum for reliability reasons.

8.9 OTHER CONSIDERATIONS

In addition to the design point performance considered thus far, some consideration was given to off design operation resulting from a decrease in the input energy to the generator or an orientation error larger than the designed limits. Also, the possibility of replacing the generator with an identical generator while in space was investigated. These three areas are discussed in the following sections.

8.9.1 EFFECT OF A DECREASE IN INPUT ENERGY

It is conceivable that during the experiment life, the energy input to the thermionic generator could decrease from the design value. For example this might occur as a result of a decrease in the solar concentrator reflectivity. The effect of a ten percent decrease in input energy is considered here.

Figure 8-8 shows that for a ten percent decrease in input energy, the energy available to the converters decreases by about 32 watts per converter. Figure 8-11 indicates that for this decrease in energy, the locus of thermally balanced conditions in the generator will be a new dashed line located approximately 25 watts lower than the dashed line shown in the figure. If, with this amount of decrease in input energy, the thermionic converters still see a load such that their output voltage remains at 0.85 volts, the converter emitter temperatures will decrease to a point where the heat available in the cavity is sufficient to produce the corresponding output current. Thermionic data taken on the Series VIII converters developed by Thermo Electron Engineering Corporation for JPL, indicates that the output current at 0.85 volts falls by 50 percent when the emitter temperature is reduced from $2000^{o}K$ to $1900^{o}K$. The corresponding cesium reservoir optimum temperature decreases by approximately $35^{o}K$. Thus, the locus of possible performance (at 0.85 volts) can be shown in Figure 8-11 as a line which connects the design point ($2000^{o}K$ emitter temperature and 42.4 amperes of output current) to the 21.4 ampere point on the $1900^{o}K$ emitter temperature line. This locus crosses the dashed line corresponding to the ten percent decrease in energy entering the cavity at an emitter temperature of approximately $1960^{o}K$. At this point the output current would be 34 amperes. This represents the new thermally balanced condition in the generator.

If the reservoir temperature decreases by $35^{o}K$ for a decrease of $100^{o}K$ in emitter temperature, a decrease from 2000^{o} to $1960^{o}K$ emitter temperature would require a decrease in reservoir temperature of $14^{o}K$. It is interesting to note the extent to which the thermal characteristics of the converter design tend to establish a new cesium reservoir temperature as close as possible to the optimum value corresponding to the emitter temperature of $1960^{o}K$. Figure 8-12 indicates that the heat transmitted to the radiator structure is 109 watts for an output current of 34 amperes at $1960^{o}K$. Figure 8-17 shows that the corresponding collector base temperature at this value of heat transfer is $795^{o}K$. Figure 8-22 in turn shows that for a collector base temperature of $795^{o}K$, the corresponding equilibrium reservoir temperature is $630^{o}K$. Therefore, with a ten percent decrease in input energy, the converter performance would be optimum with a reservoir temperature which decreases by $14^{o}K$ from its previous optimum of $639^{o}K$. The converter heat transfer parameters are

such that the cesium reservoir temperature would actually decrease by $9^{o}K$ instead of the desired $14^{o}K$. Fortunately, the reservoir temperature will remain within the range of control provided by the cesium reservoir heater, assuming that the heater has a rating of 0.1 watt. It is necessary, in order to take advantage of this self-adjusting feature, that the cesium reservoir control operate so as to always optimize the output current of a converter rather than to attempt to maintain a predetermined value of cesium reservoir temperature. The design of the control circuitry which would achieve this was not attempted in this study.

8.9.2 EFFECT OF MISORIENTATION

The effects of misorientation were calculated for angular deviations of 10 and 20 minutes. For a 50-inch diameter solar concentrator with a rim angle of 60 degrees (corresponding to a focal length of 55.0 centimeters) these deviations correspond to focal plane displacements of 0.160 and 0.320 centimeters respectively. Figure 8-35 shows graphically the procedure used to determine the changes in input solar energy resulting from these values of misorientation. The focal spot produced by the concentrator was divided into concentric rings and the energy density was calculated for each ring. The generator aperture was divided into four quadrants corresponding to the heated faces of the thermionic converters. The area in any one focal spot ring, within any given quadrant, was determined graphically and the corresponding amount of energy falling within that quadrant was computed.

Table J-1 (Appendix J) shows the results of these computations for the focal plane displacements of 0.16 and 0.32 centimeters. It shows that the overall decrease in input flux for a focal plane displacement of 0.16 centimeters is 11.8 percent; thereby corresponding to a decrease of about one percent for each minute of misorientation. For a displacement of 0.32 centimeters, the decrease in total input energy to the cavity is 19.1 percent, still corresponding to a decrease of one percent for each minute of misorientation. Table J-1 shows that the total amount of energy falling in each individual quadrant can be highly non-uniform for even small amounts of displacement. For a focal plane displacement of 0.16 centimeters, Table J-1 shows the total amount of energy falling on quadrant III is 474.0 watts, while the total amount of energy falling on quadrant I is 175.8 watts or less

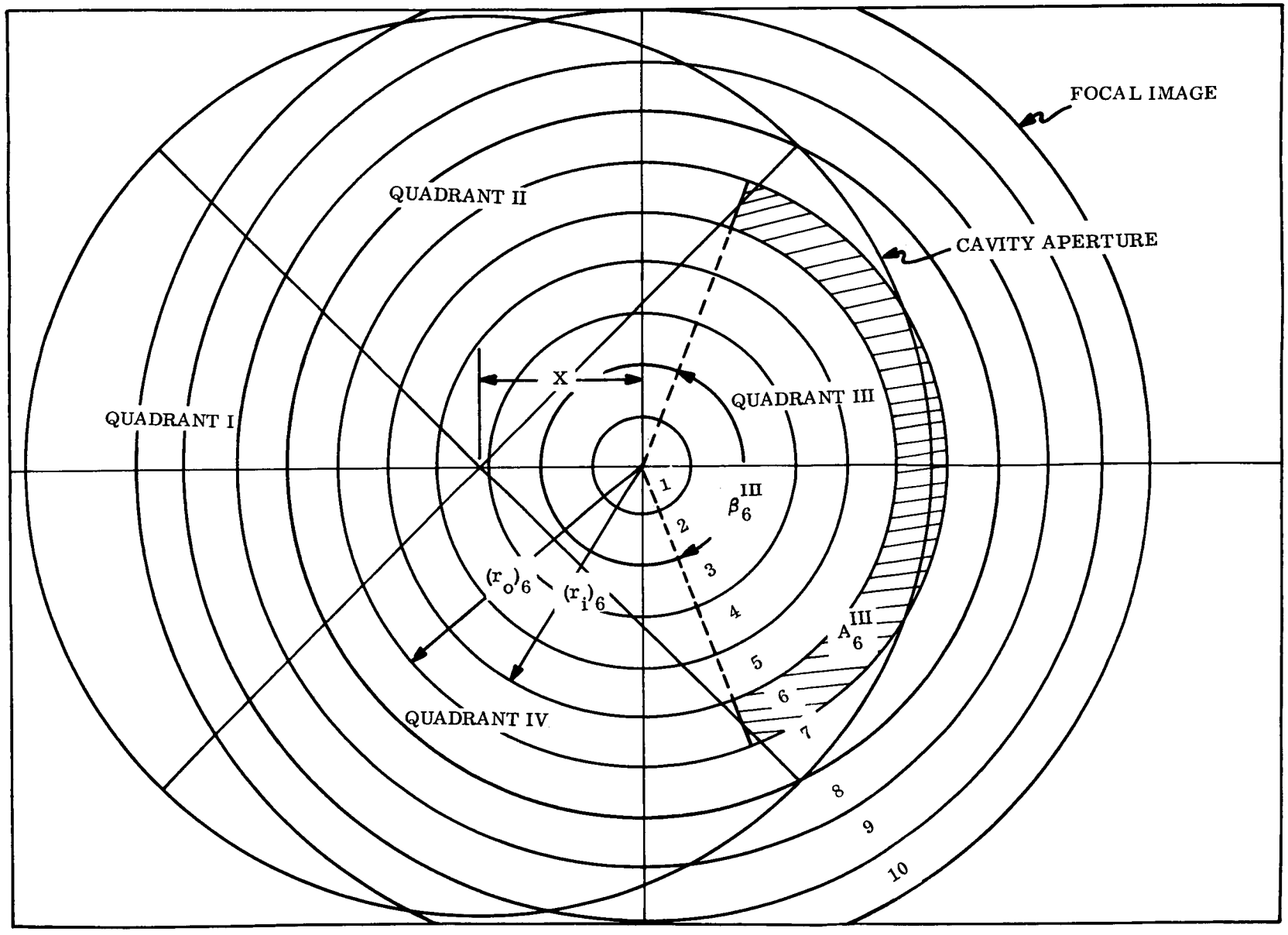

Figure 8-35. Misorientation Flux Analysis

than one-half the amount falling in quadrant III. This tends to imply that misorientation could have a significant influence on the temperature distribution among converters. However, no attempt has been made to determine how serious this effect is and it seems that an experimental approach to answer this question is in order.

Some of this data is already in existence. As a first approximation, the predicted effect of misorientation is that the energy input to the cavity will decrease by a percentage closely equal to the minutes of arc of misorientation, and that the effect on generator performance will be somewhat similar to the effects of decreases in input flux. For a decrease in input flux of ten percent, it was found that the output current decreased from 42.4 to 34 amperes (at 0.85 volts) with a corresponding decrease in emitter temperature from 2000^{o} to 1960^{o}K. For a decrease in input flux of 20 percent, one could expect double the reduction in performance or the current would drop to 25.6 amperes. This subject is discussed further in Section 11.2.

8.9.3 INFLIGHT GENERATOR REPLACEMENT

The possibility of replacing the thermionic generator with another identical generator while in orbit was considered. Obviously if this could be easily accomplished within the design constraints the chances of conducting a successful experiment would be significantly increased. Although several approaches were considered only one appears to be compatible with the imposed constraints of this application. This approach is outlined here in detail.

8.9.3.1 Description

The proposed scheme is shown in Figure 8-36. The two generators are mounted back to back to a spindle supported by a close tolerance bearing at each end. Substitution of a generator is achieved by accurately rotating this spindle through 180 degrees. Changing back to the original generator could be accomplished by rotating back through 180 degrees. The generators do not rotate through more than 180 degrees, thus enabling the electrical connections to be made through flexible pigtails rather than necessitating the use of slip rings.

Referring to Figure 8-36, rotation of the spindle is produced by a motor through a friction clutch. Rotation of the crank withdraws the locking pin by means of a link. When the locking pin is withdrawn the crank continues to rotate until it bears against the spring loaded detent. This then causes the arm to rotate with the crank, and since the arm is rigidly attached to the spindle by splines, the spindle and the two generators now rotate under the action of the motor.

When the arm has rotated through 180 degrees, it bears against an adjustable stop, causing the crank to override the spring loaded detent. At this point the arm stops rotating but the crank continues to rotate until the locking pin is once again engaged. At nearly full engagement the locking pin depresses a microswitch, cutting off the drive motor.

To reverse the process, a ground command causes the microswitch to short and the motor to reverse.

The areas requiring close tolerance machining are the locking pin, the holes it engages in the arm and housing, and the spindle and support bearing housings. The adjustable stops do not require very fine adjustment since the locking pin is self-engaging. It is anticipated that each generator would be shimmed and aligned at its four mounting holes in a fashion similar to that described in Section 8.3.3.2.

The major advantage of this approach over others considered is that it does not increase the solar concentrator blockage area appreciably over than encountered with the proposed design shown in Figure 8-3.

This approach appears feasible but requires further investigation before it could be recommended for use in a flight experiment application of the type considered here. Some of the major areas that need to be studied are outlined below.

a. How would the electrical leads be taken care of? Would one common set of leads be provided and the electrical connections switched when the generator was rotated or would each generator have its own set of leads?

b. Would the thermal losses be greater as a result of the generator support technique?

c. Could this scheme be made to operate satisfactorily under the temperatures involved?

d. Would the increased weight make it difficult to design the support structure to withstand the launch loads?

8.10 SUMMARY AND CONCLUSIONS

The solar thermionic experiment outlined in this section is based on present state-of-the-art capability and would provide a very complete evaluation of solar thermionic system performance in the space environment.

8.10.1 EXPERIMENT CONFIGURATION AND WEIGHT

The thermionic system configuration is shown in Figure 8-37. The estimated weight of the solar thermionic experiment is given in Table 8-4.

Table 8-4. Thermionic Experiment Weight

COMPONENTS	WEIGHT (Pounds)
Thermionic Generator	5.7
Solar Concentrator (including Torus)	12.5
Support Structure	2.0
Reflectometer	5.0
Control Electronics	6.0
Electrical Leads	7.0
TOTAL	38.2

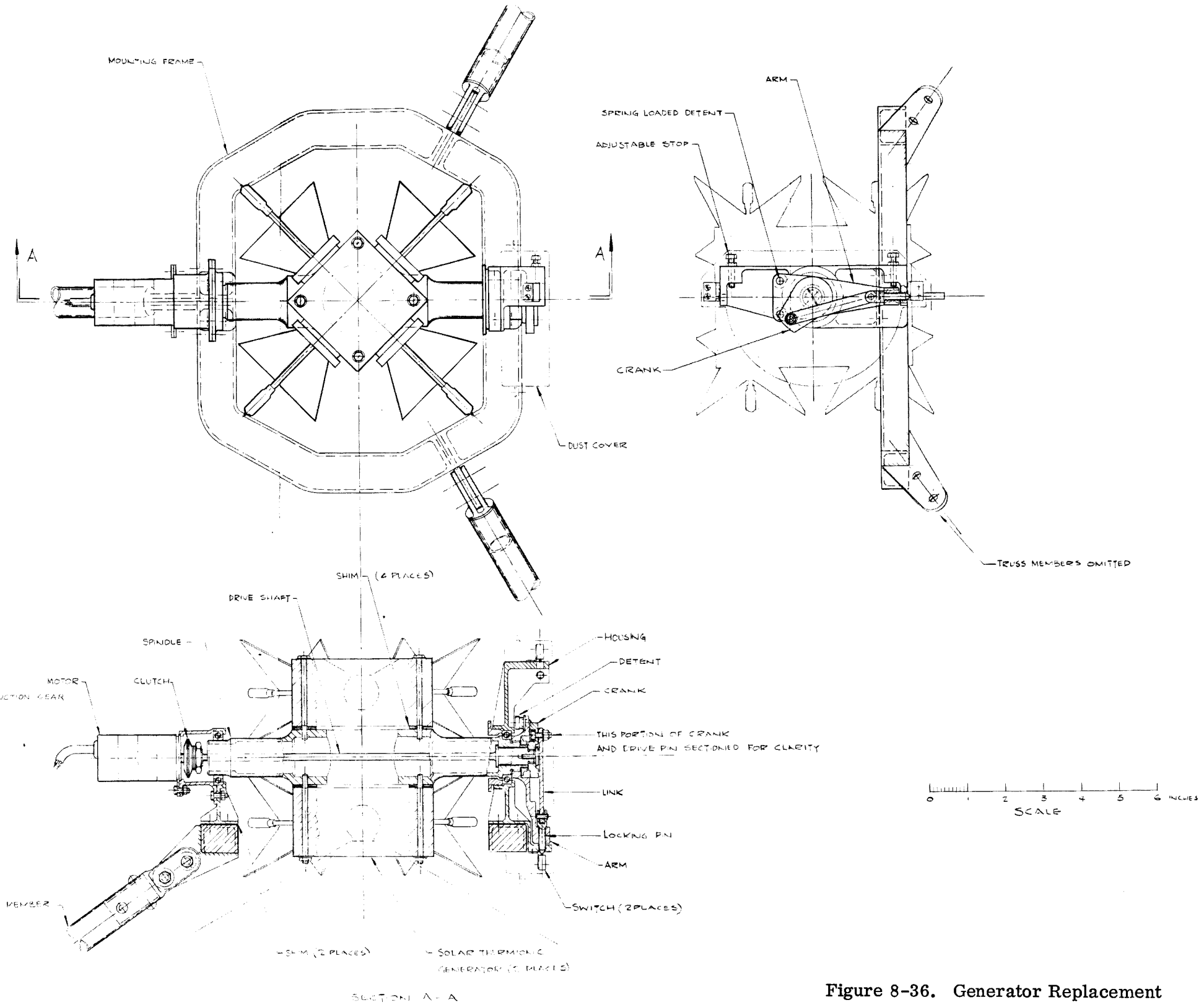

Figure 8-36. Generator Replacement Scheme

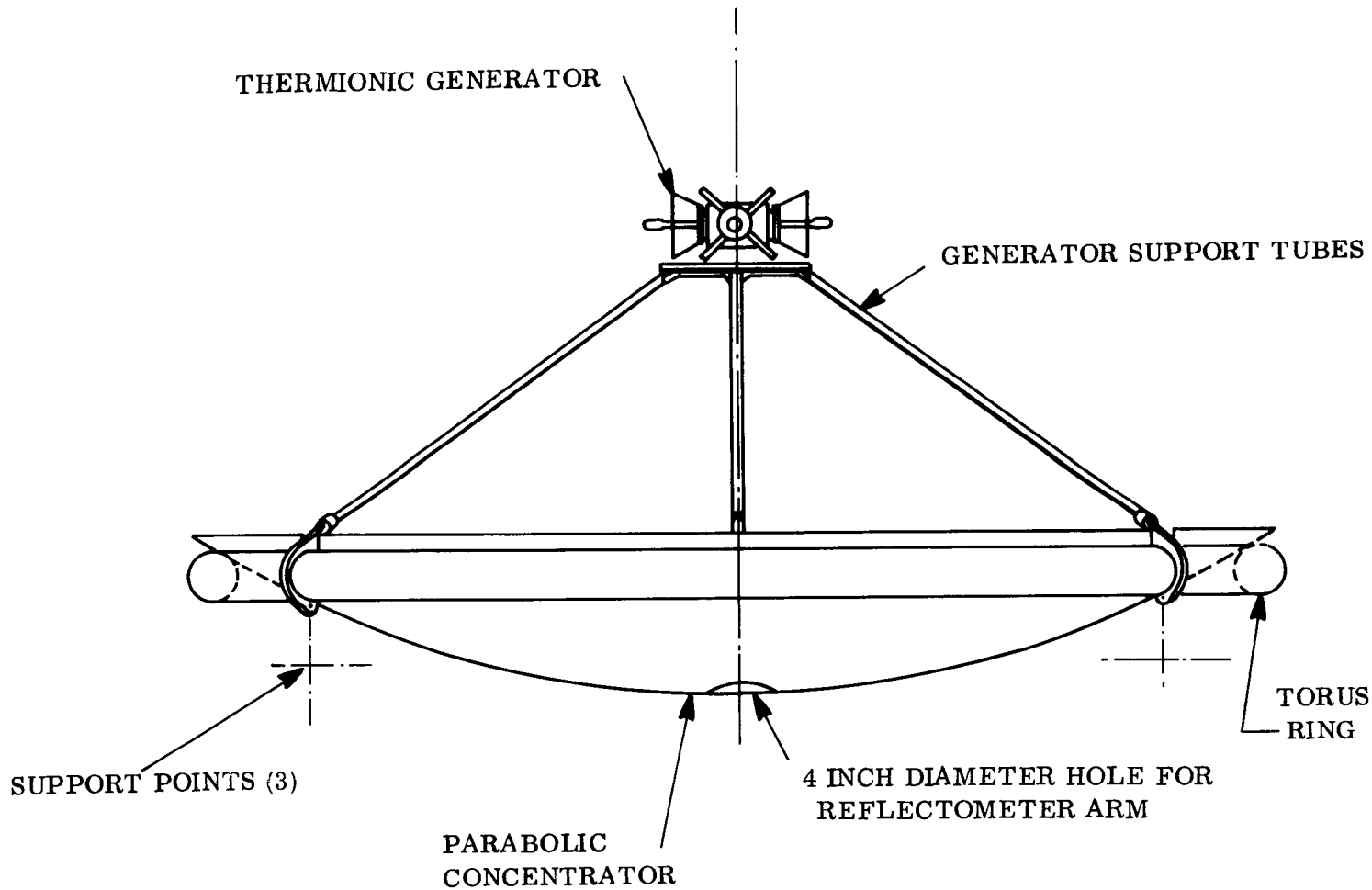

Figure 8-37. Solar Thermionic System

The configuration shown is mounted directly to the main spacecraft body at three support points.

The launch vehicle fairings allow ample volume so that the generator can be fixed in its operating position with respect to the solar concentrator. This eliminates any requirements to fold the generator in close to the concentrator during launch and then deploy the generator after the fairing has been ejected.

8.10.2 PERFORMANCE

The estimated thermionic system performance is summarized in Table 8-1. Actually the performance estimates were made in Section 4 of Volume II but since the generator design had not been established at that point it was necessary to make assumptions regarding the generator losses. The energy balance calculations performed in this section substantiate the assumptions made in Section 4 and therefore the original performance estimates are considered valid.

8.10.3 CONTROLS

As a result of this investigation there appears to be no incentative for using controls during the generator warm-up phase. Controlling the input energy to the generator cavity or applying auxiliary heating to the cesium reservoirs does not appreciably reduce the warm-up time. If the thermionic converters can withstand short temperature spikes (up to 2400^{o}K) on the emitters a simpler and more reliable system will result if no controls are used during the warm-up.

During steady-state operation the cesium reservoir temperatures would be held at their optimum values by small electrical heaters of approximately 0.1 watt capacity. The control circuit for these heaters would be designed to maximize the converter output for the given load and emitter temperature.

8.10.4 CONCENTRATOR BLOCKAGE AREA

The thermionic system performance calculations assumed a concentrator blockage factor (see Section 4.4.1.3-Volume II) of five percent. The actual blockage factor was computed in Appendix L for the configuration shown in Figure 8-37 and found to be 4.9 percent.

8.11 REFERENCES

8-1. "Forming Aluminum for Solar Energy Concentrators," General Electric Re-Entry Systems Department Final Report No. 64SD5210, prepared for NASA Langley on Contract No. NAS-1-3309, October 30, 1964.

8-2. "Research and Development Techniques for Fabrication of Solar Concentrators," Electro-Optical Systems in Company Final Report No. 1587, prepared for NASA on Contract No. NAS 7-10, December 27, 1961.

8-3. "9.5 Foot Diameter Master and Mirror," General Electric Spacecraft Department Final Report No. 64SD540, prepared for JPL on Contract No. 950239, March 20, 1964.

8-4. "Coatings," Catalogue of the Liberty Mirror Division, Libby-Owens-Ford Glass Company, Revision C-63.

8-5. "Study of a Flight Experiment of Solar-Concentrator Reflective Surfaces," EOS Report 4100-Final, Contract NAS 1-2880, November 1, 1963.

8-6. P. J. Brosens, "Solar Thermionic Generators for Space Power," ASME paper No. 64-WA/SOL-1, presented at the winter annual meeting of the ASME, November 29-December 3, 1964, New York.

8-7. L. S. Marks, Mechanical Engineers' Handbook, Fifth Edition, Mc-Graw-Hill.

SECTION 9

INSTRUMENTATION

PRINCIPAL CONTRIBUTOR:

E. W. Williams

SECTION 9
INSTRUMENTATION

9.1 INTRODUCTION

This section considers the total spacecraft instrumentation required and the resulting load on the telemetry subsystem. Also included is a general discussion of methods of making various types of instrumentation measurements.

9.2 QUANTITY OF INSTRUMENTATION

The instrumentation can be considered in three parts: (1) that required to completely evaluate the solar thermionic experiment, (2) the instrumentation associated with the secondary experiments, and (3) that needed to monitor critical spacecraft components. The instrumentation associated with the primary and secondary experiments was covered in detail in Sections 8.6 (Table 8-3) and 5.4* (Table 5-3) respectively.

A limited amount of instrumentation is necessary to keeping the spacecraft functioning in space. If ground personnel have the benefit of information such as solar cell temperature, battery charging current, battery cell temperature, quantity of attitude control gas remaining, etc., it is possible to diagnose problems and take corrective action before a failure occurs. Similarly, this sort of information is valuable in determining why a failure occurred. A preliminary estimate of the quantity of critical component instrumentation required is given in Table 9-1. If the spacecraft were designed in detail, there would undoubtedly be other critical component measurements to add to this list. Twenty miscellaneous measurements are added to the total to allow for any contingency.

These quantities would be read once every thirty seconds over the orbit period. All of the measurements should be recorded at approximately the same time. Although desirable, it is not absolutely necessary that this instrumentation be read every orbit. It could be

*Located in Volume II

Table 9-1. Critical Component Instrumentation [a]

Instrumentation	Number of Measurements	Range of Output Signal	Comments
A. Power Subsystem [b]			
1. Temperature of Battery Package	2	0-5v	Measurements Made With Thermistors
2. Battery Voltage	1	20-38v	
3. Battery Charge and Discharge Voltage	2		
4. Solar Cell Temperature on Each Paddle	2		Measurements Made with Resistance Thermometers
5. Array Voltage	1	0-28v	
6. Array Current	1	4.3 Amps (Typical)	
B. Attitude Control Subsystem [c]			
1. Gas Pressure (1 Tank)	2	0-5v	
2. Number of Valve Operations (3 Channels, 6 Valves Total)	6	0-5v	
3. Vehicle Angular Rates (3 Gyro Voltages)	3	0-5v	
4. Roll Position	3	0-5v	
5. Flywheel Voltage and Speed (2 Flywheels)	4	0-5v	
C. TT&C Subsystem			
1. Voltage Monitors	6	0-5v	
2. Temperature Monitors	4	0-5v	Measurements Made With Thermistors
3. Event Monitors	4	0-5v	
D. Miscellaneous	20	—	
TOTAL	61		

NOTES:

(a) A telemetry accuracy of one percent is adequate for all of the instrumentation in this table. The quantities should be read every 30 seconds throughout the total orbit period. Although desirable, it is not necessary that these measurements be recorded every orbit.

(b) Evaluation of the power subsystem performance also requires knowledge of the accuracy with which the solar array is oriented to the sun. This information is derived from the primary experiment instrumentation (see Table 8-3).

(c) Additional information which is essential to evaluation of the Attitude Control Subsystem is available from the primary experiment (see Table 8-3).

sampled on a periodic basis, say once per day, but this introduces the possibility that a critical situation could occur between sampling periods and it would not be detected. Therefore, if telemetry capability is available, this information should be recorded every orbit. This situation is investigated further in Section 10.

9.3 DATA COLLECTED PER ORBIT

Knowing the number of instrumentation measurements to be made, the telemetry accuracy required, and the frequency of sampling the number of bits* per orbit that must be handled by the telemetry subsystem can be calculated. This information is summarized in Table 9-2 for the three categories of instrumentation. The basic information used to formulate this table was taken from Tables 5-3,** 8-3, and 9-1. In establishing this table, only the priority "A" and priority "B" secondary experiments were considered. Since final determination of how many, and which, of the priority "B" secondary experiments to be included on each of the three spacecraft designs will not be made until the designs are formulated (Section 13), the telemetry data requirements presented in Table 9-2 represent a maximum.

If the same secondary experiments are included on the spacecraft and the same subsystem instrumentation is employed, Table 9-2 shows that the bits of data collector per orbit will vary significantly between the three orbits considered. For example, the highly elliptical orbit, because of its long orbit period, generates three times as much data per orbit as the modified sun-synchronous orbit and five times as much as the low altitude circular orbit. The large number of bits collected per orbit could represent a data storage and transmission problem depending on the spacecraft power and ground station coverage available. This potential problem is considered further in Section 10.

---

*When a measurement has N equiprobable outcomes, the average amount of information associated with an outcome is defined as log N. In particular, if the logarithm is taken to the base two, the value indicates the number of decisions between pairs of equiprobable outcomes and the unit has been named the "bit" (an acronym for binary digit).
**Located in Volume II

Table 9-2. Bits of Data Collected per Orbit

	SUBSYSTEM OR EXPERIMENT	NUMBER OF MEASUREMENTS	BITS PER SAMPLE[d]	FREQUENCY OF SAMPLING	BITS PER ORBIT[a] I	II	III
PRIMARY EXPERIMENT	THERMIONIC GENERATOR	31	186	Once every 15 seconds for 30 minutes and once every 5 minutes over the remainder of the orbit period.	25,800 (4,620)[b]	52,100 (26,500)	24,770 (2,250)
	SOLAR CONCENTRATOR	11	66	Once every 15 seconds for 30 minutes and once every 5 minutes over the remainder of the orbit period.	9,160 (1,640)	18,620 (9,430)	8,797 (799)
	ORIENTATION	7	42	Once every 15 seconds for 30 minutes and once every 5 minutes over the remainder of the orbit period.	5,830 (1,042)	11,840 (6,000)	5,598 (508)
	PRIMARY EXPERIMENT TOTALS	49	294	-	40,790 (7,302)	82,860 (41,930)	39,165 (3,557)
SECONDARY EXPERIMENTS	SPACE EVALUATION OF SOLAR REFLECTIVE SURFACES	31	186	Once per orbit after steady state has been reached in daylight portion of the orbit.	186	186	186
	MICROMETEOROID MEASUREMENT	16	96	Once per orbit.	96	96	96
	PROTON AND ELECTRON SPECTRA AND DIRECTION	6	36	Once per minute.	4,170	30,250	3,170
	MEASUREMENTS OF ULTRAVIOLET RADIATION FLUX	41 1[e]	246 6	Once per minute during the sunlight portion of the orbit.	30,500	1,280	14,900
	SPACE EVALUATION OF THERMAL COATINGS	8	48	Once per orbit after steady state has been reached in daylight portion of the orbit.	48	48	48
	LASER EXPERIMENT	5	30	Once per orbit.	30	30	30
	LOW THRUST ELECTRIC ENGINE	5	30	Once per minute for 1.4 hours every 1.2 days.	252	252	252
	RADIATION EFFECTS ON SOLAR CELLS	9	54	Once per orbit after steady state has been reached in daylight portion of the orbit.	54	c	c
	SPACE EVALUATION OF A NEW INFRARED DETECTOR	6	36	Once per orbit.	36	36	36
	SOLAR X-RAYS	2	12	Once per minute during daylight portion of the orbit.	1,490	8,570	725
	SOLAR γ - RAYS	6	36	Once per minute during daylight portion of the orbit.	4,470	25,700	2,180
	LYMAN-ALPHA EXPERIMENT	81	486	Once per minute during daylight portion of the orbit.	60,200	347,000	29,400
	EARTH ALBEDO	120	720	Once every 2.5 minutes during the daylight portion of the orbit.	c	c	17,400
	SECONDARY EXPERIMENT TOTALS	342	2,052		101,832	416,448	68,723
CRITICAL SPACECRAFT COMPONENTS	POWER SUBSYSTEM	11	66	Every 30 seconds over total orbit.	16,400	55,500	6,370
	ATTITUDE CONTROL SUBSYSTEM	18	108	Every 30 seconds over total orbit.	26,800	90,800	10,420
	TT&C SUBSYSTEM	14	84	Every 30 seconds over total orbit.	20,800	70,500	8,100
	MISCELLANEOUS	20	120	Every 30 seconds over total orbit.	29,800	100,800	11,600
	CRITICAL COMPONENT TOTALS	63	378		93,800	217,600	36,490
	TOTALS	454	2,724		236,422 (202,934)	716,908 (675,978)	144,378 (108,770)

a Orbit I - Modified sun-synchronous (1000 NM-101.84 degrees inclination - orbit period, 124 minutes - maximum shadow period, 24 minutes)

Orbit II - Highly elliptical (200 by 25,000 NM-45 degrees inclination - orbit period, 840 minutes - maximum shadow period, 125.5 minutes)

Orbit III - Low altitude circular (325 NM-30 degrees inclination - orbit period, 96.5 minutes - maximum shadow period, 36 minutes)

b The figures in brackets are for the alternate mode of cycling the instrumentation associated with the primary experiment. This method of operation calls for sampling the quantities once every five minutes during the day-light portion of the orbit.

c Not compatible with this orbit.

d Bits per sample figures based on a telemetry accuracy of one percent.

e The second set of number apply to the highly elliptical orbit case where the two earth sensors are not included as part of the ultraviolet experiment.

If the bits of data collected per orbit becomes prohibitive, there are several ways the total could be reduced. First, the bits per orbit associated with the primary experiment could be reduced by going to the "alternate mode" of sampling the data described in Section 8.6.2 (Figures presented in brackets in Table 9-2 represent this mode of operation). Although this reduces significantly the bits of data from the primary experiment, it only has a small effect on the over-all total. A second, and very effective way to reduce the data to be handled, is to reduce the number of secondary experiments included on the spacecraft. In general, the engineering type secondary experiments contribute very few bits of data per orbit and, therefore, would do very little to reduce the total. However, some of the scientific secondary experiments contribute a significant percentage of the total bits collected per orbit. By elimination or alternating* the design of these experiments the data collected per orbit could be greatly reduced. A third alternative is available and consists of making the measurements in selected groups on a periodic basis rather than sampling all of the quantities every orbit. For example, consider the modified sun-synchronous orbit (Orbit I in Table 9-2). Assume that in the normal mode of operation, only the instrumentation associated with the primary and secondary experiments is recorded and that the primary experiment instrumentation is sampled on the "alternate" cycle described in Section 8.6.2. The total bits of data collected per orbit would be:

7,302 bits/orbit	-	Primary Experiment
101,832 bits/orbit	-	Secondary Experiments
109,134 bits/orbit	-	Total

Now, at regular intervals (probably on earth command) the above data would be omitted and the data required to evaluate the transient operation of the primary experiment recorded along with the critical component instrumentation. This combination yields the following total:

*Altering the experiment design would involve reducing the frequency of sampling, reducing the number of ranges, samples, etc.

40,790 bits/orbit	-	Primary Experiment
93,800 bits/orbit	-	Critical Components
134,590 bits/orbit	-	Total

Thus, by taking this approach, the same basic information could be obtained while reducing the bits of data collected per orbit by forty-three percent (134,590 bits per orbit compared to 236,422 bits per orbit). However, it should be recognized that this approach does have a major disadvantage. Since all of the data is not recorded each orbit, it is always possible that an important event may go undetected.

If the bits collected per orbit must be reduced, a decision will be made on which of these approaches to use when the telemetry subsystem design is formulated in Section 10.

9.4 METHODS OF MAKING MEASUREMENTS

The depth of this study does not allow a detailed consideration of how each of the required measurements would be made. However, a general consideration of some of the accepted methods of making such measurements on space vehicles is included here. The types of measurements to be made generally fall into four groups: (1) temperature sensors, (2) current sensors, (3) voltage monitors, and (4) event monitors. Each of these is discussed below.

9.4.1 TEMPERATURE SENSORS

Temperature measurements can be made with thermistors, resistance thermometers or thermocouples. The selection of the type of sensing device depends primarily upon the temperature to be measured and the voltage level to be supplied to the telemetry equipment. Internal spacecraft temperatures are generally measured with thermistors because the temperature range is relatively small and the large temperature coefficient of resistance of thermistor materials permits generation of a high-level output signal. Resistance thermometers will not provide an adequately large temperature coefficient of resistivity to provide directly the normally desired 0 to 5 volts d-c signal when used between 0^{o} and 110^{o}F.

Whereas, platinum will only provide a ratio of R (max)/R (min) of 1.3, a typical thermistor will offer a ratio of 25. Therefore, a resistance thermometer would be used in a similar voltage divider circuit to measure temperatures on outer surfaces of the satellite, where the temperature excursions may be large. Both thermistors and resistance thermometers can be obtained in very small sizes and can be operated at low power levels (e.g. 40 milliwatts or less). Thermistors are available commercially that will handle temperatures as high as 575°F and resistance thermometers that will operate as high as 980°F.

One very promising device for measuring solar cell temperatures is the silicon resistance thermometer. This resistance thermometer is a thin silicon wafer several thousandths of an inch thick, a tenth of an inch long, and approximately a tenth of an inch wide. Its resistance will change approximately 0.4 percent per degree F change in temperature above ambient. The resistance of such small wafers can be made conveniently as high as 5000 ohms at room temperature. This feature is the main reason for choosing silicon resistance thermometers over other kinds of temperature measuring devices, such as platinum resistance thermometers which usually cannot provide more than 1000 ohms in a single thin unit. Platinum thermometers will change approximately 0.2 percent degree F change in temperature above ambient. Similar figures at other temperatures are given below for the comparison of platinum and silicon resistance thermometers.

TEMPERATURE CHANGE	RESISTANCE CHANGE PER DEGREE F	
	PLATINUM	SILICON
75°F to -100°F	0.21%	0.31%
75°F to 0°F	0.20%	0.34%
75°F to +200°F	0.20%	0.47%

The combination of a larger temperature coefficient of resistivity and a larger nominal resistance value enables a silicon resistance thermometer to develop a greater portion of the desired 0 to 5 volts dc output signal than can a platinum resistance thermometer with the same or less power consumption. Thus, the silicon resistance thermometer permits a temperature measurement to be made with considerably less power and a simultaneous increase in accuracy.

Thermocouples, because of their very low voltage output (millivolts), are generally not used when the temperature measurement can be made with a thermistor or a resistance thermometer. However, extremely wide temperature ranges or very high temperatures necessitate the use of thermocouples. For example, the temperatures associated with the thermionic generator, which range over thousands of degrees and reach levels as high as 3865°K, will have to be measured with thermocouples.

Common thermocouple materials and their recommended range of operation in vacuum are given below:

Thermocouple	Maximum Operating Temperature (°F)	Output at Maximum Operating Temperature (mv)
Copper-Constantan	750	20
Chromel-Alumel	2500	55.5
W-5Re/W-25Re	5000	40.6

9.4.2 CURRENT SENSORS

Electrical currents to and from the primary sources of power would be measured in order to aid in estimating the degree of charge of batteries and the condition of the solar cell array. The sensing and signal conversion techniques by which this is best done will depend upon the characteristics of the solar array, batteries, and current control equipment. One method which may be used is a magnetic amplifier type circuit in which the current to be measured is passed through a winding about the magnetic core, where it modifies the inductance of the core. Thus, by measuring the core inductance, the desired current is known.

9.4.3 VOLTAGE MONITORS

A complete knowledge of how well a spacecraft is functioning requires that numerous voltages be monitored. This is most simply done by using a voltage divider circuit which reduces the voltage being monitored to a voltage suitable to the telemetry system.

9.4.4 EVENT MONITORS

Devices would be installed on the satellite to report the accomplishment of certain important events. For example, the extension and locking of extendable booms, deployment of solar paddles, spacecraft separation from the booster, etc. The closing or opening of electrical contacts is often used as the means of confirming the accomplishment of such events.

9.5 SUMMARY AND CONCLUSIONS

This study establishes the instrumentation requirements to the degree necessary to define the information to be derived from the spacecraft and the data storage and telemetry requirements. It will be necessary to consider the exact means of making the various measurements in detail when a preliminary design of the spacecraft is developed.

Table 9-2 summarized the type and number of measurements to be made and the corresponding bits per orbit that the telemetry subsystem must handle. This information is used in Section 10 to aid in selecting the secondary experiments to be included with each of the three missions, and to establish the data storage requirements.

SECTION 10

TELEMETRY, TRACKING AND COMMAND SUBSYSTEM

PRINCIPAL CONTRIBUTOR:

D. L. HAGEN

SECTION 10

TELEMETRY, TRACKING AND COMMAND SUBSYSTEM

10.1 INTRODUCTION

The Telemetry, Tracking, and Command (TT&C) Subsystem provides the means for tracking the satellite, commanding its operation, and obtaining both experimental and housekeeping data from it. This section of the report establishes the general requirements of the TT&C subsystem and presents the trade-offs involved in the subsystem design.

The TT&C subsystem design must be based on several factors of major importance. Among the most critical of these are:

a. One-year operational lifetime
b. Nearly isotropic antenna pattern
c. Primary power limitations
d. Equipment weight limitations
e. Compatibility with established ground facilities.

First, a brief investigation of ground station coverage and orbital characteristics is presented. Pertinent capabilities and limitations of appropriate STADAN* ground facilities are described. A theoretical comparison of appropriate telemetry modulation techniques is made, and a promising technique is recommended. This analysis is sufficiently broad to remain applicable even with significant deviations from the original mission concepts. Brief analyses of the tracking and command links are then presented.

From these analyses a reasonable modus operandi for the TT&C subsystem is established, and estimates are made of typical satellite equipment for each of the three missions selected in Section 6 (see Table 6-6).

*NASA-Satellite Tracking and Data Acquisition Network. Additional material on this is included in Appendix Sections M and N.

10.2 SELECTION OF TRACKING AND DATA ACQUISITION NETWORKS

10.2.1 TYPES OF ORBITS TO BE SERVED

Five general types of orbits were initially considered for the solar thermionic flight experiment (see Section 3.1). During the mission analysis phase of this study, the desirable orbits were reduced to the three given below and the subsequent spacecraft design effort was directed toward these three orbits:

I - Modified sun-synchronous circular orbit at 1000 nautical miles altitude and an inclination of 101.84 degrees

II - Highly elliptical orbit, with 45-degree inclination, perigee of 200 nautical miles, and apogee of 25,000 nautical miles

III - Low-altitude circular orbit at 325 nautical miles altitude with 30-degree inclination.

10.2.2 APPROACH TO SELECTION OF NETWORKS

The capabilities and limitations of each NASA network which might serve such a scientific experiment were investigated. Air Force networks and the NASA Manned Space Flight Network (MSFN) were not considered, since they would probably not be available for this program.

This left only the following two major networks for consideration:

a. Satellite Tracking and Data Acquisition Network (STADAN)
This is the relatively new title for the combination of the Minitrack Stations, the Wideband Data Acquisition Net, and the Goddard Range and Range Rate (R&RR) System. There are now 15 ground stations in this network.

b. Deep-Space Instrumentation Facility (DSIF)

The DSIF comprises three large ground stations with two more under construction. At present, it is used exclusively for lunar and deep-space probes, and has not been required in previous earth-satellite programs.

10.2.3 RECOMMENDED NETWORKS

The STADAN system appears to be the most suitable for the three orbits considered here.*

Minitrack tracking (fixed-beam interferometer) should be satisfactory for Orbits I and III. The elliptical orbit (II) would probably require supplementary range and range-rate tracking in order to establish early, accurate measurements of the orbital parameters. Minitrack telemetry and the STADAN command equipment are recommended for all three of the orbits.

10.3 BRIEF DESCRIPTION OF STADAN

10.3.1 COMPOSITION OF STADAN

The NASA-Satellite Tracking and Data Acquisition Network (STADAN) consists of three major functional systems (Reference 10-1). The first, Minitrack, has been used to track all U.S. satellites containing suitable beacons (and some USSR satellites) since the beginning of the space programs in 1957 and 1958. In addition to its tracking functions, the Minitrack System has the facilities for receiving telemetry data in the 136 to 137-megacycle and 400 to 401-megacycle bands and has a planned capability for limited reception in other assigned space bands.

The second major functional system comprises the Data Acquisition Facilities (DAF). This system is equipped with multifrequency, high-gain antennas, and its capability of handling large quantities of data at high rates exceeds that of the standard Minitrack

*The STADAN system is the most suitable for each of the five types of orbits originally considered except the solar probe orbit. A solar probe orbit would require the DSIF system. Information on the DSIF tracking system is included in Appendix O.

telemetry systems currently in use. The first station in this network (ULASKA) has been constructed and is in operation near Fairbanks, Alaska. The second station (ROSMAN I) near Rosman, North Carolina, has been constructed and is in operation. A third station (GILMOR) near Fairbanks, Alaska, is rapidly approaching an operational status; a fourth (ROSMAN II) - in addition to the Rosman, North Carolina, Site - is under construction; and a fifth station is now under construction near Canberra, Australia. Since such a wideband capability is not required for this mission, the DAF will not be discussed further.

The third major system of the STADAN system is the transportable Range and Range-Rate Tracking System (R&RR) which complements the tracking capabilities of the Minitrack network by providing improved tracking data for space probes, launch vehicles, and satellites in highly elliptical orbits.

Minitrack stations are located at the sites listed in Table 10-1. Approximate locations are shown in Figure 10-1 (Reference 10-2).

The three mobile stations for the R&RR systems are presently located at:

Rosman, North Carolina, USA
Scottsdale, Arizona, USA
Carnarvon, Australia.

The General Electric Company has recently been awarded a contract to build an additional R&RR ground station at Fairbanks, Alaska, with an option to build another station at Santiago, Chile.

10.3.2 ANTENNA ELEVATION LIMITS

The minimum elevation angle at which the ground antennas can be operated limits the ground station coverage for low-altitude earth orbits. These limits are caused by physical obstructions of the line-of-sight, mechanical stops on the antenna drive system, and

Table 10-1. Geodetic Location of Minitrack Stations

Station	East Longitude	Latitude	Elevation (Feet)	Datum
Blossom Point, Md.	282-54-48.170	N-38-25-49.718	15	Vanguard
College, Alaska	212-09-47.383	N-64-52-18.582	527	Vanguard
East Grand Forks, Minnesota	262-59-21.556	N-48-01-20.668	823	Vanguard
Ft. Myers, Fla.	278-08-03.887	N-26-32-53.516	12	Vanguard
Gilmore Creek, Alaska (NO. 1)	212-29-05.794	N-64-58-36.572	966	Vanguard
Gilmore Creek, Alaska (NO. 2)	212-30-18.045	N-64-58-42.667	1,013	Vanguard
Johannesburg, South Africa	027-42-27.931	S-25-52-58.862	4,990	E. 30 Eur
(40-foot dish)	027-42-27.931	S-25-53-08.025	--	E. 30 Eur
Lima, Peru	282-50-58.184	S-11-46-36.492	161	Vanguard
Mojave, Calif.	243-06-02.776	N-35-19-48.525	3,044	Vanguard
(40-foot dish)	243-06-47.808	N-35-19-54.407	--	Vanguard
Quito, Ecuador	281-25-14.770	S-00-37-21.751	11,703	Vanguard
(40-foot dish)	281-25-08.109	S-00-37-23.241	11,690	Vanguard
Rosman, N.C.	277-07-40.532	N-35-12-00.499	2,883	Vanguard
St. Johns, Newfoundland	307-16-43.240	N-47-44-29.049	208	Vanguard
Santiago, Chile	289-19-51.283	S-33-08-58.106	2,280	Vanguard
(40-foot dish)	289-19-51.283	S-33-09-04.934	2,281	Vanguard
Winkfield, England	359-18-14.615	N-51-26-44.122	215	E. 30 Eur
Woomera, Australia	136-52-19.634	S-31-23-30.638	436	Sydney

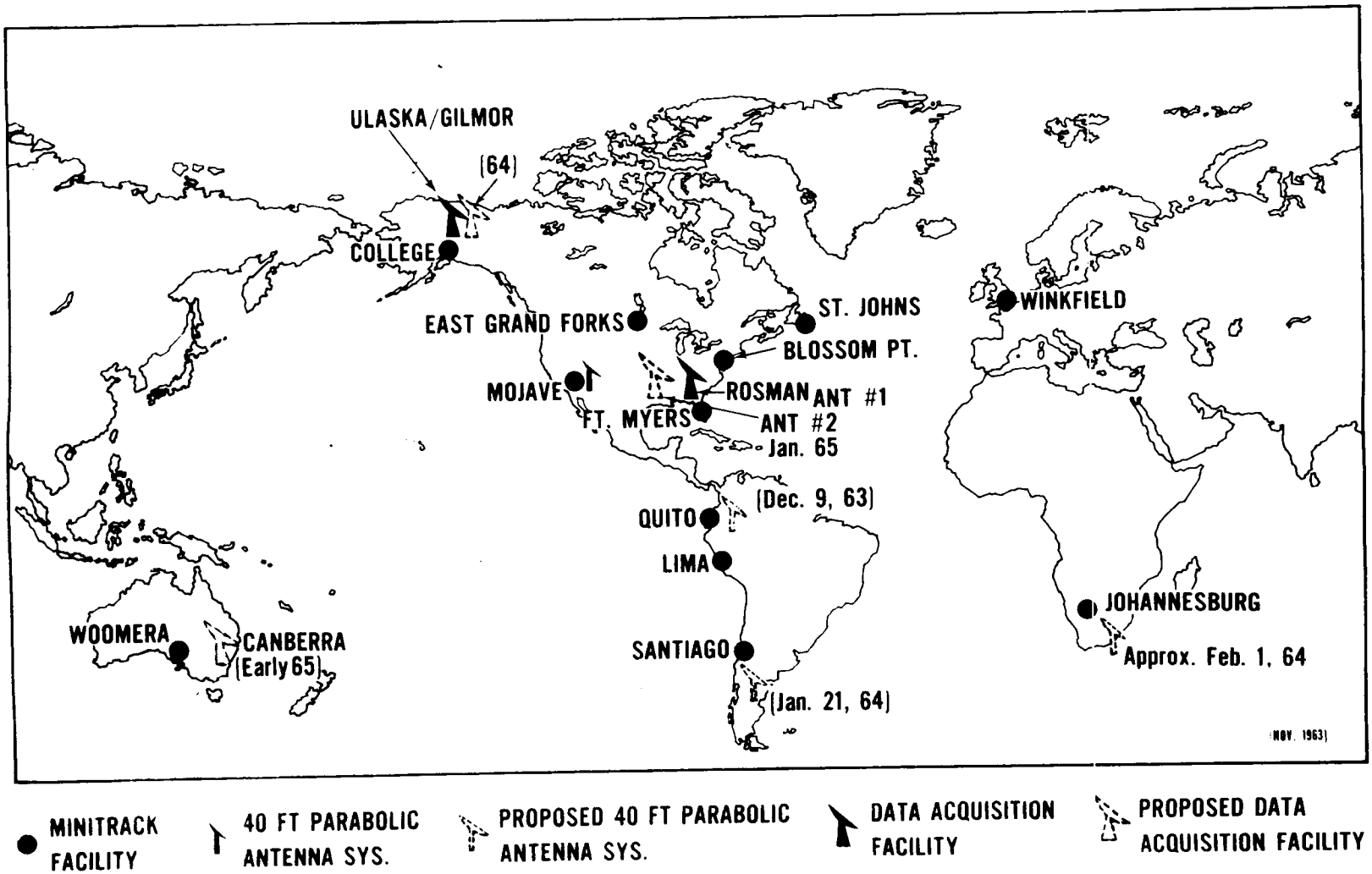

Figure 10-1. Space Tracking and Data Acquisition Network (STADAN)

antenna noise introduced when a significant portion of the receiving antenna beam intercepts the comparatively warm earth.

The antennas used for orbit determination in the STADAN system are rigidly fixed. Their fan-type antenna patterns have three-db beamwidth elevation angles of 52 degrees for the fine resolution systems and 37 degrees for the ambiguity resolving system.

The broad beamwidths of the Minitrack telemetry antennas will limit their lower elevation angles to 10 to 15 degrees. The latter figure should be safe to use for planning purposes.

The Wideband Data Acquisition Facilities have 85-foot dish antennas with much narrower beamwidths. However, the Fairbanks Station, which is of major interest because of its proximity to the North Pole, is located in the Gilmore Creek Valley, twelve miles north of Fairbanks. This valley limits the elevation angle to 13 degrees in the northerly direction. Table 10-2 shows the elevation limits of the Fairbanks antenna as a function of azimuth angle.

The Range & Range Rate tracking stations can be assumed to have a lower elevation limit of 15 degrees for the same reason as the Minitrack stations.

10.3.3 MINITRACK TELEMETRY SYSTEM

Minitrack comprises an organization of fixed ground stations, located throughout the world, which provides a means of precision tracking, command, and telemetry reception for satellites and space probes, together with a communications system to transmit this information to a computing and data processing facility at Greenbelt, Maryland.

A large number of the original stations were located along the 75th meridian to intercept satellite orbits with inclinations of less than 45 degrees. New stations have been located at higher latitudes to cope with more nearly polar orbits. Furthermore, ten of the stations have been supplemented with additional antennas aligned specifically for polar orbit.

Table 10-2. Electrical and Horizon Limits - Gilmore Antenna*

Azimuth Angle (degrees)	Minimum Elevation Angle (degrees)
000° (North)	13.0
010	10.5
020	9.0
030	7.8
040	6.0
050	5.0
060	4.2
070	4.0
080	4.8
090 (East)	4.5
100	6.8
110	7.8
120	9.4
130	10.0
140	10.7
150	11.2
160	11.5
170	10.7
180 (South)	13.0
190	10.0
200	8.5
210	6.8
220	5.2
230	4.0
240	4.0
250	4.0
260	4.0
270 (West)	4.0
280	4.0
290	4.7
300	5.7
310	7.5
320	8.0
330	10.0
340	10.7
350	11.3

*Source: C. Maskaleris, Tracking & Data Systems, GSFC 7/28/64

Telemetry receiving systems at 136 megacycles are available at all STADAN ground stations. In addition to this, 400-megacycle receiving systems are available at those stations having 40-foot dishes and at the DAF stations having 85-foot dishes.* Due to the limited availability of the 400-megacycle facilities, the emphasis in this study is on the use of the 136-megacycle equipment.

The Minitrack Mod I Telemetry Receiver System is tunable over a frequency range of 136 to 137 megacycles. Five IF pre-detection bandwidths are available ranging from ten kilocycles to one megacycle. Demodulation circuits are provided for AM and FM signals.

Preamplifiers having nominal 3.5 db noise figures are available at all stations. Some stations have tracking filters, phase-lock demodulators, and diversity combiners.

All stations have nine-Yagi array antennas, providing a gain of about 19 db. Three stations (Johannesburg, Santiago, and Quito) have sixteen-Yagi array antennas, providing a gain of about 22 db.

Detailed descriptions of the ground station equipment are contained in Reference 10-1 and are summarized in Appendix N of this report.

10.3.4 MINITRACK TRACKING SYSTEM

Historically, the first functional network to be constructed for satellite tracking was the Minitrack Network, which was transferred from the Department of Defense to NASA at the time NASA was established.

*The installation of 40-foot parabolic dishes has been completed at three Minitrack stations in the southern hemisphere (Johannesburg, Santiago, and Quito).

The prime Minitrack satellite tracking system consists of radio interferometers operating in conjunction with a transmitting beacon in the payload itself. Since the establishment of the network, certain enhancements have been added to the original station equipment to provide tracking capability by optical and Doppler means as well. While the original tracking equipment operates on or near 108 megacycles (the frequency assigned for IGY activities), additional equipment tunable over the 136 to 137 megacycle region is now in operation. Although basically the same, it incorporates certain features which further increase its flexibility.

Essentially, the radio interferometer measures two of the three direction cosines of a line from the center of the station to a satellite as a function of time while the satellite passes through the beam pattern of the receiving antennas. The third direction cosine is thus defined and the angular position of the satellite determined.

From a series of independent angle measurements from various ground stations, satellite orbital elements may be computed.

Phase comparison techniques are used to measure the difference in arrival time of the wavefront of a distant point source at pairs of receiving antennas separated by known distances in wavelengths of the transmitted frequency. Measurement of this radio path difference is accomplished by a comparison of the phase angle of the signal received at one antenna to that received at another.

The antennas are aligned along baselines in the east-west and north-south directions. Since the phase measurement system is capable of indicating phase difference to a small fraction of a wavelength, two pairs of antennas are aligned along orthogonal baselines many multiples of a wavelength long to obtain good angular resolution. These are termed "fine" antennas. As a radio source passes through the antenna pattern, the relative phase will cycle from 0 to 360 degrees for each wavelength added to the radio path difference. Since the phase meters repeat their readings every 360 electrical degrees, a number of different space angles will produce identical phase readings during a satellite transit. This ambiguity is

resolved by employing shorter baselines which produce fewer integral numbers of wavelength change as the radio source passes through the antenna beam. These are termed "medium" and "coarse" antennas. Ambiguity antenna information determines the number of full wavelengths to be added to the relative phase angle measured at the fine antennas to define a data point.

The Minitrack antennas are of the slot type with ground screens, pedestal-mounted and parallel to the ground plane. All are very precisely positioned geographically and accurately leveled. The polarization is linear and perpendicular to the long dimension of the antenna. The radiation pattern is fan-shaped, the plane of the fan being perpendicular to the long dimension. The original 108-megacycle fine antenna array is oriented to produce a fan beam 101 degrees in the north-south direction and 11 degrees east to west at the 6 db points. The ambiguity antennas contain fewer elements with a consequent broader beam pattern and reduced gain. This configuration was selected for detection of satellites in near-equatorial orbits. The 136-megacycle fine antennas are located adjacent to those of the 108-megacycle system. The 136-megacycle ambiguity antennas are offset in a hitherto unused portion of the antenna field. This parallax can be corrected by calibration methods. Stations equipped for both equatorial and polar tracking on 136 megacycles employ two additional sets of fine antennas to produce a fan beam with the wide dimension of the fan lying in the east to west direction. The desired polarization of the antenna system is selected by means of coaxial switches.

10.3.5 RANGE AND RANGE-RATE TRACKING SYSTEM

The Goddard Range and Range Rate System was developed by Motorola for the NASA Goddard Space Flight Center (Reference 10-3). The contract was awarded in January, 1962 (Reference 10-4). The three mobile ground stations now in operation are tracking the IMP satellite (VHF) and will be used to track the EGO and POGO satellites (S-Band) (Reference 10-5).

The primary function of the R&RR system is the rapid orbital (or trajectory) determination of spaceborne vehicles. The principle is based on precise measurements of range, range rate, and angle. The system is especially useful for highly elliptical orbits where "angle only" systems suffer from the disadvantages that, for a given angular error, the position error increases with distance (Reference 10-3).

Range is determined by employing ranging sidetones in which the phase delay is directly proportional to the two-way range between the ground station and the satellite. Range rate is determined by measuring received Doppler cycles per unit time, representing the average velocity over the measuring interval. Angle measurements are obtained from shaft encoders mounted on the ground antenna. The system is capable of measurements with an instrumentation* precision of $\pm$ 15 meters in range and $\pm$0.1 degrees in pointing angle**.

The system features short acquisition times, so that the signal from a satellite making a low-altitude perigee pass can be acquired in less than ten seconds (Reference 10-6).

Two basic operating modes are possible for the ground equipments: S-Band or VHF. The S-Band mode offers faster accuracy, since up to three ground stations can be operated simultaneously with the same transponder. Also, the higher carrier frequency allows a more accurate Doppler measurement. The VHF capability is designed to be utilized by small satellites which are unable to tolerate the size and weight of the S-Band transponder. Only single-station operation is available at VHF. If desired, the VHF ground receiving equipment can be used as an acquisition aid when operating with the S-Band system.

Although the present system includes only the tracking function, it can be expanded to present an integrated approach to the solution of the tracking, command, and telemetry requirements of space vehicles.

---

* The uncertainty in the propagation velocity of electromagnetic waves is about $1{:}10^6$ and must be added to this instrumentation error to yield the total error.

** At ranges out to 100,000 kilometers using the S-Band system. The VHF is almost as accurate, but requires a longer period of time to achieve the accuracy noted.

All the R&RR ground station equipment is mounted in vans which can be airlifted (Reference 10-7). The ground stations consist of: a transmitter van, with both VHF and S-Band one or ten-kilowatt transmitters; a receiver van, containing VHF and S-Band receivers, ranging and timing equipment, antenna control equipment, and special test equipment; an S-Band antenna with separate 14-foot receive and transmit dishes (33 to 35 db gain); and a 28 by 28-foot VHF array consisting of 72 cavity-backed slots (19 to 20 db gain). A typical R&RR ground station is depicted in Figure 10-2 (Reference 10-8).

10.3.6 STADAN COMMAND SYSTEM

The early NASA satellites employed elementary tone-actuated command systems. The Vanguard satellite required a single tone modulation of the command carrier; later satellite command systems utilized as many as seven tones. However, all of the satellites using these simple tone systems have been commanded repeatedly by interfering transmissions originating in all parts of the world. The immunity of these simple tone command systems to false command by extraneous signals is very poor.

Furthermore, the simple tone system required unique tones in order to prevent accidental command by a transmission intended for another satellite. Due to the limited RF spectrum available for command transmissions, it is not possible to assign unique tones to each satellite and thereby provide protection against accidental command. Because of the susceptibility of interfering signals and accidental command, simple tone-command systems are no longer recommended for satellites (Reference 10-9).

In order to provide high rejection of unwanted signals, a larger number of commands, a greater number of unique addresses for different satellites, and reliable reception of the correct command, a tone-digital command system for on-off commands was developed by Goddard Space Flight Center (GSFC).

Basically this system utilizes a four-state signal (sync, 1, 0, blank), pulse-duration modulated (PDM) with constant bit-ratio coding and repetitive word formating. A series of five

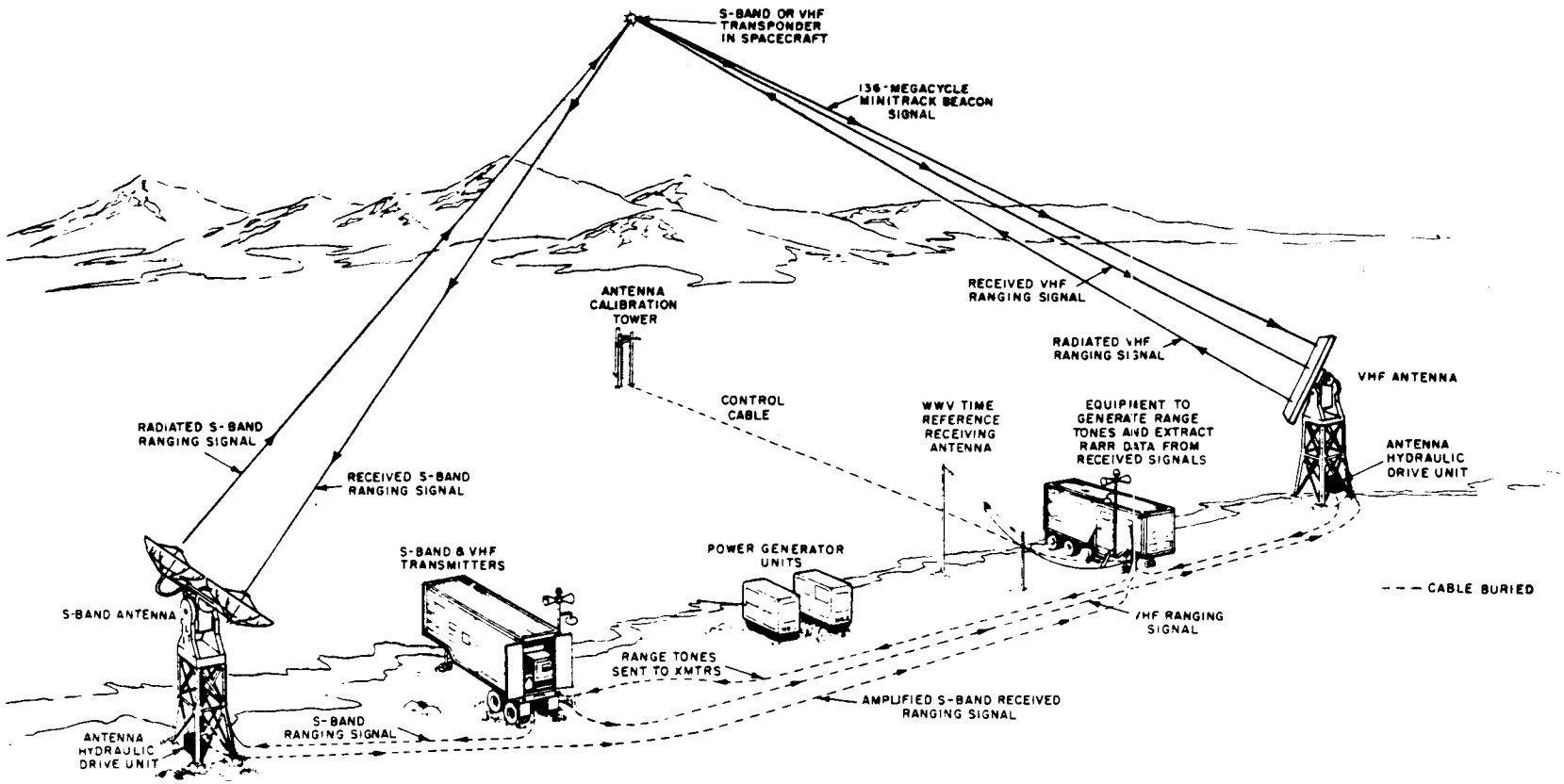

Figure 10-2. Typical Range and Range-Rate Ground Station System

words (each consisting of eight bits), together with one synchronization signal and one blank period, is sent for each command. The series generally consists of a unique address word sent twice followed by an execute word sent three times. The receipt of one correct address word and one valid execute word in the same series of five words is sufficient to effect a command. This redundancy increases the probability of receiving the correct command when the signal is weak or when interference is present.

The technique used for error detection and rejection of interfering signals consists of making the code words from a known number of zeros and ones. The address command word consists of a combination of two ones and six zeros, or of six ones and two zeros. The execute command word always contains a combination of four ones and four zeros. This fixed four-out-of-eight bit coding provides a means of detecting all odd bit errors and 43 percent of all two-bit errors. To further decrease the possibility of spurious commanding, no address or execute word may be decoded unless a sync pulse has been detected, and once the address has been detected, a valid execute word must be read within the time duration of the five-word series or it will not be detected.

In a typical tone-digital command message, the coded PDM command amplitude-modulates an audio subcarrier (tone). The coding system described above provides 56 unique address command words, thus permitting 56 satellites to use the same tone:

$$2C_2^8 = 2 \quad \frac{8!}{2!\ 6!} = 56 . \qquad (1)$$

Thirty tones are available for use in this system, lying in the band from 1,025 to 11,024 cycles per second. The total number of satellites which can be handled with this system is thus 56 X 30 = 1680.

The 4 X 4 execute command word format provides 70 different commands:

$$C_4^8 = \frac{8!}{4!\ (8-4)!} = 70 . \qquad (2)$$

Since most satellites do not require so many commands, a provision has been made in the ground station design to use six-bit words instead of the eight-bit words described above. With the six-bit words, the address command word has two ones and four zeros or four ones and two zeros, permitting

$$2C_2^6 = 2 \frac{6!}{2!\ (6-2)!} = 30 \qquad (3)$$

satellites to use the same tone. The six-bit execute command has three ones and three zeros. This format provides 20 commands:

$$C_3^6 = \frac{6!}{3!\ (6-3)!} = 20 \ . \qquad (4)$$

The Goddard tone-digital command system provides unique command messages for a very large number of satellites. Tests on this system have demonstrated that it has much greater immunity against interfering signals than the simple tone systems do. NASA recommends that all satellites requiring simple on-off commands use the Goddard tone-digital command system. The command consoles at the STADAN sites are designed to generate the tone-digital command message.

More details on this and other aspects of the STADAN Command System are contained in References 10-1, 10-10, and 10-11, and are summarized in Appendix M of this report.

10.4 GROUND STATION SELECTION

10.4.1 GENERAL APPROACH

Communications considerations with respect to orbit selection were discussed briefly in Section 3.4. As mentioned there, it would be desirable from a data handling standpoint to minimize the number of ground stations required for receiving the data. On the other hand, spacecraft weight restrictions will limit the amount of on-board storage capacity to only one

or two orbits of data, depending upon the orbital period*. Accordingly, it is desirable to select those few ground stations which have the highest probability of seeing the satellite on a typical pass at an elevation angle at least 15 degrees above the horizontal.

Table 10-3 lists the values of the pertinent orbital parameters for the three orbits under consideration.

Table 10-3. Values of Pertinent Orbital Parameters

Type of Orbit	Apogee (NM)	Perigee (NM)	Inclination (Degrees)	Period
I. Circular	1,000	1,000	101.84	124 min
II. Elliptical	25,000	200	45	14 hrs
III. Circular	325	325	30	97 min

Figures 10-3, 10-4 and 10-5 show the ground traces for the two circular orbits during the first 24 hours after injection**. Superimposed on these traces are the coverage circles for appropriate ground stations, within which the line-of-sight to the satellite is at least 15 degrees above the horizon.

Figure 10-6 shows the ground trace during the first 40 hours for the highly elliptical orbit**. Slant ranges at the 15 degree elevation angle limits and total line-of-sight times are indicated. (Coverage circles would have no significance for the highly elliptical orbit, since the altitude is continuously changing.) These figures have been used as an aid in selecting suitable ground stations for use with the three orbits. Tentative recommendations are summarized in the following three sections.

* Storage equipment is becoming lighter with time. The increasing use of such techniques as thin-film circuits may lessen the severity of the data storage problem over the next few years.

** These data were obtained by digital computer simulation.

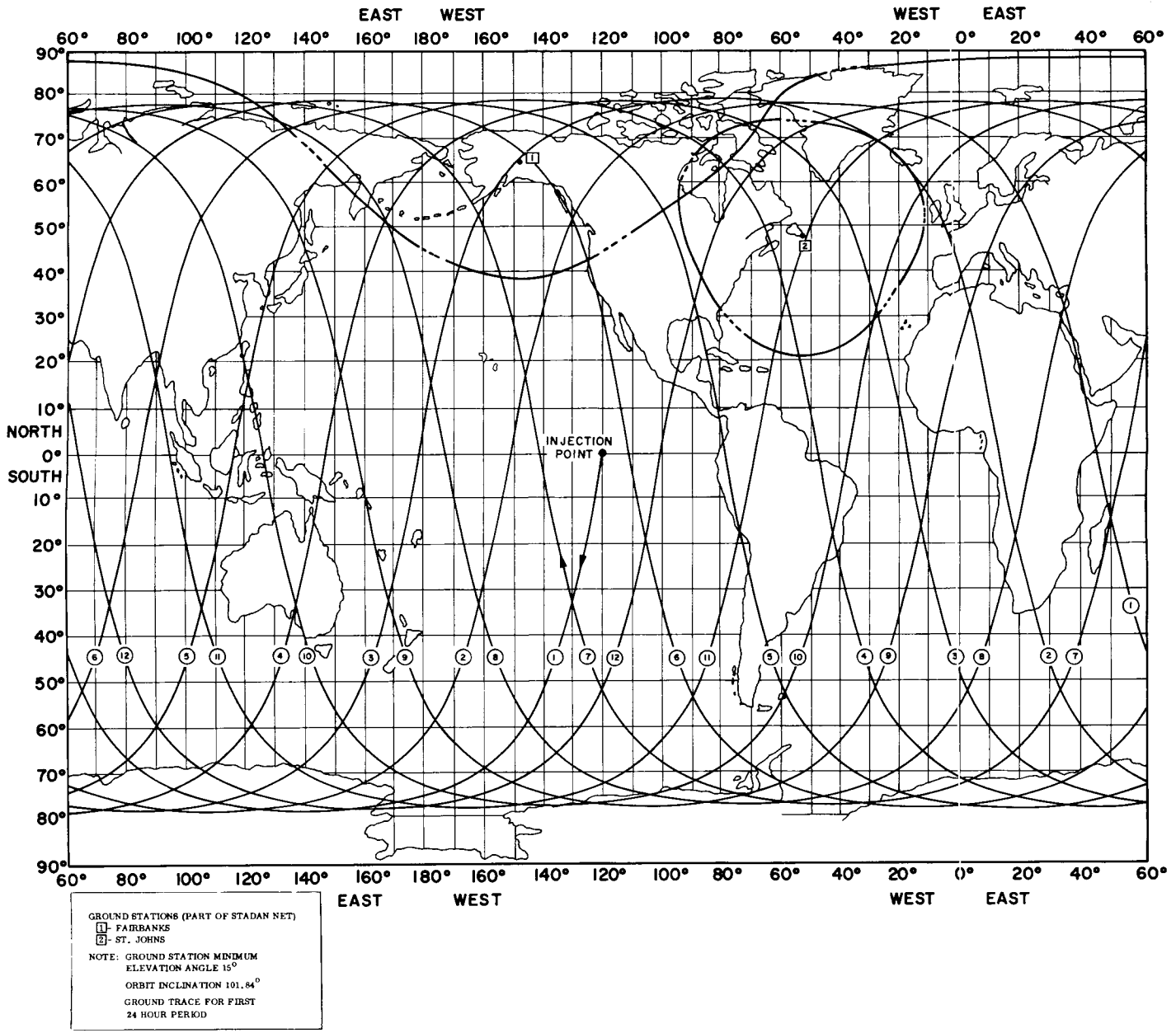

Figure 10-3. Ground Station Coverage for 1000-Nautical Mile, Modified, Sun-Synchronous Daylight Orbit

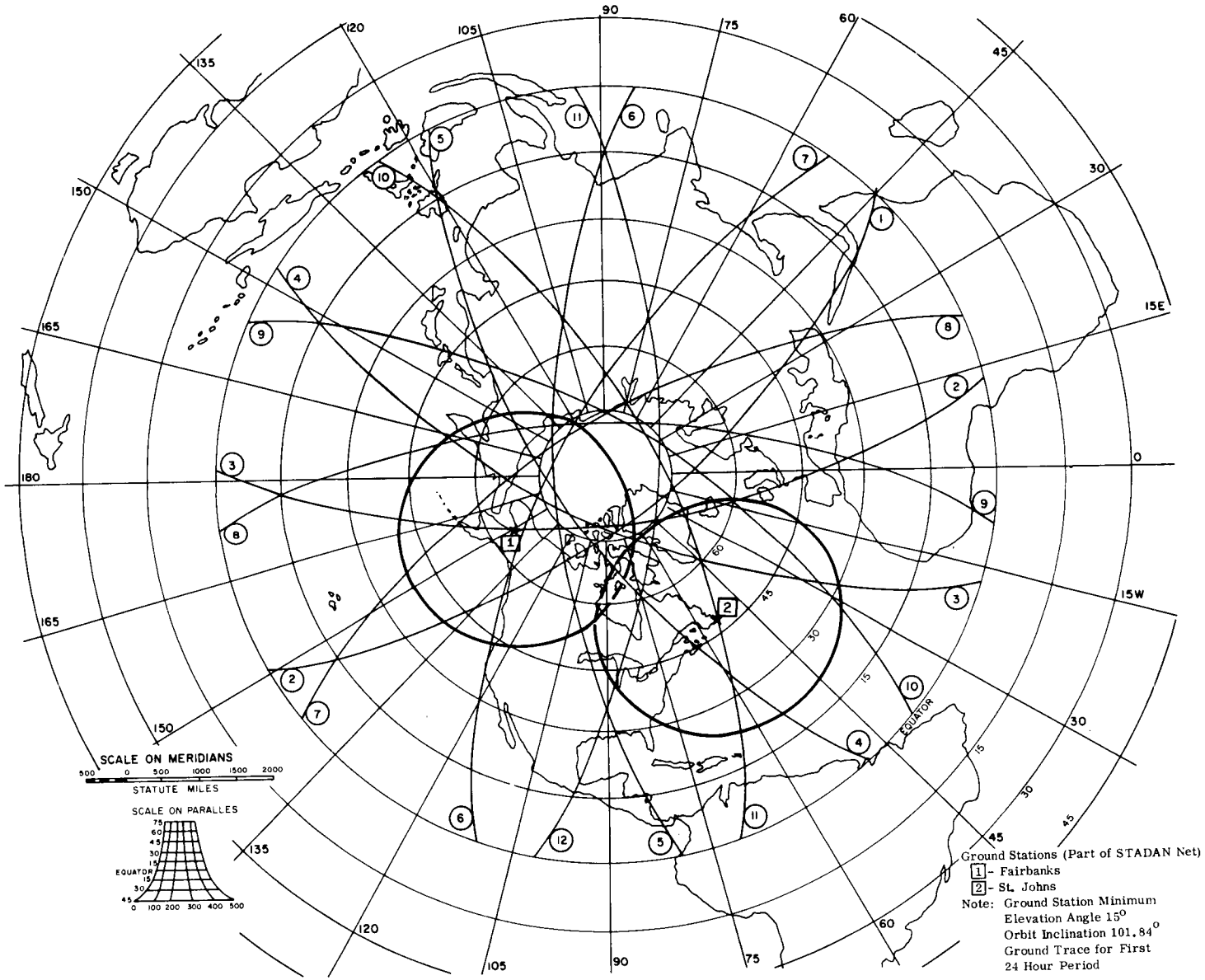

Figure 10-4. Ground Station Coverage for 1000-Nautical Mile, Modified, Sun-Synchronous Daylight Orbit (Polar Projection)

10.4.2 1000-NAUTICAL MILE CIRCULAR ORBIT

As shown in Figures 10-3 and 10-4, and discussed in Section 3.4 (Figure 3-23), a satellite in a 1000-nautical mile modified sun-synchronous orbit has ten minutes or more line-of-sight time at the Fairbanks ground station on more than half the orbits. Thus, Fairbanks appears quite attractive. However, the outages will occur in gaps. The satellite will be visible for three or four orbits in sequence and then will not be visible for the next three or four orbits. It therefore appears desirable to employ a second ground station displaced about 90 degrees in longitude from Fairbanks, in order to reduce the on-board storage requirement. St. Johns, Newfoundland, appears suitable for this purpose; if it is utilized only one or two orbits of storage capacity will be required.

10.4.3 HIGHLY ELLIPTICAL ORBIT

As shown in Figure 10-5, the perigee for this orbit lies in the Northern Hemisphere and will occur over the Continental United States about once every three orbits.

The decision must be made whether to read out the stored data at a fast rate near perigee, or at a much slower rate when closer to apogee. In Section 10.6 it will be shown that it is more efficient from a transmitter power standpoint to transmit rapidly at perigee. This also has the advantage of committing the ground station for a shorter period of time. However, the risk of losing one or two complete orbits of data must be further assessed.

For perigee read-out, Mojave, California, St. Johns, Newfoundland, and Winkfield, England, appear to be the three most promising ground stations.

For read-out near apogee, Woomera, Australia, and Johannesburg, South Africa, appear suitable.

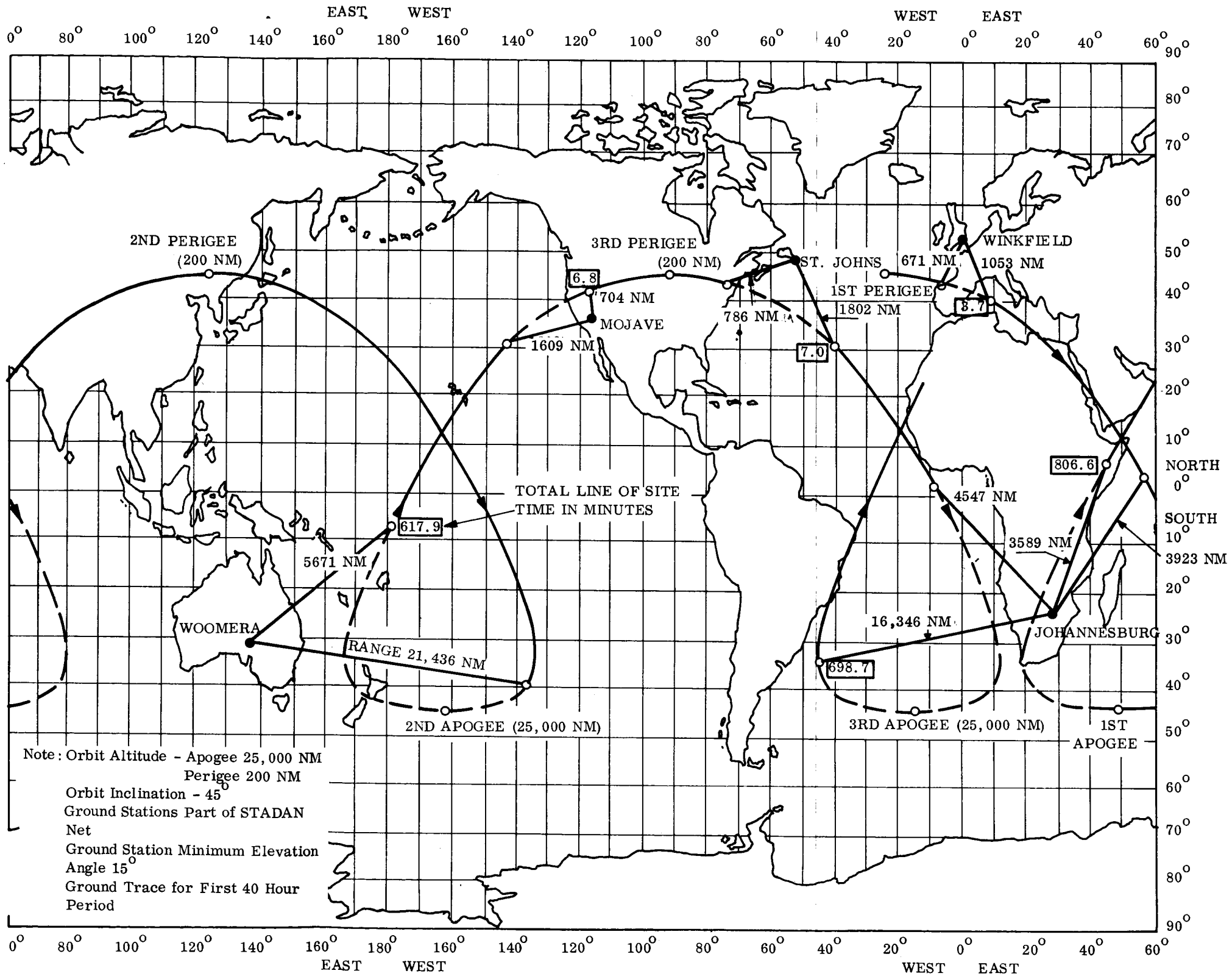

Figure 10-5. Ground Station Coverage For A Highly Elliptical Orbit

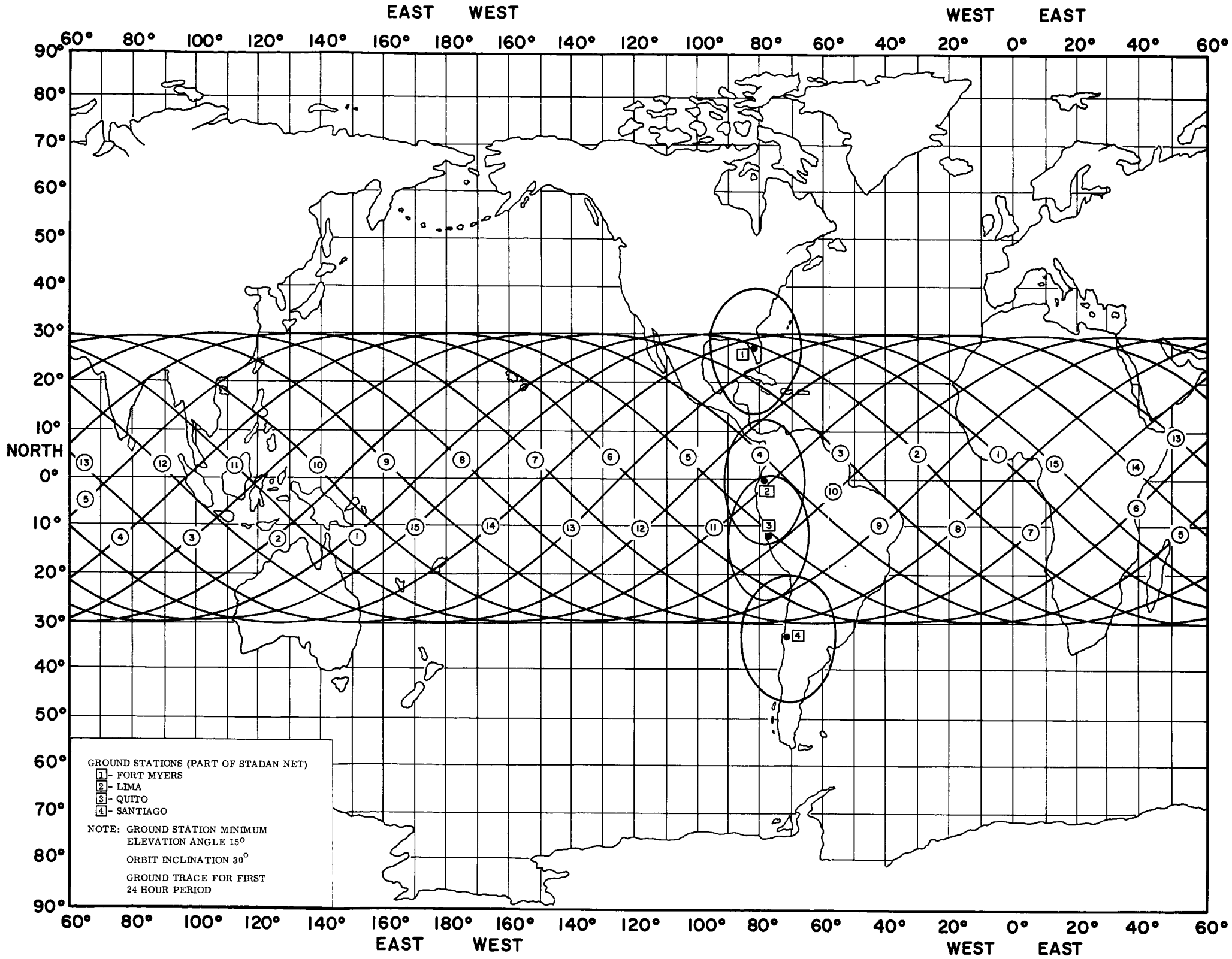

Figure 10-6. Ground Station Coverage For A 325-Nautical Mile Circular Orbit

10.4.4 325-NAUTICAL MILE CIRCULAR ORBIT

This low-altitude, low-inclination orbit suits the Minitrack Network very well, in that every orbit passes through the coverage circles along the 75th meridian (see Figure 10-6). However, it would be desirable to limit the number of stations employed. It appears that using the following four stations will permit data read-out on nearly every orbit:

Fort Myers, Florida
Santiago, Chile
Lima, Peru
Quito, Ecuador.

Due to the low orbital altitude, the maximum time in view of one of these ground stations is about seven minutes. Therefore, a reasonably safe solution would be to plan on two or three minutes of available read-out time and provide capacity for storing two full orbits of data.

10.5 DETERMINATION OF SLANT RANGE AND DOPPLER CHARACTERISTICS

10.5.1 CIRCULAR ORBITS

10.5.1.1 Background

The purpose of this section is to present a unified approach to the determination of maximum slant range, Doppler frequency, and time rate-of-change of Doppler frequency as applied to communication with satellites in circular earth orbits. Graphical results are presented for all altitudes up to synchronous. Section 10.5.2 extends this analysis to the case of elliptical orbits.

In a communication link having a relative velocity along the line joining the transmitter and the receiver, the frequency of the signal arriving at the receiver is shifted from what it

would have been if there were no motion. This is known as the Doppler effect (first explained by C. Doppler in 1842 for the optical case). If the transmitter is in motion toward the receiver, the received frequency is higher than when the transmitter is stationary; but, if the transmitter is receding, the signal arriving at the receiver is of lower frequency than when the transmitter is at rest. Similar changes occur if the receiver is in motion.

Neglecting relativistic clock effects*, the Doppler effect due to a velocity, v, along the transmission path is a frequency shift of the carrier, f_c, to f_c' given by:

$$\begin{aligned} f_c' &= f_c (1 \pm v/c) \\ &= f_c \pm f_d \end{aligned} \tag{5}$$

where c is the velocity of light and f_d is the Doppler frequency, given by:

$$f_d = (v/c) f_c \tag{6}$$

The rate of Doppler change can be obtained by differentiating Equation 6 to yield:

$$\dot{f}_d = (\dot{v}/c) f_c \ . \tag{7}$$

The communications receiver must be designed to accommodate the maximum Doppler shift (both plus and minus). This can be done either by increasing the receiver bandwidth sufficiently or by employing a tracking filter or phase-lock loop to follow the changing frequency. The latter technique improves the signal-to-noise ratio, since it permits the use of a narrower equivalent noise bandwidth; dependent only on the rate of change of Doppler $\dot{f}_d$ and not on f_d itself. However, in this technique the total frequency range over which the receiver must be able to sweep during acquisition is determined by the amount of the Doppler frequency shift (plus a small amount for oscillator instability and safety margin).

* Negligible at velocities appreciably less than that of light.

Equations 6 and 7 indicate that the first step will be to find v and $\dot{v}$ along the transmission path. From these values the Doppler and Doppler rate may then be calculated.

The satellite will be taken to be in a circular orbit at altitude h. Rotation of the earth will be neglected.* The geometry is shown in Figure 10-7.

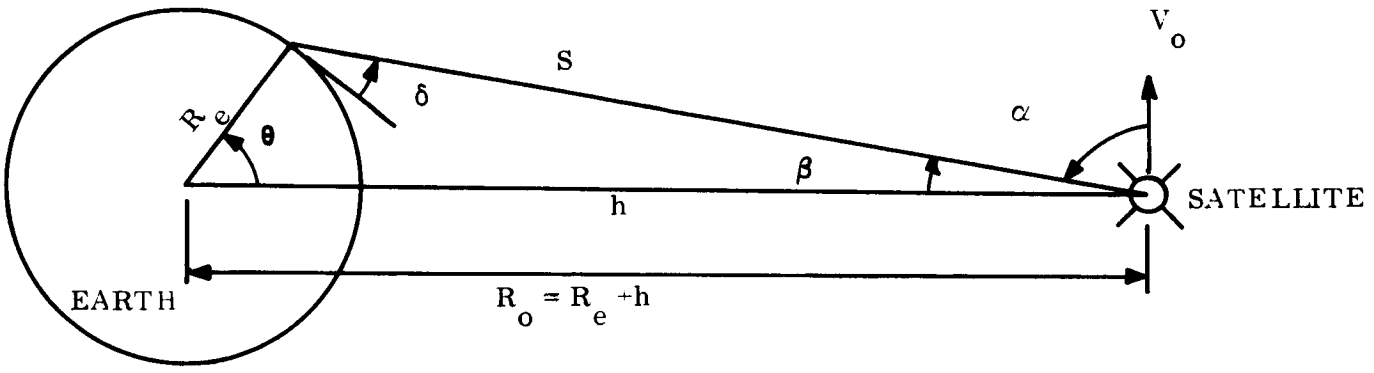

Figure 10-7. Orbital Geometry and Notation

10.5.1.2 Slant Range

The following relationships are obtained from Figure 10-7:

$$\theta = \cos^{-1}\left(\frac{R_e}{R_e+h}\cos\delta\right) - \delta \qquad (8)$$

$$\alpha = \theta + \delta \qquad (9)$$

$$\beta = 90^o - (\theta + \delta) \qquad (10)$$

*The effect of earth rotation is negligible for altitudes significantly below synchronous and for orbits with large inclinations.

$$s = R_e \frac{\sin\theta}{\sin\beta} = R_e \frac{\sin\theta}{\cos(\theta+\delta)} \quad . \tag{11}$$

Equations 8, 10, and 11 have been plotted versus orbital altitude, h, and minimum elevation angle, δ, in Figures 10-8, 10-9, and 10-10, respectively.

10.5.1.3 Orbital Period

Kepler's third law of planetary motion states that the square of the period of revolution of a planet is proportional to the cube of the major axis of its orbit.

The period (neglecting the earth's oblateness) is thus given by (Reference 10-12):

$$P = \frac{2\pi R_o^{3/2}}{\sqrt{\gamma M}} = 2\pi R_o^{3/2}/\mu^{1/2} \tag{12}$$

where

R_o = orbital radius = R_e + h

γ = universal gravitational constant

M = mass of the earth

$\mu = \gamma M$.

Substitution of appropriate values into Equation 12 yields:

$$P = 6.987 \times 10^{-6} (h + 3440)^{3/2} \text{ sidereal hours*} \tag{13}$$

where h is in nautical miles, for circular orbits. This has been plotted in Figure 10-11.

*One sidereal hour = 0.99727 mean solar hours.

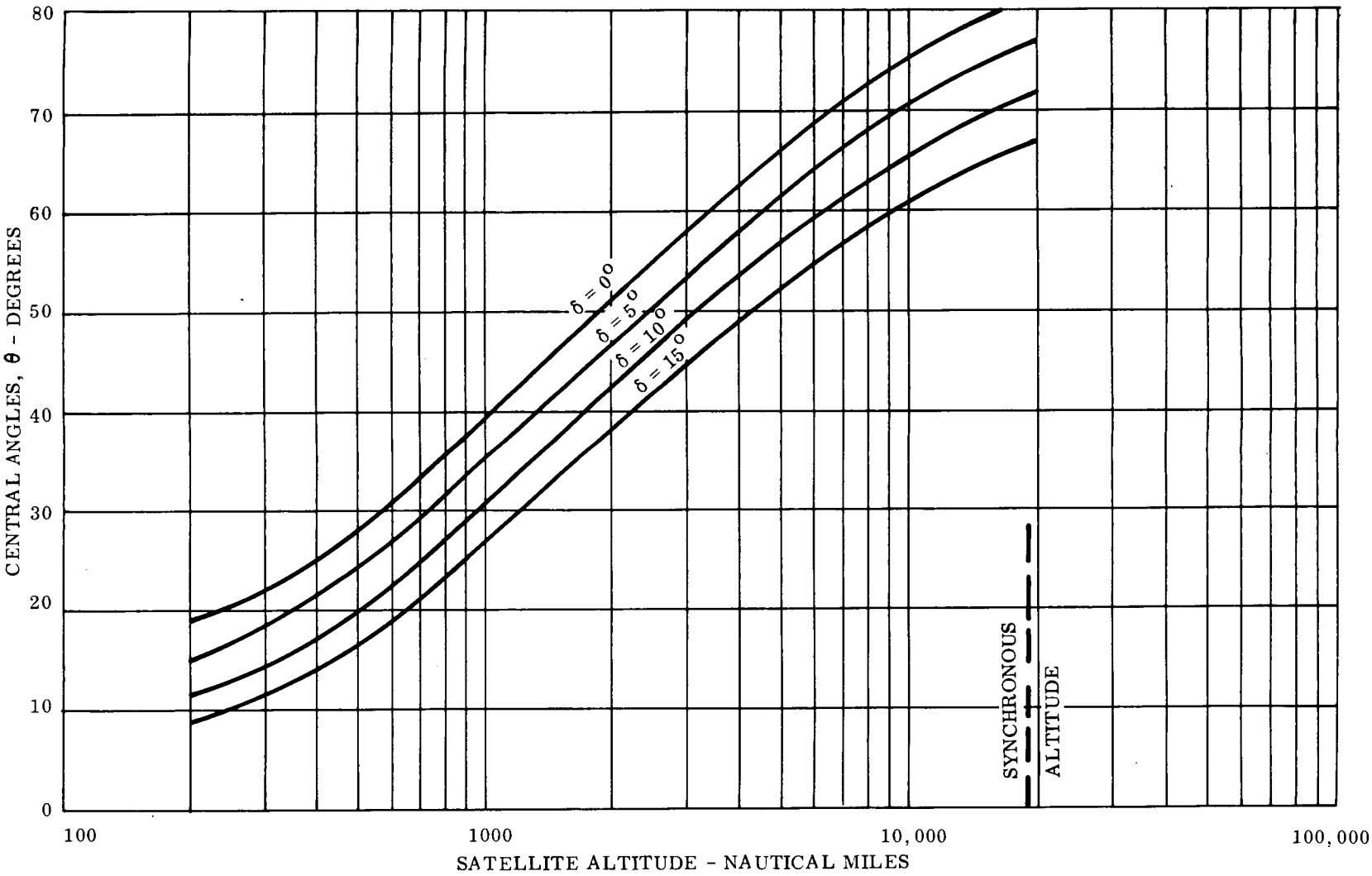

Figure 10-8. Central Angle θ vs. Orbital Altitude at Elevation Angle δ

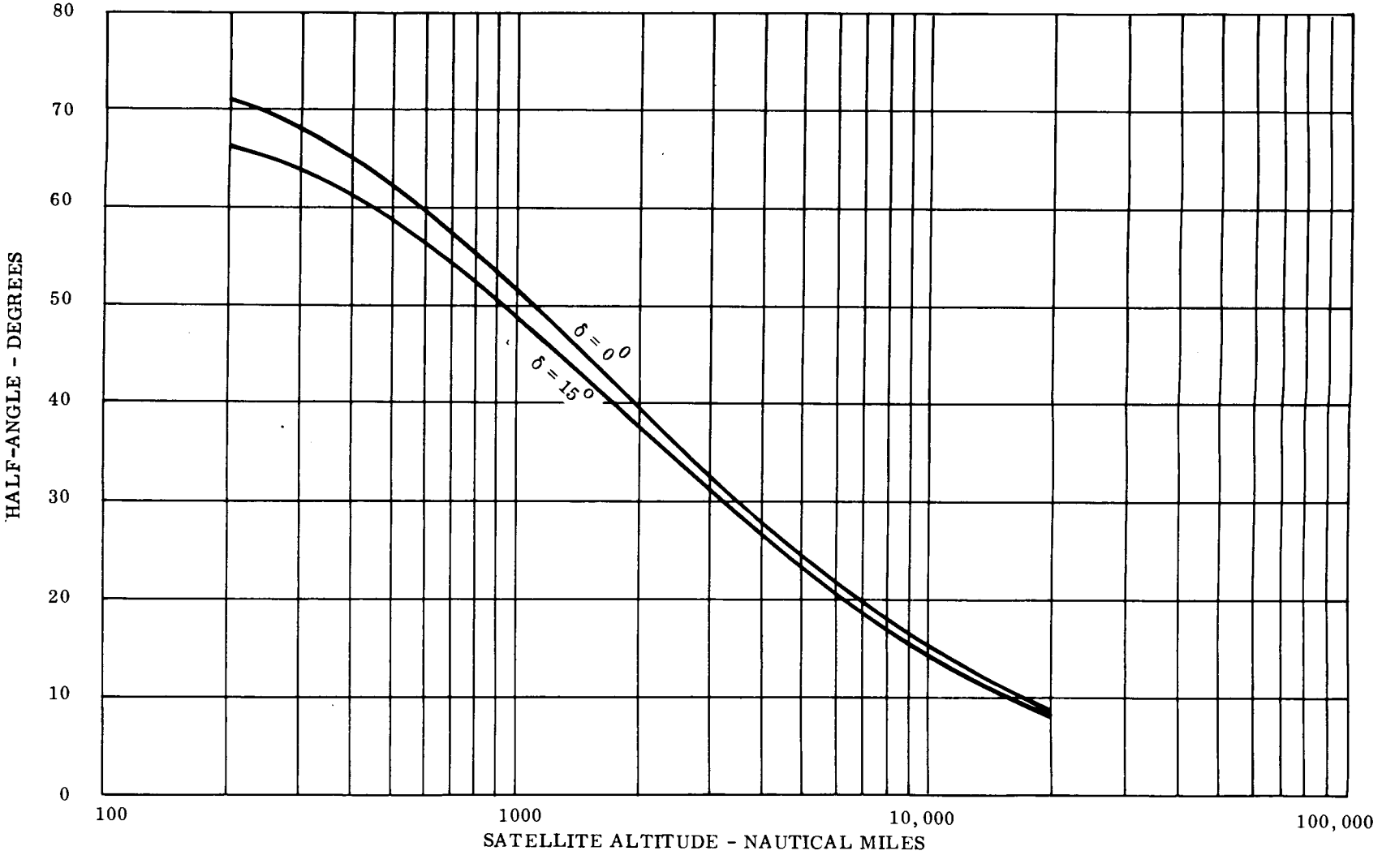

Figure 10-9. Half Angle β Subtended at Satellite vs. Orbital Altitude at Elevation Angle δ

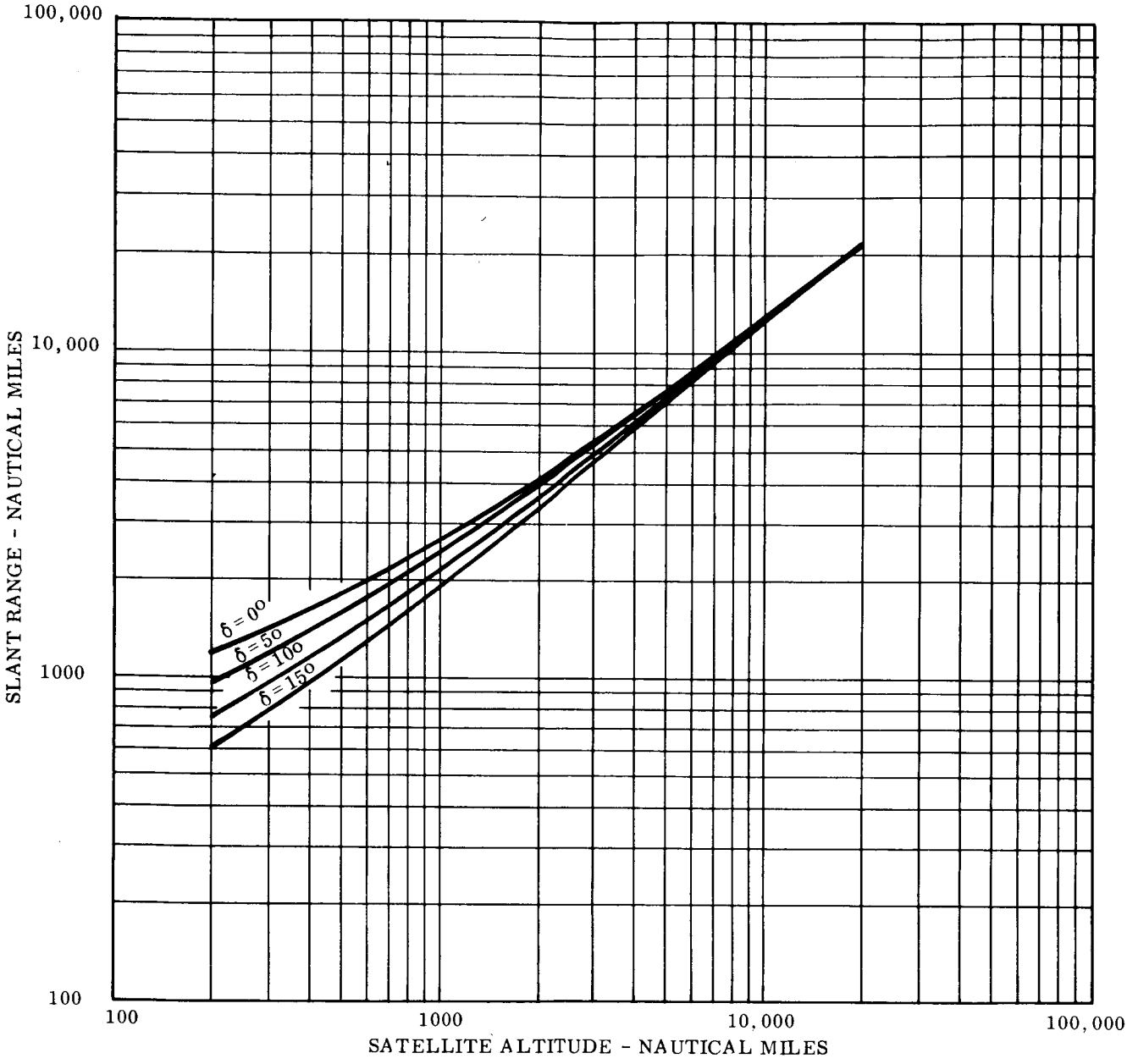

Figure 10-10. Maximum Slant Range vs. Orbital Altitude at Elevation Angle δ

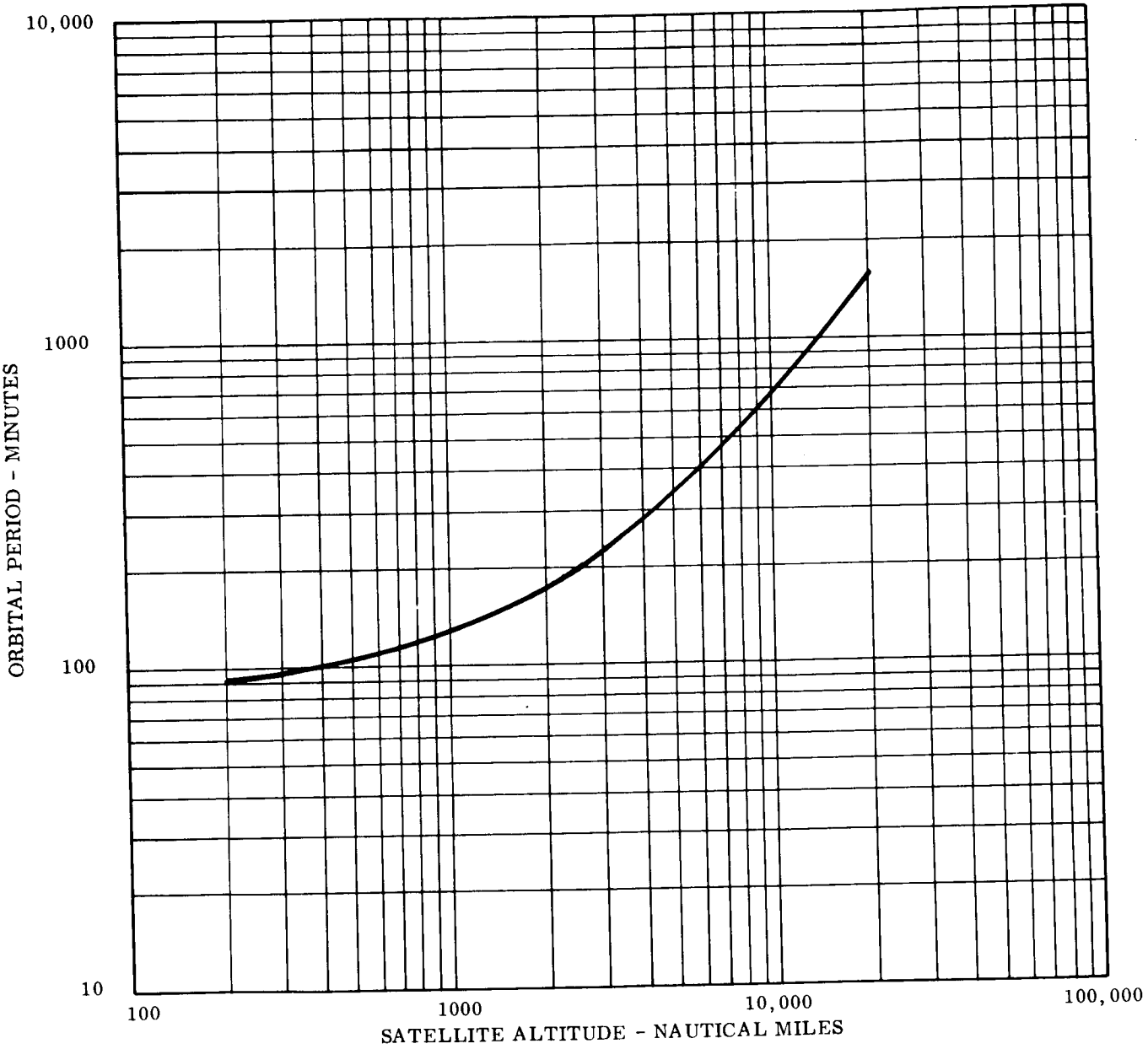

Figure 10-11. Satellite Orbital Period vs. Altitude

10.5.1.4 Range Rate

It can be seen from Figure 10-7 that the square of the slant range is given by:

$$s^2 = R_e^2 + R_o^2 - 2 R_e R_o \cos \theta \qquad (14)$$

where

$$\theta = v_o t / R_o \qquad (15)$$

and v_o is the orbital velocity, given by:

$$v_o = \sqrt{\mu / R_o} \quad \text{ft/sec} \qquad (16)$$

where

$$\mu = 1.407 \times 10^{-6} \text{ ft}^3/\text{sec}^2.$$

Equation 16 has been plotted in Figure 10-12.

Substitution of Equation 15 into Equation 14 yields:

$$s^2 = R_e^2 + R_o^2 - 2 R_e R_o \cos \frac{V_o t}{R_o} \quad . \qquad (17)$$

Differentiation of Equation 17 with respect to time yields the range rate:

$$\dot{s} = \frac{v_o R_e}{} \sin \theta \quad . \qquad (18)$$

This range rate is zero when $\theta = 0$, i.e., directly overhead, and is clearly a maximum on the horizon.

The value of θ at the minimum elevation angle δ is given by Equation 8. Substitution of Equation 11 into Equation 18 yields:

$$\dot{s}_{max} = v_o \cos(\theta + \delta) \tag{19}$$

whence, from Equation 8:

$$\dot{s}_{max} = v_o \frac{R_e}{R_o} \cos \delta. \tag{20}$$

10.5.1.5 Range Acceleration

The rate of change of range rate may be obtained by differentiating Equation 18 with respect to time. This yields:

$$\ddot{s} = \left[\frac{v_o^2 R_e}{R_o S} \cos \theta - \dot{s}^2 \right]. \tag{21}$$

At a given satellite altitude, the three quantities in Equation 21 which vary with satellite position in orbit are θ, s, and $\dot{s}$; all of which pass through their minimum values when the satellite is overhead:

$\theta = 0$

$\dot{s} = 0$

$s = h$.

Therefore, $\ddot{s}$ reaches its maximum value when the satellite is overhead, and Equation 21 shows:

$$\ddot{s}_{max} = \frac{v_o^2 R_e}{h R_o} = \frac{\mu R_e}{h R_o^2} \tag{22}$$

where v_o is given by Equation 16.

10.5.1.6 Doppler Characteristics

Substitution of $\dot{s}_{max}$ for v in Equation 6 yields an expression for the maximum doppler shift as a function of the minimum elevation angle δ:

$$f_d\Big|_{max} = \left(\frac{v_o R_e}{c R_o} \cos \delta\right) f_c \,. \tag{23}$$

This has been plotted versus orbital altitude, h, in Figure 10-13.

Similarly, substitution of $\ddot{s}_{max}$ for $\dot{v}$ in Equation 7 yields an expression for the maximum rate of change of Doppler:

$$\dot{f}_d\Big|_{max} = \left(\frac{v_o^2 R_e}{c h R_o}\right) f_c \,. \tag{24}$$

This has been plotted versus orbital altitude, h, in Figure 10-14.

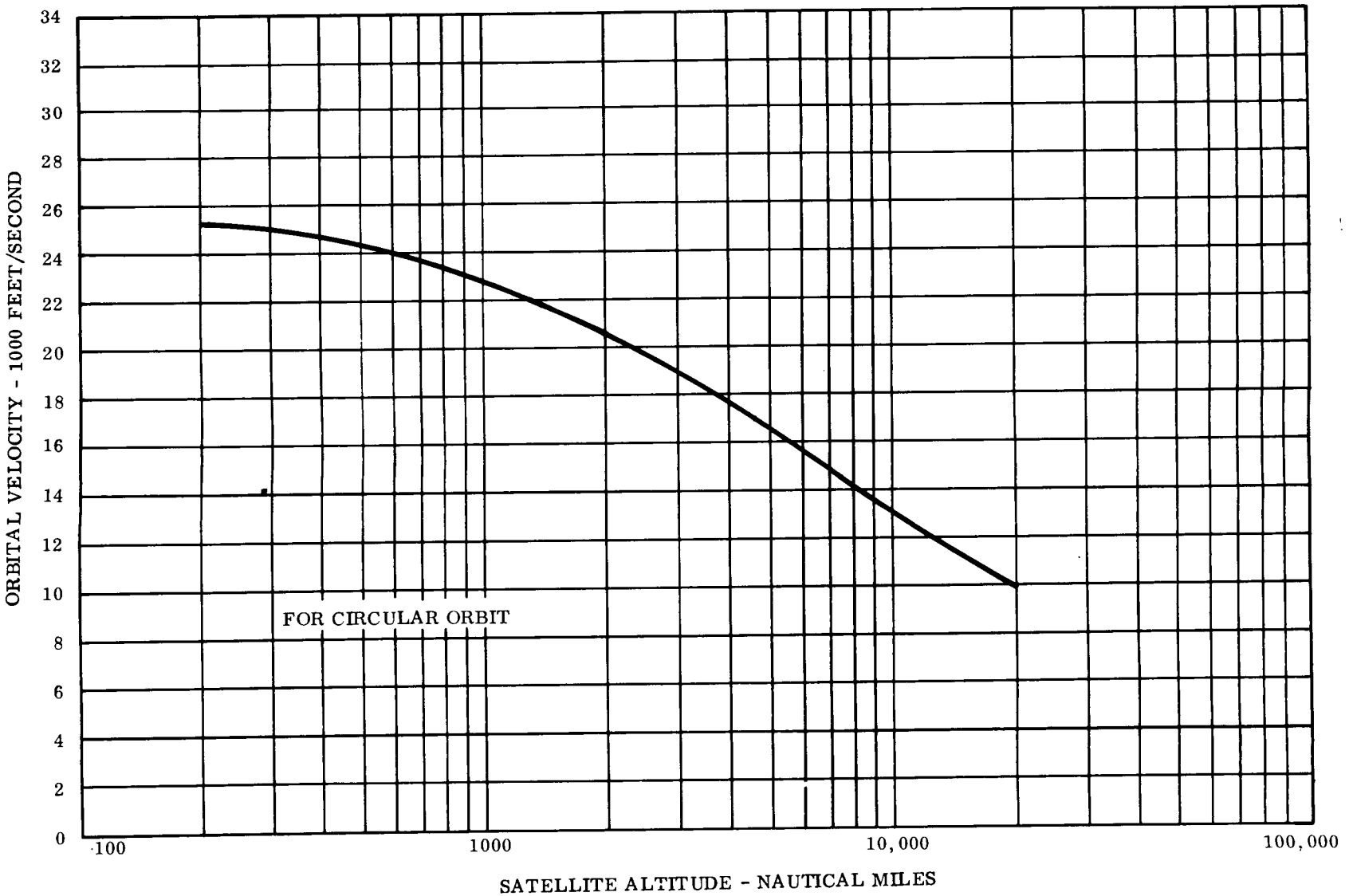

Figure 10-12. Orbital Velocity vs. Altitude

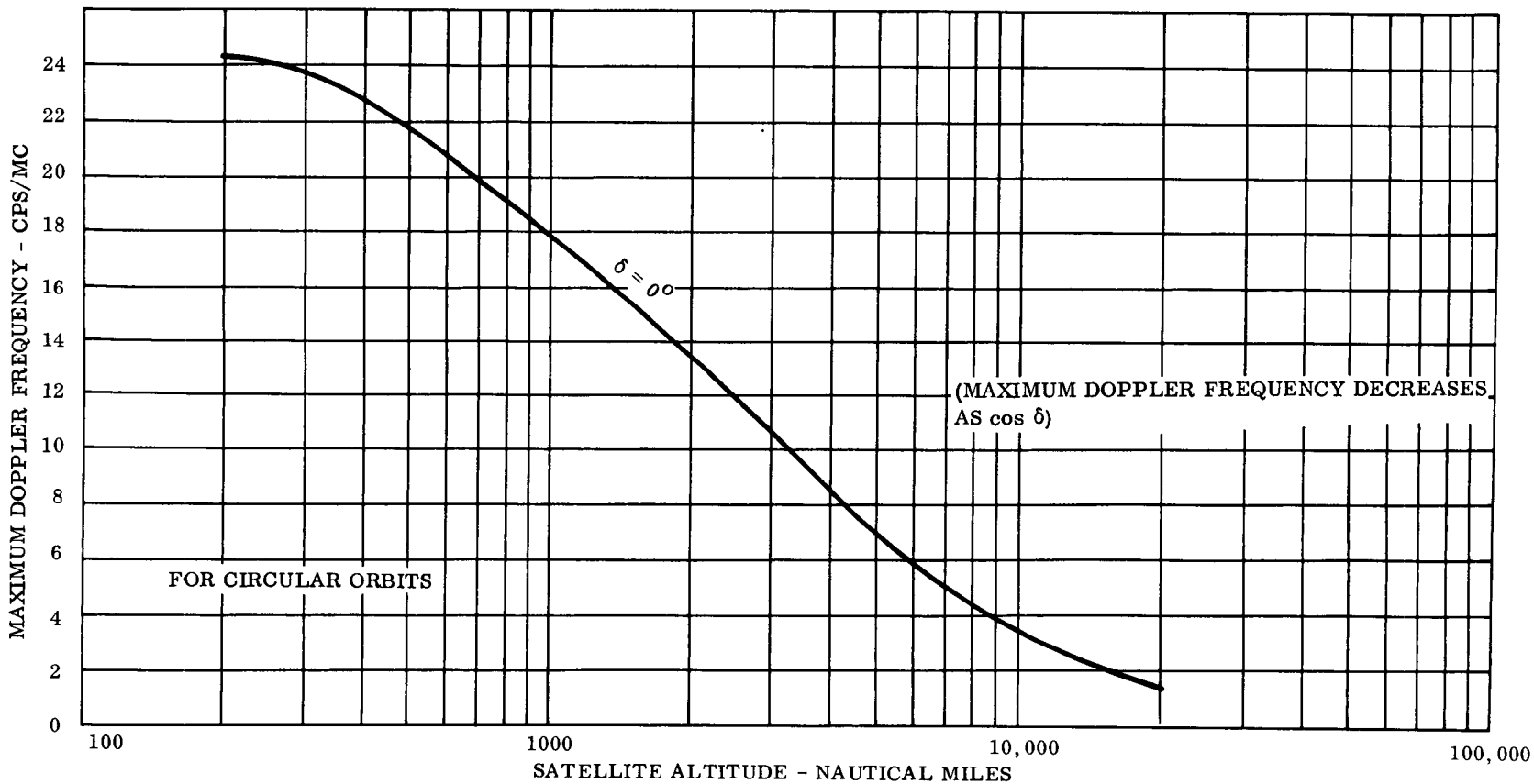

Figure 10-13. Maximum Doppler Frequency vs. Orbital Altitude, Neglecting Earth Rotation

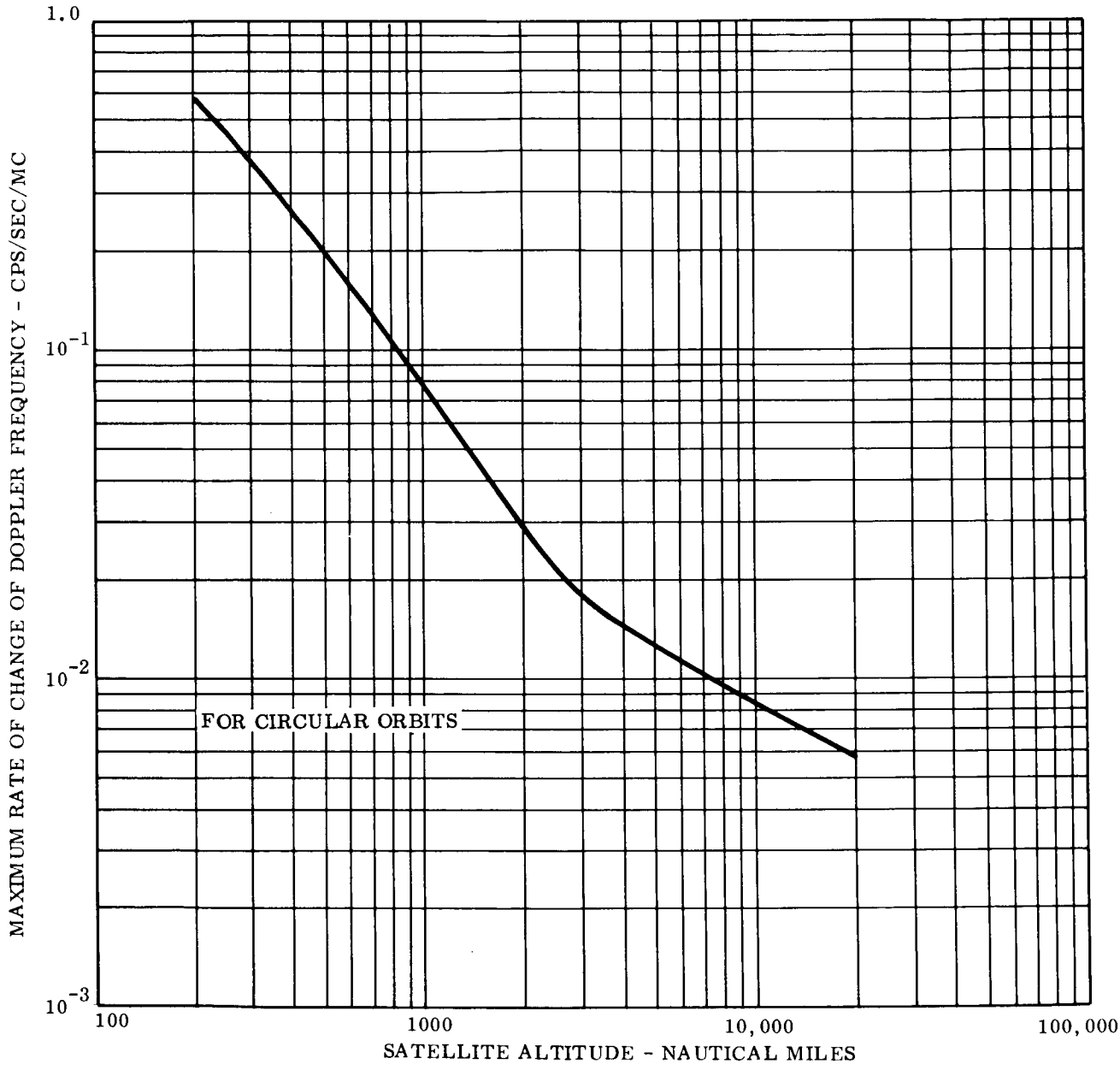

Figure 10-14. Maximum Rate of Change of Doppler Frequency vs. Orbital Altitude (Neglecting Earth Rotation)

10.5.2 ELLIPTICAL ORBITS

10.5.2.1 Background

Section 10.5.1 presented a derivation of the slant range and Doppler characteristics for earth satellites in circular orbits. The purpose of this section is to extend that analysis to the case of elliptical orbits.

The same expressions apply for the slant range as in the case of circular orbits. Moreover, as will be shown in Section 10.5.2.2, the expression for the orbital period of a satellite in a circular orbit is valid for an elliptical orbit as well, if the arithmetic mean of the apogee and perigee altitudes is used in place of the circular orbital altitude.

In order to extend the previous analysis to the case of elliptical orbits, it remains only to determine the maximum slant range rate and acceleration for a satellite in an elliptical orbit.

The satellite will be taken to be in an elliptical orbit having one focus at the center of the earth, as shown in Figure 10-15. Rotation of the earth will be neglected.

The radial distance, R_o, from the center of the earth to the satellite may be expressed as a function of the true anomaly, ϕ, (angle measured from perigee) by:

$$R_o = \frac{a(1 - e^2)}{1 + e \cos \phi} \tag{25}$$

where e is the eccentricity of the ellipse, defined by:

$$e \equiv \sqrt{1 - (b/a)^2} \quad . \tag{26}$$

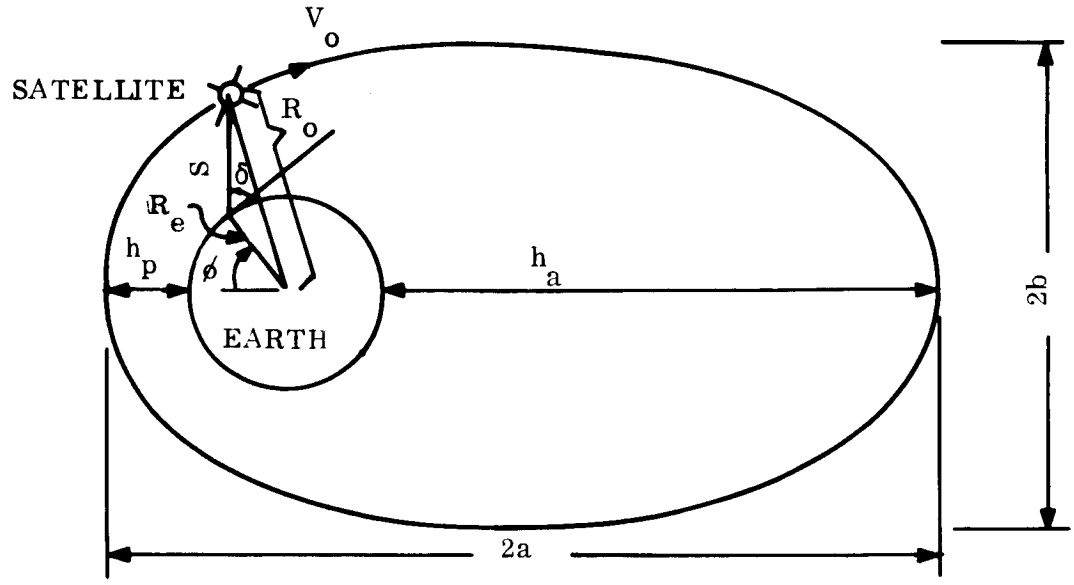

Figure 10-15. Orbital Geometry and Notation

Evaluation of Equation 25 at perigee with subsequent algebraic manipulations allows the eccentricity, e, to be determined from the perigee and apogee altitudes as:

$$e = \frac{h_a - h_p}{h_a + h_p + 2R_e} . \tag{27}$$

The velocity of the satellite as it travels in orbit is given by:

$$v_o^2 = \mu \left(\frac{2}{R_o} - \frac{1}{a} \right) . \tag{28}$$

As the radial distance, R_o, increases, the velocity decreases, and vice versa. The maximum velocity occurs at perigee, and the minimum velocity at apogee.

10.5.2.2 Orbital Period

Kepler's third law of planetary motion states that the square of the period of revolution of a planet is proportional to the cube of its semi-major axis. The period is given by (Reference 10-12):

$$T = \frac{2\pi a^{3/2}}{\mu^{1.2}} \tag{29}$$

where

a = semi-major axis

μ = earth gravitational constant = γ M.

Note that this is identical to the expression for the period in a circular orbit (see Equation 12) if the semi-major axis, a, is substituted for the circular orbital radius. The period depends only on the semi-major axis and is independent of the eccentricity.

The semi-major axis is given by:

$$a = R_e + 1/2\ (h_p + h_a) \tag{30}$$

where

h_p = perigee altitude

h_a = apogee altitude.

Thus, the period for the elliptical orbit may be obtained from:

$$P = 6.987 \times 10^{-6}\ (h + 3440)^{3/2} \text{ sidereal hours,} \tag{31}$$

and Figure 10-11 may be used for elliptical orbits as well as circular.

10.5.2.3 Maximum Range Rate

In order to determine the point of maximum Doppler, a straightforward attempt to set an expression for the derivative of the slant range rate equal to zero results in a formidable eighth-order equation in R_o. However, for reasonably low perigee altitudes, ($h_p << R_e$), physical reasoning indicates that the maximum (visible) slant range rate occurs when perigee appears at the ground station's minimum elevation angle δ, as shown in Figure 10-16.

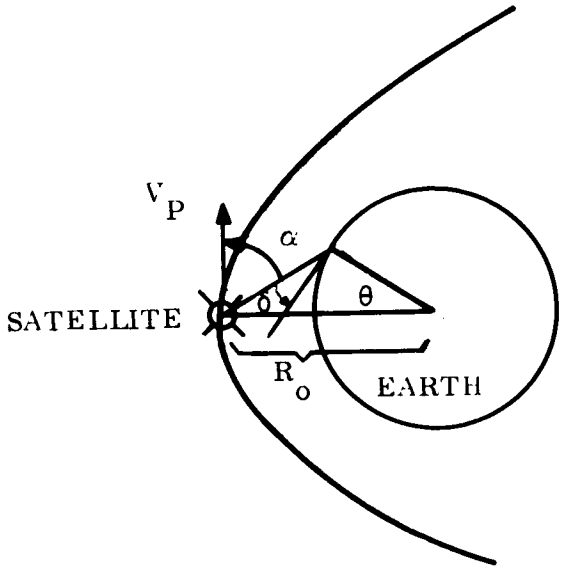

Figure 10-16. Point of Maximum Visible Slant Range Rate

At this point the perigee velocity, v_p, is normal to the R_o vector, and from Figure 10-16:

$$\dot{s}_{max} = v_p \cos(\theta + \delta) \tag{33}$$

where:

$$v_p = \left[\mu \left(\frac{2}{R_p} - \frac{1}{a}\right)\right]^{1/2} . \tag{34}$$

Application of the law of sines permits the elimination of θ from Equation 33 yielding:

$$\dot{s}_{max} = v_p \frac{R_e}{R_p} \cos \delta . \tag{35}$$

That is, the same expression for $\dot{s}_{max}$ as in the case of circular orbits may be used if v_p is substituted for v_o and R_p is substituted for R_o.

10.5.2.4 Range Acceleration

A rigorous determination of the point of occurrence and the magnitude of the maximum range acceleration is even more involved than the range rate analysis. Heuristically one might reason that the maximum range acceleration will occur when the satellite is at perigee and directly above the station, analogous to the case of the circular orbit.* This particular situation is mathematically tractable, and an analysis is presented in this section.

The situation is shown in Figure 10-17. The angle ϕ is identical to the true anomaly, because the ground station is directly beneath perigee.

* This is subject to question, and a thorough analysis should be undertaken before specifying a minimum tracking filter bandwidth for use with satellites in elliptical orbits.

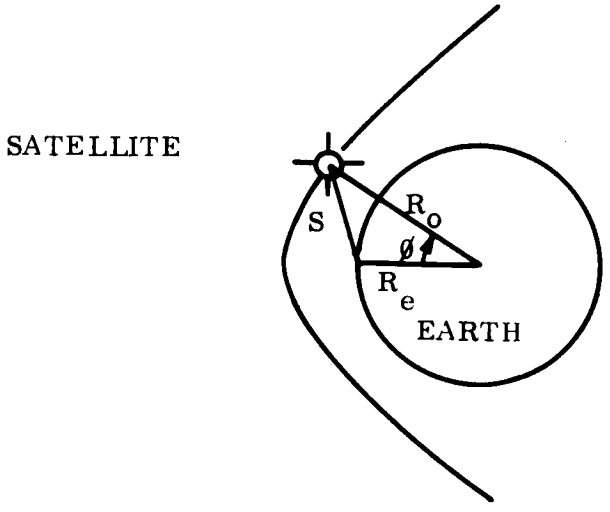

Figure 10-17. Situation Near Perigee

The slant range may be obtained from:

$$s^2 = R_e^2 + R_o^2 - 2\, R_e\, R_o \cos \phi \ . \tag{36}$$

Implicit differentiation yields:

$$s\dot{s} = R_o\, \dot{R}_o - R_e\, \dot{R}_o \cos \phi + \dot{\phi}\, R_e\, R_o \sin \phi \ . \tag{37}$$

A second differentiation then yields:

$$\dot{s}^2 + s\dot{s} = \dot{R}_o^2 + R_o\, \ddot{R}_o - R_e\, \ddot{R}_o \cos \phi + \dot{\phi}\, R_e\, \dot{R}_o \sin \phi + \dot{\phi}\, R_e\, \dot{R}_o \sin \phi \tag{38}$$

$$+ \dot{\phi}^2\, R_e\, R_o \cos \phi + \ddot{\phi}\, R_e R_o \sin \phi \ .$$

At perigee, the following values hold:

$$\begin{aligned} \phi_p &= 0 & R_p &= h_p + R_e \\ s_p &= h_p & \dot{R}_p &= 0 \\ \dot{s}_p &= 0 & \ddot{R}_p &= \mu_e / R_p^2 \end{aligned} \tag{39}$$

Substitution of these values into Equation 38 yields:

$$h_p \ddot{s}_p = (R_p - R_e) \ddot{R}_p + R_e R_p \dot{\phi}_p^2 \tag{40}$$

whence,

$$\ddot{s}_p = \frac{\mu_e}{R_p^2} + \frac{R_e R_p \dot{\phi}_p^2}{h_p} \quad . \tag{41}$$

The next step is to calculate $\dot{\phi}_p^2$.

This may be obtained from the principle of conservation of angular momentum (Reference 10-12):

$$R_o^2 \dot{\phi} = \text{constant} = R_p v_p \tag{42}$$

whence,

$$\dot{\phi} = \frac{R_p}{R_o^2} \sqrt{\mu \left(\frac{2}{R_p} - \frac{1}{a}\right)} \tag{43}$$

$$\dot{\phi}_p^2 = \frac{\mu}{R_p^2}\left(\frac{2}{R_p} - \frac{1}{a}\right) \tag{44}$$

$$= \frac{2\mu}{R_p^2}\left(\frac{1}{R_p} - \frac{1}{R_p + R_a}\right)$$

$$= \frac{2\mu}{R_p^3}\,\frac{R_a}{(R_p + R_a)}$$

$$= \frac{2\mu}{R_p^3}\,\frac{(1 + e)\,a}{(1 - e)\,a + (1 + e)\,a}$$

$$= \frac{2\mu}{R_p^3}\,\frac{(1 + e)}{2}$$

$$\dot{\phi}_p^2 = \frac{\mu\,(1 + e)}{R_p^3} \quad . \tag{45}$$

Substitution of Equation 45 into Equation 41 now yields:

$$\ddot{s}_p = \frac{\mu_e}{R_p^2} + \frac{R_e\,R_p\,\mu\,(1 + e)}{R_p^3\,h_p} \tag{46}$$

which may be reduced to*:

$$\ddot{s}_p = \frac{\mu\,(R_e + e\,R_p)}{R_p^2\,h_p} \quad . \tag{47}$$

* Note that for the special case of circular orbits, (e = o), this expression reduces to Equation 22.

10.5.2.5 Doppler Characteristics

Substitution of $\dot{s}_{max}$, as given by Equation 35, for v in Equation 6 yields an expression for the maximum Doppler shift as a function of the apogee and perigee altitudes and the minimum elevation angle δ:

$$\left.f_d\right|_{max} = \left(\frac{v_p R_e}{cR_p} \cos \delta\right) f_c \qquad (48)$$

where the perigee velocity v_p is given by Equation 34.

Equation 48 has been plotted in Figure 10-18 for apogee altitudes of 1000 to 100,000 nautical miles and perigee altitudes of 100, 200, 300, and 400 nautical miles.

Substitution of $\ddot{s}_p$, as given by Equation 47, for $\dot{v}$ in Equation 7 yields an expression for the time rate of change of Doppler frequency when the satellite is overhead and at perigee*:

$$\left.\dot{f}_d\right|_p = \frac{\mu (R_e + eR_p)}{R_p^2 h_p c} f_c \quad . \qquad (49)$$

This has been plotted in Figure 10-19 for apogee altitudes of 1000 to 100,000 nautical miles and perigee altitudes of 100, 150, 200, 300, and 400 nautical miles.

Figure 10-19 shows that $\dot{f}_d$ at perigee is a much stronger function of h_p than it is of h_a. Indeed, it varies approximately as $1/h_p$, while a factor of 100 change in h_a alters f_d by less than a factor of two.

* As noted in Section 10.5.2.4, it has not been proven that these circumstances bring about the maximum f_d.

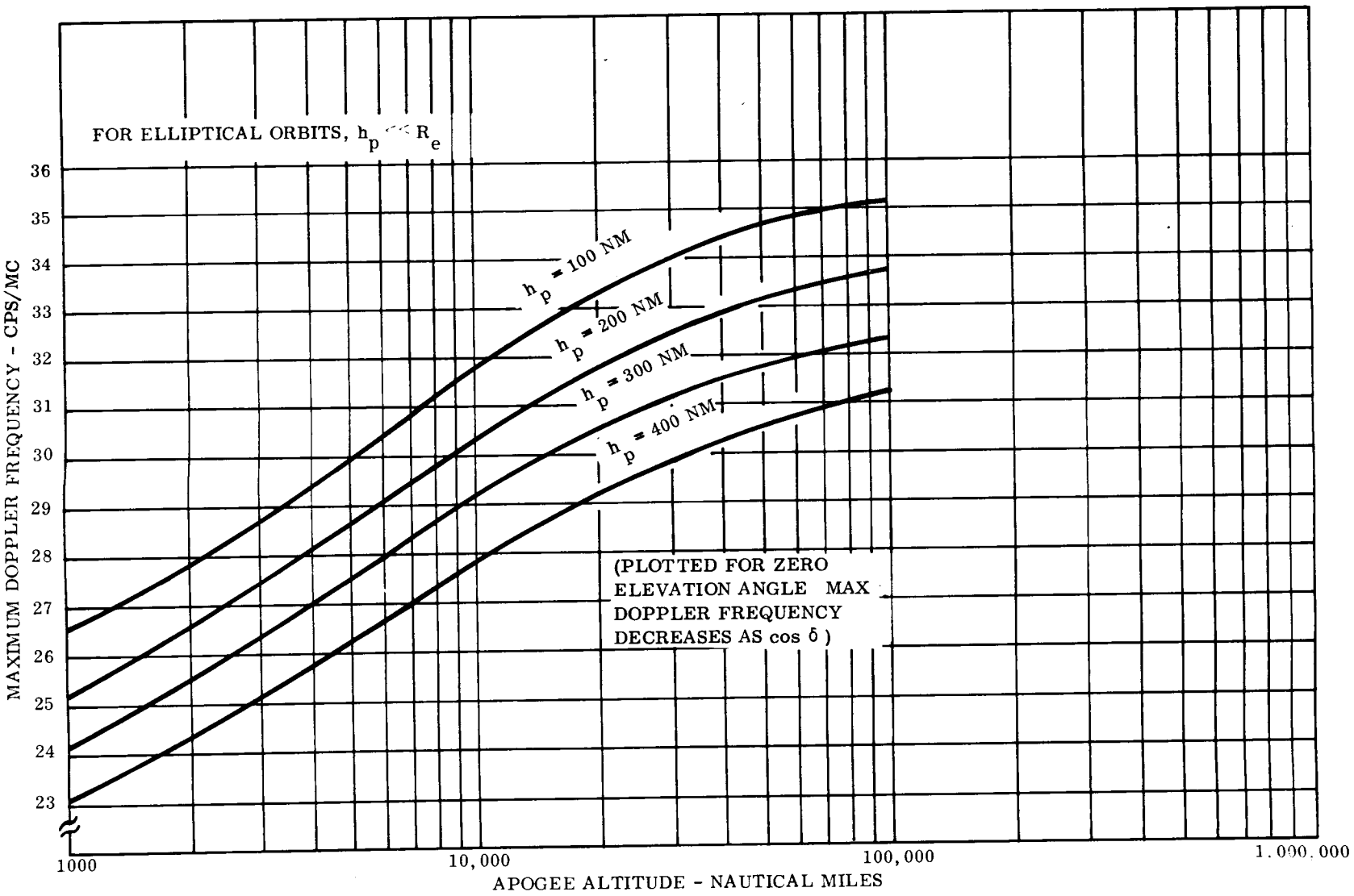

Figure 10-18. Maximum Doppler Frequency vs. Apogee Altitude for Selected Perigee Altitudes (Neglecting Earth Rotation)

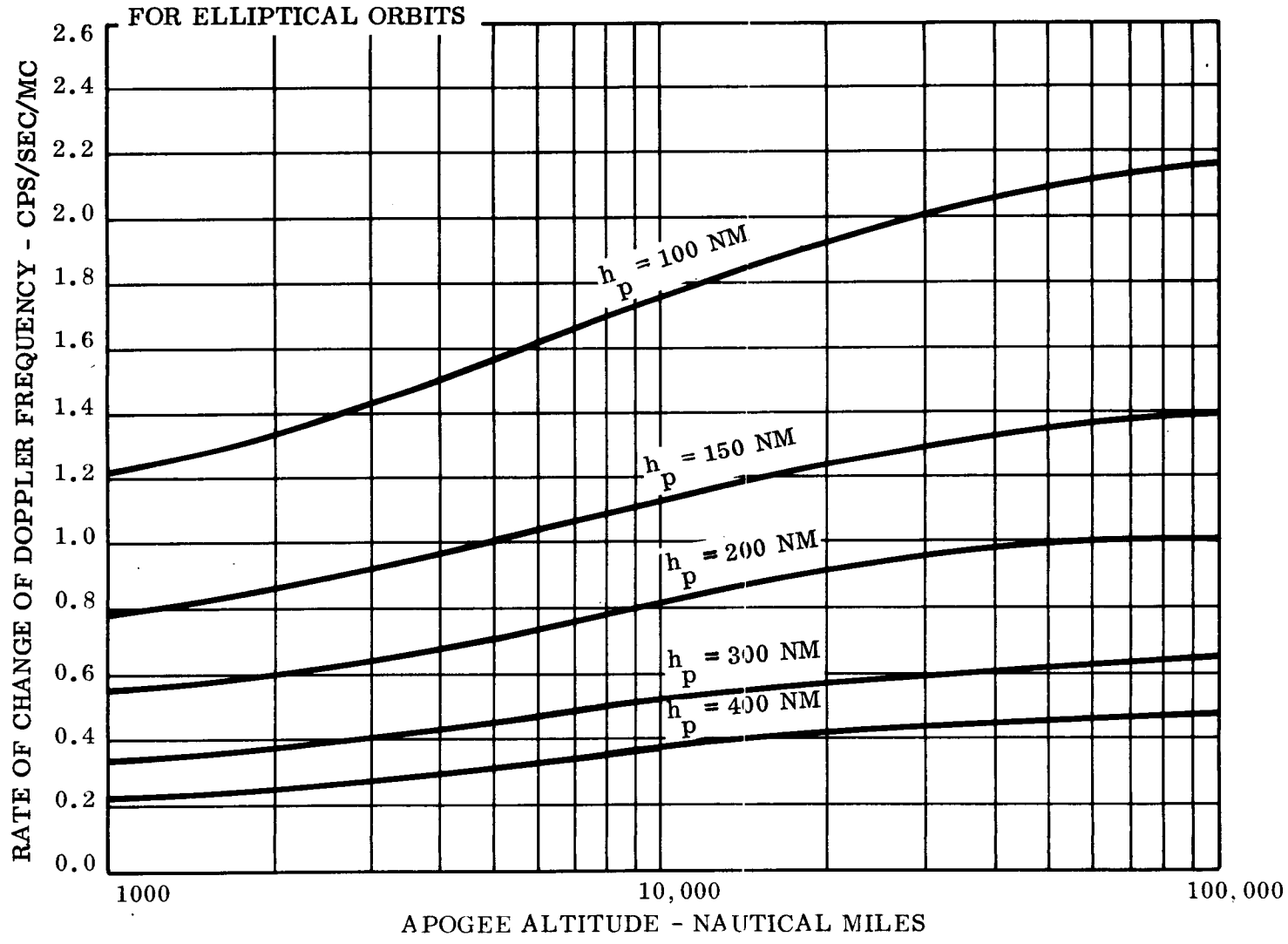

Figure 10-19. Rate of Change of Doppler Frequency at Perigee and Overhead vs. Apogee Altitude for Selected Perigee Altitudes (Neglecting Earth Rotation)

10.6 ANALYSIS OF TELEMETRY LINK

10.6.1 BACKGROUND

Satellite orbital characteristics and Minitrack telemetry ground station capabilities have been established in the preceding sections of this report. Using these, it is now possible to determine the sideband power requirements of the data and the carrier power requirements for tracking and acquisition, using appropriate modulation techniques.

As reported in a recent technology review (Reference 10-13), the trend in aerospace telemetry still points to pulse code modulation (PCM), even though it is becoming clear that pulse frequency modulation (PFM) will continue to play an important role. Both are analyzed in this section.

Briefly, in a PCM system the sensor output voltages are first sampled and quantized into discrete amplitude levels. Each of these discrete levels is then described by a unique code word comprised of binary elements which subsequently modulate a carrier or subcarrier.

Assuming that the analog-to-digital (A/D) encoder can quantize the signals to within $\pm$ one-half a quantum step, the accuracy of the quantization may be expressed by:

$$E = \pm 1/2\ (1/L) = \pm (1/2)^{n+1} \tag{50}$$

where n is the number of binary digits (bits) in the code, and L is the number of quantization levels, given by:

$$L = 2^n \ . \tag{51}$$

This yields the accuracies shown in Table 10-4.

Table 10-4. PCM Quantization Error

Number of Binary Digits, n	Quantization Accuracy, E
4	$\pm (1/2)^5 \doteq \pm 3.0\%$
5	$\pm (1/2)^6 \doteq \pm 1.5\%$
6	$\pm (1/2)^7 \doteq \pm 0.8\%$
7	$\pm (1/2)^8 \doteq \pm 0.4\%$
8	$\pm (1/2)^9 \doteq \pm 0.2\%$

Therefore, a $\pm$ 1 percent quantization accuracy requirement will require six-bit encoding. To realize the full performance advantage of six-bit PCM, the received S/N ratio should be high enough to maintain the bit error probability between 10^{-5} and 10^{-6}. At higher error rates than this, the erroneous bits will make a significant contribution to the inaccuracy of the data, and Table 10-4 will not be applicable.

PFM telemetry is characterized by a train of sequential pulses whose frequencies (tone bursts) are proportional to the amplitudes of the sampled sensor outputs. A number of small (less than 200-pound) NASA scientific satellites have utilized PFM telemetry systems (Reference 10-16). Size and weight limitations imposed on small satellites have made this type of modulation/encoding attractive where data requirements are minimal, since the satellite telemetry equipment required is fairly simple. PFM was used on the Vanguards and, more recently, on the Scout-launched Explorers. Some future Explorers again will use this form of telemetry.

The PFM waveform is comprised of a sequence of rectangular pulses, each containing many cycles of a constant frequency. The information is contained in the frequency of each of these clipped tone bursts. A typical PFM format is shown in Figure 10-20.

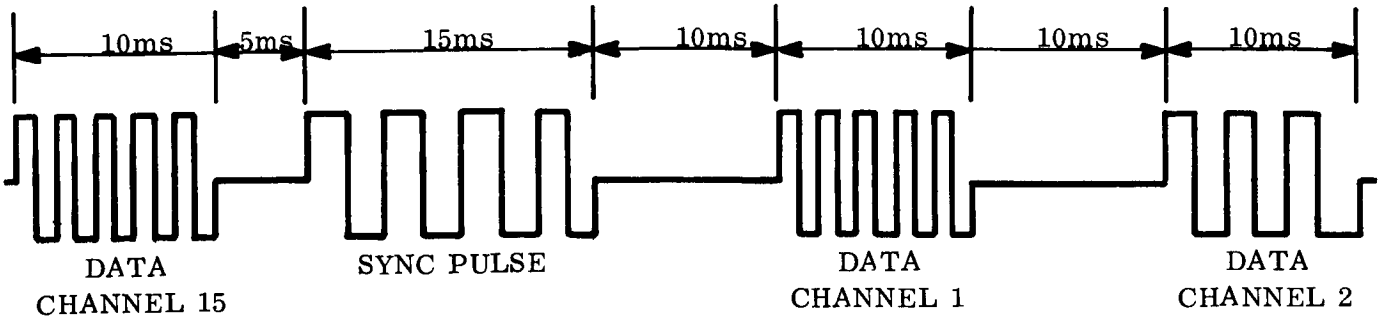

Figure 10-20. Format for a Typical PFM Signal

10.6.2 LINK PARAMETERS

Pertinent parameters for the telemetry link analysis are summarized in Table 10-5, and the satellite orbital characteristics are summarized in Table 10-6.

Table 10-5. Telemetry Link Parameters

Modulation Techniques Considered:	PCM/PSK, PCM/FSK, PCM/FM, and PFM on subcarriers; non-coherent PCM/FM
Encoding Accuracy: 6-bit	
Bit Error Probability: 1.0×10^{-5}	
Ground Antenna Gain: 19 db	
Minimum Elevation Angle: 15 degrees above horizon	
Polarization Mismatch Loss: 0 db (polarization diversity reception)	

Table 10-5. Telemetry Link Parameters (Cont)

Miscellaneous RF Losses: 3 db	
Average Galactic Noise Temperature*:	$1400^{o}K$
Antenna Sidelobe Noise Contribution (Reference 10-16):	$55^{o}K$
Preamplifier Noise Temperature (NF = 3.5 db):	$365^{o}K$
Receiving System Noise Temperature:	$T_e = 1820^{o}K$
Corresponding Noise Spectral Density: -196.0 db (w/cps)	
Design Margin: 8 db	

Table 10-6. Satellite Orbital Characteristics

Characteristics	1000-NM	Elliptical	325-NM
Designation of Orbit	I	II	III
Maximum Slant Range - nautical miles	1950	27,800	830
Maximum Doppler - cps	$\pm$2340	$\pm$4370	$\pm$3070
Doppler Rate - cps/sec	10.6	125	46.2

* The galactic noise level varies considerably across the sky. See Ko (Reference 10-14) for typical contour maps. Hogg and Mumford (Reference 10-15) have derived an empirical relationship:

$$T_g \approx 290 \lambda^2 \text{ degrees K}$$

for the average galactic noise temperature, where λ is the wavelength in meters. At 136 megacycles, this yields $T_g \approx 1400^{o}K$.

10.6.3 AVAILABLE SIGNAL POWER

The calculation of the signal power received on earth per watt of effective radiated power (ERP)* from the satellite is shown in Table 10-7.

Table 10-7. Telemetry Link Received Power Calculation

Effective Radiated Power (one watt)	+ 0. 0 dbw
Free-space Attenuation (s NM, 136 mc)	-20 log s -80.4 db
Ground Antenna Gain	+19.0 db
Miscellaneous RF Losses	- 3.0 db
	-20 log s -64.4 dbw

10.6.4 REQUIRED SIGNAL POWER

In the analysis of this section, it will be assumed that synchronous detection is performed on the carrier by ground station tracking filters, and that the data are located on subcarriers. The modulation techniques can then be compared on the basis of their respective subcarrier power requirements, which are not affected by Doppler characteristics, oscillator instability, etc.

10.6.4.1 Theoretically Ideal System

For the theoretically ideal system the data rate is equal to the channel capacity given by Shannon's fundamental theorem for the noisy channel:

$$C = B \log_2 (1 + S/N) \quad \text{bits/sec}, \tag{52}$$

* ERP is the product of transmitter output power and transmitting antenna gain.

where B is the bandwidth of the channel. For wide bandwidths and low received S/N ratios, this reduces to:

$$C = B\,(S/N)\log_2 e$$

$$= \frac{S}{N/B}\log_2 e$$

$$= 1.44\ S/(N/B)\ \text{bits/sec}; \tag{53}$$

which yields

$$S/C = ST = 0.695\ N/B\ \frac{\text{watts}}{\text{bit/sec}}$$

$$= 0.695\ N/B\ \text{joules/bit}; \tag{54}$$

whence

$$E/N_o = 0.695 = -1.6\ \text{db} \tag{55}$$

where E is the signal energy per bit, and N_o is the noise spectral density. This represents the absolute minimum received energy required per bit of data.* However, it would require an infinite encoding time delay (hence, infinite on-board storage) and no suitable code has yet been discovered.

10.6.4.2 PCM/PSK

The most efficient modulation technique for uncoded binary data in the presence of additive white Gaussian noise is phase-reversal keying of the carrier, resulting in a DSB (SC)** spectrum.

* A vanishing error probability is inherent also.
** Double sideband, suppressed carrier

The performance of such systems has been analyzed by Lawton (Reference 10-17), Reiger (Reference 10-18), and others, and the results are well known. For coherent PSK, the bit error probability has been shown to be:

$$P_e = \frac{1}{2}\left(1 - \text{erf}\sqrt{\frac{E(1-\rho)}{2N_o}}\right) \tag{56}$$

where E is the signal energy received per symbol, and ρ is the finite time correlation coefficient of the two symbol waveforms. This has been plotted in Figure 10-21.

In order to demodulate the received signal, a synchronous receiver is required (in this case at the subcarrier frequency), together with a reset integrator (matched filter) in its output.

For a 1.0×10^{-5} bit error probability, Figure 10-21 shows that a value of $E/N_o = 9.6$ db is required. This is 11.2 db inferior to Shannon's ideal, and has been plotted as such in Figure 10-26.

10.6.4.3 PCM/FSK

In non-coherent FSK detection the received envelopes are examined, and the frequency channel having the larger envelope (signal plus noise) is considered the more likely to contain the signal. It has been shown (References 10-17, 10-18) that the error probability for non-coherent FSK is:

$$P_e = 1/2\, e^{-E/2N_o}. \tag{57}$$

The difference between coherent PSK and non-coherent FSK is about 4 db for low error probabilities (Reference 10-19), and has been so plotted in Figure 10-26.

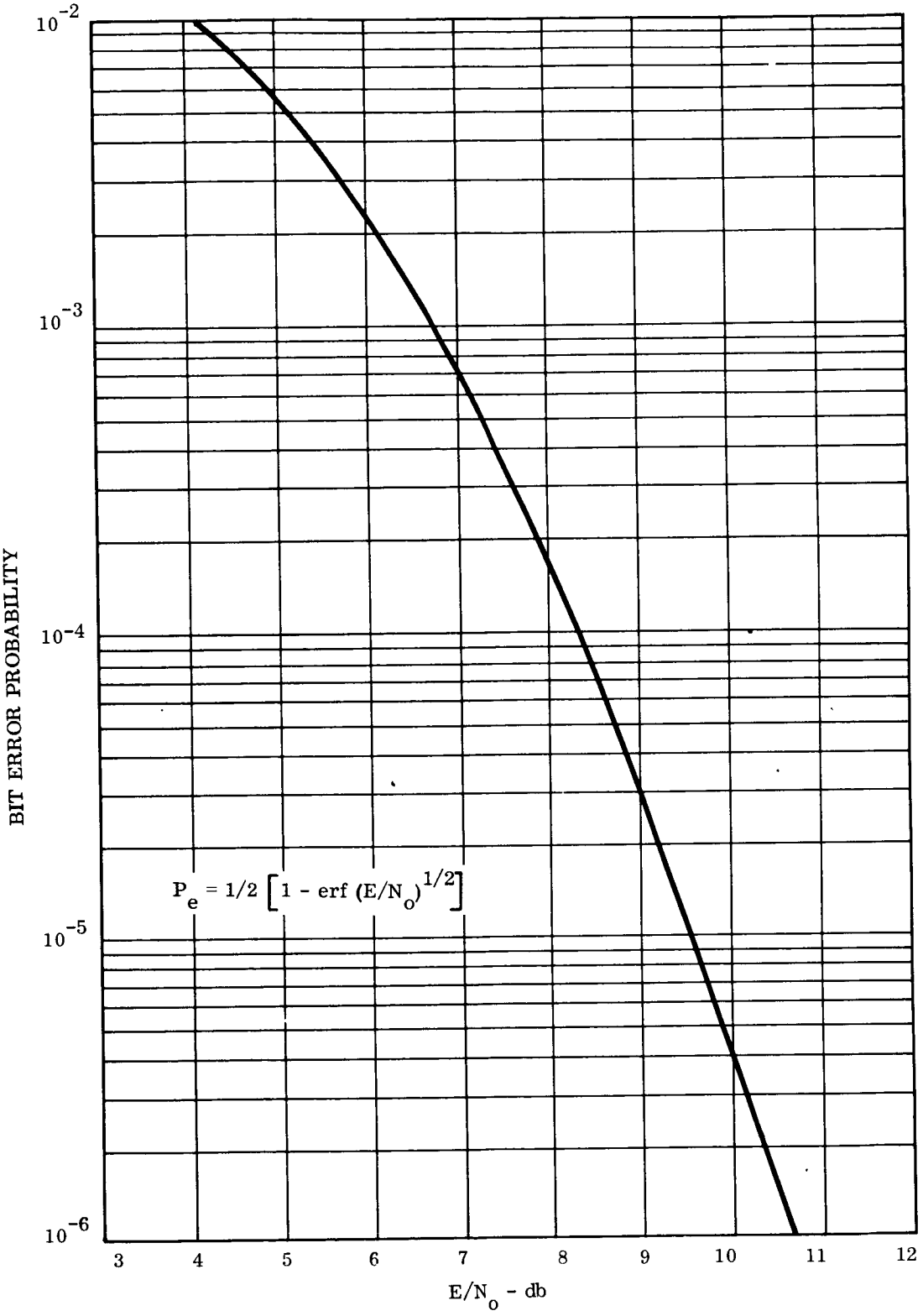

Figure 10-21. Probability of Bit Error vs. Ratio of Bit Energy to Noise Power Density for Coherent PSK

10.6.4.4 PCM/FM

The IRIG Standards (Reference 10-20) preclude the use of PCM/FSK in that they require a low-pass filter to precede the transmitter modulator, with its three-db cutoff frequency equal to one-half the nominal bit rate. This is known as PCM/FM. This minimizes the power in the higher order sidebands and thus assists in RF spectrum conversations.

Moreover, the standards recommend an IF bandwidth between 1.5 and 3.0 times the bit rate, and a S/N ratio in the IF bandwidth of 13 db for $P_e = 10^{-5}$. Thus:

$$\frac{S}{N} = \frac{S}{1.5N_o B_{IF}} = \frac{ST}{1.5N_o} = 13 \text{ db} = 20, \tag{58}$$

whence

$$\frac{E}{N_o} = 30 = 14.8 \text{ db} . \tag{59}$$

This is about 1.2 db less efficient than PCM/FSK, and has been so plotted in Figure 10-26.

10.6.4.5 Typical Improvement Afforded PCM by Error Correction Coding

Various coding techniques can be employed to take advantage of Shannon's channel capacity theorem and thereby reduce the transmitter power for the same information rate by increasing the channel bandwidth. The basic coding problem, of course, is to approach the Shannon channel capacity limit as closely as possible without requiring excessive complexity in the implementation.

In the digital encoding process, r redundant digits are added to the m information digits to form an m + r digit code word. The received code word together with additive noise enters the decoder, where detection decisions are made on a digit-by-digit basis, and the error correction is performed by logic circuits.

An alternate method of processing the received code word employs word correlation, where decisions are made on a word basis, and the error correction is implicit in the maximum likelihood detector which decides which word was sent. It is well known that correlation detection is optimum in a Gaussian noise environment, but the receiving equipment becomes unduly complex for all but relatively weak codes.

Error correction codes range from the least redundant Wagner codes, where one redundant digit is added to a block of information digits, to the most redundant orthogonal codes, where 2^m - m redundant digits are added to a block of m information digits.

For a given block of m information digits, the greatest increase in transmission efficiency is obtained by using a highly redundant code, such as a maximal length sequence, orthogonal, or bi-orthogonal code, together with correlation detection at the receiver. However, there are several practical drawbacks to this. First, the ratio of total bandwidth to information bandwidth becomes extremely large. For example, the maximal sequence code with 20 information bits per code word has a code word length of 2^{20} - 1 digits. This means that about one megacycle of bandwidth would be required to transmit 20 bits per second of information. Although this is theoretically feasible, practical considerations such as receiver thresholds and synchronization requirements ordinarily rule out such a large bandwidth expansion.

Furthermore, correlation detection requires that an incoming code word be compared with all possible code words which could have been transmitted. A maximal length sequence code having 20 information bits per code word would result in 2^{20} possible code words. This would require 2^{20} - 1 (slightly over one million) comparisons to be made upon receipt of a code word which would be rather impractical even at very low data rates.

To keep the bandwidth expansion small while obtaining a significant increase in data transmission rate requires the use of a medium redundancy code with a relatively large number of information digits per word. This usually precludes the use of correlation

detection. Digital decoding techniques are available, however, which increase in complexity only linearly with code length so that very powerful, low-redundancy codes can be implemented with relative ease.

Relatively short codes (10 to 50 information bits) of moderate redundancy (40 to 50 percent) are available (Reference 10-21) which can reduce bit error rates by factors of 10 to 400, or equivalently, permit one to three-db reductions in transmitter power when the coded system bit error rate is 10^{-6} (in the presence of Gaussian noise).

A typical code which might be used in such an application is the (73,45) Bose-Chaudhuri code. This code has a word length of 73 bits, 45 of which are information bits. It is a four-error correcting/five-error detecting shift-register code which can be readily decoded. It has the capability of correcting a relatively large number of error patterns of weight greater than four, in addition to the correction of all error patterns of weight four and less.

Figure 10-22 (Reference 10-21) shows three curves for bit error probabilities of interest in the evaluation of the effectiveness of the (73,45) code in reducing errors caused by Gaussian noise. (These data were originally obtained by simulation on an IBM 7090 computer.) The graphs show that the advantage with simple decoding of the (73,45) code exceeds one-db for output bit error rates less than 10^{-3} and exceeds 3.5 db for output bit error rates less than 10^{-7}.* At the nominal bit error rate of 10^{-5} used for the analysis of this study, the improvement is about 2.7 db. This can be subtracted directly from the required signal levels shown in the PCM analyses of the three preceding sections.

10.6.4.6 Pulse Frequency Modulation

Rochelle (References 10-16, 10-22, 10-23) has shown that PFM with quantized frequencies has the same communication efficiency, in the presence of additive white Gaussian noise,

* Just as in most signal processing techniques, the better the original signal is, the more improvement possible.

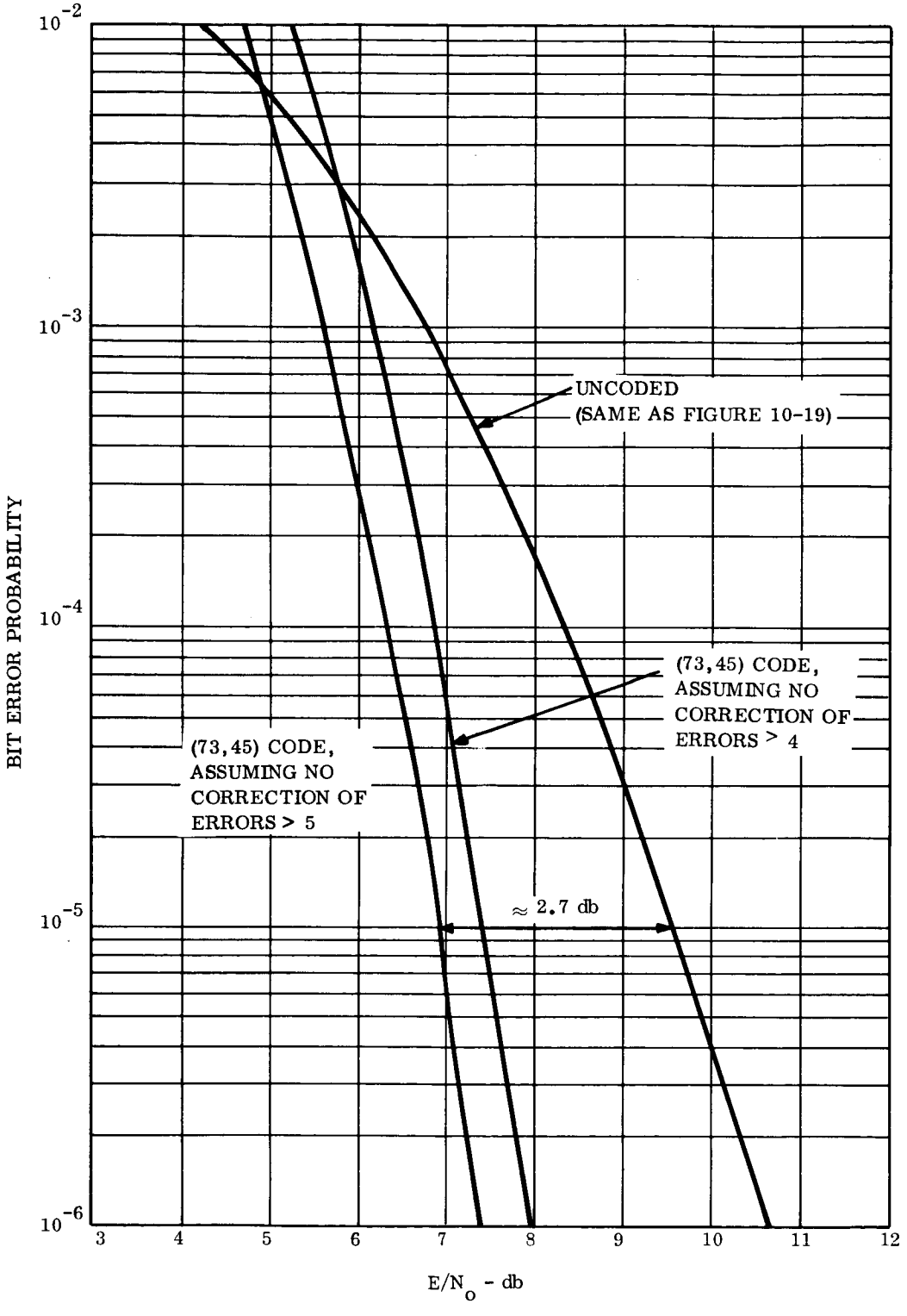

Figure 10-22. Probability of Bit Error vs. E/N_o
With and Without Error Correction Coding

as a corresponding set of coded binary sequences with an equal number of quantized levels. PFM is indeed a special binary code taken from a group of many codes which can be made up of patterns of zeros and ones, so long as the frequencies in the PFM signal are restricted to an integral number of cycles in the pulse. Each pulse can then be considered to contain a string of binary digits alternating between zero and one. For example, if the burst frequency were 6.4 kilocycles in a 10-millisecond pulse, there would be the equivalent of 64 zeros alternating with 64 ones.

A number of methods are available to detect the signal in the presence of noise. Among these the optimum method is, of course, the use of matched filters with maximum likelihood detection. The number of filters employed is a function of the desired encoding accuracy. For n-bit accuracy in a single channel measurement, $L = 2^n$ filters are required.

Although the use of matched filters is most desirable, there are many situations in which the use of unmatched filters can greatly reduce ground station implementation complexity without causing excessive degradation in error rate. It has been found (Reference 10-16) that the use of unmatched filters for PFM signals in which the number of quantized levels exceeds eight (n = 3) can result in a simplification of the operation of the detection system over a matched filter set. The unmatched filter set would consist of L contignous bandpass filters, where L is the number of quantized levels in the signal.*

Viterbi (Reference 10-24) has published curves of error probability as a function of the ratio E/N_o. These curves are plotted for both orthogonal and bi-orthogonal codes for various values of n, where n is the number of coded bits. For a PFM system using integral values of frequency and 128 coherent detectors, the value of n would be seven. Viterbi's curves can thus be used directly to evaluate a PFM signal. For example,

* As mentioned in Reference 10-23, the use of contiguous bandpass filters allows the transmission of analog frequencies (rather than discrete frequencies). A discriminator can then be added to each filter output, permitting improved accuracy under conditions of higher received S/N ratio.

Explorer XII used 100 filters. If they had been coherent detectors, n would be $\log_2 100 = 6.64$. This is equivalent to a coded binary phase-coherent system with $n = 6.64$.

Figure 10-23 shows the error-probability curves derived by Rochelle (Reference 10-16) for the unmatched filter set with maximum-likelihood detection in the presence of Rayleigh noise (i.e., following an envelope detector).* The curves were derived in terms of word error probability, instead of the bit error probability which was used for the PCM analysis. (This, of course, is natural, since PFM is encoded and decoded word-by-word instead of bit-by-bit.)

To permit a comparison of the two modulation efficiencies, it is necessary first to determine what the equivalent word error rate of the PCM word is. This is given by (Reference 10-24):

$$P_e(n) = 1 - \left[1 - P_e(b)\right]^n \approx n P_e(b) \qquad (60)$$

for $P_e(b) << 1$.

Thus, a PCM bit error rate of 10^{-5} results in a word error rate of approximately 6×10^{-5} for six-bit words. Therefore, the appropriate E/N to use in the comparison for PFM is that which will provide a word error rate of 6×10^{-5}. Figure 10-23 shows that this is E/N_o = 4.3 db, which is 5.9 db inferior to Shannon's ideal and has been so plotted in Figure 10-26.

* Under conditions of high S/N ratio, the probability of error with the unmatched filter set approaches that of the matched filter set.

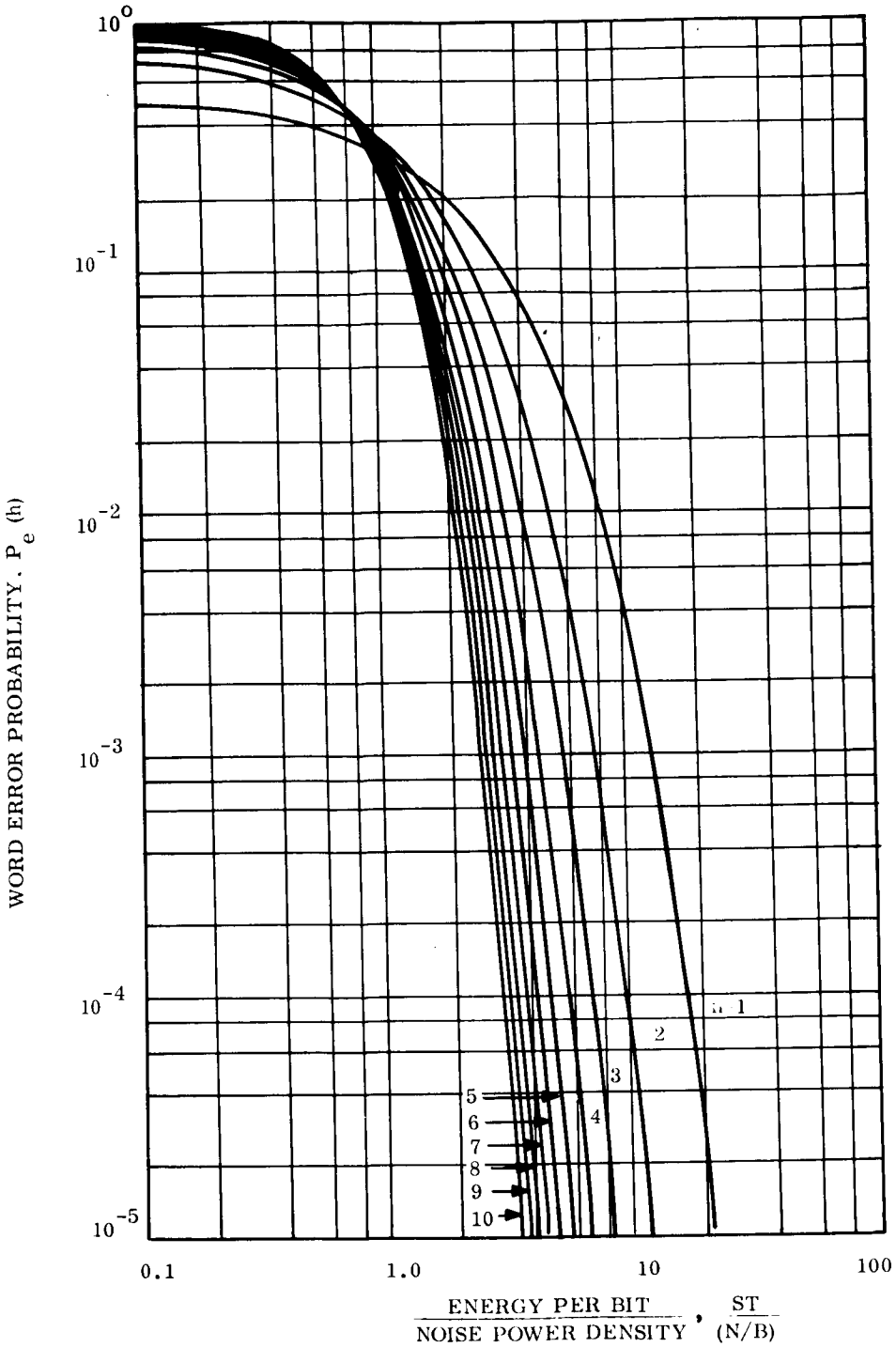

Figure 10-23. Word-Error Probability Curves for Rayleigh Noise

10.6.4.7 Carrier Loop Bandwidth and Power Requirements

A. Loop Bandwidth Requirements for Acquisition

The detection processes analyzed in the preceding sections have all assumed that synchronous detection is performed on the carrier by the ground station tracking filter. This requires that the frequency of the incoming signal first be located (acquired). Then an internally generated signal at the receiver must be locked in phase with the received carrier and must follow all further phase variations of the carrier. The capability of a phase-lock loop which will acquire and track the carrier is described in this section. Its requirements are then determined from the dynamic and electrical characteristics of the links.

The parameters of interest in the tracking loop are the effective loop noise bandwidth and the S/N ratio required in that bandwidth, since these parameters determine the amount of transmitter power required in the carrier. Several factors must be taken into account in determining the noise bandwidth. These include:

Thermal noise
Phase jitter due to instability of the transmitter and receiver oscillators
Sweep rate for signal acquisition
Doppler rate.

Although it would be desirable to minimize the loop bandwidth in order to minimize the thermal noise, the last three factors tend to limit the amount of bandwidth reduction which can be realized.

Acquisition of the incoming signal is accomplished by sweeping the locally generated signal through the frequency band in which the incoming signal is known to exist. Unless the loop can respond rapidly to the transient resulting from the coincidence of the two signals, it is unlikely that it will lock onto the signal. Increasing the loop bandwidth increases the probability of acquisition.

In addition to oscillator phase jitter and the sweeping action required for acquisition, the Doppler rate also limits the minimum loop noise bandwidth. In effect, the Doppler rate places the same type of requirement on the loop bandwidth as the acquisition sweep does. In one case the incoming frequency is changing, while in the other case the locally generated frequency is changing.

The phase-lock loop considered in this analysis is a basic Type II loop with the addition of a limiter at the output of the IF section. The Type II loop has been discussed extensively in the literature, so the theory of its operation will not be covered here. The limiter provides a gain control function, since the gain of the loop depends upon the amplitude of the incoming signal. The advantages of limiting have been set forth by Jaffe and Rechtin (Reference 10-25), and the acquisition characteristics of a Type II loop with limiting in the presence of noise have been determined by means of a GEESE* simulation of the system, the results of which have been reported by Frazier and Page (Reference 10-26).

The results of the GEESE simulation provided an empirical formula for the prediction of the sweep rate for a 90 percent probability of acquisition on the first sweep:

$$R_{90} = \frac{\left(\frac{\pi}{2} - 2.2\sigma_o\right)\left(0.9\alpha/\alpha_o\right)\omega_{no}^2}{2\ (1+\delta)} \qquad (61)$$

where

σ_o = calculated rms output phase jitter

δ = overshoot = $\exp\left(-\zeta\pi/\sqrt{1-\zeta^2}\right)$

α = signal suppression factor in limiter

α_o = supression factor for which the loop is "matched"

ω_{no} = natural frequency at match point

ζ = loop damping factor ($\zeta \geq 1/2$)

The calculated rms output phase jitter is given by:

---

*General Electric Electronic System Evaluator

$$\sigma_o^2 \approx 1/2\,(N/S)_{out} \quad rad^2 \tag{62}$$

where $(N/S)_{out}$ is the noise-to-signal ratio in the loop noise bandwidth. A value of 20 degrees is usually allowable for σ_o, corresponding to S/N = 7.5 db.*

The signal suppression factor, α, results from the characteristics of an ideal limiter in the presence of noise. At the match point $\alpha = \alpha_o$.

The noise bandwidth of the loop, B_n, (in cps) is related to the natural frequency of the loop, ω_n, (in rad/sec) by:

$$B_n \approx \frac{\omega_n}{4\zeta}\,(1 + 4\,\zeta^2). \tag{63}$$

B_n is a minimum when $\zeta = 1/2$, where it has the value:

$$B_n = \omega_n \quad cps, \tag{64}$$

Therefore, at the match point and for the optimum value of damping factor $\zeta = 1/2$ and $\sigma_o = 0.3$ rad, equation 61 becomes:

$$R_{90} = \frac{\left[\frac{\pi}{2} - (2.2)(0.3)\right]\left[0.9\,B_{no}^2\right]}{2\,\pi\,(1 + 0.17)}$$

$$= 0.111\,B_{no}^2, \tag{65}$$

whence

$$B_{no} \doteq 3\sqrt{R_{90}} \quad cps, \tag{66}$$

*It has been shown that Equation 62 is only accurate to no better than three db for IF S/N ratios below -10 db (Reference 10-26). Nevertheless, it is the value used in the empirical relationship of Equation 61.

where the sweep rate may be obtained from the sweep bandwidth, B_s, and the sweep duration T_s:

$$R_{90} = B_s/T_s \quad \text{cps/sec.} \tag{67}$$

The IF bandwidths available in the Minitrack Mod. I Telemetry Receiver range from ten kilocycles to one megacycle. Tracking filter loop bandwidths of 2.5, 5, 10, 25, 50 and 100 cps are available. Equation 66 may be solved for the maximum acquisition time (with 90 percent probability):

$$T_s = 9B_s/B^2_{no.} \tag{68}$$

This has been plotted in Figure 10-24 for the sweep and loop bandwidths of the Mod. I receiver.

The necessary sweep bandwidth depends on the amount of frequency uncertainty, which is the sum of the Doppler uncertainty and the frequency drifts of the oscillators (both transmitter and receiver). The Doppler shift will be predictable to an increasing accuracy each orbit. Thus the minimum sweep bandwidth is determined by the frequency stability. For a stability of $1:10^5$, this represents 2720 kilocycles at 136 megacycles. A loop bandwidth of 25 cycles per second would permit sweeping this band in 0.65 minutes (with 90 percent probability of lock). However, if the entire ten kilocycle band must be swept, 2.4 minutes will be required. Assuming a reasonable a priori knowledge of the orbit, a 25 cycle per second loop bandwidth appears adequate for acquisition.

B. Loop Bandwidth Requirements for Carrier Tracking

Studies conducted by Motorola (Reference 10-27) have indicated the following formula to be

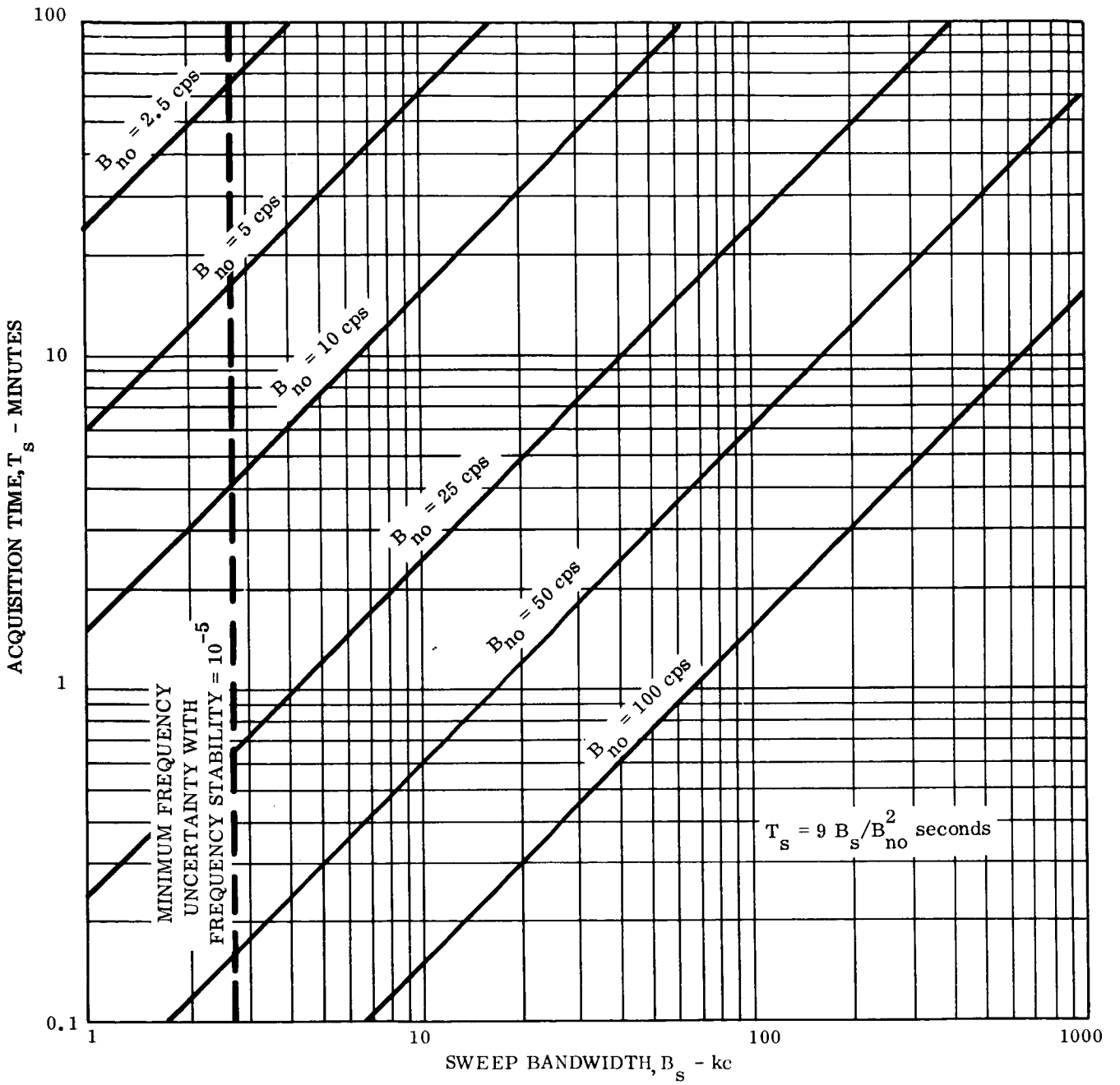

Figure 10-24. Carrier Acquisition Time vs. Sweep Bandwidth for Available Tracking Filter Loop Bandwidth

reasonable for estimating the minimum loop bandwidth required to track an incoming signal which is changing frequency at a rate df/dt:

$$B_n \approx 20 \sqrt{(df/dt)/\sigma} \qquad (69)$$

where σ_o is the actual phase error in degrees. If this is taken to be 20 degrees, Equation 69 becomes:

$$B_n \approx \sqrt{7.07\ (df/dt)} \qquad (70)$$

which is slightly less than that given by Equation 66 for acquisition.* This has been plotted in Figure 10-25 for the range of Doppler rates of interest.

The graph indicates that the 25 cycle per second tracking loop bandwidth chosen on the basis of acquisition time will be adequate for tracking the circular orbits, but to handle the elliptical orbit at perigee, the loop would have to be opened up to 50 cycles per second.

C. Carrier Power Requirements

The carrier power required will be proportional to the noise bandwidth, $B_{no,}$ of the loop. Depending upon the use for which the loop output is to be used (e.g., Doppler tracking, data demodulation, etc.), a minimum carrier-to-noise ratio is usually established, below which the output of the loop becomes too noisy to be useful.

*It is difficult to compare the two empirical relationships, since Equation 70 is based on 20 degrees actual phase error, while Equation 66 is based on 20 degree calculated phase error.

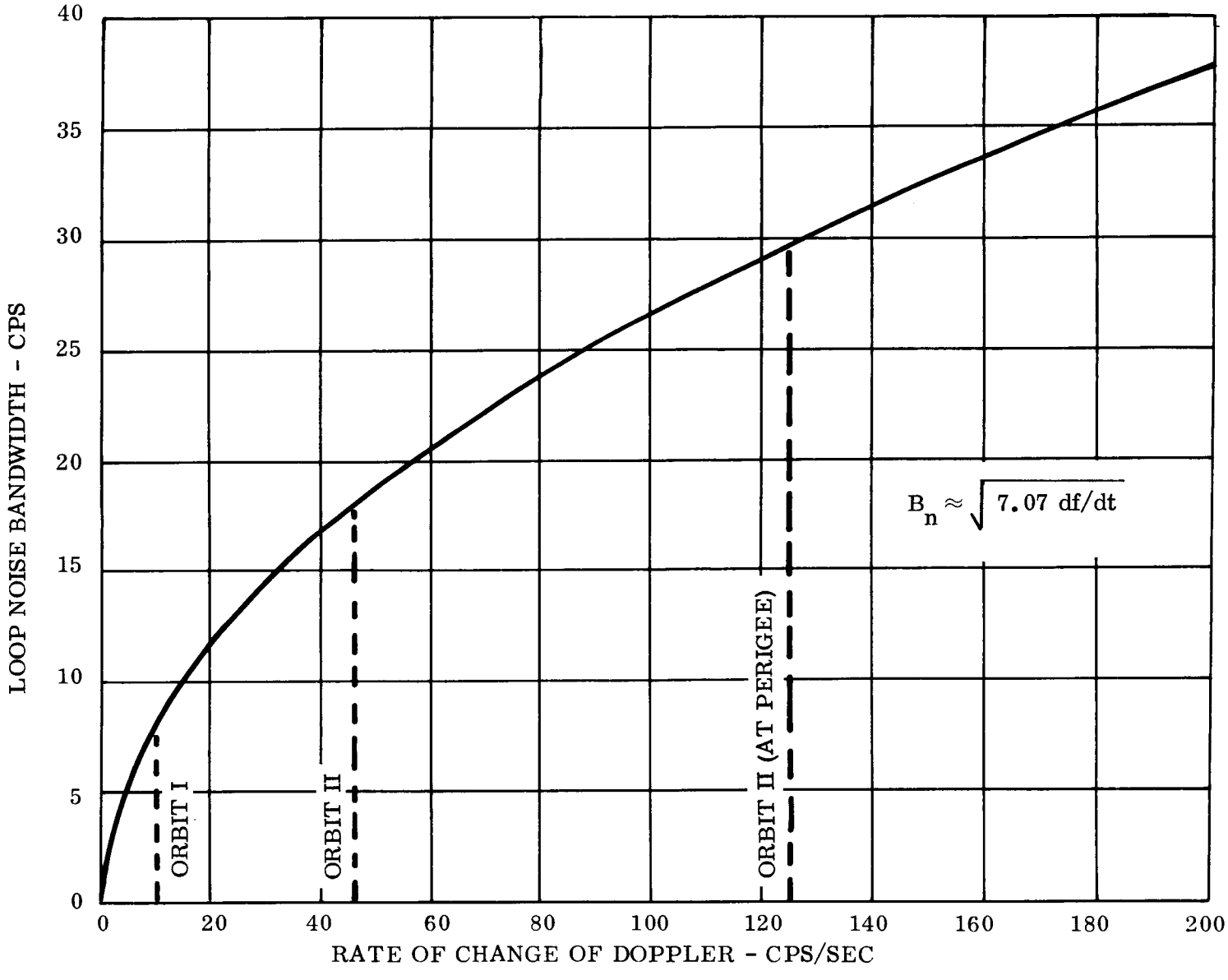

Figure 10-25. Required Tracking Loop Bandwidth vs. Doppler Rate (20-Degree Phase Error)

For tracking and acquisition it has been assumed that no more than a 20-degree rms phase error will be allowed, and the C/N ratio must be adequate to provide this. The specifications on the Electrac Phase-Lock Demodulator in use at the STADAN ground stations indicate that it requires a 9 db C/N ratio for 20 degrees phase error; while the specifications on the Interstate Tracking Filter indicate that it requires a 12 db C/N ratio. These values will be used in order that the tracking requirement may be met. They should more than satisfy the acquisition requirement.

For the assumed receiving system noise temperature of 1820^{o}K and the C/N ratios indicated above, Table 10-8 shows the minimum carrier power requirements for the tracking filter and the phase-lock demodulator for each of the loop bandwidths available.* These carrier levels establish a lower bound on the satellite transmitter power requirement, regardless of how low the data rate is.

Table 10-8. Carrier Power Requirements for Tracking Filter and PL Demodulator

Loop Bandwidth (cps)	Carrier Power Required in dbw (zero margin)	
	Tracking Filter	PL Demodulator
2.5	-180.0	------
3	------	-182.2
5	-177.0	------
10	-174.0	-177.0
25	-170.0	------
30	------	-172.2
50	-167.0	------
100	-164.0	-167.0
300	------	-162.2

*It should be noted here that the available bandwidths on the Electrac PL Demodulator are not quite the same as those on the tracking filter. The PL Demodulator offers 3, 10, 30, 100 and 300 cps, instead of 2.5, 5, 10, 25, 50, and 100 cps.

10.6.4.8 Division of Power Between Carrier and Sidebands

In a phase-modulated signal the fraction of the total power which lies in the carrier is:

$$\frac{P_c}{P_T} = J_o^2 (\Phi) \qquad (71)$$

and the fraction of the total power which lies in the first sidebands is

$$\frac{P_s}{P_T} = 2 J_1^2 (\Phi) \qquad (72)$$

where J_o = the Bessel function of the first kind of zero order
J_1 = the Bessel function of the first kind of first order
Φ = the phase modulation index (in radians).

As a slightly conservative estimate it will be assumed that the small fraction of the power which lies in the higher sidebands is not recovered.

Practical factors in the phase detector usually limit the maximum value of the modulation index to $\Phi \leq 1.4$ radians. This establishes the maximum fraction of the power which can be put into the sidebands. For reasonably high data rates this limit usually leaves ample carrier power, since the total power is then determined by the sideband power requirements of the data. However, at low data rates the carrier power requirements become important, and the modulation index must be reduced from 1.4 radians in order to provide a better balance between carrier power and sideband power.

The modulation index restriction thus shows the bounds on the carrier and sideband powers to be, respectively:

$$0.33 \leq P_c/P_T \leq 1.0 \tag{73}$$

and

$$0.0 \leq P_s/P_T \leq 0.59. \tag{74}$$

The ratios P_c/P_T and P_s/P_T are sometimes referred to as the carrier and subcarrier suppression factors, respectively.

10.6.4.9 Non-Coherent Reception

It is, of course, possible to omit the tracking filter at the ground receiver and feed the IF signal directly to an FM limiter/discriminator. If simultaneous Doppler tracking of the carrier frequency is not required (e.g., if a separate tracking beacon is used, or if it is possible to track while data are not being transmitted), then it is possible to modulate the carrier directly, using PCM/FM for example. This would eliminate the 0.59 subcarrier suppression factor and thus offer a saving in useful signal power of 2.3 db. Furthermore, no time would be required for carrier acquisition, which would be advantageous for short transmission periods.

However, the characteristics of an FM discriminator require at least a 12 db S/N ratio in the IF bandwidth in order to be above threshold. The IF bandwidth requirement (in cps) for the data is between 1.5 and 3.0 times the bit rate, and the minimum IF bandwidth of the Minitrack Mod. I receiver is 10 kilocycles. Therefore, unless the link has very little frequency uncertainty (due to Doppler and oscillator instability) and a rather high data rate, a considerable penalty in detection efficiency is paid by using noncoherent reception. Nevertheless, as will be shown in Section 10.6.6, there may be applications where non-coherent reception is advantageous.

10.6.4.10 Comparison of Modulation Techniques

The analysis in the preceding sections has offered a comparison of PCM/PSK, PCM/FSK, PCM/FM, and PFM on the basis of efficiency. The results are summarized in Table 10-9 and plotted in Figure 10-26.

Table 10-9. Theoretical Comparison of Modulation Efficiencies For Bit Error Probability = 10^{-5}

Modulation Technique	E/N_o
PCM/PSK	9.6 db
PCM/FSK	13.6 db
PCM/FM (IRIG Standards)	14.8 db
PCM Saving Possible through (73,45) Bose-Chaudhuri Coding	(2.7 db)
PFM (64 levels)	4.3 db
Shannon Theoretical Limit	-1.6 db

PCM/PSK has been shown to be quite efficient and is used for deep space communication. However, it must be eliminated because it requires a synchronous receiver (at the subcarrier frequency), and no plans are known for adding these to the existing STADAN ground station facilities.

PCM/FSK must be eliminated because of spectral incompatibility with IRIG standards.

Although PFM is the most efficient of the four techniques analyzed, it is more extravagant than PCM/FM in its use of RF spectrum. PFM is based on the use of a set of time-limited sine functions having orthonormal properties. Rochelle (Reference 10-16) has pointed out that the smallest allowed separation in frequency between any two members of a set of orthonormal frequencies is the reciprocal of twice the word length. As a practical example, a pulsed sine wave of 10-millisecond duration has zeros of its cross-correlation with other

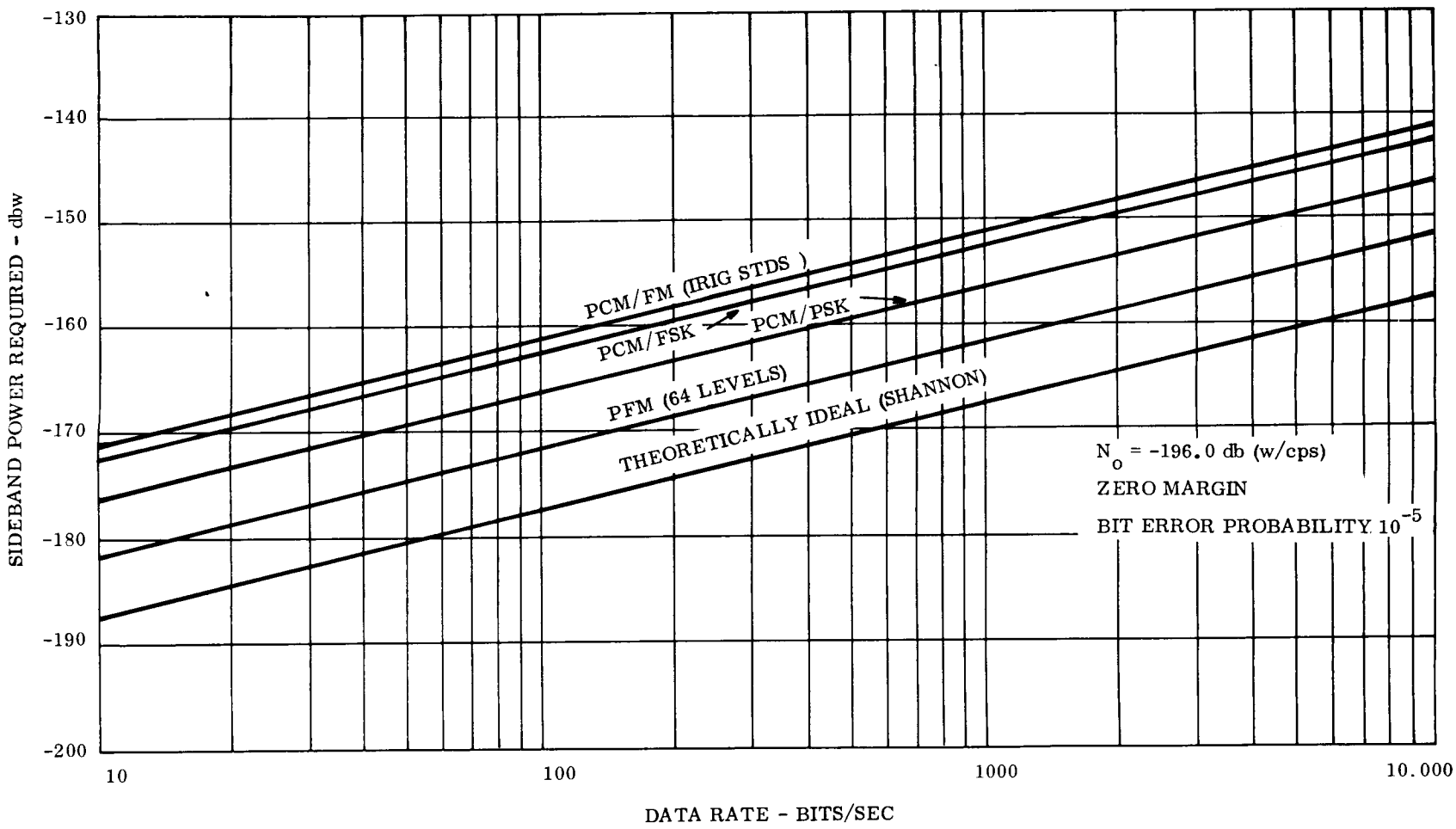

Figure 10-26. Sideband Power Required At Ground Receiver vs. Data Rate for PFM and PCM Systems

frequencies at multiples of 50 cycles per second away. Six-bit encoding accuracy requires 2^6 = 64 tones. A 10-millisecond sampling interval allows 100 samples per second, hence, 600 bits per second. With PFM this requires a bandwidth of 64 x 50 = 3200 cycles per second. A comparable PCM/FM system would require a bandwidth of only 1.5 x 600 = 900 cycles per second. Thus, for six-bit accuracy it appears that PFM occupies more than 3 1/2 times the bandwidth of PCM/FM. At very low data rates, such as those used with small satellites, this is insignificant, but it becomes increasingly important as the data rates increase.

Another difficulty with PFM lies in the fact that (in this example) $2^n - 1 = 63$ filter output comparisons must be made in each sample period. For sampling periods of 10-milliseconds duration this requires 6300 comparisons every second. A PCM signal requires only one comparison per bit, or 600 comparisons per second in this example. Thus the PFM system (for six-bit accuracy) will require over ten times as many comparisons as the PCM system does at the ground station. This poses a synchronization problem and could place an excessive burden in computation time on the ground stations in a high data rate system.

Since the data rates in this mission may become high, and satellite weight is not a critical item, PFM will not be recommended at this time.

Such reasoning leaves PCM/FM as the recommended modulation technique for this mission, with the option of employing a medium redundancy error-correcting code to provide a 2.7-db improvement if it should become necessary.

10.6.5 DETAILED ANALYSIS OF PCM/FM CAPABILITIES

10.6.5.1 PCM/FM/PM Sideband Power Requirements

The calculation of the power required in the data subcarrier channel is shown in Table 10-10.

Table 10-10. Calculation of Required Sideband Power for PCM/FM/PM

Noise Spectral Density ($T_e \approx 1820^{\circ}K$)	-196.0 db (w/cps)
Subcarrier IF Bandwidth* (1.5 times bit rate)	+1.8 + 10 log R db (cps)
Noise in Subcarrier Channel	-194.2 + 10 log R dbw
Required S/N Ratio: (for $P_e = 10^{-5}$)	+13 db
Required Power in Subcarrier Channel	-181.2 + 10 log R dbw

For a phase modulation index of $\Phi = 1.4$ radians, the subcarrier suppression factor is

$$2 J_1^2 (1.4) = 0.59 = -2.3 \text{ db.} \tag{75}$$

Therefore the total power required at the receiver (due to the data requirements) is

$$P_R = 10 \log R - 178.9 \text{ dbw} \quad \text{(plus approx. 8 db margin).} \tag{76}$$

The total power available at the ground receiver is**

$$P_A = -20 \log s - 64.4 \text{ dbw per watt ERP} \tag{77}$$

Setting P_R + margin = P_A now permits a solution for the data rate capability as a function of range to the satellite:

$$-20 \log s - 64.4 = 10 \log R - 179.8 + 8.0 \tag{78}$$

$$10 \log R = 106.5 - 20 \log s \tag{79}$$

$$R = \frac{4.5 \times 10^{10}}{s^2} \text{ bits/sec} \tag{80}$$

*Minimum possible. May be further limited by actual subcarrier discriminator in use.
**See Table 10-7.

per watt ERP, where s is in nautical miles. This has been plotted in Figure 10-27.

10.6.5.2 PCM/FM/PM Carrier Power Requirements

Equation 77 shows the total power available at the ground receiver. Section 10.6.4.8 showed that the maximum carrier suppression factor to be used is

$$J_o^2 (1.4) = 0.33 = -4.8 \text{ db} \tag{81}$$

Therefore, adding 4.8 db (plus 8 db margin) to the carrier power requirements given in Table 10-8 indicates the total power required at the receiver due to the carrier power requirements. Setting this equal to the available power, P_A, (given by Equation 77) allows a solution for the maximum range to the satellite at which carrier lock can be maintained. This has been indicated in Figure 10-25 for the 25 and 100 cycles per second loop noise bandwidths.

For lower data rates the modulation index can be reduced below 1.4 to provide more carrier power. Moreover, at the higher altitudes the Doppler rate is quite low, so a narrow tracking loop bandwidth can be employed to reduce the carrier power requirements.

Figure 10-25 provides a convenient working tool for any orbit. It can be used by selecting the maximum communications distance of the satellite link and then adjusting the ERP to provide the required data rate.

10.6.5.3 Non-Coherent Reception of PCM/FM

For comparison purposes, non-coherent detection of PCM/FM directly modulating the carrier* would require at least a 12 db S/N ratio in the predection bandwidth (10 kilocycles or more). Thus the minimum required power (at low data rates) becomes

$$P_R = -196 + 12 + 40 \text{ dbw (plus approx. 8 db margin)} = -136.0 \text{ dbw.} \tag{82}$$

*As described in Section 10.6.4.9.

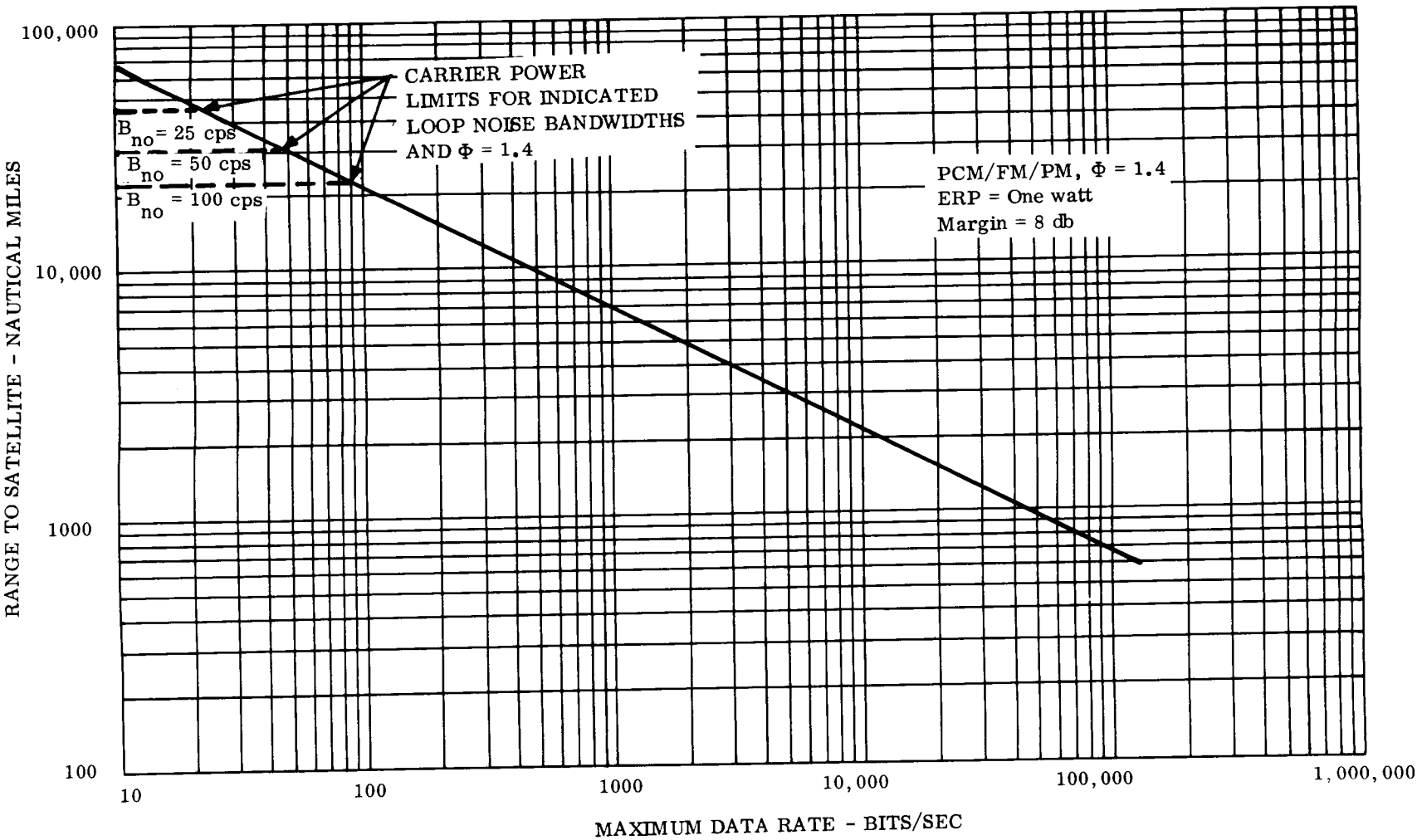

Figure 10-27. Maximum Data Rate vs. Range to Satellite

The available power is given by Equation 77. Equating this to the minimum required power shows the maximum range (for one watt ERP) at which non-coherent reception is feasible.

$$-20 \log s - 64.4 = -136.0 \text{ dbw} \tag{83}$$

$$s_{max} = 10^{3.6} = 4000 \text{ nautical miles (for one watt ERP)} \tag{84}$$

The data rates available using the 10, 30, and 100-kilocycle predetection bandwidths for the three orbits under consideration are determined in Table 10-11 and plotted along with those for other orbits in Figure 10-28. This graph will be used in Section 10.6.6 to determine the required effective radiated power for non-coherent PCM/FM for the three orbits. The method involves setting the effective radiated power equal to the square of the ratio of the maximum communications distance to the threshold range, using the smallest available receiver bandwidth to the right of the desired data rate.

10.6.6 RESULTS OF TELEMETRY LINK ANALYSIS

The analysis in the preceding sections has offered a comparison of PCM/PSK, PCM/FSK, PCM/FM, and PFM. The conclusion has been reached that PFM is the most efficient of the four techniques but for other than low data rates uses excessive bandwidth and may impose a burden on the ground station demodulators. PCM/PSK was eliminated because of incompatibility with existing ground receivers, and PCM/FSK was eliminated because of incompatibility with IRIG standards. This left PCM/FM as the recommended modulation technique for this mission.

Noncoherent reception was shown to be generally inefficient for moderate data rates, so it is recommended for the circular orbits that the PCM/FM signal be placed on an appropriate subcarrier which phase modulates the telemetry carrier, using a modulation index not to exceed 1.4. This has the added advantage of allowing simultaneous Doppler tracking by means of the telemetry carrier.

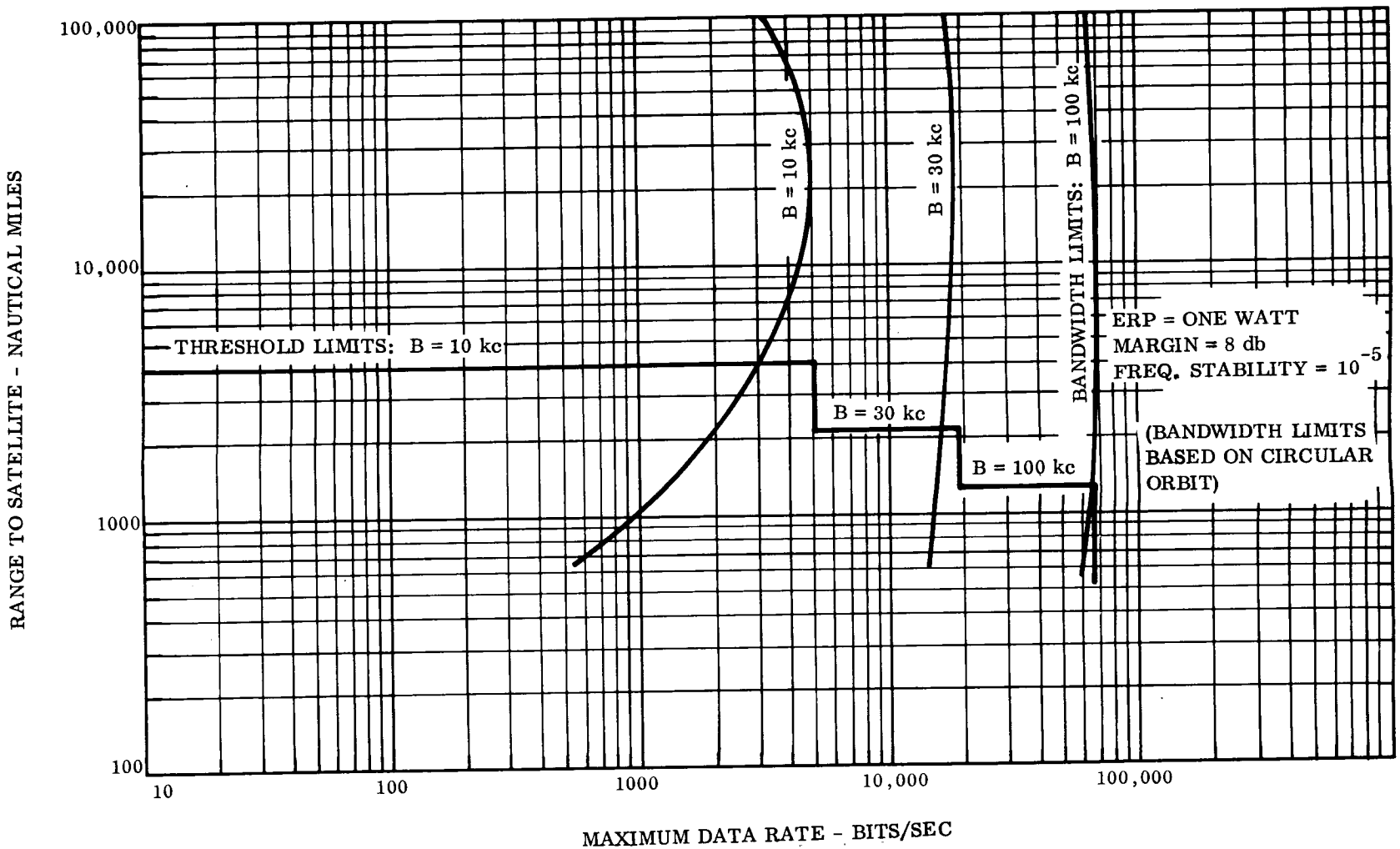

Figure 10-28. Receiver Threshold and Bandwidth Limits for Non-Coherent PCM/FM

Table 10-11. Determination of Noncoherent PCM/FM Capabilities

ITEM		ORBIT I (1000 NM)	ORBIT II (elliptical)	ORBIT III (325 NM)
Maximum Doppler (cps)		±2340	±4370	±3070
Oscillator Instability (10^{-5})[a]		±1360	±1360	±1360
Frequency Uncertainty (cps)		7400	11,460	8860
Bandwidth Available for Data (1.5 R)	B = 10 kc	2600	0	1140
	B = 30 kc	22,600	18,540	21,140
	B = 100 kc	92,600	88,540	91,140
Available Data Rate (R) (bits/second)	B = 10 kc	1740	0	760
	B = 30 kc	15,100	12,500	14,100
	B = 100 kc	62,000	59,000	61,000
Threshold Power Requirement	B = 10 kc		-136.0 dbw	
	B = 30 kc		-131.2 dbw	
	B = 100 kc		-126.0 dbw	
Maximum Range for one watt ERP (as in Equation 84)	B = 10 kc		4000 NM	
	B = 30 kc		2300 NM	
	B = 100 kc		1260 NM	
Maximum Communications Distance (NM)		1950	perigee: 600	830
Effective Radiated Power Required (mw)	B = 10 kc	240	------	43
	B = 30 kc	720	68	129
	B = 100 kc	2400	227	430

Note

a. This stability may be slightly optimistic if operation over a wide temperature range is required. Off-the-shelf PM transmitters typically have 5 X 10^{-5} stability over a temperature range of -20° to +60°C. However, they provide 5 X 10^{-6} over a limited temperature range.

However, noncoherent reception is attractive for communication from the highly elliptical orbit at perigee, where the large amount of data recorded during the long orbital period must be transmitted during a very short line-of-sight time near perigee. This requires a high data rate and a minimum acquisition time. Since a separate range and range-rate transponder will probably be used for accurate tracking in the elliptical orbit, no separate telemetry carrier requirement exists for the tracking function.

It was found that a 25-cycle per second loop bandwidth should be adequate for carrier tracking in all cases except for the elliptical orbit at perigee, where 50 cycle per second would be necessary. The 25-cycle per second bandwidth also allows acquisition in less than one minute, assuming some a priori knowledge of expected Doppler characteristics.

It was also found that a typical medium redundancy error-correcting code could offer about 2.7 db advantage where the bit error probability is 10^{-5} or less. Although entirely feasible, the modest transmitter power requirements and a low duty cycles do not indicate a strong requirement for such increased efficiency. Therefore, it is recommended that coding be held in reserve as a solution in case subsequent plans show a need for a higher data rate or a reduction in prime power.

Table 10-7 shows the received telemetry power per watt of satellite effective radiated power. Figure 10-26 shows the sideband power requirements for the modulation techniques which were analyzed, and Equation 74 indicates that a maximum of 59 percent of the total transmitter power may be placed in the sidebands. Figure 10-27 has been plotted, using data from these two graphs. It shows the data rates possible per watt of effective radiated power, as a function of the range to the satellite.

Comparison of Figure 10-27 with Figure 10-28 shows that for data rates below approximately 2000 bits per second a significant saving in transmitter power is possible by using coherent carrier demodulation. At higher data rates the frequency uncertainty becomes a smaller fraction of the receiver IF bandwidth, and the advantage of coherent carrier demodulation is reduced.

Using Figures 10-27 and 10-28 in the manner described in Section 10.6.5, the required effective radiated power for each of the three orbits has been determined and plotted in Figures 10-29, 10-30, and 10-31 as a function of data rate, for both PCM/FM/PM and non-coherent PCM/FM.

Once the data rate requirements have been established for each of the three orbits, these figures may be used to determine the required effective radiated power. The remaining step will be to make the trade-off of transmitter power versus antenna gain to provide the required effective radiated power. The antenna gain realizable will be limited by the actual configuration of the satellite.

At the high data rates to be used in these links, bit synchronization will not be a problem. The assignment of one or two words per frame as frame synchronization signals (e.g., Barker Words) should provide an adequate basis from which bit synchronization can be referenced.

10.7 ANALYSIS OF TRACKING LINKS

10.7.1 MINITRACK TRACKING ANALYSIS

Typical calculations for a 136-megacycle Minitrack tracking link are shown in Table 10-12 for one watt of effective radiated power. This tracking signal may be provided either by a separate beacon or by the telemetry carrier. The required S/N ratios were taken from those of the tracking filter listed in Table 10-8.

As described in Section 10.3.4, fixed ground antennas are used for Minitrack tracking. These are aligned along baselines in both the east-west and north-south direction. The radiation pattern is fan-shaped, and the polarization is linear and perpendicular to the long dimension of the antenna. Minimum elevation angles of 52 degrees and 37 degrees, respectively, have been assumed for the "fine" and "ambiguity" antennas, corresponding to the

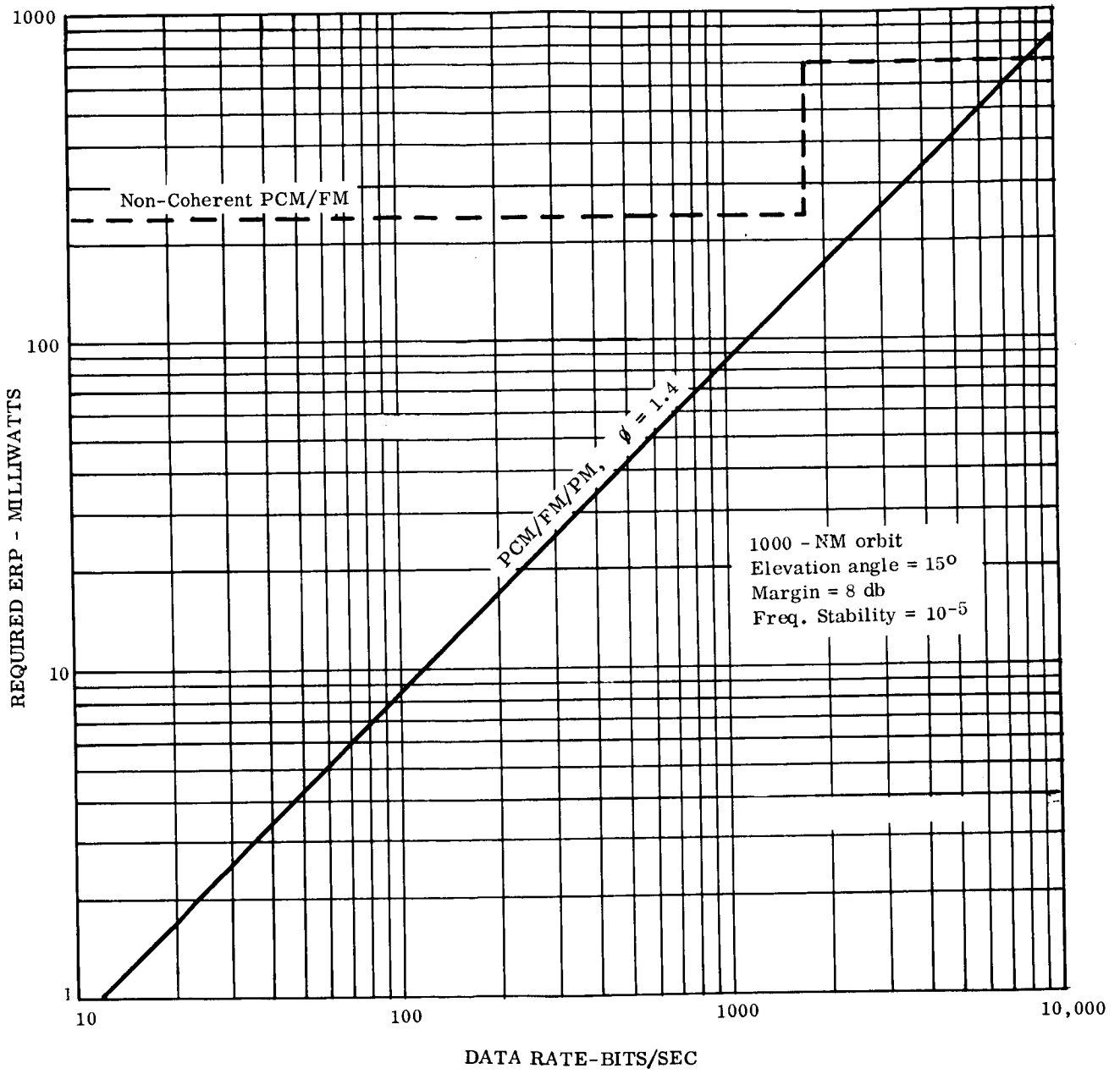

Figure 10-29. Required Effective Radiated Power vs. Data Rate for Orbit I

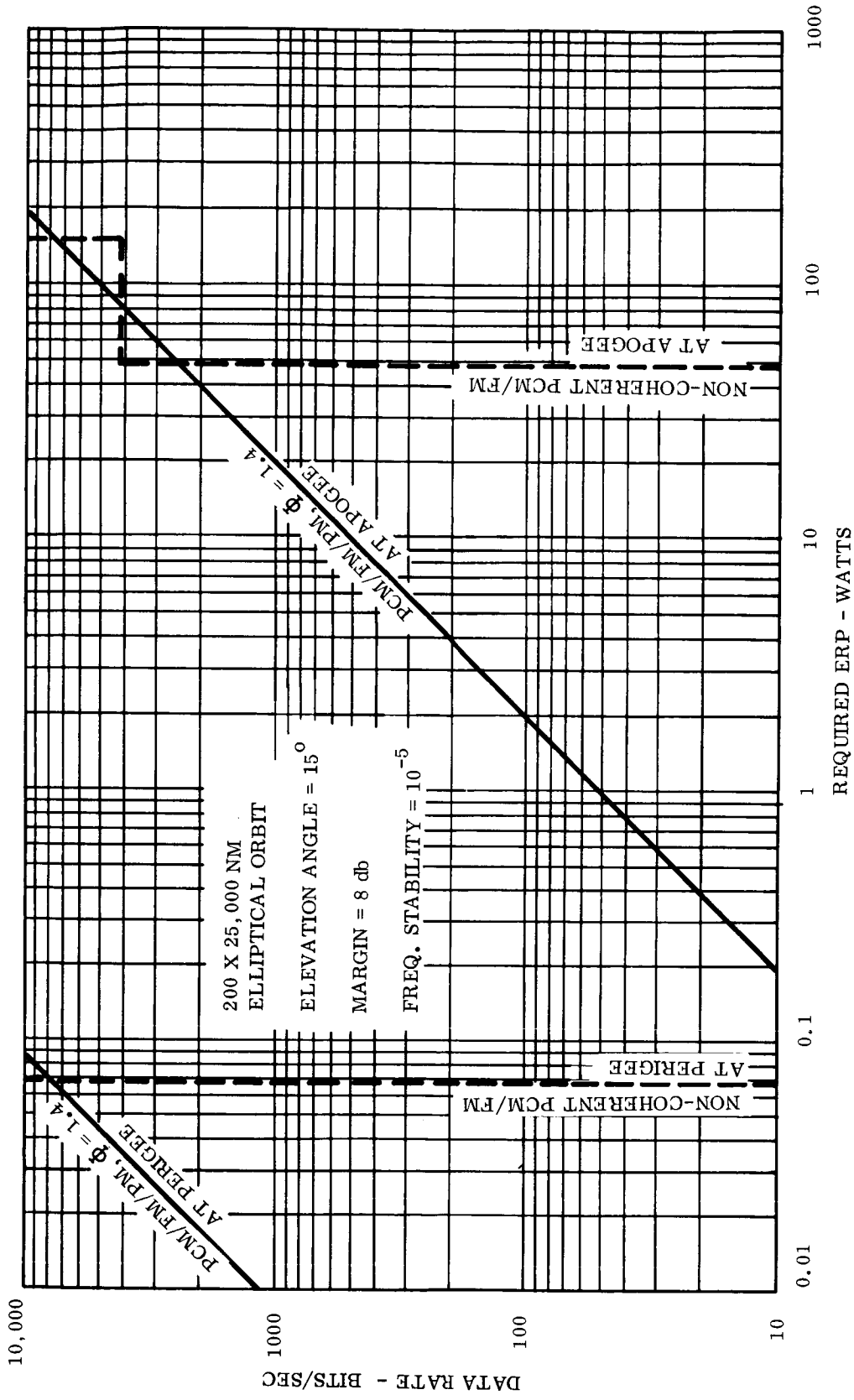

Figure 10-30. Required Effective Radiated Power vs. Data Rate for Orbit II

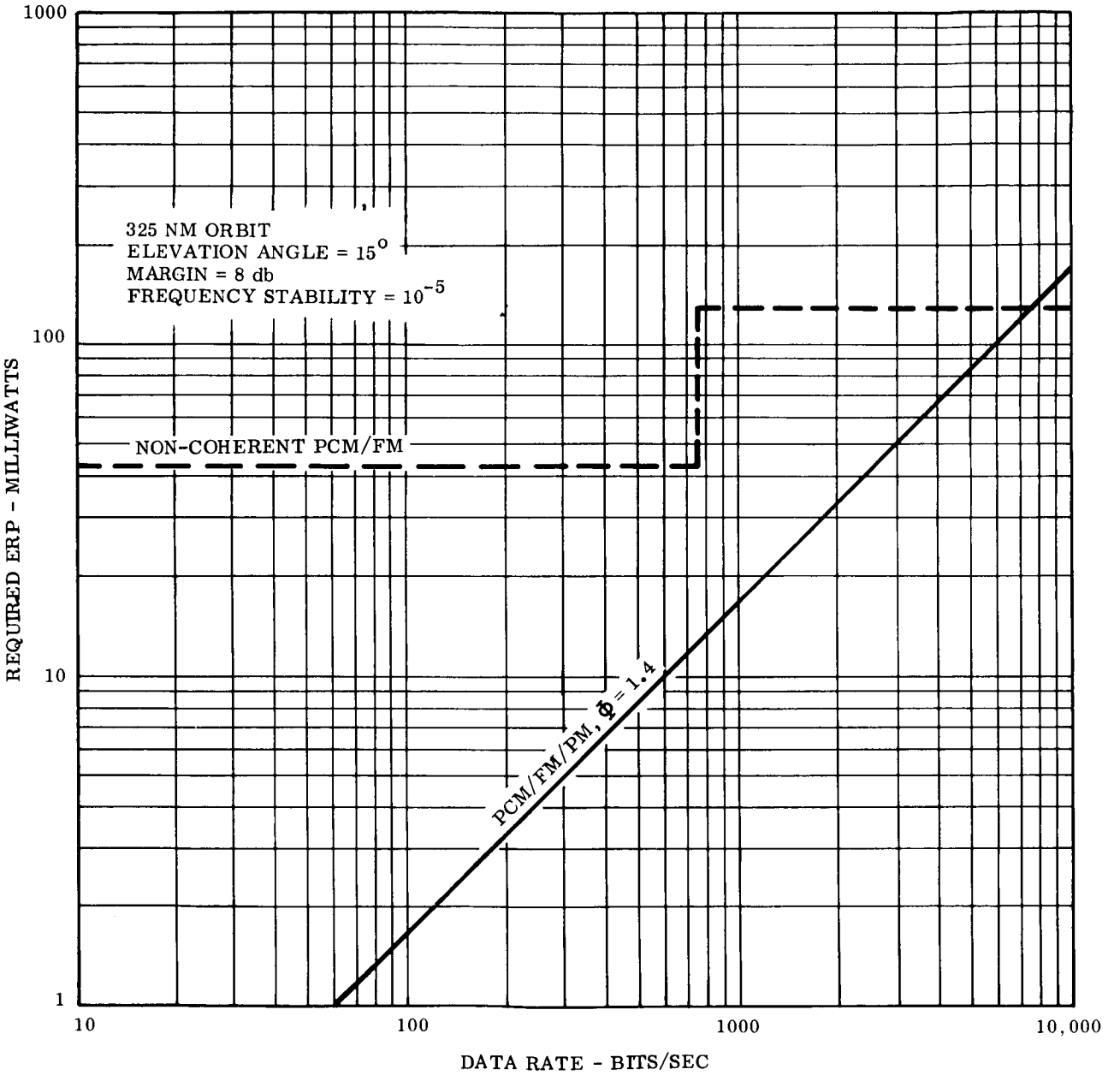

Figure 10-31. Required Effective Radiated Power vs. Data Rate for Orbit III

three-db points in the antenna patterns. The slant ranges corresponding to these elevation angles have been used (Equation 11), and the specified antenna gains have accordingly been reduced by three db in the calculations.

Since the ground antennas are linearly polarized, a polarization mismatch loss of three db has been included. This corresponds to circular polarization on the satellite and linear on the ground which might be optimistic. If, instead, the wave should arrive at the ground linearly polarized, there will be no degree of certainty that tracking can be performed satisfactorily on every pass over a ground station.* Because of this situation, considerable thought must be given to the placement of the satellite antenna and the orientation technique.

Table 10-12. Typical Minitrack Tracking Link Calculations

	Fine Antenna	Ambiguity Antenna	
Tracking Signal ERP (one watt)	+ 0.0	+ 0.0	dbw
Free-Space Attenuation (s NM, 136 mc)	-20 log s -80.4	-20 log s -80.4	db
Polarization Mismatch	- 3.0	- 3.0	db
Miscellaneous RF Losses	- 3.0	- 3.0	db
Ground Antenna Gain (at -3 db point)	+12.6	+ 3.5	db
Tracking Signal Available at Ground Receiver	-20 log s -73.8	-20 log s -82.9	dbw
	Loop Noise Bandwidth		
	B_{no} = 25 cps	B_{no} = 50 cps	
Threshold Tracking Signal	-170.0	-167.0	dbw
Design Margin	+ 8.0	+ 8.0	db
Tracking Signal Required at Ground Receiver	-162.0	-159.0	dbw

* However, the situation is better than it was a few years ago, because all but three of the Minitrack stations now generate east-west as well as north-south fan beams. Since the polarization is perpendicular to the long dimension of the antenna, this gives some degree of polarization diversity, although it will not, of course, handle a vertically polarized wave.

Equating the available power to the required power (including 8 db margin) allows a solution for the maximum tracking range (for one watt ERP). For example:

$$-20 \log s - 73.8 = 162.0 \text{ dbw} \tag{85}$$

$$s_{max} = 10^{4.4} = 25{,}000 \text{ NM} \tag{86}$$

with the fine antenna

and

$$-20 \log s - 82.9 = -162.0 \text{ dbw} \tag{87}$$

$$s_{max} = 10^{3.95} = 8900 \text{ NM} \tag{88}$$

with the ambiguity antenna

Using Equations 8 and 11, the maximum tracking altitudes corresponding to these slant ranges have been plotted in Figure 10-32 as a function of tracking signal effective radiated power for 25 and 50 cycle per second tracking loop bandwidths. Of course, at the higher orbital altitudes the rate of change of Doppler is lower, and a narrower loop bandwidth can be used, if the long acquisition time can be tolerated. Figures 10-14, 10-24, and 10-25 should be useful in establishing the minimum tracking loop bandwidth for other orbits.

Figure 10-32 indicates that for Orbit I approximately 27 milliwatts of effective radiated power will be required, while for Orbit III about 5 milliwatts of effective radiated power will be required (using a 25 cps loop bandwidth). Due to the high eccentricity of Orbit II, a range and range-rate tracking system is recommended. This will be covered in the next section.

10.7.2 RANGE AND RANGE-RATE TRACKING ANALYSIS

A brief description of the Goddard Range and Range-Rate (R&RR) Tracking System was given in Section 10.3.5. Link calculations for VHF and S-Band R&RR tracking are shown in Tables 10-13 and 10-14, respectively.

Just as in the preceding section, equating the available power to the receiver sensitivity (plus 8 db margin) allows a solution for the maximum tracking range (for one watt ERP). The maximum tracking range* has been plotted in Figures 10-33 and 10-34 as a function of the satellite effective radiated power. Ground-to-satellite link limitations and the point at which current equipment operates are indicated.

The graphs indicate that the existing VHF equipment should be adequate for tracking the Orbit II satellite all the way out to its maximum slant range of 27,800 nautical miles.

Table 10-13. VHF R&RR Tracking Link Calculations

Ground-to-Satellite Link (148 mc)	
Transmitter Power (10 kw)	+40.0 dbw
Ground Antenna Gain	+20.0 db
Free-Space Attenuation (s NM, 148 mc)	-20 log s - 81.2 db
Polarization Mismatch Loss	- 3.0 db
Miscellaneous RF Losses	- 3.0 db
Satellite Antenna Gain (minimum over more than 90% of the pattern)	-10.0 db
Tracking Signal Available at Satellite Receiver:	-20 log s -27.2 dbw
Transponder Sensitivity (Reference 10-28) : -145.0 dbw	
Satellite-to-Ground Link (136 mc)	
Tracking Signal ERP (one watt)	+ 0.0 dbw
Free-Space Attenuation (s NM, 136 mc)	-20 log s -67.4 db
Polarization Mismatch	- 3.0 db
Miscellaneous RF Losses	- 3.0 db
Ground Antenna Gain	+19.0 db
Tracking Signal Available at Ground Receiver:	-20 log s - 80.4 db
Ground Receiver Sensitivity (Reference 10-29) :-174.0 dbw	

*Slant range has been used here rather than orbital altitudes so that the curve will be more useful with elliptical orbits.

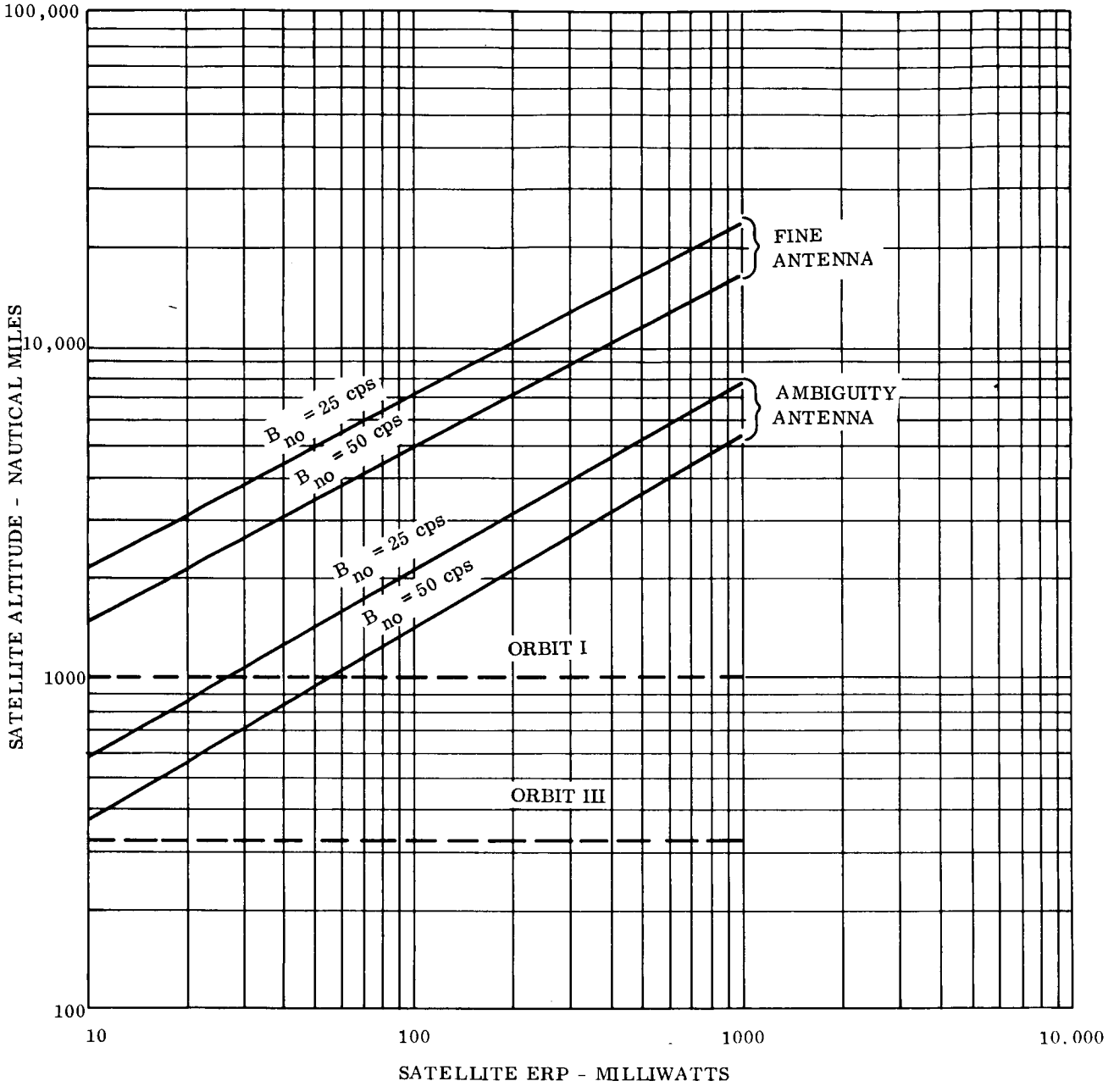

Figure 10-32. Maximum Orbital Altitude vs. Satellite Effective Radiated Power for Minitrack Tracking (8 db Margin)

Table 10-14. S-Band R&RR Tracking Link Calculations

Ground-to Satellite Link (2271 mc)		
Transmitter Power (10 kw)		+40.0 dbw
Ground Antenna Gain		+35.0 db
Free-space Attenuation (s NM, 2271 mc)	-20 log s	+104.9 db
Polarization Mismatch Loss		- 3.0 db
Miscellaneous RF Losses		- 3.0 db
Satellite Antenna Gain (minimum over more than 90% of the pattern)		-10.0 db
Tracking Signal Available at Satellite Receiver:	-20 log s	-45.9 dbw
Transponder Sensitivity (Reference 10-29) : -135.0 dbw[a].		
Satellite-to-Ground link (1705 mc)		
Tracking Signal ERP (one watt)		+ 0.0 dbw
Free-space Attenuation (s NM, 1705 mc)	-20 log s	-102.4 db
Polarization Mismatch		- 3.0 db
Miscellaneous RF Losses		- 3.0 db
Ground Antenna Gain		+33.0 db
Tracking Signal Available at Ground Receiver:	-20 log s	-75.4 dbw
Ground Receiver Sensitivity (Reference 10-29) : -178.0 dbw		

Note

a. A program is currently underway to improve the transponder sensitivity to -140 dbw (Reference 10-29).

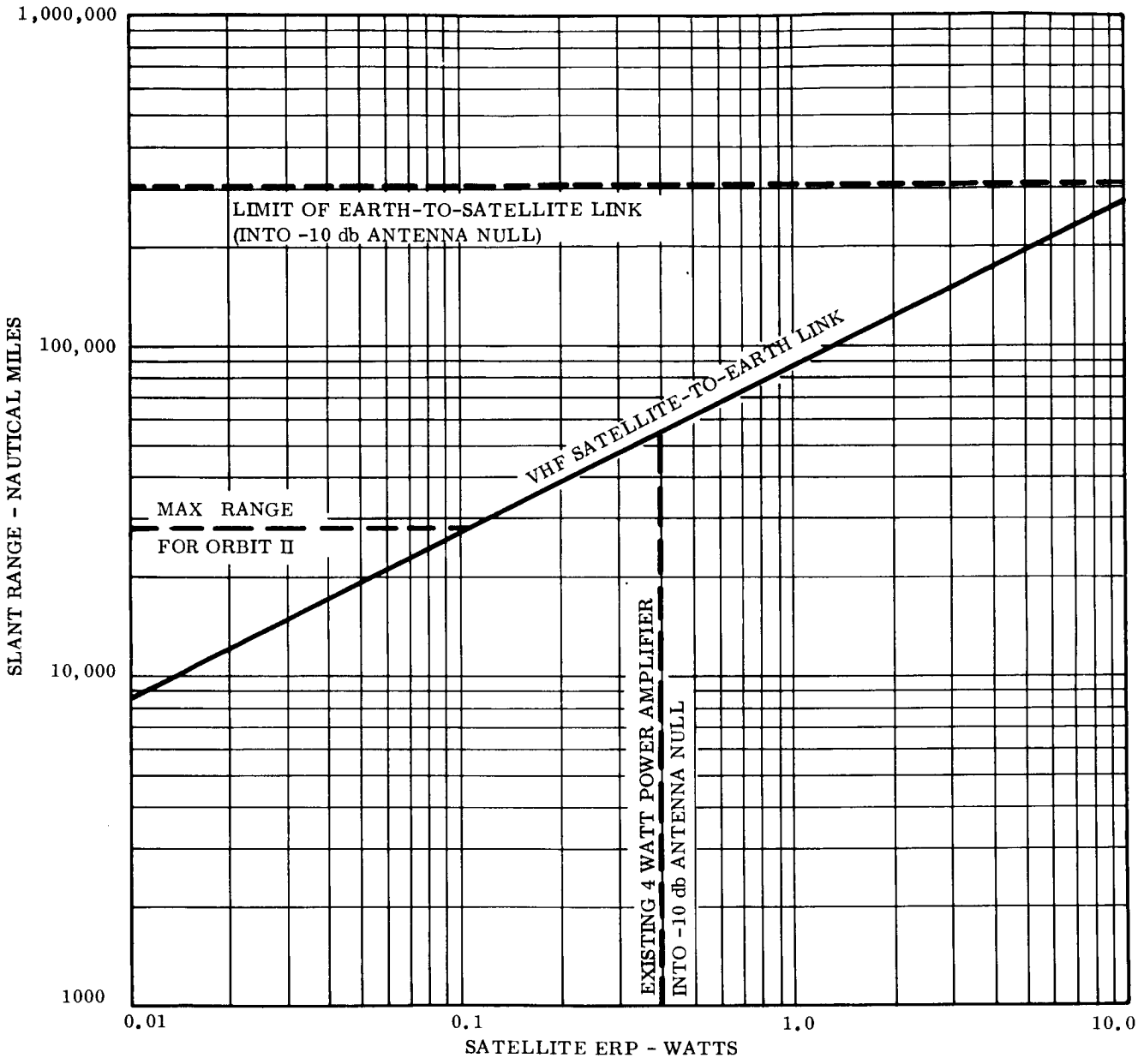

Figure 10-33. Maximum Tracking Range vs. Satellite Effective Radiated Power for VHF Range and Range Rate Tracking (8 db Margin)

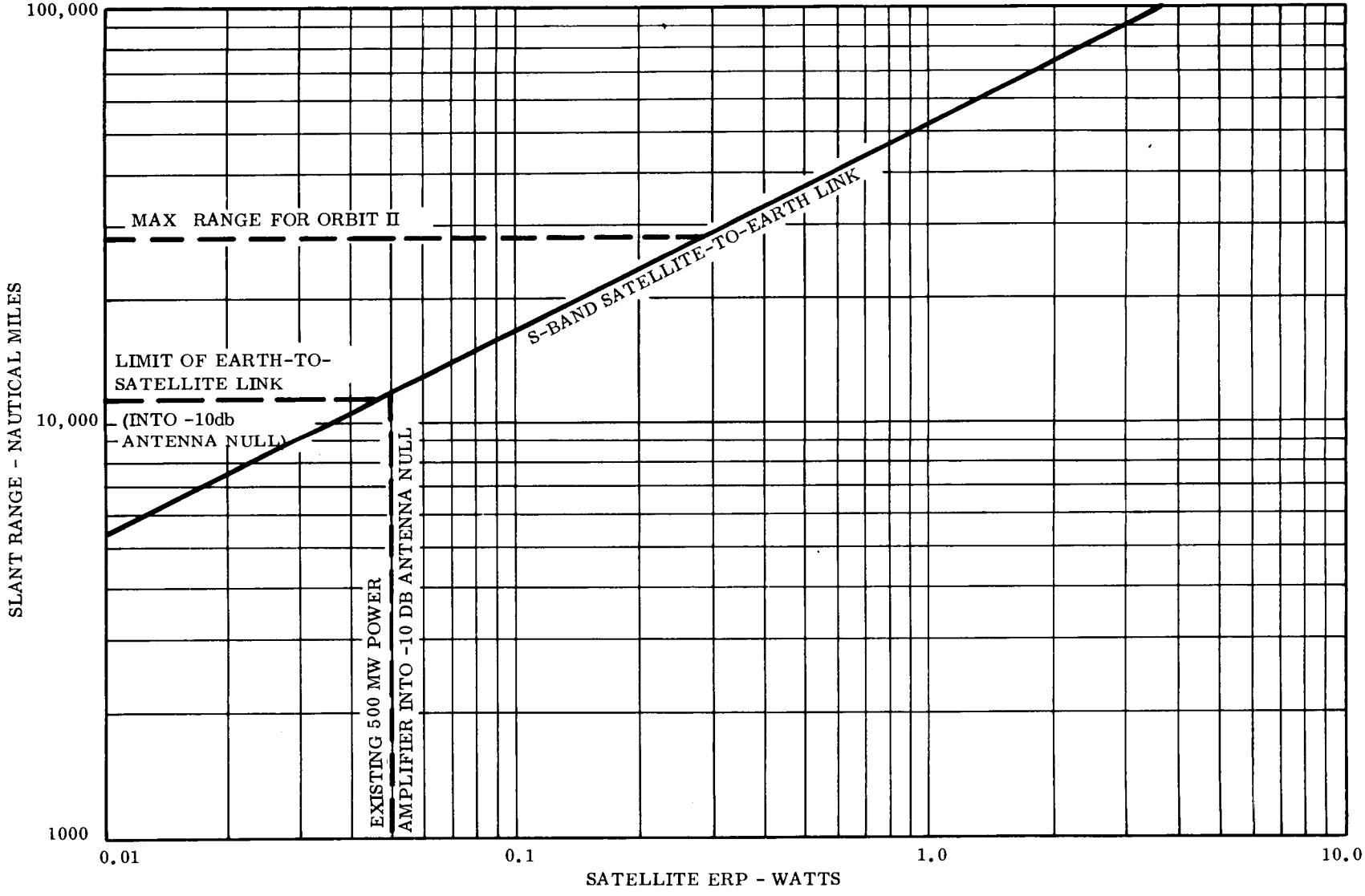

Figure 10-34. Maximum Tracking Range vs. Satellite Effective Radiated Power for S-Band Range-Rate Tracking (8 db Margin)

10.8 ANALYSIS OF COMMAND LINK

A brief description of the STADAN command system was given in Section 10.3.6. More details are contained in Appendix M.

Table 10-15 shows the calculations for a 150-megacycle STADAN command link. Equating the available command signal to the receiver sensitivity (plus 8 db margin) allows a solution for the maximum slant range at which the satellite can be commanded with confidence:

$$-20 \log s - 61.3 = 131.0 + 8.0 \quad (89)$$

$$20 \log s = 61.7 \quad (90)$$

whence,

$$s = 10^{3.085} = 1220 \text{ NM} \quad (91)$$

Table 10-6 shows that the maximum slant range for Orbit I is 1950 nautical miles; that for Orbit II is 27,800 nautical miles (at apogee); while that for Orbit III is 830 nautical miles. Thus it appears that a command link operating under the assumptions listed in Table 10-15 would be wholly satisfactory only for Orbit III. However, there are ways around this problem for the other two orbits.

Five-kilowatt transmitters (General Electric 4BT91A1) are being installed at all stations equipped with 40 or 85-foot parabolic antennas. Broadband high-power command antennas are also being installed, consisting of a disk-on-rod array having a gain of 22.5 db (Reference 10-1). Thus, by using a five-kilowatt transmitter coupled to one of the new high-power command antennas, the available power can be increased by 23.5 db. Commands can then be transmitted with confidence at a slant range out to 18,200 nautical miles.

Table 10-15. Command Link Calculations

Transmitter Power (Collins 242G-2, 200 watts, AM)		+23.0	dbw
Ground Antenna Gain (YGC1-1A/136-8S)		+13.0	db
Free-space Attenuation (s NM, 150 mc)	-20 log s	-81.3	db
Satellite Antenna Gain (minimum over more than 90% of the pattern)		-10.0	db
Polarization Mismatch Loss		- 3.0	db
Miscellaneous RF Losses		- 3.0	db
Command Signal Available at Satellite Receiver	-20 log s	-61.3	dbw
Receiver Sensitivity (2 microvolts across 50 ohms)	-131.0 dbw		

This modification should serve all three orbits quite satisfactorily. However, in the event that such equipment is not available at the sites chosen for this mission, the following possibilities exist:

a. Send commands only when the slant range permits, and store them all for delayed execution.

b. Reduce the depth of the antenna nulls from the -10 db used in the calculation.

c. Continuously command the satellite until a command is received satisfactorily, recognizing that the attitude of the satellite relative to the ground station will be continuously changing and that the deep nulls exist over only a small portion of the pattern.

d. Employ polarization diversity reception on the command receivers. This will eliminate the three-db polarization mismatch loss and extend the range by a factor of $\sqrt{2}$.

e. Arrange to relay commands in advance to a station which is equipped with a high-power transmitter.

10.9 DATA STORAGE AND TRANSMISSION REQUIREMENTS

Table 9-2 lists the amount of data collected from each sensor for each of the three orbits. The totals and their implications on the data storage and transmission requirements are summarized in Table 10-16. The transmitter effective radiated power requirements were obtained from Figures 10-29, 10-30, and 10-31.

10.10 SUMMARY OF RECOMMENDED TT&C SUBSYSTEMS AND THEIR CAPABILITIES

10.10.1 ORBIT I: 1000-NAUTICAL MILE CIRCULAR

The Orbit I satellite would collect 240,000 bits of data each orbit and would store these in eight magnetic core storage units (20 pounds of cores). After the orbit was well established, the tracking beacon would be turned off, and the telemetry carrier activated by command (either stored or real-time) to initiate the acquisition procedure.

Acquisition should be completed in less than two minutes, and the data would be read out upon command from either the Fairbanks or the St. John's ground station at a rate of 400 bits per second for ten minutes, using PCM/FM/PM.

Orbits where neither of these ground stations had a clear line-of-sight to the satellite would be extremely rare, and the loss of data on these orbits would be accepted.

10.10.2 ORBIT II: HIGHLY ELLIPTICAL

The Orbit II satellite would collect 800,000 bits of data each orbit and would store these in a magnetic tape recorder. A second tape recorder would be available as a spare and to

Table 10-16. Summary of Data Storage and Transmission Requirements

Orbit	Data Collected Per Orbit (bits)	Number of Orbits to be Stored	Total Data to be Stored (bits)	Number of Core Storage Units Required[a.]	Weight of Core Storage[b.] (lbs)	Data Transmission Time Per Orbit (min)	Transmitter Data Rate (bits/sec)	Required ERP (mw)
I	< 240,000	1	240,000	8	20	10	400	35
II	< 800,000	1	800,000	27	67.5[c.]		3340	70
		2	1,600,000	54	135[c.]	4	6680	70
III	< 150,000	1	150,000	5	12.5	2	1250	22
		2	300,000	10	25		2500	44

NOTES

a. Based on 30,000 bits per unit
b. Based on 2.5 pounds per unit
c. Weight limitations will require that a tape recorder be used instead of core storage.

provide storage for a second orbit of data on those occassions where a ground station was not available upon completion of an orbit.

Up to two orbits of stored data would be transmitted near perigee upon command to the Mojave, St. John's or Winkfield station at a rate of 6680 bits per second for four minutes, using PCM/FM and noncoherent reception. Frequency acquisition would not be necessary, and angular acquisition should be possible in less than one minute.

Because of the high eccentricity of this orbit, range and range-rate tracking would be employed for brief periods when the telemetry data are not being transmitted. More frequent tracking would be possible during the first few weeks before the solar cells have degraded and while surplus power is available.

10.10.3 ORBIT III: 325-NAUTICAL MILE CIRCULAR

The Orbit III satellite would collect 150,000 bits of data each orbit and would store up to two orbits of data in ten magnetic core storage units (25 pounds of cores).

It would be acquired in the same manner as the Orbit I satellite (in about two minutes), and the data would be read out upon command from the Fort Myers, Santiago, Lima, or Quito stations at a rate of 2500 bits per second for two minutes, using PCM/FM/PM.

Occasions where it would be necessary to go for more than two orbits without reading out the data would be extremely rare, and the loss of data on these occasions would be accepted.

10.11 TYPICAL SATELLITE TT&C EQUIPMENT

10.11.1 GENERAL CONFIGURATION

Figure 10-35 shows a functional block diagram of the TT&C Subsystem for all three missions.

Specific equipment details will vary somewhat for each mission. Components described in this report should be taken only as typical. In this preliminary study it has not been possible to apply any significant effort to the selection of specific components.

10.11.2 EQUIPMENT LISTS

Table 10-17 contains estimates of typical TT&C equipment for Orbit I, the 1000-nautical mile circular orbit. Table 10-18 contains estimates for Orbit II, the highly elliptical orbit. Table 10-19 contains estimates for Orbit III, the 325-nautical mile circular orbit.

The next phase of this program should include the establishment of detailed specifications for the equipment and the selection of suitable sources, based on such important criteria as capability, cost, reliability, flexibility, etc.

Some of the reasoning used and assumptions made in the selection and employment of these components are discussed in the following section. Section 10.11.4 contains a description of some typical components.

10.11.3 EQUIPMENT SELECTION DISCUSSION

A moderate amount of redundancy has been included in the equipment lists of the preceding section. Both command receivers and both decoders are powered continuously to guard against a command link failure. The spare magnetic tape recorder for the elliptical orbit mission has been included for use in the event of premature failure of this critical component. If both recorders are operative, the spare recorder may be used to accommodate data collection for a second orbit when necessary.

The tracking beacon has been included in the circular orbit satellites for early orbit determination. It will be used only during the first few weeks of the mission, and can utilize the excess power available from the solar cells during this period.

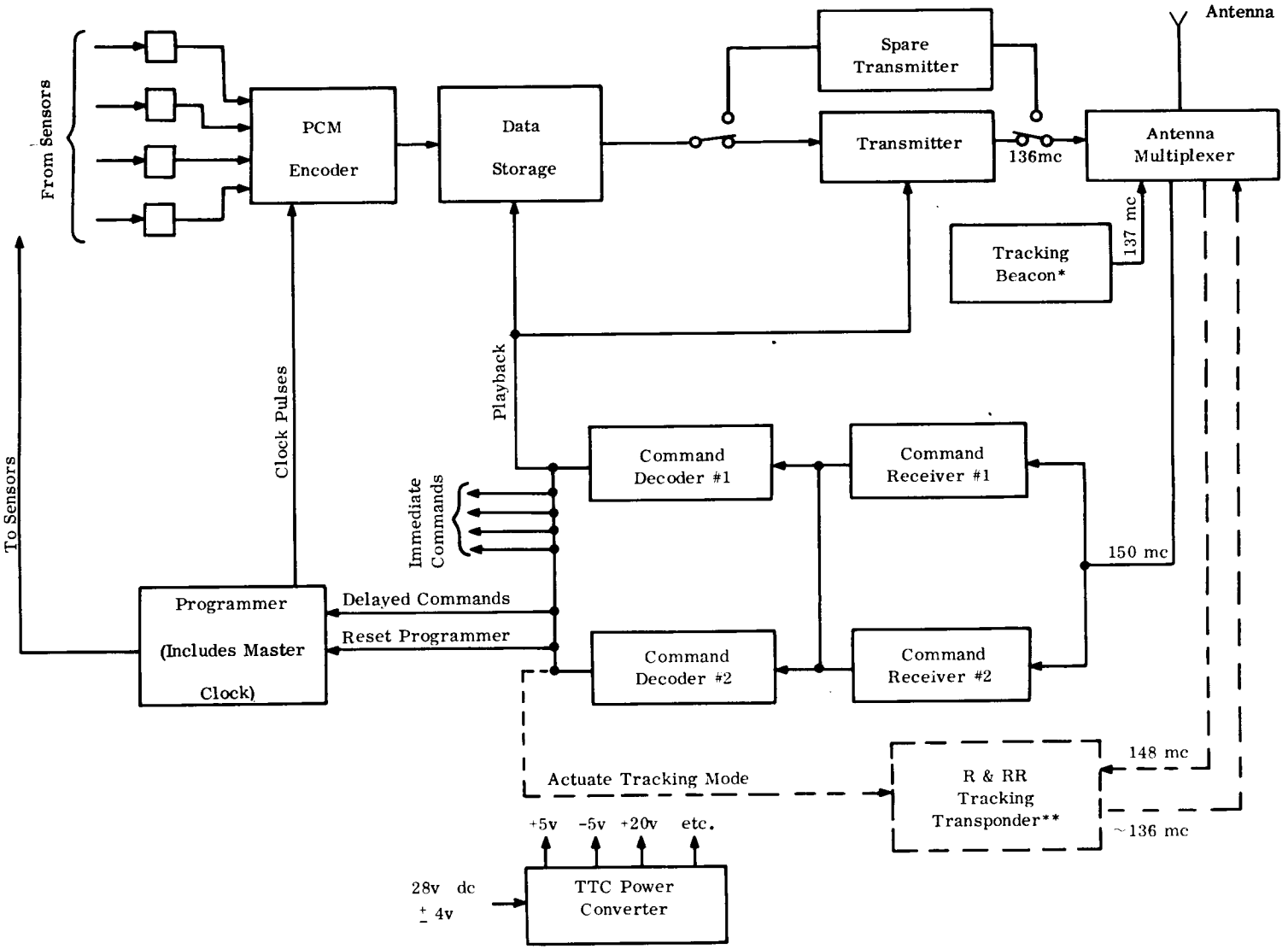

Figure 10-35. Block Diagram of TT&C System for Solar Thermionic Experiment

Table 10-17. Preliminary Estimates of TT&C Equipment for Mission A (Orbit I)

	Component	Number Required	Weight (lb, each)	Size (in., each)	Power Required (watts, each) [a.]
1.	Antenna & Connectors	1	1.0	22 (2 stubs)	---
2.	Antenna Diplexer	1	1.0	3 x 3 x 1	---
3.	Command Receiver	2	1.5	6.3 dia. x 1.13	Stby: 0.01 Interr: 0.2
4.	Command Decoder	2	2.7	6.3 dia. x 1.75	Stby: 0.002 Interr: 3.5
5.	Magnetic Core Storage Units	8	2.5	5.22 x 5.25 x 3.19	Record: 0.050 Playback: 0.25
6.	Storage Control Circuitry	1	1.0	2 x 2 x 4	0.2
7.	PCM Encoder	1	3.0	6 x 6 x 3	2.0
8.	TTC Power Converter	1	2.0	4 x 4 x 6	Coll.: 1.7 Trans.: 4.7
9.	Signal Conditioners	1 set	1.0	2 x 2 x 2	1.0
10.	Transmitter & SCO (350 mw)	2	0.7	2 x 2 x 5	1.7
11.	Tracking Beacon [b.]	1	1.0	4 x 4 x 1.25	2.0
12.	Programmer	1	2.0	5 x 5 x 5	1.0
13.	Cabling	1 set	2.0	(distributed)	---
	TOTAL FOR ORBIT I		43.8 Pounds	Mode { Data Collection: 6 watts Data Transmission: 18 watts (peak)	

a. Assume 12 minutes transmission time per orbit: 2 minutes acquisition plus 10 minutes data transmission at 400 bits per second.

b. Used only during first few weeks; not included in power total.

Table 10-18. Preliminary Estimates of TT&C Equipment for Mission B (Orbit II)

	Component	Number Required	Weight (lb, each)	Size (in., each)	Power Required (watts, each) [a.]
1.	Antennas & Connectors	1	1.0	22 (2 stubs)	---
2.	Antenna Multiplexer	1	1.0	3 x 3 x 1	---
3.	Command Receiver	2	1.5	6.3 dia. x 1.13	Stby: 0.1 Interr: 0.2
4.	Command Decoder	2	2.7	6.3 dia. x 1.75	Stby: 0.002 Interr: 3.5
5.	Magnetic Tape Recorder	2	10.0	10 x 10 x 5	Record: 10 Playback: 15
6.	PCM Encoder	1	3.0	6 x 6 x 3	2.0
7.	TTC Power Converter	1	2.0	4 x 4 x 6	Coll.: 5.8 Trans.: 10.4
8.	Signal Conditioners	1 set	1.0	2 x 2 x 2	1.0
9.	Transmitter & SCO (700 mw)	2	0.7	2 x 2 x 5	3.2
10.	VHF Tracking Transponder	1	5.0	4 x 5 x 7	12.0
11.	Programmer	1	2.0	5 x 5 x 5	1.0
12.	Cabling	1 set	2.0	(distributed)	---
	TOTAL FOR ORBIT II		46.8 pounds	Mode	Data Collection: 20 watts Data Transmission: 40 watts (peak) R&RR Tracking: 34 watts (peak)

a. Assume 5 minutes transmission time per orbit: 1 minute angular acquisition plus 4 minutes data transmission at 3340 bits per second.

Table 10-19. Preliminary Estimates of TT&C Equipment for Mission C (Orbit III)

	Component	Number Required	Weight (lb, each)	Size (in., each)	Power Required (watts, each) [a]
1.	Antennas & Connectors	1	1.0	22 (2 stubs)	---
2.	Antenna Diplexer	1	1.0	3 x 3 x 1	---
3.	Command Receiver	2	1.5	6.3 dia. x 1.13	Stby: 0.1 Interr: 0.2
4.	Command Decoder	2	2.7	6.3 dia. x 1.75	Stby: 0.002 Interr: 3.5
5.	Magnetic Core Storage Units	10	2.5	5.22 x 5.25 x 3.19	Record: 0.050 Playback: 0.25
6.	Storage Control Circuitry	1	1.0	2 x 2 x 4	0.2
7.	PCM Encoder	1	3.0	6 x 6 x 3	2.0
8.	TTC Power Converter	1	2.0	4 x 4 x 6	Coll.: 2.5 Trans.: 4.9
9.	Signal Conditioners	1 set	1.0	2 x 2 x 2	1.0
10.	Transmitter & SCO (440 mw)	2	0.7	2 x 2 x 5	1.2
11.	Tracking Beacon [b]	1	1.0	4 x 4 x 1.25	2.0
12.	Programmer	1	2.0	5 x 5 x 5	1.0
13.	Cabling	1 set	2.0	(distributed)	---
	TOTAL FOR ORBIT III		48.8 pounds	Mode	Data Collection: 7 watts Data Transmission: 18 watts (peak)

a. Assume 4 minutes transmission time per orbit: 2 minutes acquisition plus 2 minutes data transmission at 2500 bits per second.

b. Used only during first few weeks; not included in power total.

A range and range-rate transponder has been included for the elliptical orbit, in order to permit an accurate ephemeris determination as soon after injection as possible. Tracking for a period of about five minutes per orbit should generally be adequate, although somewhat longer tracking periods during the first few orbits would be desirable. Tracking does not need to be simultaneous with data transmission.

The transmitter output powers have been selected to provide the required effective radiated power through antenna nulls of -10 db.

Future phases of this program should include a continuing study of the operational philosophy of the missions in order to optimize the duty cycles. The telemetry link analysis contained in Section 10.6 is general enough to allow a fairly wide latitude of operational approaches.

10.11.4 DESCRIPTION OF TYPICAL COMPONENTS

10.11.4.1 Command Receiver

A typical STADAN command receiver is the model AD-183114 developed by AVCO under NASA contract. This is a single-conversion AM receiver utilizing all solid-state circuits. It may be used with either tone commands or tone-digital commands. Other pertinent characteristics are as follows:

Frequency: 100 to 150 megacycles

Six-db bandwidth: 35 kilocycles

Sensitivity (75% modulation):

1 microvolt for tone commands
2 microvolts for tone-digital commands

Standby power: 100 milliwatts

Power during interrogation: 200 milliwatts

Weight: 1.5 pounds

Size: 6.3 inches diameter by 1 1/8 inches thick

10.11.4.2 Command Decoder

A typical command decoder for the tone-digital system is the model P-102 developed by Consolidated Systems Corporation under NASA contract. This equipment decodes PDM tone bursts received from the satellite receiver and provides power to operate up to 70 external relays which perform desired functions aboard the satellite. The decoder utilizes transistor and magnetic core logic circuits to achieve its small size, low power consumption, and high reliability. The magnetic core register occupies a space of only 1/2 inch by 2 inches square. When tone bursts are not being processed, the only current drawn is the leakage current of the transistors. All of the circuits are specially designed to be nonconducting when in standby.

As shown in the block diagram of Figure 10-36, the decoder reads all data presented to it from the command receiver. Each serial tone burst is compared with two timing circuits to determine the information content. After this bit detection, the data are shifted, bit-by-bit, into a magnetic-core shift register. After each word is read in, this register is interrogated for its contents. If the shift register contains the prewired address for its coder, the address is detected, and the output portion of the unit is enabled. The succeeding words of the same frame are read into the shift register, and the contents are interrogated by each sync bit. When a valid command word is recognized by the command decoding section, the enabled output section supplies the proper voltage for driving an external relay. The first four-bit group is decoded to turn on an X relay driver, while the second four-bit group turns on a Y relay driver in a 16 x 16 matrix. The output signals are taken at 70 selected intersections of the 256 total, providing a signal to any one of 70 relays to actuate a satellite function. Another model (P-101) in production uses an 8 x 11 X-Y matrix to provide only 35 commands.

After the above frame has transpired, the output section is disabled. Subsequent frames are read into the shift register, but no commands are generated until the decoder's address code is recognized again.

Other pertinent characteristics are as follows:

Standby Power: 2 milliwatts

Power during interrogation: 3.5 watts

Weight: Type P-101 (35 outputs) 2.2 pounds
Type P-102 (70 outputs) 2.7 pounds

10.11.4.3 Tracking Beacon

The Tracking beacon made by RCA for the Relay I satellite is typical of the type under consideration. This unit is completely solid state and may be phase modulated. It has the following pertinent characteristics:

Frequency: 136-137 megacycles

Power Output: 250 milliwatts minimum

Power Input: 2.0 watts maximum at 28 volts

Weight: 1.0 pounds

Volume: 20 cubic inches

Size: 4.0 x 4.0 x 1.25 inches

10.11.4.4 Range and Range-Rate Tracking Transponders

10.11.4.4.1 VHF Transponder

A block diagram of the VHF R&RR tracking transponder, which was developed by Goddard Space Flight Center and is presently being flown on the IMP Satellite, is shown in Figure 10-37.

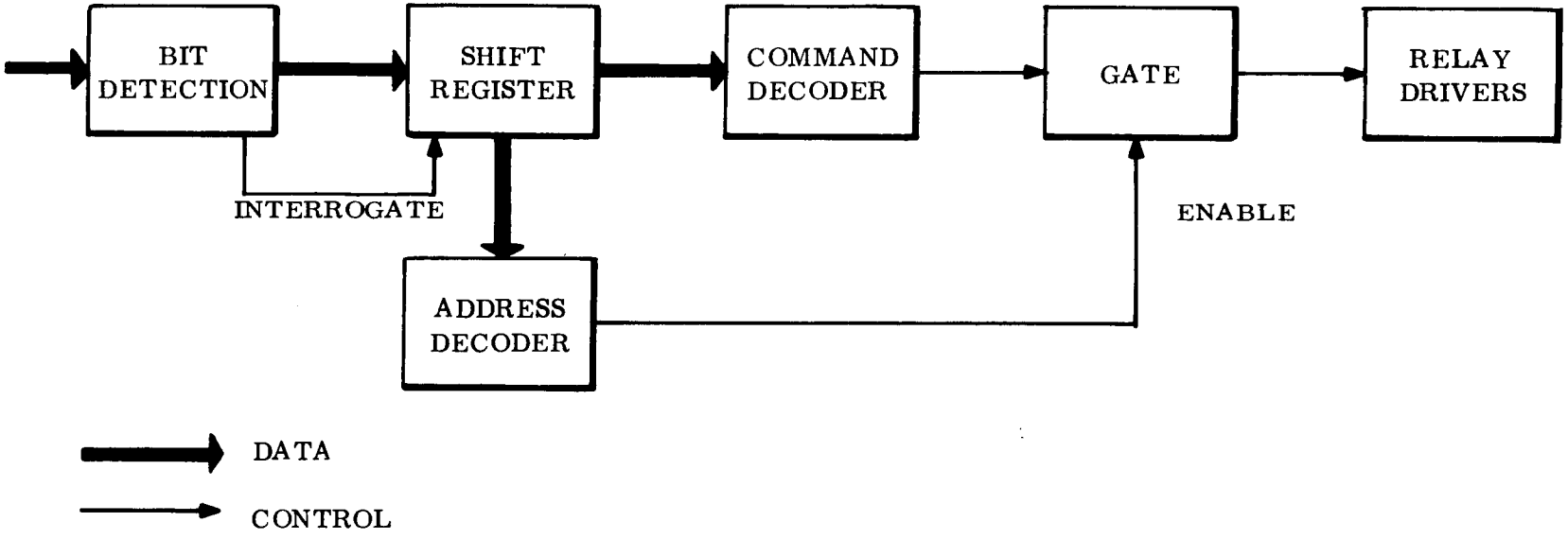

Figure 10-36. Basic Block Diagram, Digital Command Decoder

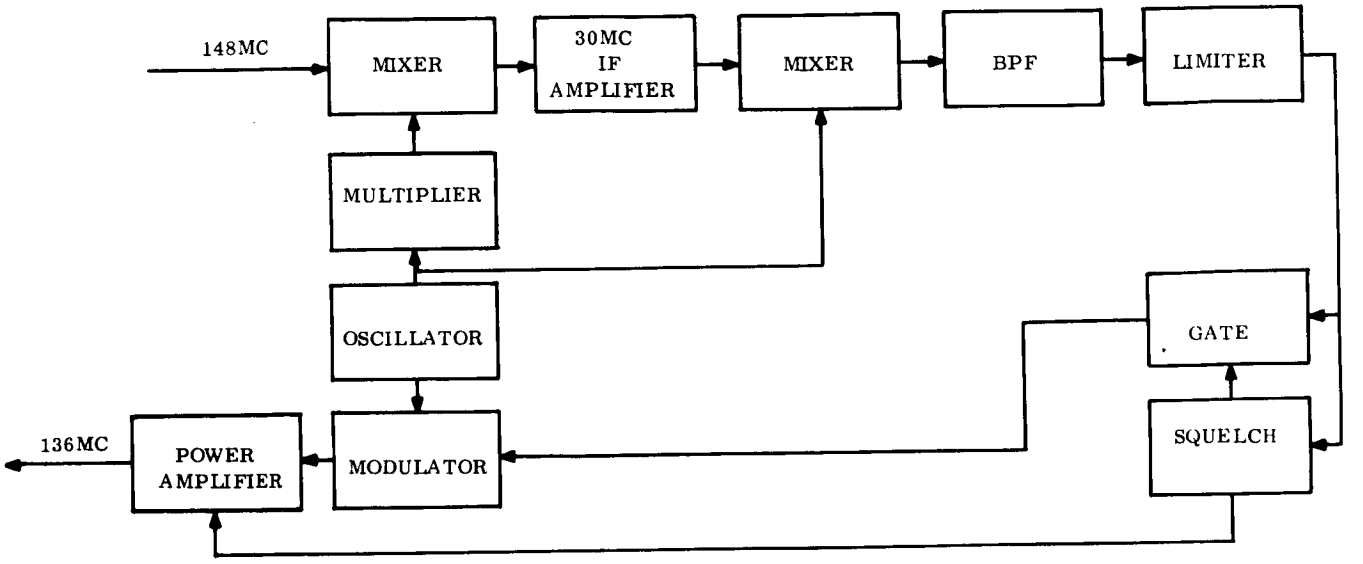

Figure 10-37. VHF R&RR Tracking Transponder

The following component data were obtained from Reference 10-28:

a. The VHF transponder is packaged in a trapezoidal shape, 7 inches wide at the base, tapering to 5 inches at the top, and 5 inches deep. It is comprised of four modules, each about 1-1/4 inch thick, and weighs 5 pounds.

b. The d-c power input requirement is 12 watts (requires 12 and 50-volt inputs).

c. Transmitter RF output power is 4 watts. (On IMP the telemetry is on a sub-carrier, so only 2 watts are available in the carrier for tracking).

d. The sensitivity is -115 dbm.

10.11.4.4.2 S-Band Transponder

The S-Band transponder is made by Motorola. A block diagram of the two-channel configuration is shown in Figure 10-38 (Reference 10-8).

The following component data were obtained from References 10-8 and 10-29:

The transponder is available in two configurations, as below:

	POGO	EGO
Height	5.0 inches	6.3 inches
Length	13.0 inches	9.0 inches
Width	8.0 inches	6.2 inches
Weight	7.8 pounds	7.8 pounds

The addition of a third channel would add about 3/4 pound.

The d-c power input requirement (at 28 volts) is:

4 watts (standby)
15 watts (low-power transmitting)
24 watts (high-power transmitting)

Transmitter RF output power is 200 milliwatts for low-power operation and 500 milliwatts for high power.

The sensitivity is -105 dbm. (A program is underway to improve this to -110 dbm.)

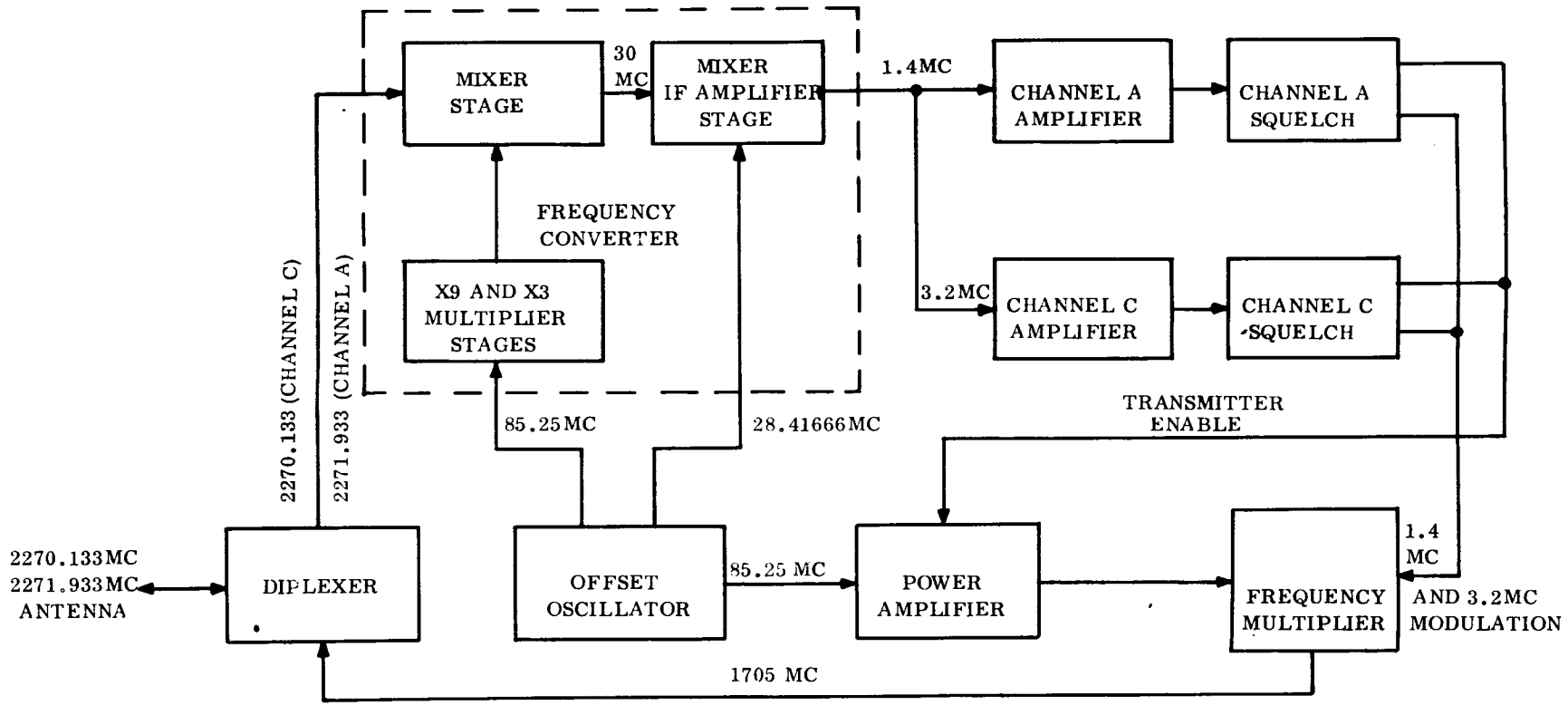

Figure 10-38. Goddard Range and Range-Rate, S-Band Transponder Block Diatram (Two Channel Configuration)

10.11.4.5 Programmer

The programmer provides the basic clock signals required by the PCM encoder and other units and stores and automatically executes a predetermined program of commands governing such events as separation of satellite and booster, deployment of solar panels, transmitter turn-on, etc. Back-up for some of the programmed commands can be furnished by transmitting commands from the ground. Provision should also be made to store a limited number of transmitted commands for delayed execution.

The programmer includes a crystal oscillator, counter, decoding matrices, and output buffers. The counter counts the oscillator output pulses, and the contents of the counter are decoded to provide the required clock signals and commands through the output buffers.

Programmer operation is normally initiated on the launch pad. Shortly before liftoff the counter is pre-set so that the program of commands is synchronized with liftoff time. Counting in the programmer can be interrupted during holds in the launch countdown by means of umbilical line disconnects, so that synchronism can be maintained.

10.11.4.6 PCM Encoder

The PCM encoder sequentially samples parallel analog or digital signal inputs from the various sensors and converts them to a serially programmed digital output stream which is stored in the data storage unit until read-out is commanded from the ground.

From the basic clock pulses provided by the programmer, the timing generator in the encoder controls the sampling sequence of the sensor inputs and the internal functions required for analog-to-digital conversion, generation of the synchronization pattern and satellite identification signals.

The encoder multiplexer gates the analog signals to the analog-to-digital converter, where the stream of digital information representative of the analog input is generated. The output of the converter is combined with digital inputs, satellite identification, and synchronization signals to make up the total output stream of digital information which flows to the data storage unit.

10.11.4.7 Data Storage

For the two circular orbits, the orbital period is short enough that all the data collected can be stored in highly reliable magnetic core storage units. For the elliptical orbit, the 14-hour orbital period results in the accumulation of a rather large amount of data on each orbit (see Table 10-16). The weight of an adequate number of core storage units for this case would be unreasonable, so a less reliable magnetic tape recorder will be required. These are nearly all custom-assembled for each program, and a detailed investigation of tape recorders (and any other more reliable alternatives) should be made after the requirements have been firmly established.

One possible core storage unit is the Model MSA-1A-INT-30,096, made by Di/An Controls, Inc. It is a sequential access, coincident current core memory with internal addressing and counting. Its ruggedness, small size, wide temperature range, and completely solid state magnetic drive, with no internal heating or temperature control requirements, make it quite suitable for aerospace applications. It has been fully qualified in accordance with MIL-Q-9858. Data input and output is asynchronous, one bit at a time, at any rate up to 20,000 bits per second, and the capacity is 30,096 bits.

Data are read out sequentially, one bit at a time, and then re-stored in the memory. Thus, the information stored in a particular core is erased only when that core is required for new information. After the unit has once been filled, it will always contain the last 30,096 bits received from the encoder.

The weight estimates for the core storage units in Tables 10-17 and 10-19 have been made under the assumption that several of these separate units will be used in the satellite, with appropriate control circuitry to switch among them as they are filled. This is probably a conservative estimate, since a lighter unit could be achieved by packaging the required number of cores in a single chassis.

Another core storage possibility is a 10,000-bit unit weighing 1.5 pounds, as announced by Electronic Memories, Inc. (EMI) in Reference 10-30.

10.11.4.8 Transmitter

Lightweight, reliable, solid-state 136 megacycle transmitters are available from many sources. A tailor-made transmitter can be built economically and with confidence once the output power requirements have been firmly established. The spare transmitter shown in Figure 10-33 will probably not be needed, but has been included since the weight penalty of this redundancy is less than 3/4 pound.

As mentioned in Section 10.6, a frequency stability of $1:10^5$ is desirable in order to minimize the acquisition time.

10.11.4.9 Antennas

Since the satellite will be sun-oriented, a nearly isotropic antenna pattern is desirable for communications with the earth. This will be difficult to achieve, due to the large solar concentrator and the solar panels.

The most satisfactory approach, as shown in Figure 13-3, appears to be the use of two quarter-wave (22-inch) monopoles, fed in quadrature. These are currently being used by General Electric on the Biosatellite program. They are lightweight and flexible, having an appearance similar to an ordinary steel measuring tape. They fold down conveniently

against the satellite body during launch and automatically spring into position after the shroud has been ejected.

The use of polarization diversity combiners at the ground stations will maximize the signal received from these antennas.

10.12 SUMMARY AND CONCLUSIONS

Based on the results of this investigation it appears that the telemetry, tracking and command requirements for all three missions can be satisfied using conventional techniques and in general components which have already been developed and used in satellite applications. The telemetry link analyses have indicated that the transmitter power requirements in all cases are extremely modest. Therefore, it will be possible to realize a bit error probability of 10^{-5} without paying an unreasonable price in transmitter power requirements.

This analysis also indicates that the maximum data handling requirements outlined in Table 9-2 can be met without creating any serious problems. As a result the TT&C subsystem does not impose any restrictions on including all of the priority "A" and priority "B" secondary experiments on the spacecraft.

A block diagram of the proposed TT&C subsystem is given in Figure 10-35. A listing of the required components and their size, weight, and power requirements for missions A, B, and C are given in Tables 10-17, 10-18 and 10-19 respectively.

10-13 REFERENCES

10-1 "Satellite Tracking and Data Acquisition Network Facilities Report (STADAN)," Report No. X-539-64-159, Goddard Space Flight Center, Greenbelt, Maryland, June, 1964.

10-2 Mengel, J. T., "Satellite Ground Data Networks," presented at Northeast Electronics Research and Engineering Meeting, November, 1963, Cambridge, Mass.

10-3 Kirch, James E., "The Goddard Range and Range Rate System for Satellite Tracking," Proceedings of the Tenth Annual East Coast Conference on Aerospace and Navigational Electronics, Baltimore, Maryland, October 21-23, 1963.

10-4 Missiles and Rockets, March 12, 1962.

10-5 Private conversation with Mr. Robert J. Solem, Motorola, Inc., Scottsdale, Arizona, 4/6/64.

10-6 Solem, Robert J., "An Error Analysis of the Goddard Range and Range Rate Tracking System," Proceedings of the 1962 Symposium on Space Electronics and Telemetry, Miami Beach, Florida, October 2-4, 1962.

10-7 Thomas, S., Satellite Tracking Facilities, Holt, Rinehart, and Winston, Inc., New York, N.Y., 1963.

10-8 Shaner, J. R., "An S-Band, Multi-Channel, Phase-Coherent Transponder for the Goddard Range and Range Rate Tracking System," Proceedings of the Aerospace Electro-Technology Conference, Phoenix, Arizona, April, 1964.

10-9 NASA-GSFC, "Satellite Command System Recommendations for Goddard Space Flight Center," No. I-560-62-49, May, 1962.

10-10 NASA-GSFC, "Aerospace Data Systems Standards":

Part II, Section 1, "Tone Command Standard," 4/4/63
Part II, Section 2, "Tone Digital Command Standard," 1/15/63.

10-11 Sturgis, D. P., "A Digital Command System for Satellites," Consolidated Systems Corporation, Systems Engineering Bulletin No. 212, June 22, 1962.

10-12 Page, L., Introduction to Theoretical Physics, D. Van Nostrand Co., Inc., Princeton, N.J., Third Edition, 1952, p. 114.

10-13 Schwartz, L. S., "Telemetry," Space/Aeronautics Magazine Research and Development Technical Handbook 1964/1965, Sept., 1964.

10-14 Ko, H. C., "The Distribution of Cosmic Radio Background Radiation," Proc. IRE, Vol. 46, pp. 208-215, Jan., 1958.

10-15 Hogg, D. C., and Mumford, W. W., "The Effective Noise Temperature of the Sky," The Microwave Journal, March, 1960.

10-16 Rochelle, R. W., "Pulse-Frequency Modulation Telemetry," Ph.D. Thesis, University of Maryland, 1963.

10-17 Lawton, J. G., "Comparison of Binary Data Transmission Systems," Proceedings of Second National Conference on Military Electronics, 1958.

10-18 Reiger, S., "Error Probabilities of Binary Data Transmission Systems in the Presence of Random Noise," Part 8, Convention Record of the IRE, 1953.

10-19 Glenn, A. B., "Comparison of PSK vs FSK and PSK-AM vs FSK-AM Binary-Coded TransmissionSystems," IRE Trans. on Communications Systems, June, 1960, pp. 87-100.

10-20 Inter-Range Instrumentation Group (IRIG), Document No. 106-60, Dec. 1, 1960.

10-21 Mitchell, M. E., "Performance of Error-Correcting Codes," IRE Trans. on Communications Systems, March, 1962, pp. 72-85.

10-22 Rochelle, R. W., "Earth Satellite Telemetry Coding System," Electrical Engineering December, 1957, pp. 1062-1065.

10-23 Rochelle, R. W., "Pulse-Frequency Modulation," IRE Trans. on Space Electronics and Telemetry," June, 1962, pp. 107-111.

10-24 Viterbi, A., "On Coded Phase-Coherent Communications," IRE Trans. on Space Electronics and Telemetry, March, 1961, pp. 3-14.

10-25 Jaffe, R. and Rechtin, R., "Design and Performance of Phase-Lock Circuits Capable of Near-Optimum Performance over a Wide Range of Input Signal and Noise Levels," IRE Trans. on Information Theory, March, 1955, pp. 66-76.

10-26 Frazier, J. P., and Page, J., "Phase-Lock Loop Frequency Acquisition Study," IRE Trans. on Space Electronics and Telemetry, Sept., 1962, pp. 210-227.

10-27 Motorola, Inc., Military Electronics Division, Engineering Bulletin, Vol. 9, No. 1, 1961.

10-28 Private conversation with Mr. David Hepler, NASA-GSFC, April 8, 1964.

10-29 Private conversation with Mr. Dick Hale, Motorola, Inc. Scottsdale, Arizona, April 7, 1964.

10-30 Egger, A., and Knowles, W. S., "System Design Concepts for Satellite Magnetic Core Memories," Proceedings of the National Telemetering Conference, Paper No. 7-3, May, 1962.

SECTION 11

ATTITUDE CONTROL SUBSYSTEM

PRINCIPAL CONTRIBUTORS:

F. B. WOESTEMEYER
S. MILLMAN
L. L. DUTRAM
J. L. SCHWARTZ
S. M. WEINBERGER

SECTION 11

ATTITUDE CONTROL SUBSYSTEM

11.1 INTRODUCTION

The Attitude Control Subsystem has four major functions: (1) to accomplish initial stabilization and orientation of the spacecraft after separation from the launch vehicle, (2) to provide the required sun pointing accuracy for the solar thermionic experiment and the solar cell panels, (3) to maintain a spacecraft attitude during the dark segment of the orbit such that the maneuvers required for reorientation will be minimized, and (4) reorientation of the spacecraft to the sun after each dark period.

At the outset of this study the decision was made to orient the entire spacecraft to the sun during the daylight portion of the orbit rather than attempt to orient the solar thermionic system, solar cell panels, etc., to the sun and the remainder of the spacecraft to the earth. The following were major factors in arriving at this decision:

a. If the main spacecraft body was earth oriented, the solar thermionic system, solar cell panels*, sun pointing secondary experiments, etc., would all have to move with respect to the spacecraft body and this would add considerable complexity and weight to the vehicle.

b. There is no major requirement for the spacecraft to be earth oriented.

In consideration of these factors, there appears to be significant advantages, primarily in simplifying the spacecraft design and increasing the overall reliability, to orienting the total spacecraft to the sun. At the same time, there are no major disadvantages apparent in this approach.

*The spacecraft power requirements and the constraints placed on the vehicle by the solar concentrator are of sufficient magnitude that fixed solar cell panels, or solar cells mounted to the spacecraft body, do not provide a satisfactory means of obtaining the required electrical power.

In the following sections, the required orientation accuracy is established, various methods of performing the attitude control functions are considered, and an approach selected for each of the three missions being studied. Block diagrams are presented for the chosen systems; size, weight and power estimates are made.

The attitude control subsystem design is based on a spacecraft life of one year.

11.2 ORIENTATION ACCURACY REQUIRED

Having chosen to orient the total vehicle to the sun, the required spacecraft orientation accuracy is determined by the solar thermionic system. A solar thermionic system requires very precise sun orientation if it is to operate near maximum system efficiency. To understand the reasons for this, consider the thermionic generator cavity and how it functions.

The energy collected by the solar concentrator gains entrance to the generator cavity through an aperture opening. The size of this opening is very critical to the thermionic system performance. As described in Section 4.4 (Volume II), selection of the aperture diameter is based on maximizing the concentrator-absorber efficiency which is defined by:

$$\eta_{ca} = \frac{\text{Net Energy Available in Cavity } (Q_n)}{\text{Concentrator Projected Area } (A_c) \times \text{Solar Intensity } (S)}$$

The factor of interest here is the net energy available in the cavity, Q_n. Net energy is defined as the energy entering the aperture minus that lost by reflection and re-radiation back out the aperture. Net energy then represents that energy available in the generator cavity for thermal insulation losses and for use by the thermionic converters. For a given aperture diameter a certain amount of energy will enter the generator cavity. If the aperture diameter is sufficiently large, all of the energy reflected from the concentrator surface will enter the cavity. However, a portion of the energy entering the cavity will be lost by reflection and re-radiation back out the aperture opening. Thus the larger the aperture opening the more energy will enter the cavity (up to a point) but the greater the cavity losses will be from

reflection and re-radiation. Therefore, if for a given concentrator and orientation error, a plot is made of net energy versus aperture diameter, the resulting curve will have a definite peak which defines the optimum aperture diameter.

Obviously, any factors that tend to increase the aperture diameter increase the reflection and re-radiation losses and subsequently reduces the system efficiency. The orientation accuracy then has a very significant effect on the system efficiency, since the larger the orientation error the larger the optimum aperture diameter and the greater the cavity losses. The effect of increasing orientation error on concentrator-absorber efficiency is shown in Figure 11-1 (Reference 11-1). This plot is for a concentrator radial geometric error of $3\sigma = 12$ minutes and a cavity temperature of $2000^{o}K$. These conditions are identical to those assumed in this study. This curve shows that the concentrator-absorber efficiency decreases approximately one percentage point for every one minute increase in orientation error.* Therefore, the concentrator-absorber efficiency for a six-minute orientation error angle, has dropped from 74 percent at zero orientation error to 68 percent.

Although the decrease in concentrator-absorber efficiency with increasing orientation error is significant, this is only part of the picture. Consider a fixed generator size, as the concentrator-absorber efficiency decreases the energy available to the thermionic converters becomes less and the emitter temperature drops. Since thermionic converter power density increase with temperature is greater than linear, a relatively small decrease in emitter temperature can result in a sizable decrease in thermionic converter power output. This condition is illustrated by Figure 11-2 (Reference 11-2). This figure presents the decrease in generator power output, in percent of the perfect orientation value, as a function of orientation error. The results presented in this figure are based on experimental measurements made by the General Electric Spacecraft Department on a three converter thermionic generator operated with a five-foot-diameter solar concentrator. The details of how these measurements were made are covered in Reference 11-2. This curve shows a three percent

*This result verifies the conclusion reached in Section 8.9.2, which was based on a completely independent analysis.

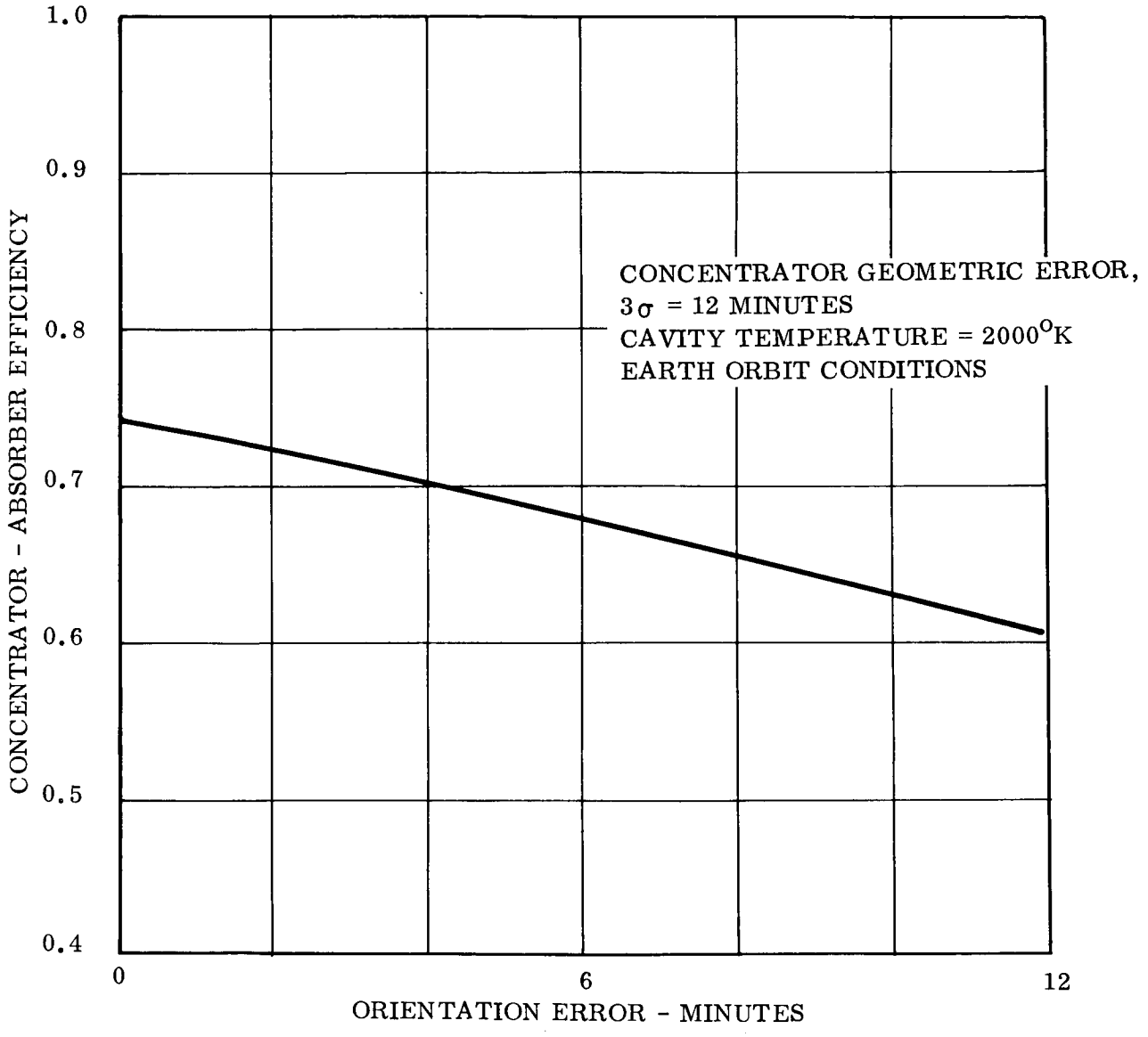

Figure 11-1. Collector-Absorber Efficiency vs Orientation Error

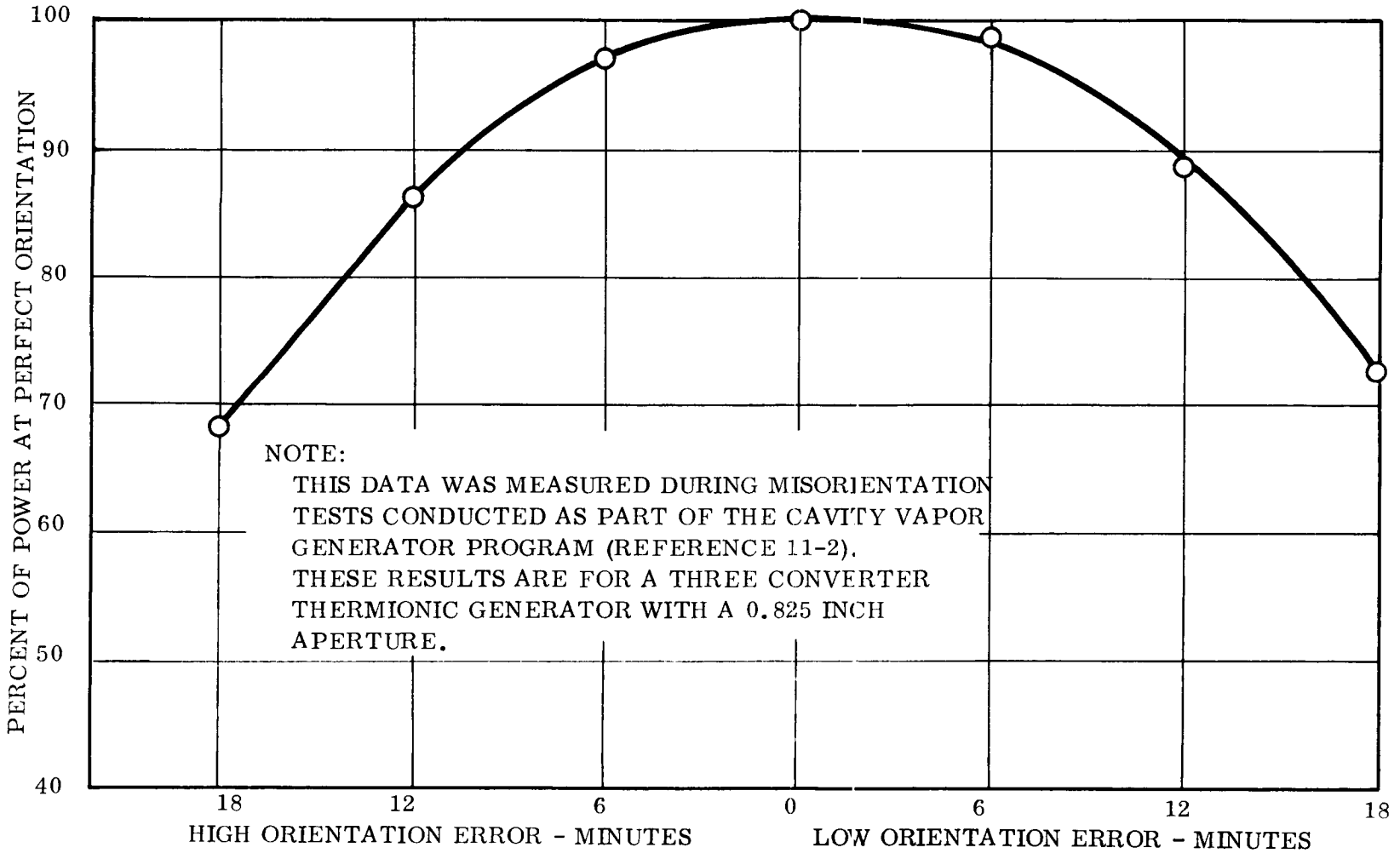

Figure 11-2. Misorientation Effect on Thermionic Generator Power Output

decrease in generator power output between the zero and six-minute orientation error points and a 13 percent decrease between the zero and 12-minute points. Doubling the orientation error then more than quadrupled the percentage decrease in generator power output. Also, as the misorientation error becomes greater, the problem of non-uniform temperature distribution within the cavity becomes more acute.

Obviously, it is desirable to keep the orientation error as small as possible. A value of ± 6 minutes was chosen for this design because it can be achieved with existing techniques which have been demonstrated, and as indicated in Figures 10-1 and 10-2, this degree or orientation accuracy will permit a high level of thermionic system performance.

11.3 DISTURBANCE TORQUES

There are a number of natural phenomena that exert forces on a space vehicle and thereby give rise to torques about the vehicle's control axes. These torques constitute disturbances and so the spacecraft attitude control subsystem must be designed to cope with them. Disturbance torques may be classified in two general categories; those that are cumulative and those that are cyclic. The momentum changes that the spacecraft experiences due to these disturbance torques must be compensated for by momentum exchanging or dumping devices.

Momentum changes due to cumulative disturbance torques are dumped (i.e., removed) from the spacecraft by the application of external torques in the opposite sense on the spacecraft body. These external torques are generally applied by means of pneumatic mass expulsion devices.

Momentum changes due to cyclic disturbance torques (i.e., torques that provide a net momentum contribution of zero at the end of each orbit) can be compensated for by the use of momentum-interchange devices such as flywheels.

The following disturbance torques were considered in this study:

a. Gravity gradient

b. Aerodynamic drag

c. Solar radiation pressure

d. Micrometeoroid impacts

e. Magnetic field

f. Orbit eccentricity.

The magnitude of each of these disturbance torques is estimated in the following sections for the spacecraft configuration given in Figure 13-3 of Section 13. The pertinent spacecraft parameters needed for the disturbance torque calculations are presented in Table 11-1. The values presented in Table 11-1 were computed in Section 13.

To evaluate each of these disturbance torques in detail would be a costly undertaking which was beyond the scope of this study. As a result, the disturbance torque estimates made in the following sections are generally based on limiting worst case conditions. As a consequence of this approach, the estimated disturbance torques are considered conservative and a detailed analysis should yield significantly smaller demands on the attitude control subsystem.

11.3.1 GRAVITY GRADIENT

The gravitational torque results from a displacement of the center of gravity from the center of mass in any direction which is not colinear with the gravity gradient. Since the force of gravity, ignoring the earth's oblateness, is inversely proportional to the square of the distance from the earth's gravitational center, a body with finite dimensions cannot have a coincident center of mass and center of gravity. The displacement results from the fact that the points below the center of mass are closer to the center of attraction, and each element of mass at these points is subject to a larger force. The inference may be made that the gravitation torque depends upon the mass distribution of the body and the orientation of the body with respect to the local vertical.

11.3.1.1 Governing Equation

The angular impulse due to the gravity gradient disturbance torques is made up of cumulative

TABLE 11-1

Spacecraft Parameters Used In Disturbance Torque Calculations

PARAMETER	NUMERICAL VALUE
Projected area of spacecraft-looking down the roll axis, A_1	36.8 ft^2
Projected area of spacecraft-looking down the pitch or yaw axis, A_2	8.3 ft^2
Spacecraft inertia about the yaw axis, I_{oy}	35.2 slug-ft^2
Spacecraft inertia about the pitch axis, I_{ox}	35.2 slug-ft^2
Spacecraft inertia about the roll axis, I_{oz}	49.3 slug-ft^2
Distance between center of pressure and center of mass-looking down the roll axis, d_1	0.208 ft
Distance between center of pressure and center of mass-looking down the pitch or yaw axis, d_2	0.067 ft

and cyclic components. Expressions defining the maximum values of these two components are developed in Reference 11-3 and are represented by Equations 1 and 2 below.

$$H\,(\text{cum})_{max} = \frac{3}{2} \frac{(GM)^{1/2}}{\left[a(1-e^2)\right]^{3/2}} \begin{bmatrix} I_{oy} - I_{ox} \\ I_{ox} - I_{oz} \\ I_{oz} - I_{oy} \end{bmatrix} \pi \qquad (1)$$

$$H(\text{cyclic})_{max} = \frac{3}{2} \frac{(GM)^{1/2}}{\left[a\,(1-e^2)\right]^{3/2}} \begin{bmatrix} I_{oy} - I_{ox} \\ I_{ox} - I_{oz} \\ I_{oz} - I_{oy} \end{bmatrix} (0.5 + 0.33\ e) \qquad (2)$$

where

a = One half the major axis of the orbit, ft

e = Eccentricity of the orbit

G = Universal constant of gravity, $ft^3/lb\text{-}sec^2$

M = Total mass of the earth, lb

I_{ox} = Moment of inertia about the pitch axis, $slug\text{-}ft^2$

I_{oy} = Moment of inertia about the yaw axis, $slug\text{-}ft^2$

I_{oz} = Moment of inertia about the roll (sun pointing) axis, $slug\text{-}ft^2$.

11.3.1.2 Numerical Calculations

A. Mission A

The following parameters apply for a 1000-nautical mile circular orbit with an inclination of 101.84 degrees

$a = (3440 + 1000)\ 6.08 \times 10^3 = 2.7 \times 10^7$ ft

$e = 0$

P (Orbit period) $= 7450$ sec

$GM = 1.408 \times 10^{16}$ ft^3/sec^2

$I_{ox} = I_{oy} = 35.2$ slug-ft^2

$I_{oz} = 49.3$ slug-ft^2

Substituting these numerical values into Equation 1 gives

$$H(\text{cum})_{max} = \frac{3}{2}\left[\frac{1.408 \times 10^{16}}{(2.7 \times 10^{7})^3}\right]^{1/2} \begin{bmatrix} 0 \\ -14 \\ 14 \end{bmatrix} \pi$$

$$= \begin{bmatrix} 0 \\ -1^* \\ 1 \end{bmatrix} 5.6 \times 10^{-2} \text{ ft-lb-sec}$$

The attitude control subsystem mass expulsion devices are required to generate that component of angular momentum which is cumulative. The angular momentum storage devices (i.e., flywheels) are required to store the maximum value of the angular impulse (both cyclic and cumulative) which occurs during the period of control. The period of control could be as short as one orbital period or as long as several periods, if the cumulative component of torque could be stored economically for these several periods. Since the cyclic component of torque will be relatively high when all cyclic components of the various disturbance torques are added, the period of control was chosen to be one orbit.

The mass expulsion devices will be required to generate the following maximum amount of angular momentum in one year for the 1000-nautical mile orbit in order to handle the gravity gradient disturbance alone.

*The negative sign denotes direction and since the concern here is with magnitude only the signs will be dropped in the remainder of this analysis.

$$H\,(\text{Gravity})_{max} = H\,(\text{cum})_{\text{max pitch}} + H\,(\text{cum})_{\text{max yaw}} \times \text{number of orbit periods in one year}$$

$$= 2 \times 5.6 \times 10^{-2} \times 4.23 \times 10^{3}$$

$$= 472 \text{ ft-lb-sec}$$

The maximum cyclic capacity required of the momentum storage device can be calculated from Equation 2.

$$H\,(\text{Cyclic})_{max} = \frac{3}{2} \left[\frac{1.408 \times 10^{16}}{(2.7 \times 10^{7})^{3}}\right]^{1/2} \begin{bmatrix} 0 \\ -14 \\ 14 \end{bmatrix} 0.5$$

$$= \begin{bmatrix} 0 \\ -1 \\ 1 \end{bmatrix} 8.87 \times 10^{-3} \text{ ft-lb-sec}$$

Following the same procedure outlined here the angular impulse and momentum storage requirements resulting from the gravity gradient disturbance torques are computed below for the Mission B and C cases.

B. Mission B

The following parameters apply for a 200 by 25,000-nautical mile orbit with an inclination of 45 degrees.

$2a = (6876 + 25,000 + 200)\ 6.08 \times 10^{3} = 1.95 \times 10^{8}$ ft

$e = 0.77$

$P = 50,400$ sec

$GM = 1.408 \times 10^{16}$ ft^3/sec^2

$I_{ox} = I_{oy} = 35.2$ slug-ft^2

$I_{oz} = 49.3$ slug-ft^2

Therefore,

$$H\,(\mathrm{Cum})_{max} = \frac{3}{2}\left[\frac{1.408 \times 10^{16}}{(6.24 \times 10^{7})^{3}}\right]^{1/2}\begin{bmatrix}0\\-14\\14\end{bmatrix}\pi$$

$$=\begin{bmatrix}0\\-1\\1\end{bmatrix} 1.6 \times 10^{-2}\ \text{ft-lb-sec}$$

The total maximum cumulative momentum for a one year period then is

$$\Delta\, H\,(\mathrm{Gravity})_{max} = 2 \times 1.6 \times 10^{-2} \times 0.625 \times 10^{3}$$

$$= 20\ \text{ft-lb-sec}$$

The maximum cyclic capacity required of the momentum storage device is

$$H\,(\mathrm{Cyclic})_{max} = \frac{3}{2}\left[\frac{1.408 \times 10^{16}}{(6.24 \times 10^{7})^{3}}\right]^{1/2}\begin{bmatrix}0\\-14\\14\end{bmatrix}(0.5 + 0.254)$$

$$=\begin{bmatrix}0\\-1\\1\end{bmatrix} 3.86 \times 10^{-3}\ \text{ft-lb-sec.}$$

C. Mission C

The following parameters apply for a 325-nautical mile circular orbit with a 30 degree inclination.

$a = (3440 + 325)\ 6.08 \times 10^{3} = 2.3 \times 10^{7}$ ft

$e = 0$

$P = 5800$ sec

$GM = 1.408 \times 10^{16}\ \text{ft}^3/\text{sec}^2$

$I_{ox} = I_{oy} = 35.2\ \text{slug-ft}^2$

$I_{oz} = 49.3\ \text{slug-ft}^2$

Therefore,

$$H\,(\mathrm{Cum})_{max} = \frac{3}{2}\left[\frac{1.408 \times 10^{16}}{(2.3 \times 10^{7})^{3}}\right]^{1/2}\begin{bmatrix}0\\-14\\14\end{bmatrix}\pi$$

$$= \begin{bmatrix}0\\-1\\1\end{bmatrix} 0.071 \text{ ft-lb-sec.}$$

The total maximum cumulative momentum for a one year period then is

$$\Delta H(\mathrm{Gravity})_{max} = 2 \times 0.071 \times 5.44 \times 10^{3}$$

$$= 772 \text{ ft-lb-sec.}$$

The maximum cyclic capacity required of the momentum storage device is

$$H\,(\mathrm{Cyclic})_{max} = \frac{3}{2}\left[\frac{1.408 \times 10^{16}}{(2.3 \times 10^{7})^{3}}\right]^{1/2}\begin{bmatrix}0\\-14\\14\end{bmatrix} 0.5$$

$$= \begin{bmatrix}0\\-1\\1\end{bmatrix} 0.011 \text{ ft-lb-sec.}$$

The angular impulse and momentum storage requirements resulting from the gravity gradient torques are summarized in Table 11-2.

11.3.2 AERODYNAMIC DRAG

In low altitude earth orbits, the air density is sufficient to cause an appreciable atmospheric drag on the spacecraft. The product of this atmospheric drag and the distance between the spacecraft center of mass and the center of pressure results in an aerodynamic torque on the vehicle.

Table 11-2. Angular Impulse and Momentum Storage Requirements Resulting From Gravity Gradient Torques

Control Axis	Maximum Angular Impulse Requirements Ft-Lb-Sec/year			Momentum Storage Requirements Ft-Lb-Sec/orbit		
	Mission A 1000NM	Mission B 200by2500 NM	Mission C 325 NM	Mission A 1000 NM	Mission B 200by2500 NM	Mission C 325 NM
Roll	0	0	0	0	0	0
Pitch	236	10	386	6.49×10^{-2}	2.0×10^{-2}	8.2×10^{-2}
Yaw	236	10	386	6.49×10^{-2}	2.0×10^{-2}	8.2×10^{-2}

11.3.2.1 Governing Equation

The aerodynamic drag is given by:

$$\text{Aerodynamic drag} = C_D\, q\, A$$

$$= C_D\, (1/2\, \rho\, V^2)\, A$$

$$= \frac{C_D}{2}\, \rho \left(\frac{2\, \pi\, R}{P}\right)^2 A$$

where C_D = Coefficient of drag = 2.2 (Reference 11-4)

q = Dynamic Pressure, lbs/ft^2

R = Orbit radius ft

P = Orbit period, seconds

$= 2\, \pi \left(\frac{R}{g}\right)^{1/2}$ for circular orbits

g = Acceleration of gravity, ft/sec^2

ρ = Atmospheric mass density at orbit altitude, $lb\text{-}sec^2/ft^4$

A = Vehicle projected area, ft^2.

Substituting ρ_1/g for ρ and $2\pi\left(\frac{R}{g}\right)^{1/2}$ for P, where ρ_1 equals the atmospheric specific weight at orbit altitude (lb/ft^3), yields

$$\text{Aerodynamic drag} = 1.1\,\rho_1\,RA$$

Multiplying the aerodynamic drag by the distance between the center of pressure and the center of mass gives the aerodynamic torque. Referring to Figure 11-3 the aerodynamic disturbance torque as a function of the spacecraft's position in orbit is:

$$T = 1.1\,\rho_1\,R\left[A_1\,|\sin\theta|\,(d_1\sin\theta) + A_2\,|\cos\theta|\,(d_2\cos\theta)\right]$$

where

A_1 = Area in the pitch-yaw plane, ft^2

A_2 = Area in the pitch-roll (or yaw-roll) plane

d_1 = Distance between center of pressure and center of mass for area A_1, ft

d_2 = Distance between center of pressure and center of mass for area A_2, ft

θ = Is the angle between the aerodynamic force and a normal to the surface on which it acts (See Figure 11-3), degrees.

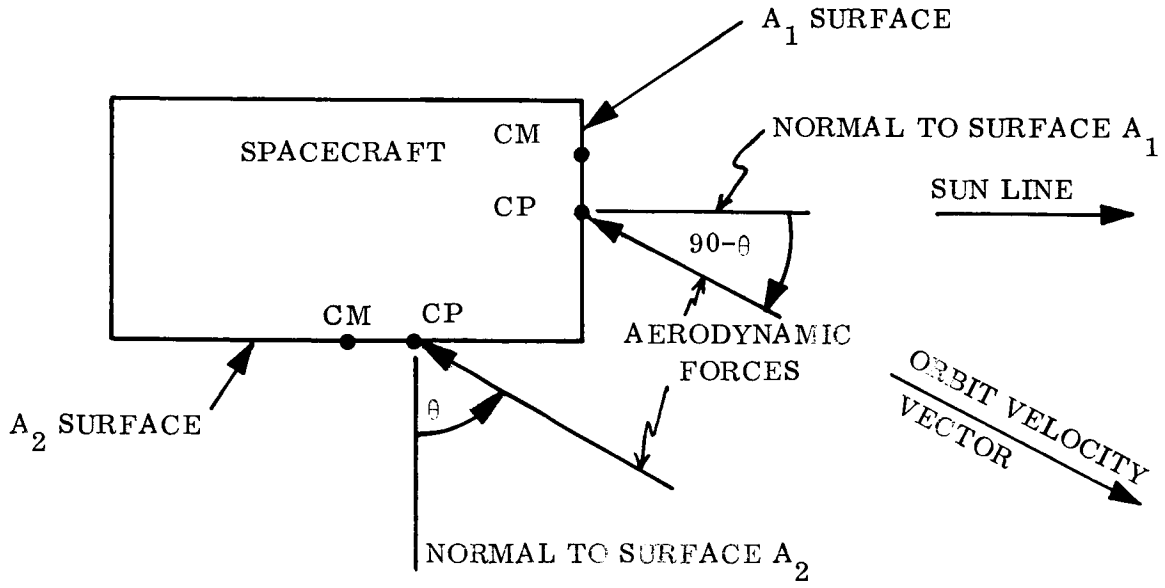

Figure 11-3. Aerodynamic Forces Acting on Vehicle

Obviously the maximum value of aerodynamic torque occurs when θ = 90 degrees. For this case the aerodynamic torque expression becomes

$$T_{max} = 1.1 \rho_1 R (A_1 d_1 + A_2 d_2) \quad (3)$$

11.3.2.2 Numerical Calculations

A. Mission A

The Mission A spacecraft is in a 1000-nautical mile circular orbit inclined at 101.84 degrees. At this high an altitude the aerodynamic drag is very low, producing negligible aerodynamic torques.

B. Mission B

The Mission B spacecraft is in a highly elliptical orbit with a perigee of 200 nautical miles and an apogee of 25,000 nautical miles. This orbit has an inclination of 45 degrees. This case is complicated by the fact that the orbit is not circular and the spacecraft encounters an extremely wide variation in aerodynamic drag throughout the orbit. In addition, the cumulative momentum is generally not zero since aerodynamic drag is full-period cyclic rather than half-period cyclic as gravity gradient and magnetic torques are. Since the aerodynamic torques encountered near apogee are negligible in comparison to those experienced at perigee, the cumulative momentum will not be zero at the end of each complete orbit.

For this case the following parameters apply.

$A_1 = 36.8 \text{ ft}^2$ $\quad d_1 = 0.208 \text{ ft}$

$A_2 = 8.3 \text{ ft}^2$ $\quad d_2 = 0.067 \text{ ft}$

Perigee	Apogee
$\rho_1 = 7.25 \times 10^{-13}$ lb/ft^3 (Maximum value, taken from Figure 11-4)	ρ_1 = negligible

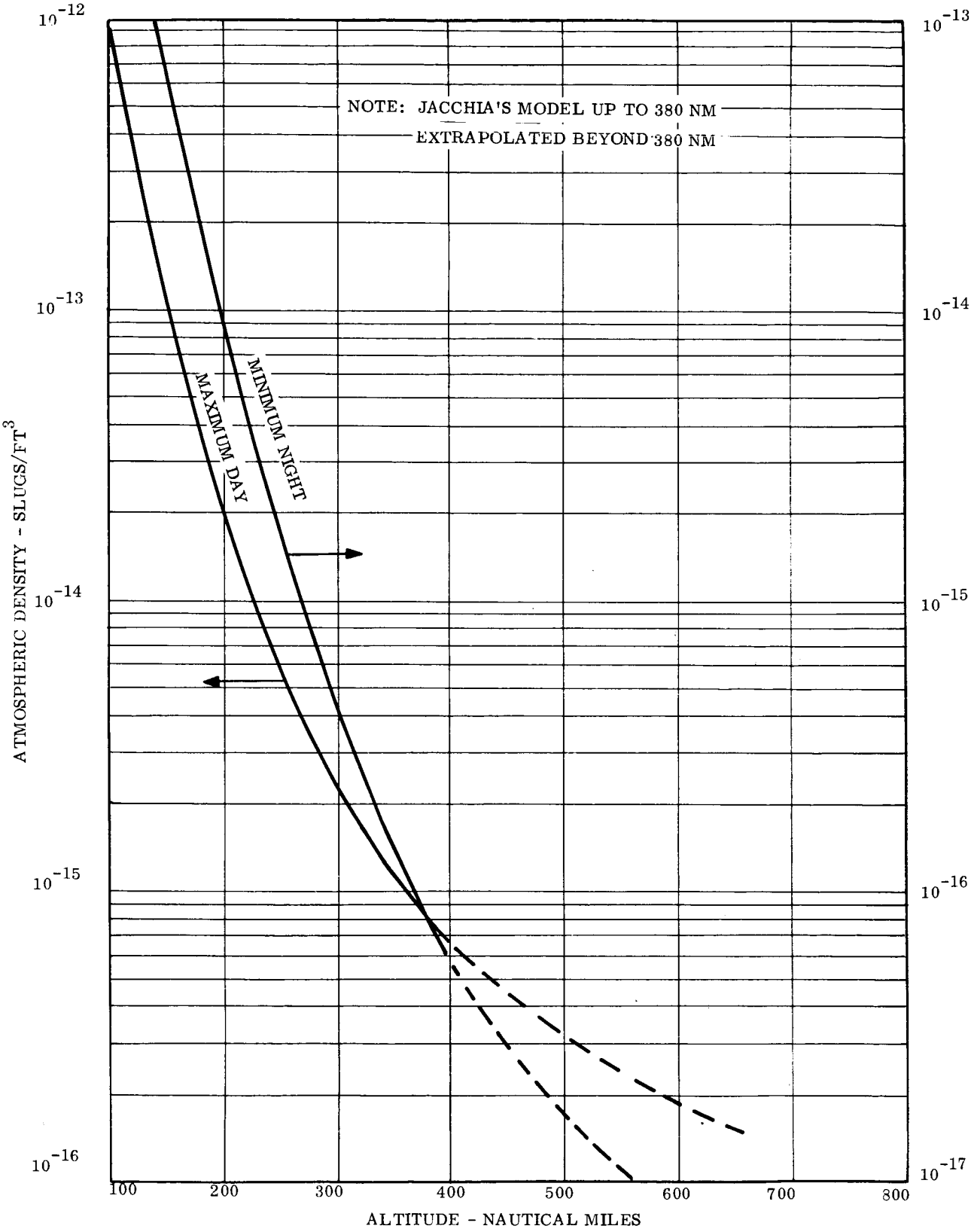

Figure 11-4. Atmospheric Density

$$R = (3440 + 200)\, 6.08 \times 10^{3} = 2.22 \times 10^{7} \text{ ft} \qquad R = (3440 + 25,000)\, 6.08 \times 10^{3} = 17.3 \times 10^{7} \text{ ft}$$

Obviously the maximum aerodynamic torque occurs at perigee and can be computed using Equation 3.

$$T_{max} = 1.1 \times 7.25 \times 10^{-13} \times 2.22 \times 10^{-7} (36.8 \times 0.28 + 8.3 \times 0.067)$$
$$= 14.5 \times 10^{-5} \text{ ft-lb}$$

The time required for the spacecraft to go from perigee (200 nautical miles) to various altitudes was computed and is shown below:

Orbit Altitude-Nautical Miles	Time-Seconds
250	151
325	201
400	252
1000	550

As a worst case condition the maximum torque calculated for the 200-nautical mile point will be assumed to act on the spacecraft for the time required to travel from the 325-nautical mile point on one side of perigee to the 325-nautical mile point on the other side. As shown above, this takes 402 seconds. The torque calculated, in the following section for the 325-nautical mile altitude will be assumed to act on the vehicle from the 400-nautical mile points to the 325-nautical mile points or for a period of 102 seconds. The aerodynamic drag will be considered negligible above 400-nautical miles. Therefore,

$$H_{max} = 14.5 \times 10^{-5} (402) + 5.07 \times 10^{-6} (102)$$
$$= 5.87 \times 10^{-2} \text{ ft-lb-sec.}$$

Since the torque cannot be considered cyclic in this orbit, aerodynamic effects impose angular impulse requirements on the mass expulsion control devices as well as on the momentum storage devices. The angular impulse requirements for one year are:

$$H_{max} = 5.87 \times 10^{-2} \times \text{orbits/year}$$
$$= 5.87 \times 10^{-2} \times 0.625 \times 10^{3}$$
$$= 36.7 \text{ ft-lb-sec.}$$

C. Mission C

The Mission C spacecraft is in a 325-nautical mile circular orbit with an inclination of 30 degrees. For this case the following parameters apply:

$A_1 = 36.8 \text{ ft}^2$ $\quad d_1 = 0.208 \text{ ft}$

$A_2 = 8.3 \text{ ft}^2$ $\quad d_2 = 0.067 \text{ ft}$

$\rho_1 = 2.45 \times 10^{-14} \text{ lb/ft}^3$ (Average value taken from Figure 11-4)

$R = (3440 + 325)\ 6.08 \times 10^{3} = 2.29 \times 10^{7} \text{ ft.}$

Substituting these values into Equation 3 yields,

$$T_{max} = 1.1 \times 2.45 \times 10^{-14} \times 2.29 \times 10^{7} (36.8 \times 0.208 + 8.3 \times 0.067)$$
$$= 5.07 \times 10^{-6} \text{ ft-lb.}$$

Assuming that this maximum disturbance torque exists throughout the orbit, the maximum momentum storage requirements for half of an orbit would be:

$$\Delta H_{max} = T_{max} \times \frac{P}{2}$$
$$= 5.07 \times 10^{-6} \times \frac{96.7}{2} \times 60$$
$$= 14.7 \times 10^{-3} \text{ ft-lb-sec.}$$

The angular impulse and momentum storage requirements resulting from the aerodynamic torques are summarized in Table 11-3.

Table 11-3. Angular Impulse and Momentum Storage Requirements Resulting from Aerodynamic Torques

Control Axis	Maximum Angular Impulse Requirements Ft-Lb-Sec/year			Momentum Storage Requirements Ft-Lb-Sec/orbit		
	Mission A 1000NM	Mission B 200 by 2500 NM	Mission C 325 NM	Mission A 1000 NM	Mission B 200 by 2500 NM	Mission C 325 NM
Roll	0	0	0	0	0	0
Pitch	0	36.7	0	0	5.87×10^{-2}	14.7×10^{-3}
Yaw	0	36.7	0	0	5.87×10^{-2}	14.7×10^{-3}

11.3.3 SOLAR RADIATION PRESSURE

In a medium in which waves are propogated, there is a pressure in the direction normal to the waves. The photons emitted from the sun exert a pressure on the surfaces of a space vehicle. The resulting forces and torques exerted on the spacecraft depend upon the geometry of the configuration, the nature of the surfaces, the angle from which the solar rays arrive, and the distance from the sun.

11.3.3.1 Governing Equation

The force on a body of area A due to solar radiation pressure is given by

$$\bar{F}_P = \frac{Po}{D^2} A \cos\theta \left[(\alpha + \rho_d) \bar{S} + (2\rho_s \cos\theta + \frac{2}{3} \rho_d) \bar{n} \right]$$

where

P_o = Solar pressure constant (at 1AU) = 0.965×10^{-7} lb/ft^2

D = Distance of body from the sun, AU

θ = Angle of incidence between the sun's rays and a normal to the body surface

α = Fraction of the incident solar energy absorbed by the surface

ρ_d = Fraction of the incident solar energy diffusely reflected from the surface

ρ_s = Fraction of the incident solar energy specularly reflected from the surface

$\bar{s}$ = Unit vector in the direction of the incident energy on the surface

$\bar{n}$ = Normal unit vector with its positive sense normal to the surface.

For this application the spacecraft will be sun pointing with an accuracy of $\pm$ 0.1 degree so θ is essentially zero degrees and the cos θ term is one. For all three missions the spacecraft's distance from the sun, D, is 1 AU. Applying these conditions the governing equation reduces to

$$\bar{F}_P = 0.965 \times 10^{-7} A \left[(\alpha + \rho_d) \bar{s} + (2\rho_s + \frac{2}{3} \rho_d) \bar{n} \right] . \quad (4)$$

The torque acting on the spacecraft due to solar radiation pressure is

$$T_p = F_p \times d_1 \quad \text{ft-lb} \quad (5)$$

where

d_1 = Distance in feet between the center of pressure and center of mass looking down the roll axis.

11.3.3.2 Numerical Calculations

The torque resulting from solar radiation pressure is essentially the same for all three missions* and will be computed first.

The projected area of the spacecraft facing the sun is made up predominantly of the solar concentrator, the secondary experiment panels and the solar cell panels. The area, absorptivity, and reflectivity of these three areas is estimated below:

	$A\text{-}Ft^2$	α	ρ_d	ρ_s
Solar cell panels	14	0.65	0.3	0.05
Secondary experiment panels	8	0.2	0.75	0.05
Solar concentrator	13.6	0.1	0.01	0.89

Substituting these numerical values into Equation 4 gives

$$F_p = 0.965 \times 10^{-7} \left\{ 14 \left[(0.65 + 0.3) + (2 \times 0.05 + \frac{2}{3} \times 0.3) \right] + 8 \left[(0.2 + 0.75) + (2 \times 0.05 + \frac{2}{3} \times 0.75) \right] + 13.6 \left[(0.1 + 0.01) + (2 \times 0.89 + \frac{2}{3} \times 0.01) \right] \right\}$$

$$= 5.45 \times 10^{-6} \text{ lb.}$$

From Table 11-1 the distance between the center of pressure and the center of mass when looking down the roll axis is 0.208 feet. Substituting numerical values into Equation 5 gives the solar radiation pressure torque on the vehicle.

$$T_p = 5.45 \times 10^{-6} \times 0.208$$
$$= 11.3 \times 10^{-7} \text{ ft-lb.}$$

*The torque acting on the spacecraft would be approximately 13 percent higher in the Mission C case because of the slightly larger solar cell panels (see Figure 13-3 in Section 13).

The solar radiation pressure torque will be cumulative. The momentum storage and angular impulse requirements can now be calculated.

A. Mission A

The period for the 1000-nautical mile orbit is 2.07 hours and during the initial phase of the experiment there will be no shadow periods.

The maximum momentum storage requirement then for one orbit is

$$H = T_p \times \text{time in sunlight}$$
$$= 11.3 \times 10^{-7} \times 2.07 \times 3600$$
$$= 8.52 \times 10^{-3} \text{ ft-lb-sec.}$$

Refer to Figure 3-18 in Section 3.3.4 (Volume II). The orbit will be shadow free for the first 162 days and the shadow period will average approximately 14 minutes per orbit over the remaining 203 days of the mission life. For a 2.07 hour orbit period the vehicle will make 11.6 orbits per day. The angular impulse required for one year then is

$$\Delta H = 11.3 \times 10^{-7} (162 \times 24 \times 3600 + 203 \times 11.6 \times 110 \times 60)$$
$$= 33.4 \text{ ft-lb-sec.}$$

B. Mission B

The period for the 200 by 25,000-nautical mile elliptical orbit is 14 hours. Referring to Figure 3-19 in Section 3.3.5 (Volume II) it is apparent that a short period exists where no shadow is encountered.

The maximum momentum storage requirement then for one orbit is

$$H = 11.3 \times 10^{-7} \times 14 \times 3600$$

$$H = 5.68 \times 10^{-2} \text{ ft-lb-sec.}$$

Again referring to Figure 3-19, the average shadow period per orbit will be 20 minutes (this figure takes into account that there are orbits during the one year life where no shadow period is encountered). The spacecraft will make 1.71 orbits per day in this orbit. The angular impulse requirement for one year is then:

$$\Delta H = 11.3 \times 10^{-7} (365 \times 1.71 \times 13.7 \times 3600)$$
$$= 34.5 \text{ ft-lb-sec.}$$

C. Mission C

The orbit period for the 325-nautical mile circular orbit is 1.61 hours. Referring to Figure 3-4 in Section 3.3.1 (Volume II), the average shadow period per orbit is 36 minutes. There are no periods during the one year life when a shadow period is not encountered during an orbit.

The momentum storage requirement for one orbit then is:

$$H = 11.3 \times 10^{-7} \times (1.61 - \frac{36}{60}) \ 3600$$
$$= 4.1 \times 10^{-3} \text{ ft-lb-sec.}$$

The spacecraft makes 14.9 orbits per day in this orbit. The angular impulse required for one year then is:

$$\Delta H = 11.3 \times 10^{-7} (365 \times 14.9 \times 1.01 \times 3600)$$

$$= 22.4 \text{ ft-lb-sec.}$$

The angular impulse and momentum storage requirements resulting from the solar radiation pressure torques are summarized in Table 11-4.

Table 11-4. Angular Impulse and Momentum Storage Requirements Resulting From Solar Pressure Torques

Control Axis	Angular Impulse Requirements Ft-Lb-Sec/year			Momentum Storage Requirements Ft-Lb-Sec/orbit		
	Mission A 1000NM	Mission B 200x25000NM	Mission C 325NM	Mission A 1000NM	Mission B 200x25000NM	Mission C 325NM
Roll	0	0	0	0	0	0
Pitch	33.4	34.5	22.4	8.52×10^{-3}	5.68×10^{-2}	4.1×10^{-3}
Yaw	33.4	34.5	22.4	8.52×10^{-3}	5.68×10^{-2}	4.1×10^{-3}

11.3.4 MICROMETEOROID IMPACTS

The micrometeoroids striking the spacecraft during each orbit will impart an angular momentum to the vehicle which must be counteracted.

11.3.4.1 Governing Equations

The number of meteoroids striking the spacecraft in one day may be approximated by the following relationship:

$$n_m = \frac{A_s}{A_e} \frac{N_m}{2}$$

where

n_m = Number of meteoroids, of magnitude m, to strike the spacecraft per day

N_m = Number of meteoroids, of magnitude m, to strike the earth per day

A_s = Exposed surface area of the spacecraft, ft^2

A_e = Surface area of the earth = 5.49×10^{15} ft^2.

The factor of 1/2 in the above equation is due to the shadowing effect provided by the earth which for a circular orbit tends to diminish the number of meteoroids hitting the spacecraft by one-half.

The total surface area of the spacecraft (see Figure 13-3 Section 13) is approximately 104 square feet. Substituting numerical values for A_s and A_e into the basic equation gives

$$n_m = 9.47 \times 10^{-15} N_m. \tag{6}$$

Only those particles with at least a fifty percent probability of hitting the spacecraft will be considered in the calculation of the meteorite disturbance effect. The probability of K hits in a fixed interval of time, T, is given by Poisson's distribution.

$$P(K, \lambda T) = \bar{e}^{\lambda T} \frac{(\lambda T)^k}{K!}$$

where

λ = The average number of hits per unit time, T

T = Orbit period.

A fifty percent probability of being hit at least once is equivalent to a fifty percent probability of not being hit (i.e., K=0). Therefore

$$P(0, \lambda T) = \bar{e}^{\lambda T}.$$

Setting this equation equal to 0.5 and solving for λT (average number of hits in time T) gives

$$\lambda T = \log_e (0.5) = 0.693 \tag{7}$$

This equation states that those meteoroids, of magnitude m, that hit the spacecraft less than 0.693 times in one orbit, have less than a 50 percent probability of hitting it in that orbit.

11.3.4.2 Numerical Calculations

Since in the vicinity of earth the meteoroid density increases as the distance from the earth decreases* the worst case will occur in the 325-nautical mile orbit associated with Mission C. This case will be considered first.

A. Mission C

An experimental study of the meteor population in the vicinity of earth was made by Whipple (Reference 11-4) and the results are summarized in Table 11-5. The data presented in Table 11-5 was used along with Equations 6 and 7 to generate the data presented in Table 11-6. This table does not consider any particles smaller than visual magnitude 22. The reasoning behind this is based on the Poynting-Robertson effect which theorizes that the smaller particles are swept away from the earth by solar radiation pressure.

From Table 11-6, the only particle size that has a larger than 50 percent probability of hitting the spacecraft during one orbit, is the particle size with a visual magnitude of 22. As a worst case assume that the particle strikes the spacecraft at the point most distant from the center of mass. For the spacecraft configuration shown in Figure 13-3 in Section 13, this distance would be approximately five feet. The maximum momentum storage requirement for one orbit would be

$$H_{max} = M_{22} \times V \times r \times n_{22}$$

*This is true up to the point where the atmospheric density becomes significant and the particles burn up in the atmosphere.

Table 11-5. Data Concerning Meteoroids

METEOR VISUAL MAGNITUDE (M)	MASS ($gm - sec^2$ /cm)	RADIUS (μ)	ASSUMED VELOCITY (km/sec)	NUMBER STRIKING EARTH (per day)
0	25.0	49,200	28	-
1	9.95	36,200	28	-
2	3.96	26,600	28	-
3	1.58	19,600	28	-
4	0.628	14,400	28	-
5	0.250	10,600	28	2×10^{8}
6	9.95×10^{-2}	7,800	28	5.02×10^{8}
7	3.96×10^{-2}	5,740	28	1.27×10^{9}
8	1.58×10^{-2}	4,220	27	3.18×10^{9}
9	6.28×10^{-3}	3,110	26	7.97×10^{9}
10	2.50×10^{-3}	2,290	25	2×10^{10}
11	9.95×10^{-4}	1,680	24	5.20×10^{10}
12	3.96×10^{-4}	1,240	23	1.27×10^{11}
13	1.58×10^{-4}	910	22	3.18×10^{11}
14	6.28×10^{-5}	669	21	7.97×10^{11}
15	2.50×10^{-5}	492	20	2×10^{12}
16	9.95×10^{-6}	362	19	5.02×10^{12}
17	3.96×10^{-6}	266	18	1.27×10^{13}
18	1.58×10^{-6}	196	17	3.18×10^{13}
19	6.28×10^{-7}	144	16	7.97×10^{13}
20	2.50×10^{-7}	106	15	2×10^{14}
21	9.95×10^{-8}	78.0	15	5.02×10^{14}
22	3.96×10^{-8}	57.4	15	1.27×10^{15}
23	1.58×10^{-8}	39.8*	15	3.18×10^{15}
24	6.28×10^{-9}	25.1*	15	7.97×10^{15}
25	2.50×10^{-9}	15.8*	15	2×10^{16}
26	9.95×10^{-10}	10.0*	15	5.02×10^{16}
27	3.96×10^{-10}	6.30*	15	1.27×10^{17}
28	1.58×10^{-10}	3.98*	15	3.18×10^{17}
29	6.28×10^{-11}	2.51*	15	7.97×10^{17}
30	2.50×10^{-11}	1.58*	15	2×10^{18}
31	9.95×10^{-12}	1.00	15	5.02×10^{18}

Note:

* Maximum radius permitted by solar light pressure

where

M_{22} = The mass of magnitude 22 meteoroids, lb-sec^2/ft

V = Velocity of magnitude 22 meteoroids (see Table 11-5), ft/sec

r = Distance between impact point and the spacecraft center of mass, ft

n_{22} = Number of hits per orbit (See Table 11-6)

The numerical values which apply to this case are:

$M_{22} = 4 \times 10^{-8}$ gm - sec^2/cm

V = 15 km/sec

r = 5 ft

n_{22} = 0.88.

Substituting numerical values and the appropriate conversion factors gives,

$$H_{max} = 4 \times 10^{-8} \times 2.2 \times 10^{-3} \times 15 \times 3.28 \times 10^{3} \times 5 \times 0.88$$
$$= 1.9 \times 10^{-5} \text{ ft-lb-sec.}$$

Table 11-6. Meteoroid Impacts for 325-Nautical Mile Orbit

Meteor Visual Magnitude	Mass (gm-sec^2 /cm)	Number Striking Spacecraft Per Orbit	Number Striking Spacecraft Per Year	Percent Probability Of Hitting at Least One Time	
				In One Orbit	In One Year
10	2.5×10^{-3}	1.4×10^{-5}	7.3×10^{-2}	-	7
11	1×10^{-3}	3.4×10^{-5}	1.8×10^{-1}	-	16.5
12	4×10^{-4}	8.8×10^{-5}	4.7×10^{-1}	-	37.5
13	1.6×10^{-4}	2.2×10^{-4}	1.2	-	70
14	6.3×10^{-5}	5.4×10^{-4}	2.9	-	94.5
15	2.5×10^{-5}	1.4×10^{-3}	7.3	-	100
16	1×10^{-5}	3.4×10^{-3}	18	-	100
17	4×10^{-6}	8.8×10^{-3}	47	1	100
18	1.6×10^{-6}	2.2×10^{-2}	1.2×10^{2}	2	100
19	6.3×10^{-7}	5.4×10^{-2}	2.9×10^{2}	5	100
20	2.5×10^{-7}	1.4×10^{-1}	7.3×10^{2}	13	100
21	1×10^{-7}	3.4×10^{-1}	1.8×10^{3}	29	100
22	4×10^{-8}	8.8×10^{-1}	4.7×10^{3}	58.5	100

In calculating the mass expulsion requirements for one year, all of the particle sizes between magnitudes 13 and 22 must be considered since they all have a larger than 50 percent probability of striking the spacecraft in the one year period. Assuming that the cumulative effect of the meteroids would be equivalent to the total meteoroid mass of all magnitudes acting at the center of pressure, the angular impulse required for one year is given by:

$$\Delta H = M_T \times V \times \ell$$

where

$$M_T = \sum_{i=13}^{i=22} M_i n_i$$

M = Mass of meteoroids of magnitude i, $lb\text{-}sec^2\text{-}ft$

n_i = Number of meteoroids of magnitude i to strike the spacecraft in one year (see Table 11-6)

V = Velocity of meteoroids (see Table 11-5), ft/sec

ℓ = Distance from center of mass to center of pressure, ft

Substituting the numerical values given in Table 11-6 into the above expression and solving for M_T yields 1.85×10^{-3} gm-sec^2/cm. From Table 11-5 the average velocity of the particles in the magnitude range from 13 to 22 is approximately 20 km/sec. Referring to Section 13.5.3, the distance from the spacecraft center of mass to the center of pressure is $\sqrt{2.5^2 + 0.8^2} = 2.63$ inches or 0.218 feet. Substituting numerical values and the appropriate conversion factors the angular impulse required for one year is:

$$H = 1.85 \times 10^{-3} \times 2.2 \times 10^{-3} \times 20 \times 3.28 \times 10^{3} \times 0.218$$

$$= 5.82 \times 10^{-2} \text{ lb-sec-ft.}$$

Comparing the angular impulse and momentum storage requirements for the gravity gradient, aerodynamic drag, and solar pressure disturbance torques, with those resulting from meteoroid impacts indicates that the latter are negligible.

Since the Mission C orbit represents the worst case for meteoroid impacts, and it imposes negligible requirements on the attitude control subsystem, Missions A and B were considered negligible also.

11.3.5 MAGNETIC FIELD

Torques will be exerted on the spacecraft due to the magnetic interaction of the earth's ambient magnetic field with ferromagnetic materials and current circuits on the vehicle. These magnetic effects can be considered in three groups: (1) permanent magnet effects, (2) induced magnetic effects, and (3) current loops.

11.3.5.1 Governing Equations

Permanent magnetic effects result from components which act like permanent magnets. Some of the more common sources are d-c motors and inductors of transformers which carry direct current in their windings. Any ferromagnetic material can exhibit permanent magnetic effects since all ferromagnetic materials have a finite residual flux density and a coercive force. This material can become magnetized during fabrication, test, storage, etc., and retain a portion of this magnetization after removal of the magnetizing force. The magnitude of the retained flux is a function of the geometrical shape of the ferromagnetic material, its residual flux and coercive force, and the magnitude of the magnetizing force. The permanent magnetic torque is given by the fundamental equation

$$T_p = \frac{B\,V\,H}{4\,\pi} \text{ dyne-cm} \qquad (8)$$

where T_p = Permanent Magnet Torque, dyne-cm

B = Internal Flux Density, gauss

H = External Field Intensity, oersteds

V = Volume, cm^3.

Induced magnetic effects result from a difference in the internally stored magnetic energy in ferromagnetic materials as a function of position relative to an external magnetic field. Where there is a difference in the stored magnetic energy, the ferromagnetic material will align itself so that the stored energy is maximized. As the shape of the material departs from symmetry, the difference in stored energy increases. For example, a sphere of ferromagnetic material will show no preferred orientation. A rod is not symmetrical and will orient itself so that the axis of the rod is in the direction of the field. A sheet of material will orient its plane parallel to the field. The greater the asymmetry, the greater the aligning torque for a given volume of material. In addition to symmetry, a second important criteria is the magnetic characteristics of the material. The torque imparted by the stored magnetic energy is:

$$T_I = \frac{B\,H\,V}{8\,\pi} \text{ dyne-cm} \qquad (9)$$

where T_I = Induced stored magnetic energy, dyne cm

B = Internal flux density, gauss

H = Internal field intensity, oersteds

V = Volume, cm^3

Thus, the material having the greatest flux density for the given field will produce the greatest stored energy, or stated differently, the internal energy is proportional to the permability of the material.

Currents flowing in a closed electrical circuit in a magnetic field will produce a torque. This torque is proportional to the number of ampere turns in the loop and the loop area. The d-c component of current is the only one which will produce a torque; the a-c component will average out to zero. The basic equation for the torque produced by a current loop is given by

$$T_c = 0.1\,HAIN \text{ dyne cm} \qquad (10)$$

where T_c = Torque produced by current loop, dyne-cm

A = Area of loop, cm^2

I = Current, amperes

N = Turns

H = External field intensity, oersteds.

The torque on the current loop will tend to align the loop with the magnetic field. Since the spacecraft is not defined in detail it is impossible to account for all the potential disturbance torques resulting from magnetic field effects. In this study only magnetic torques associated with the thermionic generator current loop and the nickel solar concentrator were considered.

11.3.5.2 Numerical Calculations

Since the magnetic disturbance torques are directly proportional to the earth's magnetic field strength, which is a function of altitude, the torques will first be estimated for the 325-nautual mile orbit (worst case) associated with Mission C, and then scaled down by the field strength for Missions A and B.

The magnetic field intensity, H, in a 325-nautual mile orbit is approximately 0.3 oersteds. The solar concentrator design presented in Section 8.3.1 would be made up of approximately 770 cubic centimeters of nickel. The concentrator is 50 inches in diameter and has a skin thickness of 0.015 inches which yields a diameter to thickness ratio of 3330. Assuming that the concentrator were to come in contact with a magnetic field it would become magnetized and for a D/t ratio of 3330 the saturation value of the internal flux density, B, would be approximately 1300 gauss. Substituting numerical values into Equation 8 gives the torque on the spacecraft resulting from permanent magnetic effects in the nickel solar concentrator.

$$T_p = \frac{1300 \times 770 \times 0.3}{4\pi} = 23,900 \text{ dyne-cm}$$

$$\text{or } 1.76 \times 10^{-3} \text{ ft-lb}$$

This torque will be the result of random magnetization across the face of the concentrator in a fixed but unknown direction.

The torque imposed on the vehicle as a result of the magnetic field induced in the concentrator from the earth's magnetic field is given by Equation 9. For an earth magnetic field intensity of 0.3 oersteds and a concentrator D/t ratio of 3330 the internal flux density would be approximately 500 gauss and the internal field intensity 0.15 oersteds. Substituting numerical values into Equation 9 gives

$$T_I = \frac{500 \times 0.15 \times 770}{8\pi} = 2290 \text{ dyne-cm}$$

$$\text{or } 1.69 \times 10^{-4} \text{ ft-lbs.}$$

This torque will attempt to align the plane of the solar concentrator parallel to the ambient field.

The torque produced by the thermionic generator current loop can be approximated by applying Equation 10. For the thermionic system design presented in Section 8, the current loop would be approximately 5.5 feet long and assuming a 0.1-inch spacing between leads the area of the loop would be $(5.5 \times 0.1/12)\ 6.45 \times 144 = 42.6 \text{ cm}^2$. At the design point the thermionic generator current output is 42.2 amperes. Substituting numerical values into Equation 10 yields:

$$T_c = 0.1 \times 0.3 \times 42.6 \times 42.2 \times 1$$

$$= 53.8 \text{ dyne-cm or } 4.1 \times 10^{-6} \text{ ft-lbs.}$$

This torque will tend to align the plane of the loop perpendicular to the ambient field.

The torques experienced in the 1000-nautical mile orbit (Mission A) will be approximately 35 percent of those calculated for the 325-nautical mile orbit. The mean distance from the earth during the elliptical orbit will be equal to the semi-minor axis of the ellipse, or

10,250 nautical miles. The torques at this altitude will be assumed to be two percent of those calculated for the 325-nautical mile case.

The information is now available with which the mass expulsion and momentum storage requirements can be computed. There will not be any cumulative disturbance torques due to the permanent or induced magnetic effects and therefore no mass expulsion requirements are necessitated by them. The momentum storage requirements will be calculated on the basis that a constant torque equal to 70 percent of the peak torque value is applied for one quarter of an orbit (the torque polarity will be reversed after one quarter of an orbit).

The current loop torques will be cumulative for those orbits that have a dark period. This is because there is no current existing during the dark portion of the orbit and therefore the momentum acquired during the daylight segment of the orbit will not be cancelled by an opposite polarity momentum that would have resulted had there been no darkness.

Using the assumptions outlined above the momentum storage and mass expulsion requirements for each mission are computed below.

A. Mission A

The Mission A spacecraft has an orbit period of 124 minutes so the momentum storage requirement is

$$\Delta H = \frac{\text{Orbit Period}}{4} \times (T_P + T_I + T_C) \; 0.7 \times 0.36$$

$$= \frac{124}{4} \; 60 \times (1.76 + 0.169 + 0.0041) \times 10^{-3} \times 0.7 \times 0.36$$

$$= 0.92 \text{ ft-lb-sec.}$$

The cumulative momentum in one orbit resulting from the current loop torque is

$$H_{cum} = \left(\frac{\text{Orbit Period}}{2} - \text{Avg. Dark Period}\right) T_C \times 0.36$$

$$= \left(\frac{124}{2} - 26\right) 60 \times 0.41 \times 10^{-5} \times 0.36$$

$$= 5.17 \times 10^{-3} \text{ ft-lb-sec.}$$

The total impulse required for one year then is

$$\Delta H_{cum} = H_{cum} \text{ (per orbit) x number of orbits with dark periods}$$

$$= 5.17 \times 10^{-3} \times 203 \text{ days} \times 11.6 \text{ orbits/day}$$

$$= 12.3 \text{ ft-lb-sec.}$$

B. Mission B

The Mission B spacecraft has an orbit period of 840 minutes so the momentum storage requirement is

$$\Delta H = \frac{840}{4} \times 60 \times 1.93 \times 10^{-3} \times 0.7 \times 0.02$$

$$= 0.34 \text{ ft-lb-sec.}$$

The average dark period in the elliptical orbit is 20 minutes. The cumulative momentum per orbit then as a result of the current loop torque is

$$H_{cum} = \left(\frac{840}{2} - 20\right) 60 \times 0.41 \times 10^{-5} \times 0.02$$

$$= 1.97 \times 10^{-3} \text{ ft-lb-sec.}$$

The total impulse required for one year then is

$$\Delta H_{cum} = 1.97 \times 10^{-3} \times 295 \text{ days} \times 1.71 \text{ orbits/day}$$

$$= 0.993 \text{ ft-lb-sec.}$$

C. Mission C

The Mission C spacecraft has an orbit period of 96.7 minutes so the momentum storage requirement is

$$\Delta H = \frac{96.7}{4} \times 60 \times 1.93 \times 10^{-3} \times 0.7$$

$$= 1.96 \text{ ft-lb-sec.}$$

The average dark period in the 325-nautical mile orbit is 36 minutes and there are no orbits which do not involve a dark period. The cumulative momentum per orbit then as a result of the current loop torque is

$$H_{cum} = \left(\frac{96.7}{2} - 36\right) 60 \times 0.41 \times 10^{-5}$$

$$= 3.03 \times 10^{-3} \text{ ft-lb-sec.}$$

The total impulse required for one year then is

$$\Delta H_{cum} = 3.03 \times 10^{-3} \times 365 \frac{\text{days}}{\text{yr}} \times 14.9 \frac{\text{orbits}}{\text{day}}$$

$$= 16.5 \text{ ft-lb-sec.}$$

The angular impulse and momentum storage requirements resulting from the magnetic disturbance torques are summarized in Table 11-7.

If the nickel concentrator were replaced by an aluminum one, the only magnetic disturbance torques would be due to the current-loop effects. The momentum storage requirements were computed for this case using the same approach previously outlined except with the permanent and induced magnetic torques, T_P and T_I, respectively, equal to zero. These results are also shown in Table 11-7. It is apparent from a comparison of the results presented in Table 11-7 that if the nickel solar concentrator could be replaced by an aluminum one, the magnetic disturbance torques would be greatly reduced.

TABLE 11-7. Angular Impulse and Momentum Storage Requirements Resulting From Magnetic Torques

Control Axis	Maximum Angular Impulse Requirements Ft-Lb-Sec/Year			Momentum Storage Requirements Ft-Lb-Sec/Orbit		
	MISSION A 1000 NM	MISSION B 200 by 25,000 NM	MISSION C 325 NM	MISSION A 1000 NM	MISSION B 200 by 25,000 NM	MISSION C 325 NM
Roll	0	0	0	0	0	0
Pitch	12.3	0.99	16.5	$0.92/1.92 \times 10^{-3}$ [a]	$0.34/0.72 \times 10^{-3}$	$1.96/4.17 \times 10^{-3}$
Yaw	12.3	0.99	16.5	$0.92/1.92 \times 10^{-3}$	$0.34/0.72 \times 10^{-3}$	$1.96/4.17 \times 10^{-3}$

Note

a - The second number given under the momentum storage requirements is for the case when the solar concentrator is made from aluminum rather than nickel

11.3.6 ORBIT ECCENTRICITY

A spacecraft rotating about the earth and aligned to a set of earth referenced coordinate axes will have to rotate at a rate equal to the rate of change of the true anomaly of its orbit. The rate of change of the true anomaly must be a constant for a circular orbit in order to satisfy Kepler's law. When the orbit eccentricity is not zero, momentum must be added to or removed from the spacecraft in order to keep it aligned to its earth reference.

The spacecraft being considered in this study are all in earth orbits but they are aligned to a semi-inertial reference (i.e., the sun). Since the spacecraft are not earth oriented, there is no angular acceleration requirement about any of the principal axes when the vehicle is tracking its reference. Therefore, there are no disturbance torques due to orbit eccentricity.

11.3.7 SUMMARY OF ANGULAR IMPULSE AND MOMENTUM STORAGE REQUIREMENTS

The momentum storage and angular impulse requirements may be determined by taking the root sum squared of all the peak external and internal momentum disturbance sources acting on the spacecraft. The root sum square values are used to account for the fact that these peak values will not occur concurrently.

The momentum storage requirements must be based upon the root sum squared of all the peak momentum disturbance sources acting on each axis (pitch and yaw) of the spacecraft. The momentum storage device chosen must be capable of storing this total momentum for at least one orbit at which time the momentum may be unloaded by mass expulsion devices. The total angular impulse requirement must be based upon the impulse requirements for both axes. Since the peak momentum disturbance cannot occur in both axes at the same time the root sum squared of the pitch and yaw impulse requirements for each type of disturbance is then equal to the total impulse requirement. There would be some additional impulse requirements associated with the initial stabilization and acquisition sequence; however, these requirements should be negligible in comparison with the disturbance torque requirements.

The angular impulse and momentum storage requirements computed in the preceding sections for the individual disturbance torques are summarized in Tables 11-8 and 11-9. These tables include the effects of all the external disturbances and an assumed value for the internal momentum sources (i.e., tape recorders, gyros, etc.).

Table 11-8. Total Angular Impulse Requirements For One Year (Pitch Plus Yaw Axes)

DISTURBANCE SOURCE	ANGULAR IMPULSE REQUIREMENTS FT-LB-SEC/YR		
	MISSION A 1000 NM	MISSION B 200 by 25,000 NM	MISSION C 325 NM
Gravity Gradient	472	20.0	772
Aerodynamic Drag	0	73.4	0
Solar Pressure	66.8	69.0	44.8
Micrometeorites	0	0	0
Magnetics	24.6	2.0	23.0
Orbit Eccentricity	0	0	0
ROOT SUM SQUARED TOTAL	394	115.0	588

Table 11-9. Momentum Storage Requirements For One Orbit (Pitch And Yaw Axes)

Disturbance Source	Momentum Storage Requirements Ft-Lb-Sec/Orbit		
	MISSION A 1000 NM	MISSION B 200 by 25,000 NM	MISSION C 325 NM
Gravity Gradient	6.49×10^{-2}	2.0×10^{-2}	8.2×10^{-2}
Aerodynamic Drag	0	5.87×10^{-2}	14.7×10^{-3}
Solar Pressure	8.52×10^{-3}	5.68×10^{-2}	4.1×10^{-3}
Micrometeorites	0	0	0
Magnetics	$0.92/1.92 \times 10^{-3}$ (a)	$0.34/0.72 \times 10^{-3}$	$1.96/4.17 \times 10^{-3}$
Orbit Eccentricity	0	0	0
Internal Disturbances	5×10^{-2}	5×10^{-2}	5×10^{-2}
ROOT SUM SQUARED TOTAL	0.92/0.09	0.35/0.1	2.0/0.10

Note

(a) The second number given is for the case when the solar concentrator is made from aluminum rather than nickel.

Now that the type and magnitude of the disturbance torques have been identified, a method for handling the imposed angular impulse and momentum storage requirements can be considered.

11.4 ATTITUDE CONTROL TECHNIQUES

How the attitude control subsystem performs its functions depends primarily on the technique chosen for the fine pointing control. The fine pointing control not only provides the sun orientation requirements, but is generally an integral part of maintaining the space-

craft attitude during the shadow period, reorientation of the vehicle after each shadow period, and initial stabilization and orientation of the spacecraft. For this reason the first step is to select the fine pointing control technique to be used.

An additional area to be considered, which is not always linked with the fine pointing control, is the means of despinning the spacecraft if the requirement exists. The IMPROVED DELTA DSV-3E launch vehicle has been chosen for Missions A and B and since it has a spin stabilized third stage, there is a requirement to despin the spacecraft in these two cases. The Mission C spacecraft uses the IMPROVED DELTA DSV-3H which does not employ a spin stabilized final stage and there is no requirement to despin the vehicle.

The various techniques for performing the fine pointing control and despinning the spacecraft are considered below and a method selected for this application.

11.4.1 FINE POINTING CONTROL

The fine pointing control must be able to align the spacecraft roll axis (same as solar concentrator optical axis) within $\pm$ 0.1 degree of the sunline (whenever the sun is visible) for a mission design life of one year. To accomplish this the system must remove the momentum from the vehicle which accumulates due to the disturbance torques.

The following three methods of fine pointing control were considered:

a. Cold gas-flywheels
b. Cold gas-derived rate limit cycle
c. Solar pressure.

Each of these approaches is discussed below with the selected technique considered first.

11.4.1.1 Cold Gas-Flywheel

The method selected for the fine pointing control of the roll axis to the sunline is the cold gas-flywheel technique. With this method flywheels are used to store the momentum imparted to the spacecraft by disturbance torques, and cold gas expulsion is used to unload the flywheels when their momentum storage capacity is reached. This method was selected because it is a very efficient one for dealing with cyclic disturbance torques, can readily maintain the precise accuracy requirements needed, has proven flight experience, and makes good use of its basic components for initial stabilization of the spacecraft. A detailed description of this control system and its mode of operation is included in Section 11.5.1.1.

11.4.1.2 Cold Gas - Derived Rate Limit Cycle

This control scheme utilizes a position error sensor and cold gas expulsion torquing elements. Damping is obtained by feeding back pseudo rate information and combining it with the sensor output. This pseudo or "derived rate" information is obtained by integrating the vehicle's control acceleration when it is present. The theory is that the control torques are much larger than the disturbance torques, and thus the vehicle's angular rate is solely a function of the on time of the control jets. The control jets cause the vehicle to have a constant acceleration and this acceleration may then be integrated to obtain the instantaneous rate. This integration is accomplished by feeding the pneumatic solenoid actuation signal into a lag network, the output of which is then combined with the position sensor error signal (see Figure 11-5). The lag network output does not represent the angular rate unless the time constant of the network is large compared to the time between jet firings. The operation of this system is such that the spacecraft operates at a limit cycle rate, moving from one side of the pneumatic deadband to the other side (see Figure 11-6).

As shown in Section 11.3.7, the magnetic disturbance torques represent the largest cyclic torque acting on the vehicle. To maintain an optimum gas-use efficiency, it is desirable to have a limit cycle in which gas is discharged at one limit only (i.e., the torque impulse

of the pneumatic jets just balance the torque impulse of the disturbance). This is a 100 percent efficient limit cycle since the theoretical minimum quantity of gas is being used (see Figure 11-7).

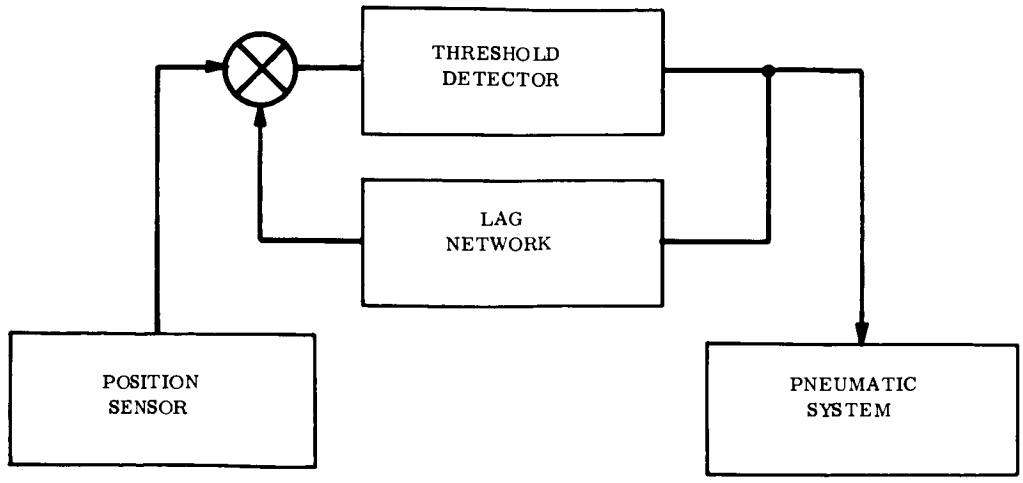

Figure 11-5. Block Diagram of Derived-Rate Control System

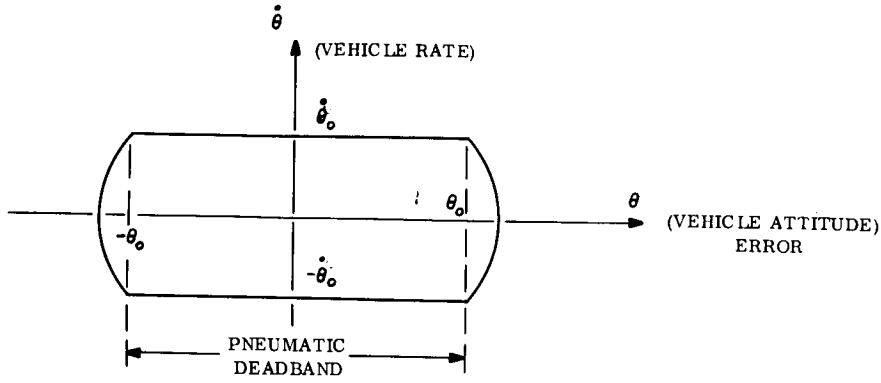

Figure 11-6. Limit Cycle Operation With No Disturbing Torques

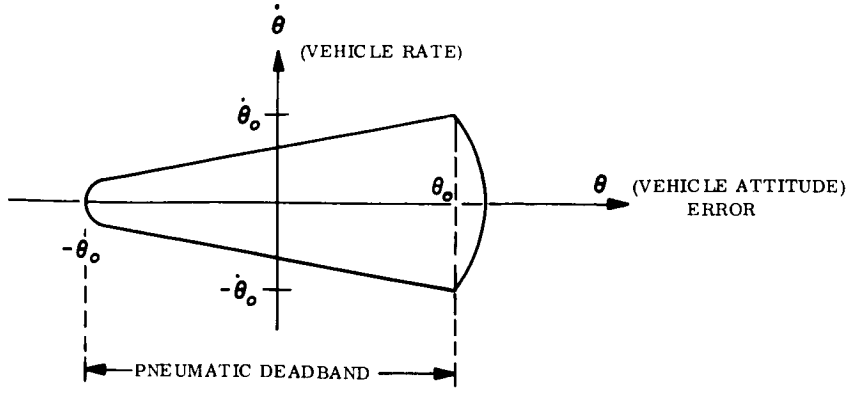

Figure 11-7. Optimum Limit Cycle Operation With Constant Disturbing Torques

The optimum limit cycle may be found by integrating the following equation:

$$T = I \ddot{\theta} \tag{11}$$

where

T = Disturbance torque about the controlled axis

I = Moment of inertia about the controlled axis

$\ddot{\theta}$ = Angular acceleration about the controlled axis.

Integrating Equation 11 with respect to time gives

$$\dot{\theta} = \frac{T}{I} t + \dot{\theta}_o \tag{12}$$

Integrating once more,

$$\theta = 1/2 \frac{T}{I} t^2 + \dot{\theta}_o t + \theta_o \tag{13}$$

Eliminating t by means of combining Equation 12 and 13 results in

$$(\theta - \theta_o) = 1/2 \frac{I}{T} (\dot{\theta} - \dot{\theta}_o)^2 + \dot{\theta}_o (\dot{\theta}_o - \dot{\theta}_o) \frac{I}{T} \tag{14}$$

where

θ_o = Half of the pneumatic deadband

θ = Instantaneous attitude error about the controlled axis

$\dot{\theta}$ = Instantaneous rate about the controlled axis

$\dot{\theta}_o$ = Optimum limit cycle rate.

The objective is to have the instantaneous rate, $\dot{\theta}$, equal zero and the instantaneous attitude error equal $(-\theta_o)$ at the maximum excursion point (see Figure 11-7),

$$2 \theta_o = 1/2 (\dot{\theta}_o)^2 \frac{I}{T} \tag{15}$$

The maximum disturbances, as shown in Section 11.3.5, are due to magnetic torques and may be considered to be an average magnitude of 1.4×10^{-3} ft-lb. The fine pointing requirements dictate a pneumatic deadband of $\pm$ 0.1 degrees. Setting $T = 1.4 \times 10^{-3}$ ft-lb, θ_o = 0.1 degrees, and I = 35.2 slug-ft^2 into Equation 15 and solving for $\dot{\theta}_o$,

$$\dot{\theta}_o = \left(\frac{4 \times 1.4 \times 10^{-3} \times 0.1}{35.2 \times 57.3} \right)^{1/2} = 0.53 \times 10^{-3} \text{ rad/sec} \quad \text{or } 0.03 \text{ deg/sec} \tag{16}$$

Substituting this value of $\dot{\theta}_o$ (in radians/second) into Equation 12 and solving for t yields 13.3 seconds. A limit cycle period of 26.6 seconds is completely impractical since it would necessitate over one million solenoid firings for the one year mission life and present state-of-the-art limits solenoid operations to approximately 50,000. In addition, the weight of the gas required would lie completely out the realm of practicality.

It should be pointed out that even if the magnetic disturbance torques were made negligible by using an aluminum rather than a nickel solar concentrator, the cold gas-derived rate limit cycle approach still would not be practical because of the excessive number of solenoid firings. Assumung the magnetic disturbances were negligible, the next most significant disturbance is that due to gravity gradient. The average gravity gradient torque for the 325-nautical miles orbit is 2.7×10^{-5} ft-lb. Substituting this value of torque into Equations 12 and 15, the optimum limit cycle rate would be 41.9×10^{-4} degrees/second and the time between solenoid firings would be approximately 192 seconds. This condition would require over 160,000 solenoid firings per year which is still over three times greater than the present state-of-the-art capability.

11.4.1.3 Solar Pressure Control Systems

Two solar pressure control schemes were considered for the fine pointing mode of operation. Both of these schemes require that the spacecraft center of pressure and center of mass both lie along the sun pointing roll axis and the center of mass is located closer to the sun side of the vehicle than the center of pressure when the solar concentrator is aligned to the sun. This construction will cause solar radiation pressure to always exert restoring torques on the vehicle. The difference between the two approaches is in the method of providing damping.

A. Solar Pressure-Balancing Vanes

With this method the spacecraft is balanced by adding motor driven movable surfaces at the end of a large moment arm, such as the ends of the solar paddles. When the position error increases to a preset value due to disturbance torques, a restoring pneumatic jet would fire and in so doing would signal a balancing vane to move a fixed increment. In this manner, the solar pressure force would balance the disturbance force after a number of oscillations of the limit cycle. An additional surface is added to each balancing surface for the purpose of damping; these surfaces are operated by means of bi-metallic thermo-mechanical actuators which adjust surface position through a time lag.

This method is most practical when the disturbance torques experienced by the vehicle are relatively constant and approximately the same magnitude as the solar radiation pressure torques. As shown in Section 11.3 this is not the case for this application, since the magnetic disturbance torques are cyclic and are several magnitudes higher than the solar pressure torques. Another disadvantage of this scheme is the complete loss of closed-loop control when the vehicle enters the shadow period. In addition it is not felt that this method could maintain $\pm$ 0.1 degree orientation accuracy because of its slow response characteristics.

B. Solar Pressure-Fluid Flywheel

This control approach appears more feasible than the balancing vane technique since it has momentum storage capability which makes it better suited to handling cyclic torques.

This system consists of a fine sun sensor connected to the pump of a fluid flywheel. When disturbance torques move the spacecraft off attitude null, the attitude error is sensed by the fine sun sensor and current is delivered to the pump. The polarity of the electrical connections to the pump are such that the flywheel will generate momentum to counteract the effect of the disturbance torque and move the vehicle back towards attitude null. Since the spacecraft's center of mass is required to be closer than the center of pressure to the

sun side of the vehicle, solar radiation pressure will also exert a restoring torque back towards attitude null. Thus the disturbance momentum, imparted to the vehicle and stored in the fluid flywheel, may be dumped by using the external torques due to solar radiation pressure.

This method is not acceptable for fine pointing in this application for the following reasons:

a. The solar radiation pressure must have the capability of dumping the cumulative disturbance momentum that is acquired each orbit. The major source of cumulative disturbance momentum is the gravity gradient for the Mission A and C orbits, and aerodynamic drag and gravity gradient for the Mission B orbit (see Section 11.3.7). The solar pressure restoring torque is proportional to the distance between the center of pressure and the center of mass multiplied by the sine of the attitude error angle (which must be maintained at a value less than 0.1 degrees). The elliptical orbit associated with Mission B would provide the most favorable conditions, since for a short portion of the one-year life there would be no dark periods occurring and the total 14 hour orbit period would be available to accumulate the necessary 9×10^{-2} ft-lb-sec of momentum resulting from gravity gradient and aerodynamic drag. Calculations for this case indicate that the center of pressure would have to be hundreds of feet behind the center of mass in order to have the cumulative disturbance torques cancelled in one orbit by solar pressure. Obviously this represents an impractical situation.

b. Since a cold gas mass expulsion system would still have to be incorporated on the vehicle for initial stabilization, there would not be any substantial savings in the number of components required.

c. There is much more flight experience available on motor driven flywheels than there is on fluid flywheels.

11.4.2 SPACECRAFT DESPIN

If the final stage of the launch vehicle is spin stabilized, as it is in the Mission A and B cases, the spacecraft spin about the roll axis after third stage cutoff will have to be reduced. Four techniques for accomplishing this were considered.

a. Solid propellant rockets
b. Cold gas (separate blow down tank)
c. Cold gas (high roll torque level on main tank)
d. Yo-Yo.

A description of each of these approaches follows.

11.4.2.1 Description of Despin Techniques

A. Solid Propellant Rockets

Two solid propellant rockets ignited by an electrical impulse signal to two redundant squib ignitors could provide the angular impulse for despin. The two rockets would be mounted on the vehicle's exterior surface or on the adapter between the final launch vehicle stage and the spacecraft. If they were located in the latter position despin would have to occur before separation.

Solid propellant rockets provide a proven, simple method for despin with high reliability when using redundant ignition squibs. Expense associated with qualifying the rockets is much higher than that associated with the other despin methods. Another disadvantage of solid rockets is that they provide the worst despin tolerance of the techniques considered. A typical despin tolerance for solar rockets is $\pm$ 10 percent of the initial spin rate with transverse rates of several degrees per second due to thrust vector and center of gravity tolerances.

B. Cold Gas (Separate Blow Down Tank)

In this approach a cold gas storage tank, separate from the attitude control tank, would be charged with enough gas to despin the spacecraft. No pressure regulator would be used and despin would be initiated by an electric signal to a redundant squib burst disc. The thrust level would follow an exponential delay until the gas was exhuasted. The despin nozzles would be located on the spacecraft near the center of mass plane.

This approach offers reliability as high, or higher, than solid rockets. Additional vehicle complexity and weight is involved in mounting a second* tank and nozzle set on the spacecraft. Despin tolerance capability for this technique is approximately $\pm$ 5 percent.

C. Cold Gas (High Roll Torque Level on Main Tank)

This technique is similar to the preceeding one except that the cold gas is supplied from the main attitude control tank through the pressure regulator. A high thrust level would be achieved by large nozzle areas. A timed electrical pulse would hold the solenoid valves open for the period required to provide the required despin impulse.

This approach requires one extra solenoid valve and two extra nozzles in the attitude control pneumatic system. These solenoids and nozzles would be sized for high thrust and would significantly increase the probability of large gas leaks occuring.

D. Yo-Yo

Despin by the Yo-Yo method would be accomplished through torque exerted on the vehicle by wire cables attached to weights which are allowed to unwind from the spinning spacecraft, or from around the final stage booster if despin is accomplished prior to separation from the third stage. The cables would be held in the wrapped position until freed by an electrical signal to two squib release mechanisms.

* One tank and nozzle set is required for the fine pointing technique chosen.

The Yo-Yo method is a proven technique which provides high reliability. This approach requires additional structure in the form of a track to hold the cables, but the added weight is small. Despin tolerance with this scheme is very good and should result in negligible rates after despin. This characteristic is due to the fact that sizing the weights and lengths of the cables is solely dependent on the vehicle parameters, which may be accurately measured, and not on the initial spin rate.

11.4.2.2 Selected Despin Technique

The Yo-Yo despin method was selected because of its simplicity, proven reliability, and the low residual rates it provides after despin. The Yo-Yo mechanism would be mounted on the adapter between the third stage engine and the spacecraft. As a result despin would have to occur before separation from the third stage of the launch vehicle.

11.5 ATTITUDE CONTROL SUBSYSTEM DESIGN

Having selected the attitude control techniques to be used, this section combines them into the proposed subsystem design, describes how it operates, defines the major components involved and their size, weight and power requirements.

11.5.1 DESCRIPTION OF SUBSYSTEM

A block diagram of the attitude control subystem is given in Figure 11-8. The attitude control subsystem must control the spacecraft under three primary modes of operation:

a. Fine pointing control during the sunlight portion of the orbit
b. Initial stabilization and sun acquisition
c. Dark period operation and sun reorientation.

Each of these modes of operation are discussed further in the following sections.

11.5.1.1 Fine Pointing Control

The fine pointing mode of operation represents that portion of the mission when the spacecraft pitch and yaw attitude errors must be held to within $\pm$ 0.1 degree. The pitch and yaw fine pointing control systems would be functionally identical and are shown in Figure 11-9.

A fine sun sensor would be used as the primary attitude error sensing device. The sensor output saturates for errors greater than one degree. A second attitude sensor would be provided in the form of a thermal device that senses the position of the solar concentrator focal point with respect to the thermionic generator aperture. This sensor would be used as a backup for the fine sensor in the event that the concentrator optical axis and the fine sensor axis become misaligned, or the thermionic generator was displaced off the concentrator optical axis. The purpose for this backup sensor is discussed further in Section 11.5.2.4.

The destination of the fine sensor output would be dependent on whether the spacecraft was operating in a "continuous daylight" phase or in the normal "daylight-shadow" phase. For daylight-shadow operation the fine sensor output would be used to update a rate-integrating gyro. This would be accomplished by feeding a biasing current to the coils of the gyro torquer that was proportional to the difference between the gyro output and the fine sensor output. In this manner, the fine sensor would cancel the inherent drift of the gyro during the daylight portion of the orbit. When the vehicle entered the shadow period the gyro would continue to control its attitude, although its drift would no longer be cancelled by the fine sensor output. Thus the attitude error when the spacecraft emerged from the shadow would be directly proportional to the gyro drift. The gyro output would then be delivered to the input of a passive lead network, which would be used for rate damping. The lead network would act as a differentiator and thus a measure of vehicle rate would be provided, together with attitude error, to the control system torquing devices.

The "continuous-daylight" control scheme would differ from the daylight-shadow approach only in the use of the rate-integrating gyro. In the continuous-daylight scheme, the fine

ROLL CONTROL LOOP

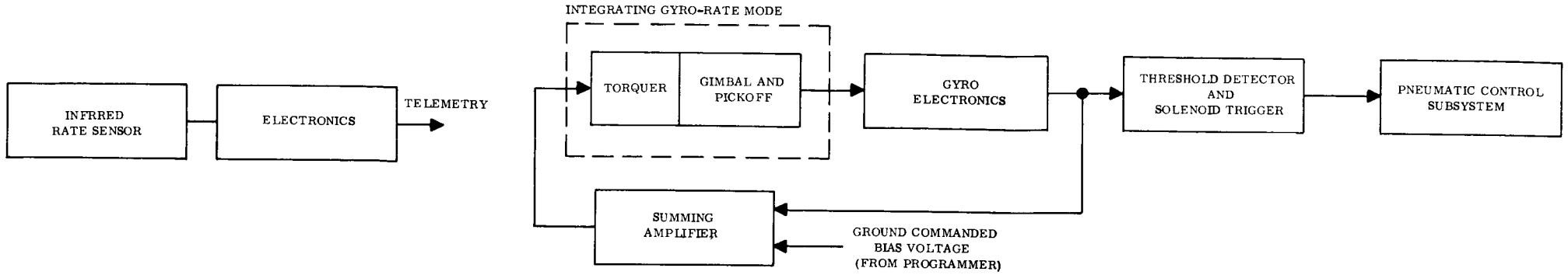

PITCH OR YAW CONTROL LOOP

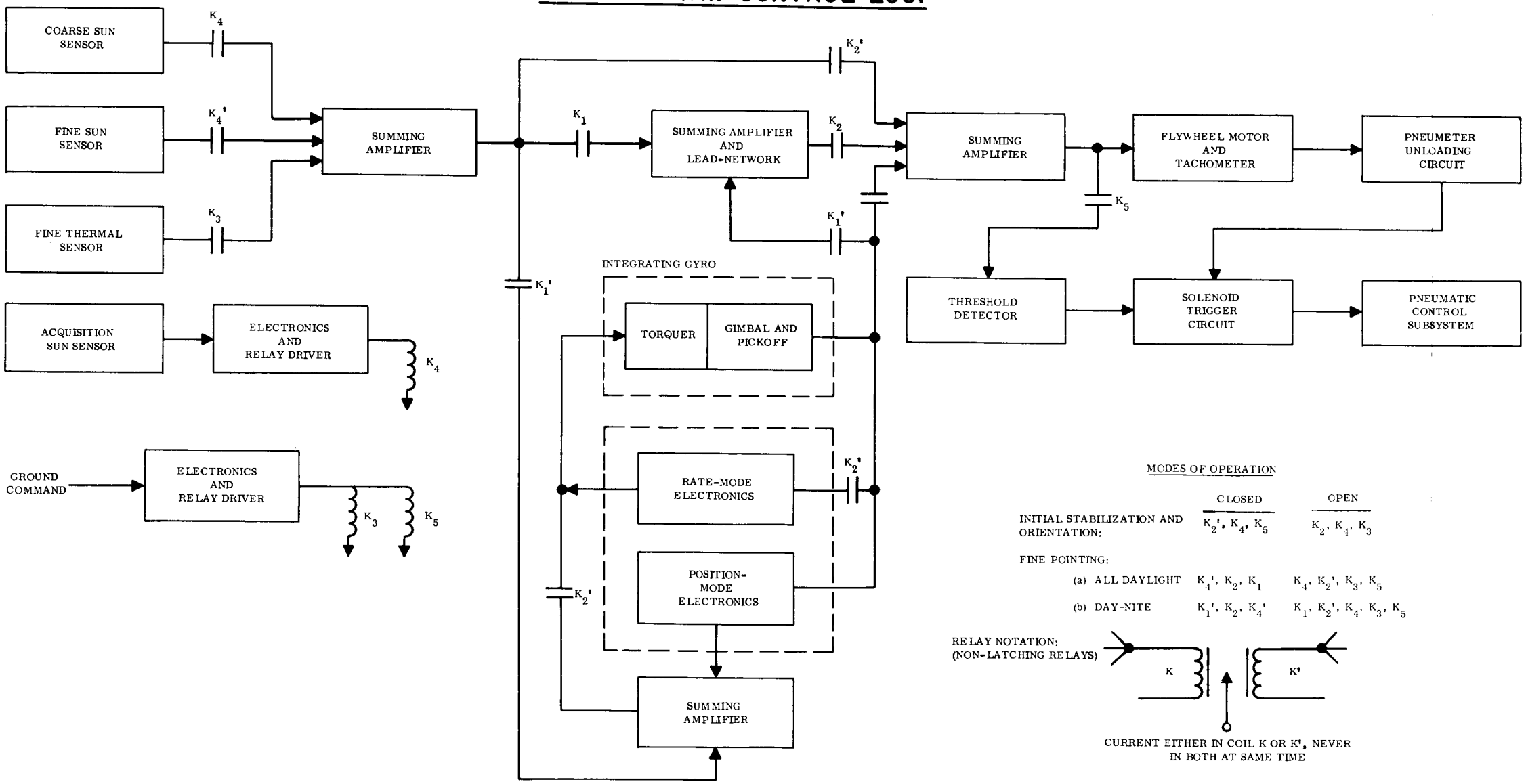

MODES OF OPERATION

	CLOSED	OPEN
INITIAL STABILIZATION AND ORIENTATION:	K_2', K_4, K_5	K_2, K_4, K_3
FINE POINTING:		
(a) ALL DAYLIGHT	K_4', K_2, K_1	K_4, K_2', K_3, K_5
(b) DAY-NITE	K_1', K_2, K_4'	K_1, K_2', K_4, K_3, K_5

RELAY NOTATION: (NON-LATCHING RELAYS)

CURRENT EITHER IN COIL K OR K', NEVER IN BOTH AT SAME TIME

Figure 11-8. Attitude Control System Block Diagram

a. DAYLIGHT FINE POINTING CONTROL SCHEME

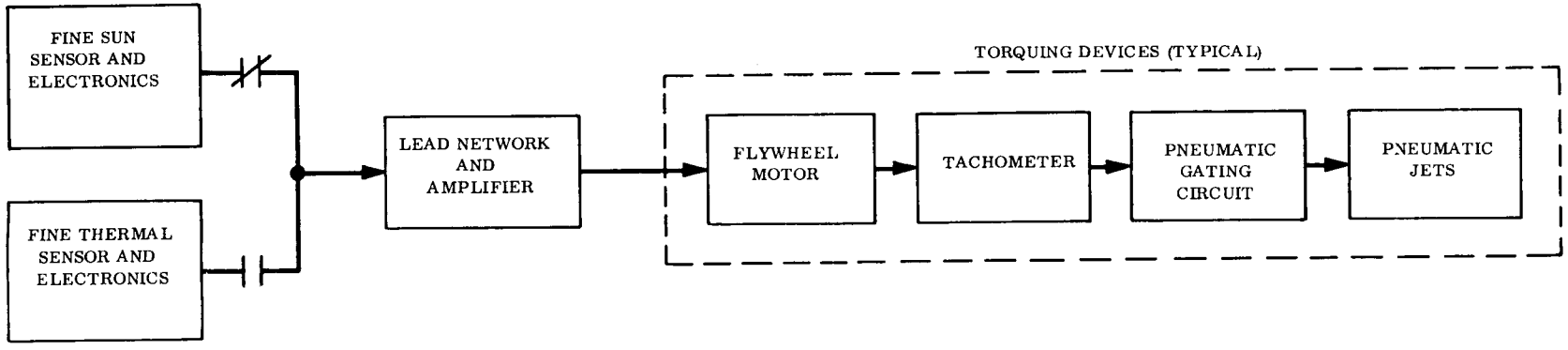

b. DAY-NITE FINE POINTING CONTROL SCHEME

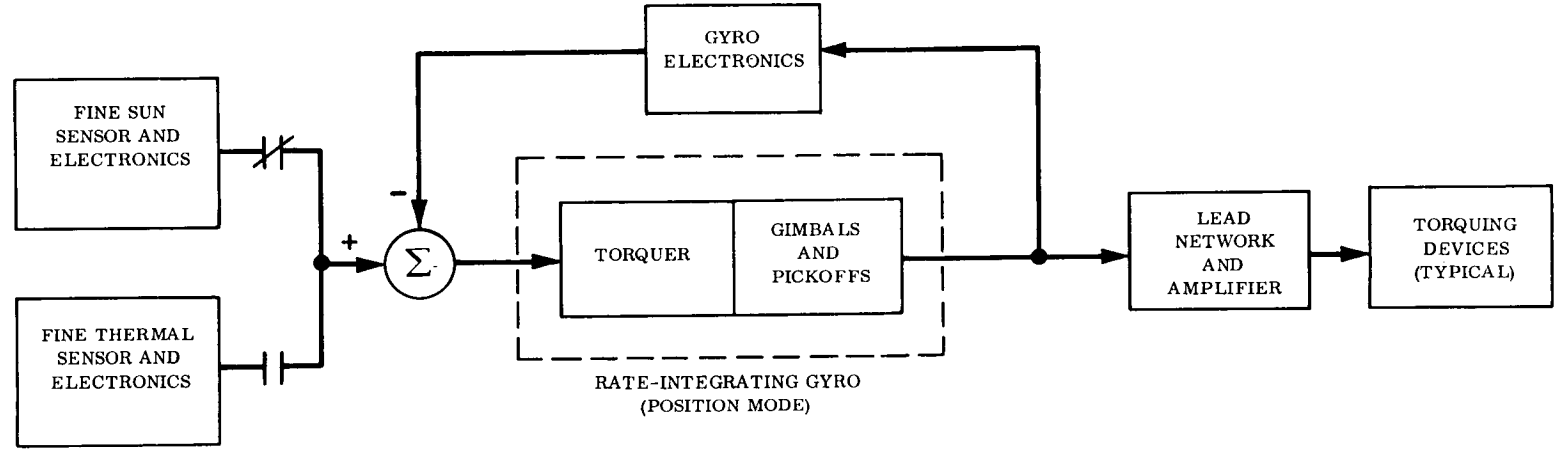

Figure 11-9. Fine Pointing Control Block Diagram

sensor output would be brought directly to the lead network, and from there to the control torquing devices. There would be no need for the gyro because position information would always be available from the fine sensor, since there would be no shadow periods. This continuous-daylight mode of operation could be used for approximately six months in the Mission A (modified sun-synchronous orbit) case and approximately seventy days in the Mission B (highly elliptical orbit) case. However, this technique could not be used in the Mission C (325 nautical mile orbit) case since there are no shadow-free orbits The advantage of providing a continuous-daylight as well as a daylight-shadow mode of operation for Missions A and B would be greater reliability. Although the gyro selected for the daylight-shadow mode would have a high probability of performing adequately for the one year mission life, the reliability figure would be improved if the required operating time was decreased. In addition, the power requirements would be decreased when the continuous-daylight scheme was in use, since the pitch and yaw gyros would be turned off. The only penalty incurred in providing the two control modes would be the added weight due to the addition of several relays and some circuit and harness modification. The change from one control mode to the other would be accomplished by ground-command.

The attitude error and rate information provided by the sun sensor and gyros would be fed into the flywheel motor control and would thereby control the speed of the flywheel. Fine attitude control about the pitch and yaw axes would be maintained by the method of momentum-interchange between the spacecraft body and the flywheels. Since the spacecraft would be a free body in space, any momentum that the spacecraft absorbed from external torquing forces would be maintained in an inertial sense (i. e. , the total momentum vector would remain in a fixed orientation in space and act through the spacecraft center of mass). The component of momentum about the spacecraft body axis would be transferred to the flywheel by changing the steady state speed of the flywheel whose spin axis was aligned parallel to the body axis. The acceleration of the flywheel would be accomplished by exerting a torque on the wheel through changes in its control phase excitation. This torque would be reflected in the opposite sense on the spacecraft body, thereby resulting in a transfer of momentum from the spacecraft body to the flywheel. Momentum would be transferred between the flywheel and the spacecraft up to the maximum

storage capacity of the flywheel, which would be limited by the no-load speed of the flywheel motor and the inertia of the flywheel.

The sequence of flywheel fine control would be as follows. As external torques were applied to the vehicle, the spacecraft would begin to move off attitude null. This attitude error would be sensed by the fine sensor and a signal applied to the control phase of the flywheel, causing it to increase in speed and apply a torque in a sense opposite to the disturbance torque. In this manner, body momentum caused by disturbing torques would be transferred to the flywheel. The attitude error would therefore be equivalent to that error required to maintain the flywheel at a speed that will cancel the body-absorbed momentum due to external torques. This momentum-storing technique operates most efficiently on vehicles that experience cyclic disturbance torques; the flywheel momentum storing capability is made larger than the maximum momentum imparted to the spacecraft by these cyclic torques, thus no external torques need be applied by the mass expulsion devices to counteract these disturbances.

In addition to the cyclic torques on the spacecraft, there would also be cumulative disturbance torques acting. As the momentum due to the combination of cumulative and cyclic torques absorbed by the flywheel increased, the wheel speed would increase to its no-load speed. At that point the flywheel could not absorb any additional momentum and it is referred to as a "saturated flywheel". Once saturated the flywheel could not respond to further increases in error signal and therefore could not control the spacecraft attitude until desaturated (slowed down). Momentum would be removed (or dumped) from the flywheel by the pneumatic reaction system. The action of expelled gas would apply an external torque to the spacecraft which would subtract from the total momentum about that axis. As the spacecraft rotated due to this external torque, a change in position would be noted by the fine sensor; this would decrease the signal to the control phase of the flywheel and it would decelerate. The resultant torque due to the flywheel deceleration would reduce the spacecraft body rate. Operation of the control loop would result in an equilibrium condition of zero body rate with the spacecraft holding the steady pointing error necessary to maintain the flywheel speed corresponding to the spacecraft momentum component about the body axis.

11.5.1.2 Initial Stabilization and Sun Acquisition

As discussed in Section 11.4.2, the spacecraft would be despun in the Mission A and B cases prior to separation from the final booster stage by the yo-yo technique. The residual angular rates about the pitch and yaw axes after the despin maneuver would be removed by a combination of cold gas torquing and momentum storing. The residual rates about the sun pointing or roll axis would be removed by cold gas torquing alone.

The sequence of events would be as follows. The yo-yo system would decrease the roll rates to less than $\pm$ 5 degrees per second, and leave maximum pitch and yaw rates of tenths of degrees per second (due to misalignment of the yo-yo support track with the control axes). Roll rate limiting would then be accomplished by using cold gas torquing for as long as the roll rate exceeded a prescribed value; a rate gyro and a threshold trigger circuit would be used to implement this technique (see Figure 11-10a). Since the spacecraft would experience large cyclic disturbance torques, relatively large capacity momentum storage devices must be used. The flywheels for Mission C and possibly Mission A would have the capacity to store the total initial momentum due to residual despin rates of up to several degrees per second. These flywheels would be held at zero speed until enabled and thus would have their full momentum storage capacity at the time of initial stabilization. Mass expulsion stabilizing techniques would not be required for the Mission C and possibly the Mission A cases. Further study will be necessary to confirm operation in this manner. The elliptical orbit would use a control scheme employing momentum wheels and mass expulsion for initial orientation. Disturbance torques would not be a factor during initial stabilization due to the short period envolved. Pitch and yaw attitude error information would be obtained from coarse sun sensors and combined with rate information obtained from rate-integrating gyros used in the rate mode (see Figure 11-10b). Rate information would be provided by gyros since the coarse sun sensors would not be operating in their linear region and thus would provide only a saturated output. The rate and position information would be delivered to the control phase of the flywheel which, by the method of momentum storing and mass expulsion momentum wheel unloading, would move the spacecraft sun pointing axis towards the sun. The acquisition sun sensor would

be used to sense when the sun was within the field of view of the fine sun sensor and determine when control should be switched to this sensor. The signal from the fine sensor itself could not be used since a null would be obtained for both zero attitude error and very large attitude errors.

The roll control loop, as shown in Figure 11-10a. would consist of a rate measuring gyro, a threshold trigger circuit, and pneumatic control. There would be no roll position control. For economy as well as technical convenience the gyro used for the roll axis would most likely be the same as those used in the pitch and yaw control loops. Determination of the roll rate threshold would require a more detailed study, but it will probably be of the same magnitude as the fine pointing mode rates existing in pitch and yaw in order to keep inter-loop coupling at a minimum. The long-term rate error uncertainty would be less than ± 10 degrees per hour for the type of gyro being considered; if it is determined that the rate threshold value need be less than 10 degrees per hour, an infrared sensor could be incorporated that would sense the earth at least once per orbit. This infrared earth sensor information would be telemetered to the ground and used to calculate the vehicle's roll rate. The capability would be provided to bias out the long term error rate uncertainty by means of ground command.

11.5.1.3 Dark Period Operation and Reorientation

During the orbit dark periods, the roll axis control would function exactly as it does during the daylight portion since it does not depend on a sun reference. The pitch and yaw control loops would remain in the fine pointing mode throughout the dark period. Since there would be no sun information available, the fine sun sensor would relinquish its part as the prime control sensing device to the position sensing gyro. Due to the fact that the sun sensor would no longer be biasing out the gyro, the gyro output may drift at the maximum short-term rate of 0.1 degree per hour. Therefore, for the worst case condition of a two hour dark period (Mission B), the vehicle would be 0.2 degree away from null upon emergence from the dark. At this point, the fine sun sensor would again resume its prime sensing function.

a. - ROLL CONTROL SCHEME

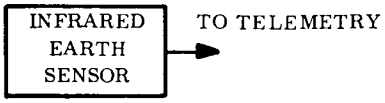

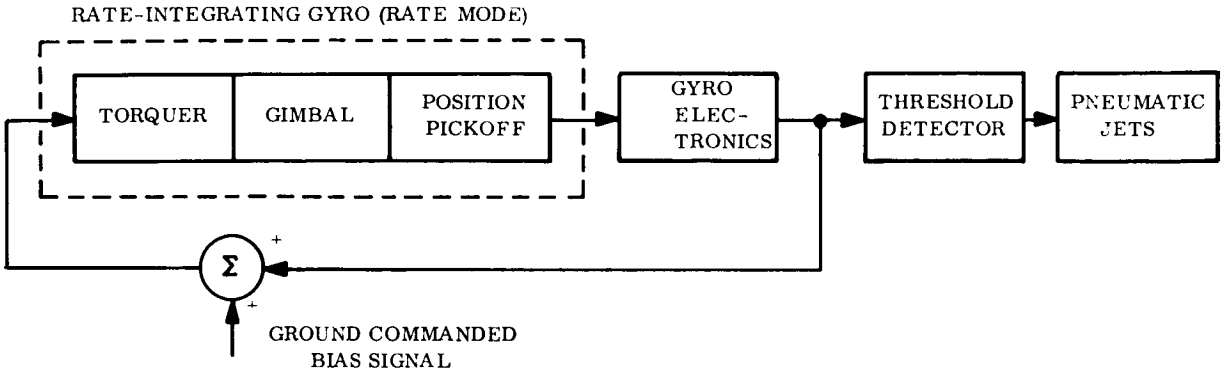

b. - PITCH AND YAW INITIAL STABILIZATION AND COARSE POINTING SCHEME

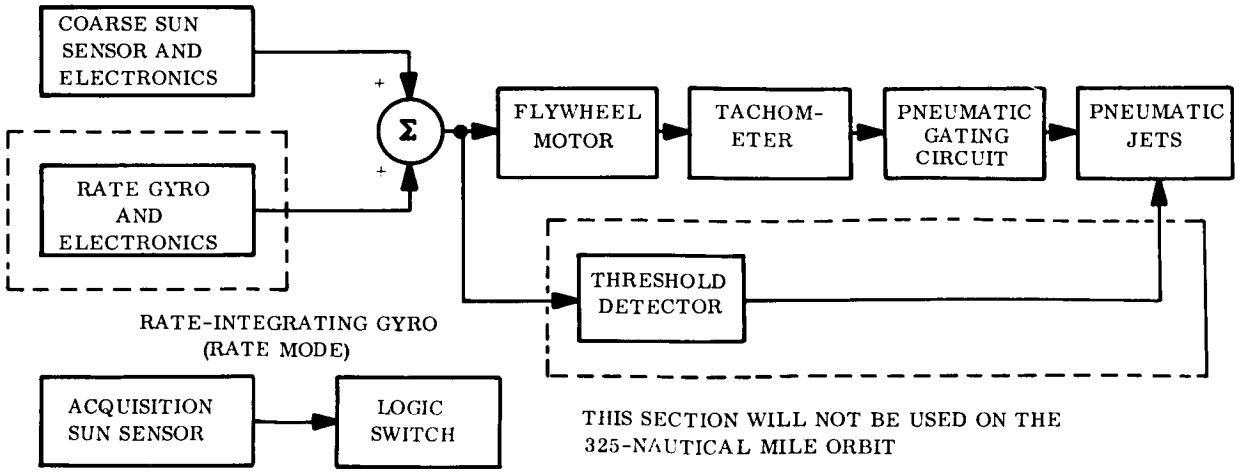

Figure 11-10. Block Diagram of Initial Stabilization and Orientation Scheme

11.5.2 DESCRIPTION OF COMPONENTS

A more detailed description of the components employed in the subsystem design and how they would perform their function is included here. Since detailed component designs are beyond the scope of this study the exact techniques employed in the component designs are unknown. However, the component descriptions given here assume approaches presently used in the design of similar components.

11.5.2.1 Flywheels

Flywheels would be used as the momentum storage devices in the proposed subsystem design. Two identical flywheels would be required, one each for the pitch and yaw control axes. The design characteristics of these flywheels are established in Section 11.5.4.1 and are tabulated in Table 11-10. The flywheel requirements are state of the art with similar flywheels having been developed for the Nimbus, OGO, and OAO spacecraft. The flywheels used on the OAO spacecraft are approximately the same size as those needed for this application. The OAO flywheels are manufactured by Bendix Corporation and have been flight qualified.

11.5.2.2 Integrating-Rate Gyro

The rate information required by the pitch, yaw, and roll axes for initial stabilization and orientation, and the position information required by the pitch and yaw axes during orbital park periods, will be provided by rate-integrating gyros. Three will be required, oriented to provide independent outputs for the pitch, yaw, and roll axes.

The type of gyro deemed suitable would be the Kearfott C70-2565 Alpha series. Flight experience exists on this type of gyro and sufficient running time has been accumulated on it to ensure a high reliability for up to ten thousand hours of operation. This gyro is also being considered for use on the Advanced Nimbus and OAO spacecraft. The null accuracy in the rate mode is better than 5×10^{-3} degrees/second and in the position mode is

approximately 10 arc seconds. The maximum dynamic range of the gyro in the rate mode is ± 4.5 degrees per second and is ± 6 degrees in the position mode (the dynamic range required will most likely be less than this).

11.5.2.3 Sun Sensors

Three types of sun sensors are employed in the subsystem design: (1) coarse sensor, (2) fine sensor, and (3) acquisition sensor. These three types of sun sensors are discussed below.

A. Coarse Sun Sensors

The function of the coarse sun sensors is to provide pitch and yaw attitude control signals for orienting the roll axis to the sunline. The coarse sensors would provide complete spherical coverage in each axis and should not require a null accuracy of better than ± 1 degree. Four coarse sensors would be used operating in pairs to provide pitch and yaw information. Each individual sensor would have a hemispherical field of view. The coarse sensors would be mounted on the sides of the spacecraft. The two sensors making up a pair would be mounted opposite each other as shown in Figure 13-3 in Section 13. The design characteristics considered most desirable for the coarse sun sensors are: simplicity, optimum transfer function (maximum slope) in the vicinity of null, and minimum interference from earth reflected sunlight. Sensors having these characteristics have been developed and flown on numerous space vehicles.

B. Fine Sun Sensor

The function of the fine sun sensors would be to provide pitch and yaw attitude control signals for precise sun orientation. The fine sun sensors would provide a field of view of approximately ± 5 degrees and should have a null accuracy of better than ± 1 minute of arc about each control axis. This requirement is close to that of the OAO fine sun sensors which have a field of view of ± 10 degrees and a null accuracy of ± 3 minutes of arc. If the

requirements specified for this application could not be met, a fine sun sensor with a smaller field of view could be used in conjunction with an intermediate sensor to be used between the coarse and fine sensor control modes. However, it is felt that the requirements specified could be fulfilled without the use of an intermediate sensor. The sensor output need be linear only to ± 1 degree.

C. Acquisition Sensor

The purpose of the acquisition sensor is to indicate when control should be switched from the coarse to the fine sun sensors. The signal from the fine sensor cannot be used for this purpose because a null will be obtained for both zero attitude error and large attitude errors. The acquisition sensor would perform this function by providing a constant output signal whenever the sun is within the field of view of the fine sensors, hence its field of view would be the same as the fine sun sensors.

11.5.2.4 Fine Thermal Sensor

The proposed subsystem design is very dependent on accurate alignment of the fine sun sensor axis with the solar concentrator optical axis. This can be done with a high degree of precision before launch but should the two axes become misaligned or should the thermionic generator be displaced off the concentrator optical axis after launch the thermionic generator performance could be seriously affected. This misorientation or displacement could be brought about by thermal expansion, deformation under launch loads, etc.

A potential way around this problem would be to sense the energy distribution at the thermionic generator aperture opening and attempt to maximize the energy entering the aperture rather than sensing the sun and depending on proper alignment between the sensor axis, the solar concentrator axis, and the thermionic generator aperture opening. In this manner the problem of misalignment between the sensor axis and the concentrator optical axis would be eliminated and if the thermionic generator were displaced off the

concentrator optical axis the thermal sensors would cause the solar concentrator to be misoriented so that the concentrator focal spot fell on the aperture opening. Of course the solar concentrator performance would be degraded somewhat depending on the amount of misorientation required. However, it would be better to accept this degradation and provide some energy to the thermionic generator than to provide essentially no energy at all, as would occur for the proposed design should the sensor and concentrator axes become badly misaligned or the generator displaced off the concentrator optical axes be sizeable.

The problem was considered in detail in Appendix P and the results indicate that the thermal sensor approach would provide much higher thermionic system performance, should relatively large values of misalignment error or generator displacement be encountered, than could be obtained with the fine sun sensor scheme.

Since no known development work has been done on the thermal sensor approach a proven concept cannot be presented but an approach which appears promising is described here. The thermal sensor would consist of a circular array of four thermocouples mounted on the thermionic generator heat shield at 90-degree intervals around the aperture opening. Since even under normal operating conditions the fringe energy in the focal plane implinges on the heat shield, this energy would provide a thermal input to the thermocouple sensors. The optimum distance for locating the thermocouples from the aperture center is discussed in Appendix P. These thermocouples would provide a millivolt output in relation to the energy flux implinging on them. These voltages would be used as error signals to the attitude control subsystem logic. The sensors would provide an error signal that would attempt to locate the solar concentrator so that the sensors received equal energy inputs and, as shown in Appendix P, this situation leads to near maximum energy input to the generator for the amount of concentrator misorientation required.

Of course, the major question in this approach is what to use for the thermal sensors. Thermocouples were suggested because they appear to be the most logical sensor to use at this point. The life of the thermocouples at the expected high temperatures might prove to be a problem. This potential problem was discussed with the General Electric

Instrument Department and they recommended the use of tungsten 5 percent rhenium/ tungsten 26 percent rhenium for the thermocouple material. They have been making W-5Re/W-26Re thermocouples in a molybdenum sheath with beryllium oxide insulation for RCA. In RCA's application these thermocouples are operated in furnaces at 3000^{o}F and atmospheric pressure with a dew point between -20 to +70. Through February 1965 these couples had been in continuous operation for over 6500 hours. The couples are checked daily against a pyrometer reading and the shift was less than 10^{o}F over this period (a repeatability of 0.33 percent). Although certaintly not conclusive, these results indicate that it may be possible to obtain the required life and repeatability with thermocouples.

If a system of this type could be developed, it is proposed that it be included as a back up to the fine sun sensor. Assuming thorough space simulation testing of the spacecraft before launch, it is felt that assurance can be established that proper alignemnt will prevail in space between the fine sun sensor axis and the concentrator optical axis, and the thermionic generator aperture and the concentrator axis. However, having the thermal sensor as a back up would provide a safety factor should large alignment or displacement errors be encountered and would also provide an opportunity to evaluate the thermal sensor approach in the space environment. Switching from the primary fine sun sensor to the back up thermal sensor and vice versa would be accomplished by ground command.

11.5.2.5 Roll Rate Infrared Sensor

An infrared sensor with a narrow field of view would be used to measure the spacecraft's roll rate for the purpose of updating the roll rate gyro. This would be accomplished only if it was determined that the gyro drift could not be tolerated. The method of operation would be as described below.

Four infrared earth sensors would be located on the spacecraft's periphery, spaced 90 degrees apart, with the center lines of their fields of view perpendicular to the roll axis. The roll of the spacecraft would provide the necessary scanning motion and a signal would

produced when the earth was in the field of view of one of the sensors. Measuring the time period between output signals on two adjacent sensors would provide a measure of the spacecraft roll rate. Four sensors would be necessary to insure that a roll rate measurement was obtained during each orbit. The output of each sensor would be recorded and stored in the telemetry subsystem for playback over the appropriate ground station. Using the information obtained from these infrared sensors, the roll gyro drift rate could be biased out by applying the necessary bias step voltage. This would be accomplished by ground command.

11.5.2.6 Cold-Gas Pneumatic System

A cold gas propulsion system, such as the one proposed for this application, is one in which heat is not employed to increase the specific impulse of the gas. The gas is stored on board the spacecraft at ambient temperature. Because of the low density of most gases, and the vehicle volume and tank mounting considerations, the gas is generally stored at pressures of 2500 psia and above. A pressure of 3000 psia was used in this study for sizing the tank.

The schematic of the pneumatic system is shown in Figure 11-11. The system consist of the following hardware:

a. A fill valve which is used to charge the system to its initial pressure
b. A check valve which prevents a back-flow of gas
c. A gas storage tank which is the reservoir for the activating gas
d. A high pressure transducer which is used for telemetry monitoring of gas consumption
e. A tank solenoid valve which provides a redundant safety feature to prevent excessive gas leakage (This solenoid is open in parallel with any other control solenoid.)
f. A pressure regulator used to provide a constant pressure to the nozzles
g. A low pressure transducer used for telemetry monitoring of the pressure regulator

h. Control solenoid valves which regulate the gas flow

i. Nozzles which produce the required thrust.

The pneumatic subsystem will be used along with the flywheels for initial stabilization in the Mission A and B cases but it appears that the flywheels alone will handle the Mission C case. In all three missions the pneumatic subsystem would be used to unload the flywheels when they become saturated and to limit the spacecraft roll rates. Pneumatics would not be required for reorientation after the spacecraft emerges from the earth's shadow since this would be handled by the flywheels.

Size and weight estimates for the gas and gas tank for each mission are presented in Section 11.5.4.2.

11.5.3 ALLOCATION OF POINTING ERROR

The fine pointing control must align the spacecraft sun pointing axis to within $\pm$ 0.1 degree of the sunline. This requirement would be satisfied with a pitch and yaw attitude error of $\pm$ $6/\sqrt{2}$ minutes of arc. The allocation of errors (based on one σ values) contributing to a total loop inaccuracy is defined below.

The fine sun sensor can be made with an accuracy of several seconds of arc, but a sensor with this degree of accuracy must inherently have a small field of view. As a compromise between accuracy requirements and field of view, a sensor with a null uncertainty of one minute of arc has been chosen. This null uncertainty takes into account mounting misalignment, temperature effects, and manufacturing imperfections. The preamplifier and signal amplifier would contribute 0.5 minutes drift and 0.05 minutes noise. The input axis of the integrating-rate gyro used in the fine pointing mode can, in itself, be aligned to the control axis to less than eight minutes of arc. In addition to the gyro's misalignment, it may drift by several tenths of a degree over an extended period. These misalignment and drift errors will not enter into the fine pointing control loop accuracy since the gyro

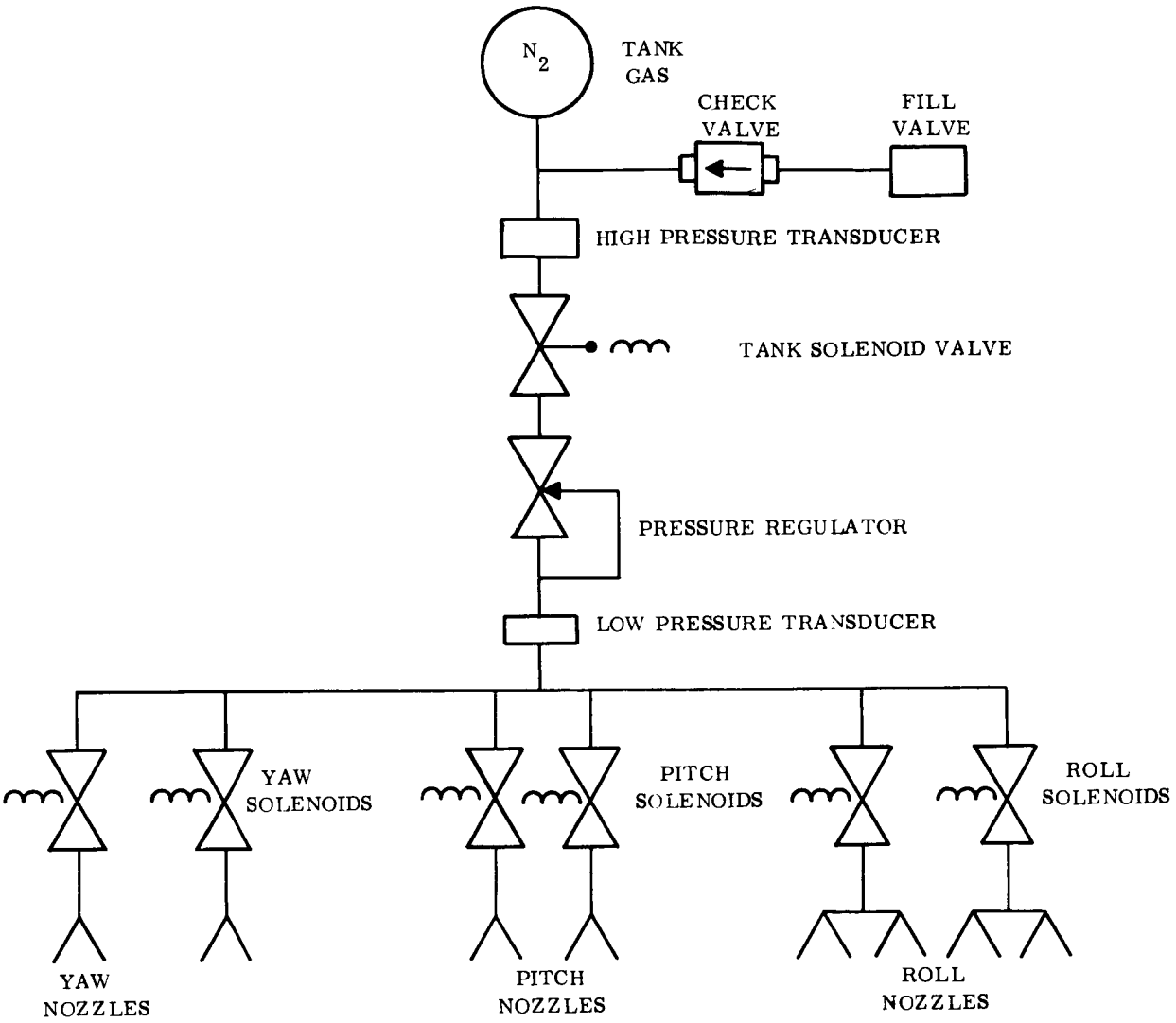

Figure 11-11. Pneumatic Subsystem Schematic

is slaved to the fine sun sensor and all errors will be biased out by having the sensor torque the gyro. The only contribution of the gyro to the error allocation will be that due to noise, which would be approximately 0.2 minutes of arc. The electronics associated with the fine momentum control would contribute 1.5 minutes of error due to drift and 0.15 minutes due to noise. Static friction in the momentum wheel will contribute a threshold error of 0.15 minutes of arc.

In general the drift errors will not add algebraically, thus they will be combined on a root-sum-squared basis and added to the error due to noise. On this basis, the root-sum-squared error is approximately 1.9 minutes, and the total loop error would be 2.3 minutes per axis.

As a result of the cumulative disturbance torques acting on the vehicle, a gradual increase in flywheel speed must occur as the stored momentum builds up. This increase in speed must also be accompanied by a gradual increase in spacecraft attitude error in order to allow the sensors to supply the increased motor voltage required. The actuator error must be added to the above error allocation. Therefore, the loop gain must be adjusted so that the flywheel speed at which momentum unloading begins occurs when the attitude error is 2 minutes of arc (i.e., $6/\sqrt{2}$ - 2.3). It is unlikely that both the pitch and yaw axes would have $6/\sqrt{2}$ minutes error at the same time and therefore, on a one σ basis, the actual roll axis error with respect to the sunline would be 4.05 minutes.

This error allocation was based, to a large extent, on experience obtained on the Orbiting Astronomical Observatory spacecraft, which has a coarse pointing accuracy of ± 1 minute of arc and holds the attitude to within $\pm$ 15 seconds of arc for not less than 50 minutes. The fine pointing mode aligns the optical axis to within 0.1 seconds of arc. This system uses a cold gas-flywheel type control scheme of the same type proposed for this application.

11.5.4 SIZING OF ATTITUDE CONTROL SUBSYSTEM

There are two principal components to be sized in connection with the attitude control scheme proposed: (1) the size of the momentum flywheels, and (2) the quantity of gas

required by the pneumatic system. The angular impulse and momentum storage requirements, which define these quantities, were computed in Section 11.3 and are summarized in Tables 11-8 and 11-9. Using these parameters the size of the flywheels and the volume of cold gas required is determined below.

11.5.4.1 Flywheel Size

Table 11-9 provides a tabulation of the flywheel momentum storage requirements. This table includes the effects of all the external disturbances and an assumed value for the internal momentum sources (i.e., tape recorder and gyros). The main source of disturbance torque is the magnetic field and its effects on the nickel solar concentrator. Since these torques on the spacecraft are not related to the vehicle inertias, the flywheels will seem oversized in comparison to other vehicles of simular configuration and inertia. This large ratio of momentum storage capacity to vehicle inertia would be utilized during the initial stabilization and orientation sequence. The parameters governing the flywheel size could be greatly reduced, as indicated by the results in Table 11-9, if the concentrator was fabricated from aluminum. However, for reasons discussed in Section 8.3.1, the design proposed in this study is based on a nickel concentrator.

Consider the Mission A case. From Table 11-9 the momentum storage capacity required for the pitch and yaw flywheels is 0.92 ft-lb-sec/orbit. The flywheel design parameters are selected below.

a. Momentum storage capacity = 1.3 ft-lb-sec

(A 25 percent safety factor is provided at no-load speed)

b. Stall torque = 2.0 ounce-inches

c. Time constant = $\frac{\text{Momentum @ no load speed}}{\text{Stall torque}}$

$= \frac{1.3 \times 16 \times 12}{2.0}$

$= 125$ seconds

d. No load speed = 1250 rpm

e. Synchronous speed = 1500 rpm

f. Power at stall $= \frac{2 \text{ (stall torque) (synch speed)}}{7.04}$

$= \frac{2 \times 2 \times 1500}{16 \times 12 \times 7.04}$

$= 4.5$ watts

g. Power at no load = 0.6x(power at stall)

$= 0.6 \times 4.5$

$= 2.7$ watts

h. Based on past experience a flywheel with these characteristics would weigh approximately 5.5 pounds.

Similar calculations were performed for the Mission B and C cases and the results for all three missions are summarized in Table 11-10.

Table 11-10. Flywheel Design Parameters (Pitch and Yaw Axes)

PARAMETERS	MISSION A	MISSION B	MISSION C
Momentum Storage Capacity, ft-lb-sec	1.3	0.5	2.5
Stall Torque, oz-in	2.0	2.0	2.0
Time Constant, seconds	125	48	240
No Load Speed, rpm	1250	1250	1250
Synchronous Speed, rpm	1500	1500	1500
Power at Stall, watts	4.5	4.5	4.5
Power at No Load, watts	2.7	2.7	2.7
Weight, lb	5.5	4.5	8.5

11.5.4.2 Pneumatic System Size

Table 11-8 tabulates the angular impulse requirements for the mass expulsion system. A cold gas pneumatic system was selected to satisy this requirement. The most common

gases used in this type of system are nitrogen or Freon-14. Nitrogen was assumed in this study with a specific impulse of 70 seconds. The weight of gas required to provide a given angular impulse requirement is defined by

$$W_g = \frac{\Delta H}{I_{sp} r} ,$$

where

W_g = Weight of gas, lb

ΔH = Angular impulse requirement, ft-lb-sec

I_{sp} = Specific impulse of gas, sec

r = Radius of nozzle moment arm (distance from the gas nozzle to the spacecraft center of mass), ft.

From Figure 13-3 in Section 13, the radius of the nozzle moment arm, r , is 28 inches. For Mission A the total angular impulse requirement given in Table 11-8 is 394 ft-lb-sec/yr. Substituting numerical values into the above equation the required gas weight is

$$W_g = \frac{394 \times 12}{0.80 \times 70 \times 28} = 3.0 \text{ pounds}$$

A twenty percent safety factor is included in the above computation to allow for the roll axis requirement and any gas leakage.

The gas tank weight may be determined from the following equation which assumes a tank made from 6AL-4V Titanium with a burst-to-operating pressure ratio of two and a storage temperature of $530^{o}R$.

$$W_T = 0.0238 \, Z \, RW_g$$

where

W_T = Weight of gas tank, lb.

Z = Compressibility factor for gas
= 1.05 (for N_2 at 3000 psi)

R = Gas constant, ft/^oR
= 55.13 ft/^oR for nitrogen

W_g = Weight of gas, pounds.

Substituting numerical values gives

$$W_T = 1.38\ W_g = 1.38 \times 3.0 = 4.1 \text{ pounds.}$$

The volume of gas can be computed from the perfect gas law equation

$$PV = W_g RT$$

where

P = The tank pressure, lb/ft^2

V = The tank volume, ft^3

T = The gas storage temperature, ^oR.

For a tank pressure of 3000 psi and a storage temperature of 530^oR the required tank volume is

$$V = \frac{3.0 \times 55.13 \times 530}{3000 \times 144} = 0.206 \text{ ft}^3.$$

Assuming a spherical tank, the tank radius, r, is given by

$$r^3 = \frac{3V}{4\pi} = \frac{3 \times 0.206}{4\pi} = 0.049$$

$r = 0.367$ ft or a diameter of 8.8 inches.

These calculations were repeated for the Mission B and C cases and the results for all three missions are summarized in Table 11-11.

Table 11-11. Pneumatic System Design Parameters

PARAMETERS	MISSION A	MISSION B	MISSION C
Angular Impulse Requirements, ft-lb-sec/yr	394	115.	588
Weight of N_2 Gas Required, lb	3.0	0.88	4.5
Weight of Gas Tank, lb	4.1	1.5*	6.2
Volume of Gas Required, ft^3	0.2	0.06	0.3
Diameter of Tank, in	8.8	5.8	10.0

Note

*Assumed to be the smallest practical tank weight.

11.5.5 Size, Weight and Power Requirements

An estimate of the size, weight and power requirements for the attitude control subsystem components are presented in this section. These estimates are based on the sizing calculations performed in Section 11.5.4 and on experience gained in the development of the attitude control subsystems for the Nimbus and Orbiting Astronomical Observatory spacecraft. Table 11-12 summarizes the size and weight estimates and Table 11-13 the power requirements.

Table 11-12. Size and Weight Estimates for the Attitude Control Subsystem Components

COMPONENTS	MISSION A		MISSION B		MISSION C	
	Size (Each) (Inches)	Total Weight (Pounds)	Size (Each) (Inches)	Total Weight (Pounds)	Size (Each) (Inches)	Total Weight (Pounds)
Momentum Flywheel (2)	10 Dia x 3	11	10 Dia x 3	9	10 Dia x 3	17
Roll, Pitch, Yaw Gyros and Electronics	8x5x3 (Gyro) 8x11x3(Electronics)	11	8x5x3 (Gyro) 8x11x3(Electronics)	11	8x5x3 (Gyro) 8x11x3(Electronics)	11
Power Supply (ac and dc)	4x10x4	11.5	4x10x4	11.5	4x10x4	11.5
Sun Sensors & Electronics		2.0		2.0		2.0
Fine Sensor (2)	cyl. 5x2 Dia		cyl. 5x2 Dia		cyl. 5x2 Dia	
Coarse Sensor (4)	4x3x2		4x3x2		4x3x2	
Electronics	4x4x4		4x4x4		4x4x4	
Programmer and Logic	12x6x6	2.5	12x6x6	2.5	12x6x6	2.5
Attitude Control Electronics (3)		7.0		7.0		7.0
Roll Axis	6x6x6		6x6x6		6x6x6	
Pitch Axis	12x6x6		12x6x6		12x6x6	
Yaw Axis	12x6x6		12x6x6		12x6x6	
IR Sensors (2) and Electronics	3x3 (Sensor)	1.0	3x3 (Sensor)	1.0	3x3 (Sensor)	1.0
Thermal Sensor	-	0.2	-	0.2	-	0.2
Pneumatic System Gas						
Gas	-	3.0	-	0.9	-	4.5
Tank	8.8 Dia	4.1	5.8 Dia	1.5	10.0 Dia	6.2
Fill and Check Valves & Filter	-	2.2	-	2.2	-	2.2
Pressure Transducer (2)	-	0.8	-	0.8	-	0.8
Regulator	-	2.5	-	2.5	-	2.5
Solenoids (7)	-	2.8	-	2.8	-	2.8
Nozzles and Orifices (8)	-	1.0	-	1.0	-	1.0
Relief Valve	-	0.8	-	0.8	-	0.8
Lines, Fittings, Clips Bracketry	-	2.5	-	2.5	-	2.5
TOTALS	-	65.9	-	59.2	-	75.5

Table 11-13. Power Requirements for Attitude Control Subsystem[a]

Components	Continuous Power (Watts)	Peak Power	
		Level-Watts	Duration-Minutes
Gyro (3)	15	-	-
Flywheel (2)	4	7	10 minutes [b]
Control Electronics (3)	9	-	-
Logic Devices	3	-	-
AC and DC Power Supplies (75 percent Efficiency)	5	6	10 minutes [b]
Pneumatic Solenoids	-	60 40	0.25 minutes [c] 3.0 minutes [d]
TOTAL	36		

Notes

a. These estimated power requirements apply to Mission A, B and C.

b. Peak associated with the flywheel's demand for more power during the reorientation phase after each shadow period.

c. Peak associated with unloading the flywheels.

d. Peak associated with reorienting the spacecraft when it emerges from the earth's shadow.

11.6 SUMMARY AND CONCLUSIONS

The proposed cold gas-flywheel attitude control technique is particularly well suited to this application because of the precise sun pointing accuracy necessary and the cyclic momentum storage requirements. This approach to attitude control is considered present state of the art having been used on the Nimbus and OGO vehicles and the hardware having been flight qualified for the OAO spacecraft which is scheduled for flight in late 1965. On the OAO

vehicle the coarse pointing requirement is $\pm$ 1 minute of arc and the fine pointing mode calls for an accuracy of 0.1 second of arc. Therefore, the six-minute sun pointing accuracy needed for the solar thermionic system can be provided using proven techniques.

A more detailed analysis of the disturbance torques is needed to realistically size the attitude control subsystem. The disturbance torque estimates made in this study are the result of a worst case analysis and are felt to be considerably more severe than what the spacecraft would actually experience. As a result, the attitude control subsystem size and weight estimates presented should be conservative (higher than actually required).

The magnetic disturbance torques represent the major momentum storage requirement as shown in Table 11-9. If these requirements could be reduced the flywheels could be made smaller with a resulting decrease in the weight and power requirements. Ways of minimizing the magnetic disturbances are discussed below.

The permanent magnetic effects could be reduced significantly by fabricating the solar concentrator from a non-magnetic material such as aluminum*. The possibility of either electroforming or stretch forming an aluminum concentrator with the desired accuracy should be investigated. If nickel must be used the permanent magnetic effects could be reduced by demagnetizing the concentrator and subsequently preventing further magnetization by avoiding close proximity to strong magnetic fields. Of course a lower limit on demagnetization is set by the earth's magnetic field at sea level. In some cases, if the magnitude and direction of the permanent field is known, its effects can be reduced by using small bar magnets of equal and opposite polarity. This approach might be used for some of the small spacecraft components but does not offer promise for solving the concentrator problem.

Like the permanent magnetic effects, the spacecraft induced magnetic effects would be greatly reduced if the solar concentrator could be made from aluminum rather than nickel.

* The concentrator's contribution to the total spacecraft's permanent magnetic effects would be zero if a non-magnetic material was used.

Wherever possible, the induced magnetic effects can be reduced by making components fabricated from magnetic material as symmetrical as possible.

Magnetic torques resulting from current loops can be reduced if twisted conductors are used. By twisting the current carrying conductors upon themselves, the net area of the current loop can be greatly reduced. This is a simple technique which is often used effectively to reduce the magnetic effects of current loops. This technique should definitely be used on the thermionic generator leads which carry relatively high current.

Even if the magnetic disturbance torques could be reduced by replacing the nickel solar concentrator with an aluminum one, the other disturbance torques provide cyclic momentum storage requirements of such magnitude that the cold gas-flywheel approach would still represent the most attractive attitude control scheme for this application.

11.7 REFERENCES

11-1 "Design and Fabrication of a Master and Concentrator", General Electric Spacecraft Department, Proposal No. N-10051 in response to JPL RFP 2749, March 12, 1962.

11-2 F. Blake and R. Herrick, "Cavity Vapor Generator Performance-Endurance Solar Test Program", General Electric Spacecraft Report No. ASP-TM-022, July, 1963.

11-3 P. Holthenrichs, "Gravitational Torque History for an Attitude Controlled Satellite Vehicle Stabilized to a Reference Other Than Planetocentric", General Electric Spacecraft Department Technical Memo No. 9752-CSA-013, July 19, 1963.

11-4 Hoerner, Fluid Dynamic Drag

11-5 F. L. Whipple, "The Meteoritic Risk to Space Vehicles", Vistas in Astronautics, Vol. I, 1958.

SECTION 12

SPACECRAFT POWER SUBSYSTEM

PRINCIPAL CONTRIBUTORS:

E.W. Williams
J.C. Peden

SECTION 12
SPACECRAFT POWER SUBSYSTEM

12.1 INTRODUCTION

To properly evaluate the performance of the solar thermionics portion of the experiment, it is necessary to have a separate spacecraft power supply; so there is no dependence on the power generated by the thermionic generator. In this manner, if there were a degradation or complete failure of the thermionic generator, the spacecraft would still be operational and the reasons for the failure could be evaluated. In addition, failure of the thermionic generator would by no means put an end to the value of the experiment. Valuable information could still be obtained from the orientation and solar concentrator subsystems which will be instrumented to allow performance evaluation. Also, the secondary experiments would yield valuable engineering and scientific data.

Silicon solar cells were selected for the spacecraft power supply for two reasons: (1) their proven reliability in space, and (2) the fact that the spacecraft is required to be solar oriented in order to conduct the solar thermionic experiment. Nickel-cadmium secondary batteries were chosen to supply the cyclic energy storage requirements. Primary silver oxide-zinc batteries are used to supply the power requirements associated with initial stabilization of the spacecraft. Both of these types of batteries have demonstrated reliability in space applications.

The performance estimates presented in this section are based to some degree on experimental measurements made by the General Electric Spacecraft Department. These measurements were not made in connection with this study, but rather on past contracts and company funded programs.

12.2 RADIATION ENVIRONMENT

This section considers the radiation environment for the three orbits of interest and its influence on semiconductor components.

12.2.1 ENVIRONMENTAL DESCRIPTION

The environment estimates given here consider three components of the radiation environment: (1) the trapped electron field, (2) the trapped proton field, and (3) the solar flare protons. The estimates for the trapped electron and proton fields are based on data from the Explorer 15 satellite. These estimates, for three different orbit inclinations, are given in Figures 12-1 and 12-2 for electrons and protons respectively for attitudes up to 2500 nautical miles. The figures show the daily average fluxes as determined from a B-L coordinate computer program.*

The electron flux in Figure 12-1 is for the intensity of particles whose energy is greater than 0.5 Mev. Since these are mostly particles from the Starfish experiment, they have been normalized to January 1963. The electron energy spectrum assumed for the present calculations, for all altitudes, is shown in Figure 12-3. This energy spectrum resulted from the early beta decay of fission products.

The proton intensity distributions shown in Figure 12-2 are for those particles with energy between 40 and 110 Mev. The energy spectrum assumed for the protons for all altitudes is shown in Figure 12-4.

How applicable these electron estimates are for the 1967 to 1969 time period is questionable. This is particularly so for altitudes below 1000 nautical miles. The electrons injected into the magnetic field by the Starfish experiment are known to be decaying. The rate of decay is a strong function of the magnetic shell (L-shell) in which the electrons are trapped. It is very difficult to estimate the average orbital flux decay, particularly for highly inclined orbits since many L shells are crossed on each orbit. In order to obtain a better estimate

*The B-L Coordinate System is the natural (magnetic) coordinate system presently used in most descriptions of charged particle motion within several earth radii of the earth's surface. It is a magnetic coordinate system, quite different from the polar coordinate system because the magnetic field of the earth is irregular and not concentric with the earth's center. B is the magnetic field strength and L is approximately equal to the distance to the equatorial crossing of one particular magnetic field line.

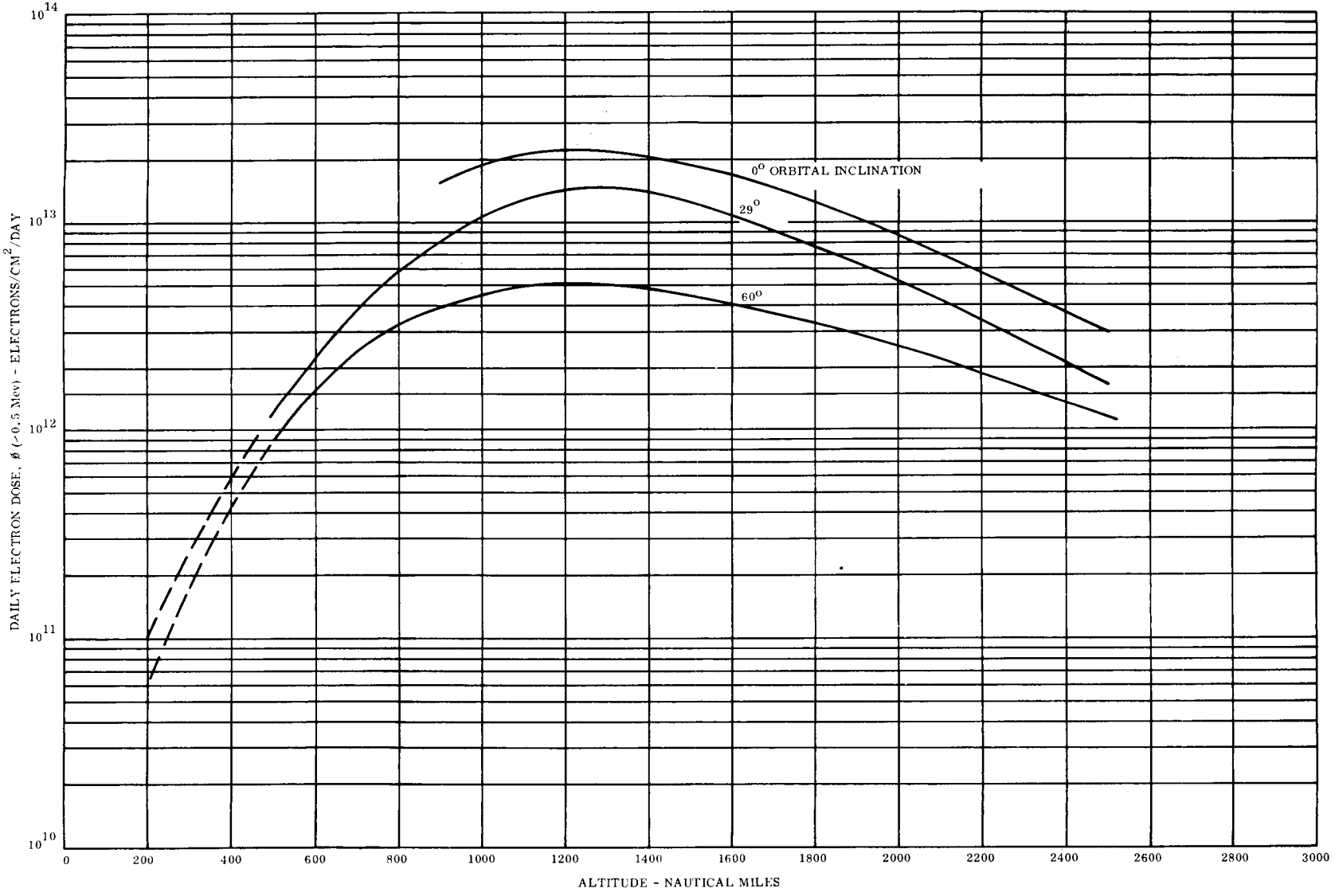

Figure 12-1. Daily Electron Dose (E > 0.5 Mev) vs. Altitude

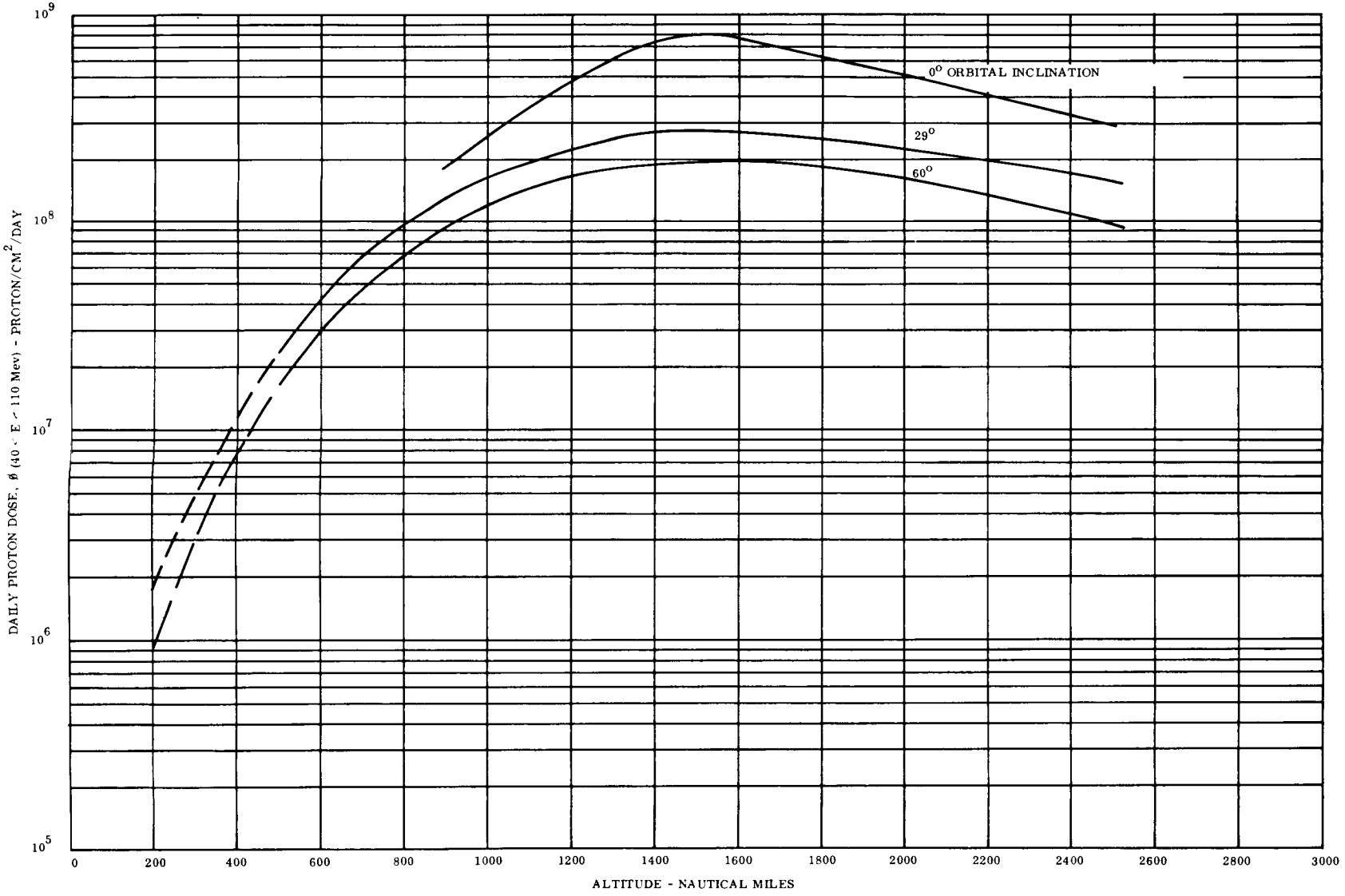

Figure 12-2. Daily Proton Dose (40 < E < 110 Mev) vs. Altitude

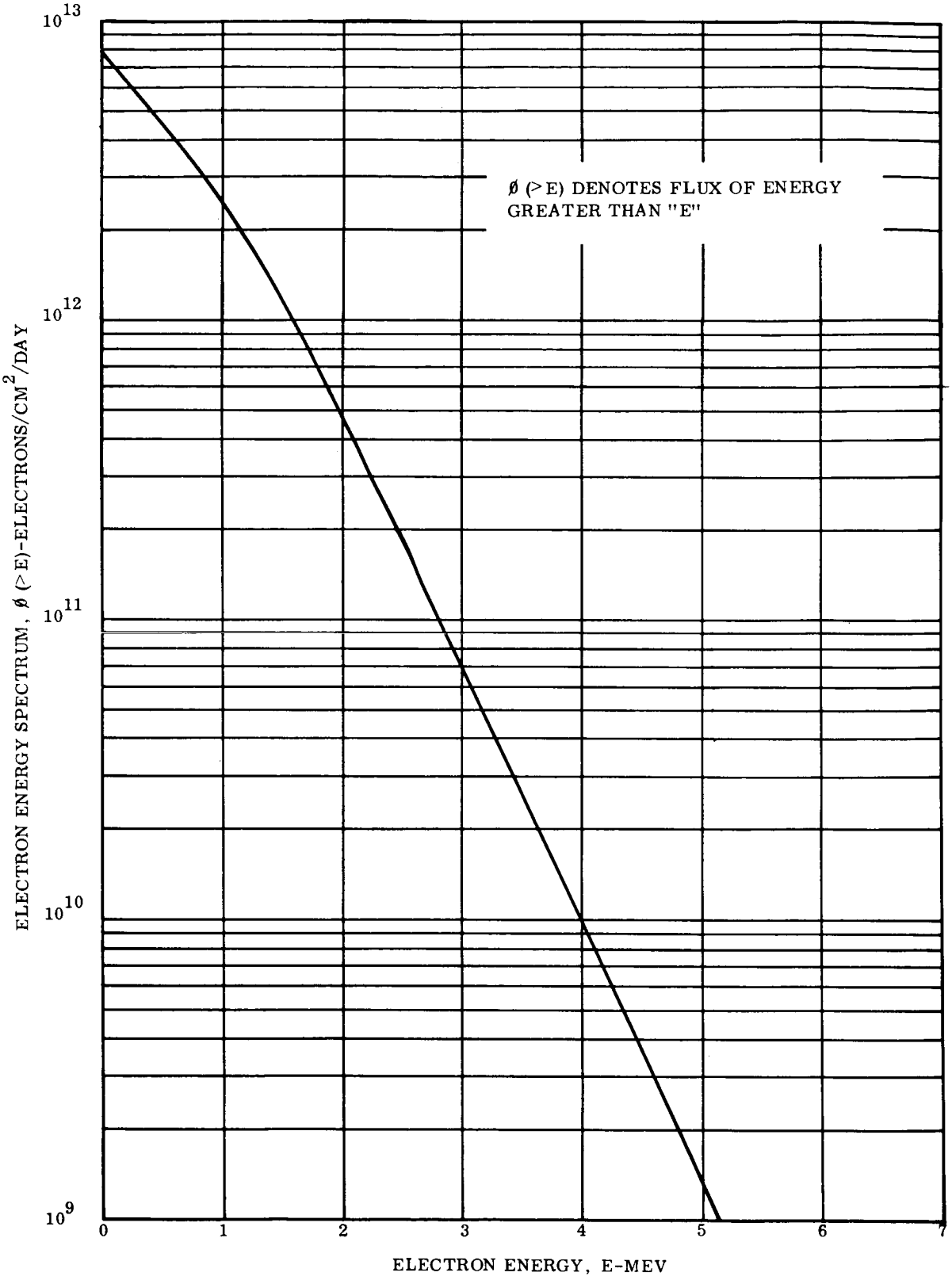

Figure 12-3. Integral Electron Spectrum

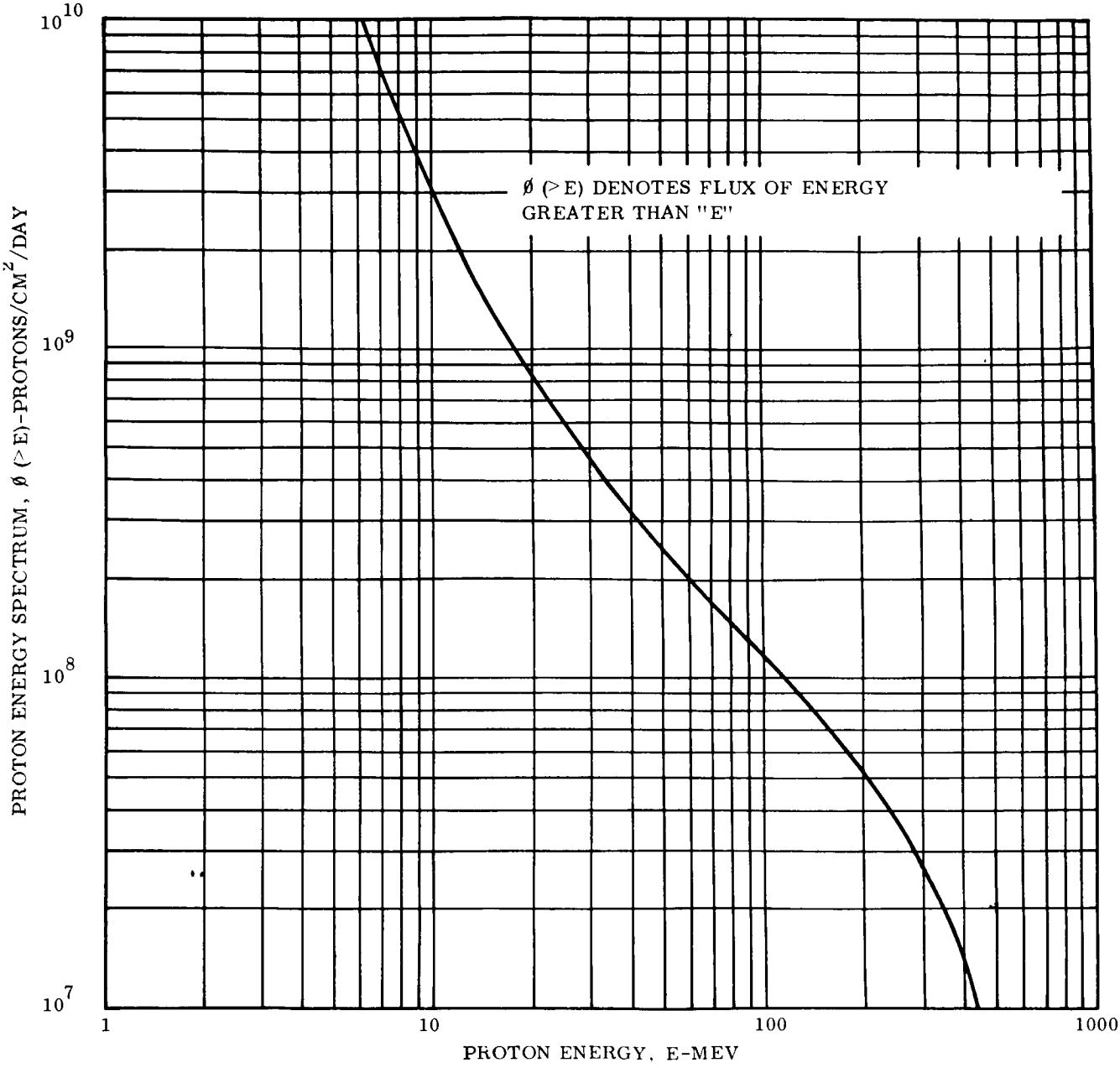

Figure 12-4. Integral Proton Spectrum

of the average decay time for each orbit, the decay times of the fluxes encountered at each point in the orbit should be weighed as a function of the integrated flux at each orbit point.

The assumption of a fission energy spectrum for the electrons is also questionable since it is known that the decay of the electrons is resulting in changes in the energy spectrum of these electrons as well.

The other environmental component of importance here is that due to solar flare protons. Figure 12-5 shows the average yearly, free-space, flux of solar protons assumed for the 1967 to 1969 time period. The spectrum shape shown is similar to that seen on a number of large, 3+ magnitude, flares. The particle intensity assumed (3×10^9 protons/cm^2/year, E > 40 Mev) would correspond to the assumption that two 3+ magnitude flares, similar to the May 10, 1959 event, would occur during any given year.

The above environment components have been used to define the environment for the specific orbits of interest here. For the 325-nautical mile, 30-degree inclined orbit, the flux values in Figures 12-1 and 12-2 for the 29-degree inclination curve have been assumed. Also, no solar flare protons are considered for this orbit since it is assumed that by virtue of its low inclination and altitude the earth's magnetic field will effectively shield it against the majority of solar protons.

For the 1000-nautical mile, 101.84-degree inclined orbit, the flux values in Figures 12-1 and 12-2 for the 60-degree inclination curve have been assumed. Since this orbit is highly inclined and of relatively high altitude, one-half of the full, free-space, flux of solar protons given in Figure 12-5 is also included in the yearly dose.

For the highly elliptical 200 by 25,000-nautical mile, 45-degree inclined orbit, the estimates of Figures 12-1 and 12-2 cannot be used, since a significant portion of the orbital time is spent out of the radiation belts. Here a special computer run of the B-L coordinate program was required. Figure 12-6 shows the results of such a calculation for the average daily trapped proton flux. Although, a specific calculation was not accomplished for the electron

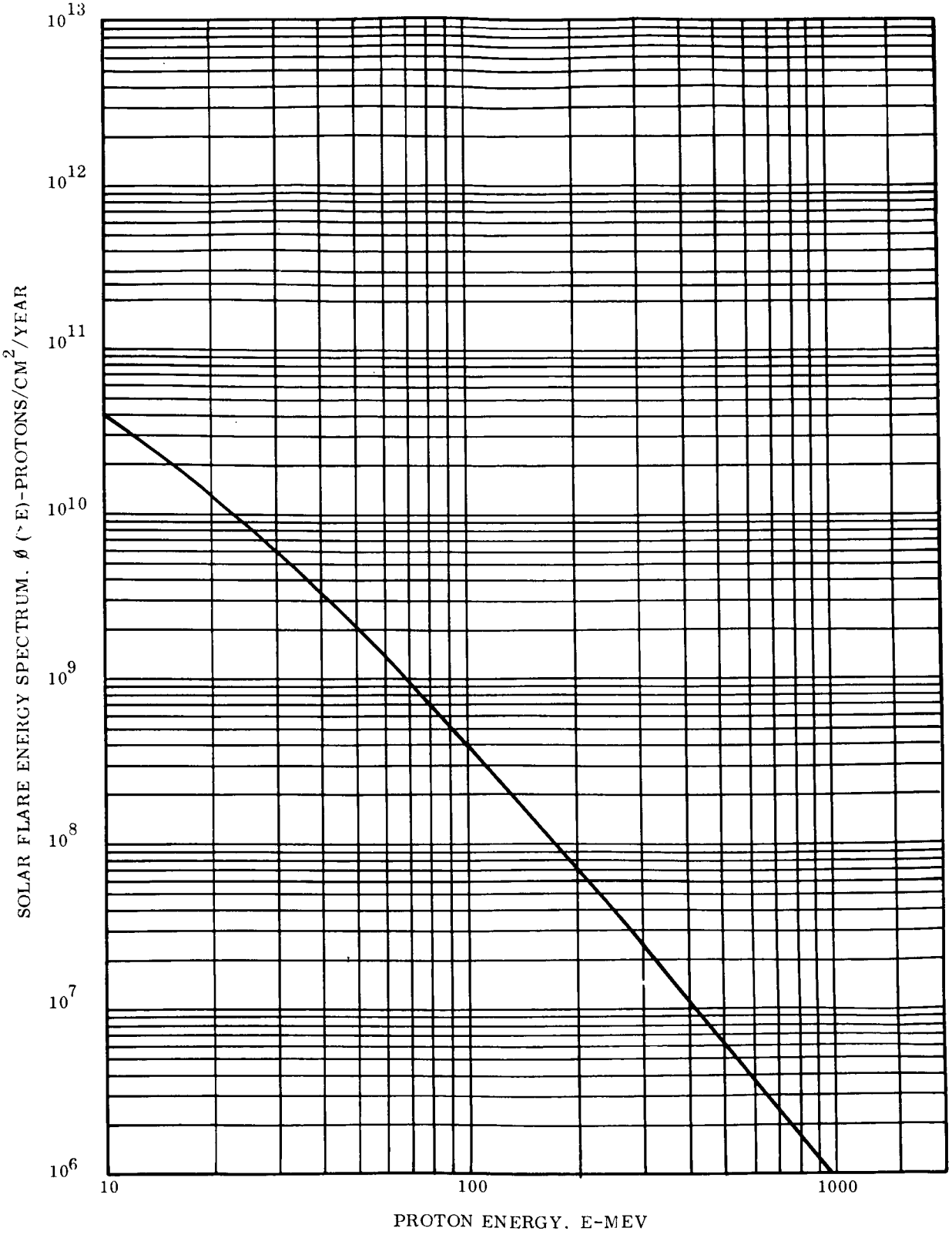

Figure 12-5. Integral Isotopic Solar Flare Spectrum

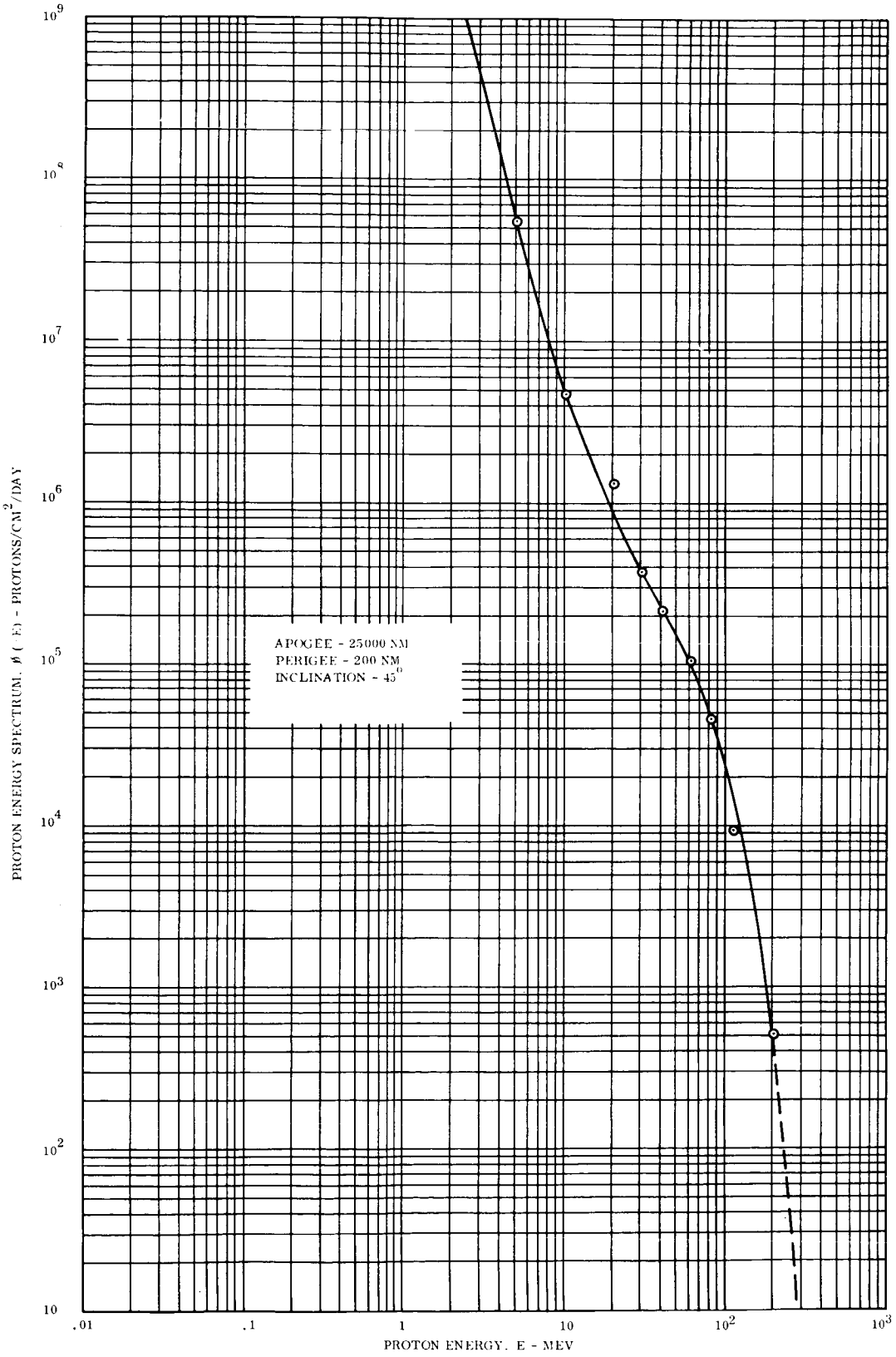

Figure 12-6. Integral Proton Spectrum for Elliptical Orbit

component, it has been estimated that the average daily electron flux would be about 2×10^{11} electrons/square centimeter/day normalized to January 1963 and considering the computed orbit trajectory in B-L coordinates. Also, the full free-space flux of solar protons given in Figure 12-5 is included in the yearly dose for this orbit.

The average yearly particle dose for each orbit is summarized in Table 12-1.

Table 12-1. Summary of Yearly Particle Doses
(Particles/cm^2/year)

	ORBIT		
	325 NM	1000 NM	200 by 25,000 NM
Trapped Electrons (E > 0.5 Mev)	1×10^{14}	1.6×10^{15}	7×10^{13}
Trapped Protons (40 < E < 110 Mev)	2×10^{9}	4.4×10^{10}	8×10^{7}
Solar Flares (E > 40 Mev)	-	1.5×10^{9}	3×10^{9}

In order to assess the effect of this radiation environment on operating semiconductor components, such as transistors and diodes, the total ionization due to these particle doses, and also its ability to cause bulk damage (that is atomic displacements) in semiconductors, is required. An estimate of the ionization dose, in terms of Rads (air) per year, for several shield thicknesses is given in Table 12-2. In these calculations, the incident flux is assumed to be isotropic and the shielding geometry is assumed to be a spherical shell. The calculated dose is that at the center of this spherical shell and therefore represents the maximum dose for this shielding configuration. Scattering of the incident flux is neglected. As can be seen from these figures, the ionization dose is primarily due to the electron environment up to a shield thickness of 4.0 grams per square centimeter. As pointed out below, the aspect of the environment (that is, the ionization) is very important as far as its effect on the vehicle electronics is concerned. In order to conveniently assess the bulk damage in

Table 12-2. Summary of Yearly Radiation Doses

	Ionization Dose, Rads (Air)			Equivalent Neutron Dose, Neuts/cm^2			Shielding	
	325 NM	1000 NM	200 by 25000 NM	325 NM	1000 NM	200 by 25000 NM	Grams/cm^2	Aluminum (mils)
Electrons	$3x10^5$	$6x10^6$	$2x10^5$	$1x10^{10}$	$2x10^{11}$	$7x10^9$	1.0	150
	$5x10^4$	$1x10^6$	$3x10^4$	$3.7x10^9$	$7.5x10^{10}$	$2.6x10^9$	2.0	300
	-	-	-	-	-	-	4.0	600
Protons	$1.2x10^3$	$2.4x10^4$	~50	$4.8x10^{10}$	$1x10^{12}$	$2.1x10^9$	1.0	150
	$7.2x10^2$	$1.4x10^4$	~30	$2.7x10^{10}$	$5.4x10^{11}$	$1.3x10^9$	2.0	300
	$4.5x10^2$	$9x10^3$	~20	$1.7x10^{10}$	$3.3x10^{11}$	$8x10^8$	4.0	600
Solar Flare Protons	-	$1x10^3$	$2x10^3$	-	$4.0x10^{10}$	$8x10^{10}$	1.0	150
	-	$6x10^2$	$1.9x10^3$	-	$2.5x10^{10}$	$5x10^{10}$	2.0	300
	-	$4x10^2$	$8x10^2$	-	$1.5x10^{10}$	$3x10^{10}$	4.0	600
Cosmic Rays	~50	~50	~50	$\sim 10^9$	$\sim 10^9$	$\sim 10^9$	>4.0	>600
TOTAL	$3x10^5$	$6x10^6$	$2x10^5$	$5.9x10^{10}$	$1.2x10^{12}$	$9x10^{10}$	1.0	150
	$5x10^4$	$1x10^6$	$3.1x10^4$	$3.2x10^{10}$	$6.4x10^{11}$	$5.5x10^{10}$	2.0	300
	$6x10^2$	$9.4x10^3$	$8.7x10^2$	$1.8x10^{10}$	$3.4x10^{11}$	$3.2x10^{10}$	4.0	600
TOTAL (Without Electrons)	$1.2x10^3$	$2.5x10^4$	$2.1x10^3$	$4.9x10^{10}$	$1x10^{12}$	$8.3x10^{10}$	1.0	150
	$7.5x10^2$	$1.5x10^4$	$1.4x10^3$	$2.8x10^{10}$	$5.6x10^{11}$	$5.2x10^{10}$	2.0	300
	$5x10^2$	$9.4x10^3$	$8.7x10^2$	$1.8x10^{10}$	$3.4x10^{11}$	$3.2x10^{10}$	4.0	600

semiconductor electronics, the incident electron and proton radiation has been converted to an equivalent fast neutron flux that would cause equal damage in semiconductors. This is also shown in Table 12-2 in terms of equivalent fast neutrons/square centimeter/year for several shield thicknesses. The assumptions for the shielding geometry are similar to those for the ionization dose calculations.

For this effect, the electron decay is not as important as for the ionization effects since the protons cause most of the bulk damage as can be seen from Table 12-2.

12.2.2 EFFECTS ON SEMICONDUCTOR ELECTRONICS

The main effects of ionizing radiation on semiconductor electronics, particularly transistors, are the bulk damage effects and the so-called radiation induced surface effects. The bulk damage effect is the disruption of the crystal lattice of the semiconductor material. In transistors, this effect causes a decrease in carrier lifetime in the base region of the device. The effect takes place whether the device is electrically active or not. The surface effects phenomenon, on the other hand, is more predominate when the devices are simultaneously under electrical stress and exposed to ionizing radiation. This effect is due mainly to the interaction of the ionized gas (in the hermetrically sealed transistor) with the semiconductor surface.

Both of these effects (bulk and surface) can effect the transistor gains quite drastically. In addition, the surface effects can also alter junction leakage currents considerably. The extent to which device parameters are altered for a given radiation dose can depend to a large degree on device construction and initial electrical characteristics.

Consider first the bulk damage aspect. Since neutrons can cause similar bulk damage as energetic electrons and protons, and since most of the available bulk damage data on transistors is for neutrons, the above environment was converted to equivalent fast neutron doses. The amount of gain degradation a device will experience for a given radiation dose depends upon the basic material (silicon or germanium), its initial gain value, and the width of its

base region (the alpha cut-off frequency can be used as a measure of base width). Figure 12-7 shows the gain degradation as a function of fast neutron dose of silicon and germanium devices with initial gain values of 50 for several values of alpha cut-off frequency. Figure 12-8 shows the gain degradation of a 50-kilocycle alpha cut-off frequency germanium device as a function of fast neutron dose for several initial gain values.

Considering a minimum shielding thickness of 1.0 grams per square centimeter ($\sim$ 0.4 cm of aluminum) the equivalent neutron dose for a one-year period, as given in Table 12-2, would be $6 \times 10^{10}/cm^2$, $1.2 \times 10^{12}/cm^2$ and $9 \times 10^{10}/cm^2$ for altitudes of 325, 1000 and 200 by 25,000 nautical miles, respectively. As can be seen from Figure 12-7, these doses are not serious for high frequency signal devices (alpha cut-off frequency greater than 50 megacycles). However, they can very drastically effect high gain, low frequency power devices as depicted in Figure 12-8. On the other hand, these doses would have little effect on diodes. It is interesting to note that this bulk damage is primarily due to the proton environment and therefore is not influenced by the large uncertainties associated with the electron environment.

The surface effects, on the other hand, could be a very serious problem. So far as is known, this effect, for gas-filled mesa and planar devices, is essentially dependent on the total accumulated ionization dose absorbed in the gas. The effect is apparently strongly dependent on surface contamination, thickness of the passivation layer and other process variables; resulting in a very random behavior. A surface effects experiment was recently conducted by General Electric on some 100 planar passivated high frequency signal devices. In this experiment the collector-base junctions were reverse biased with 10 volts continually throughout the experiment. The ionizing radiation source was Cobalt-60 gamma rays. The average gain degradation at a dose of 10^5 Rads (air) was 40 percent (that is, the devices retained 60 percent of their initial value). The spread in the gain degradation of the individual devices was from 10 to 90 percent. Similarly at a dose of 10^7 Rads (air) the average gain degradation was 66 percent and the spread ranging from 30 to 95 percent. The variation in collector-base leakage currents was even more variable ranging from no change to 6 orders-of-magnitude change at 10^7 Rads (air).

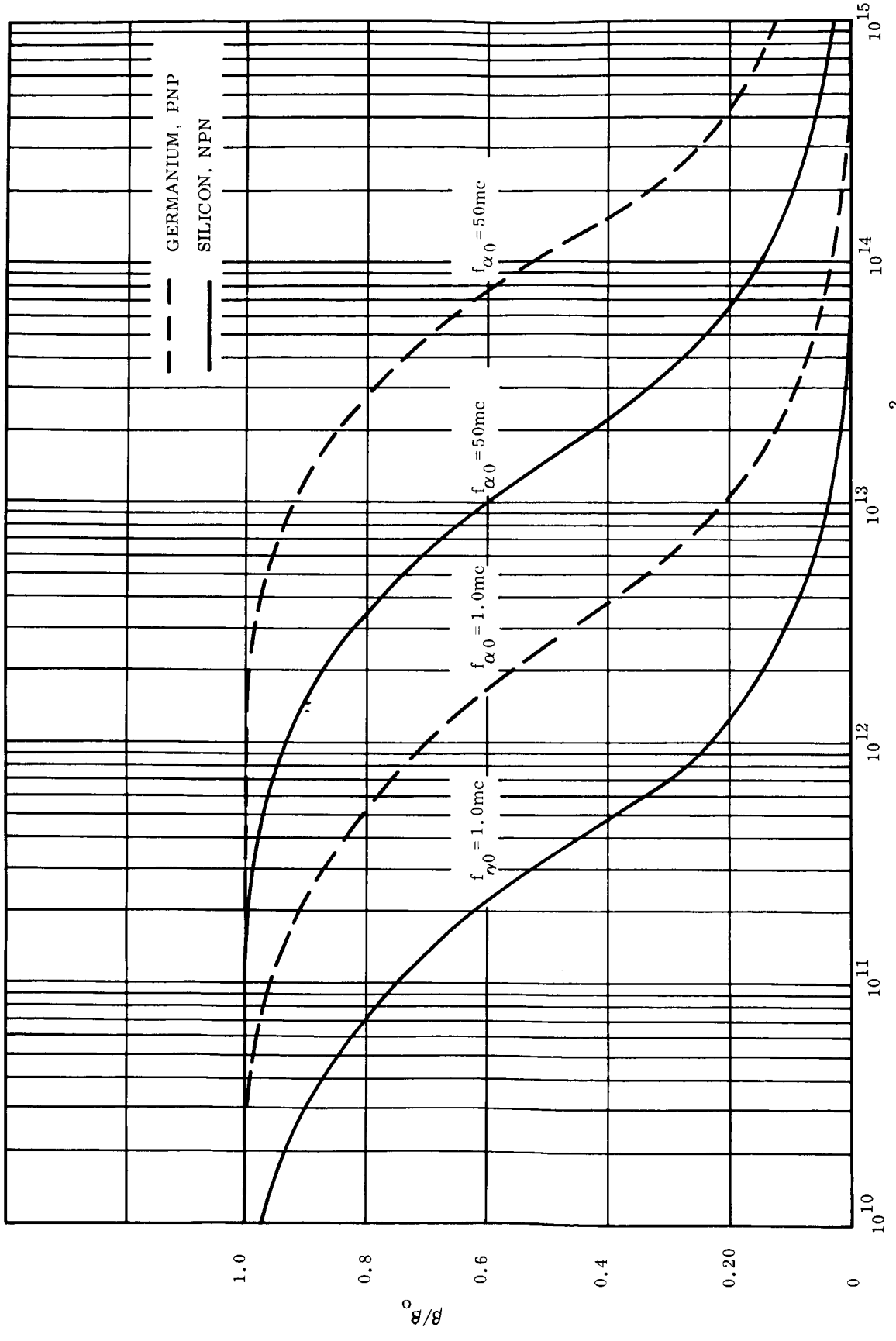

Figure 12-7. Degradation of Common Emitter Current Gain, $\beta_o = 50$

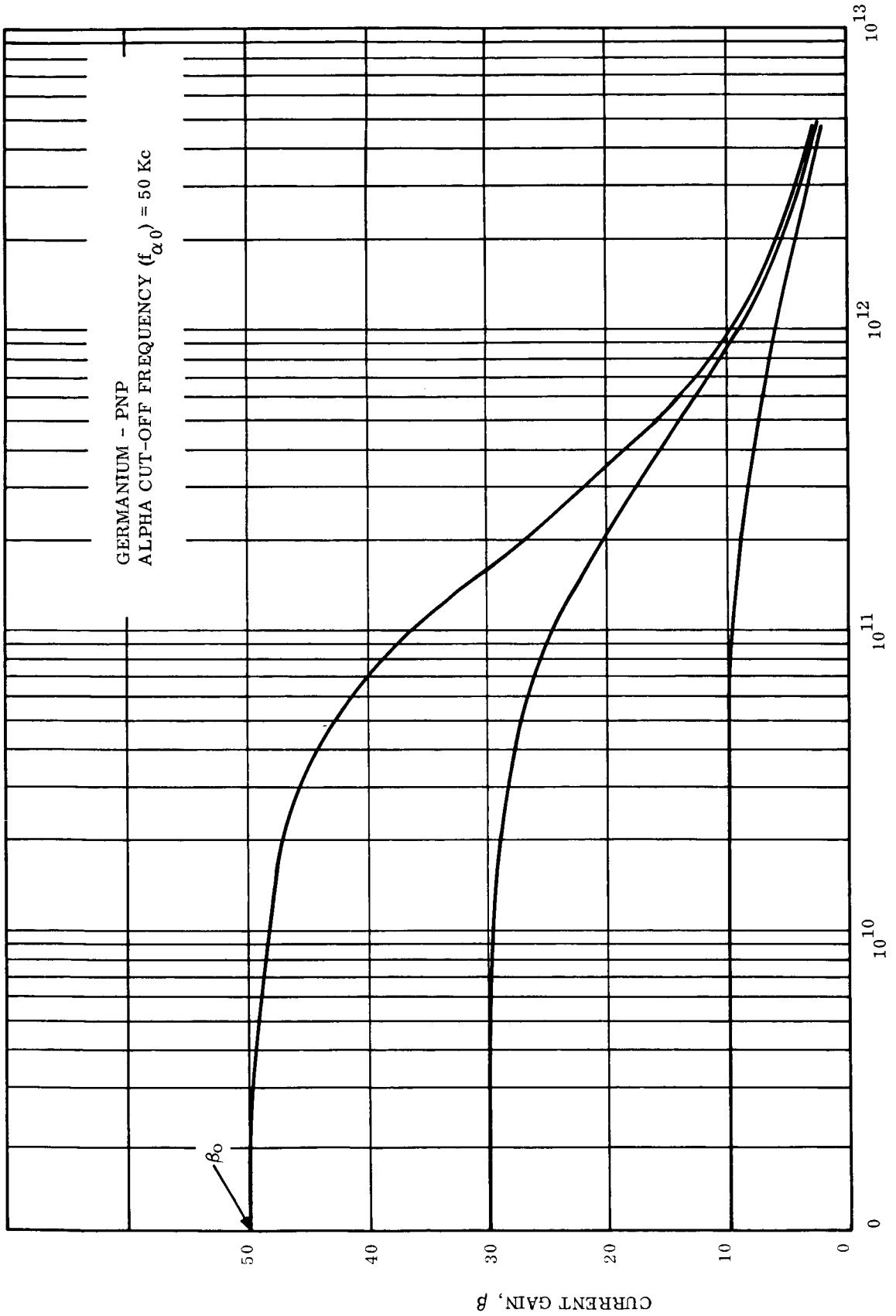

Figure 12-8. Degradation of Common Emitter Current Gain

The gain degradation appears to be a fairly strong function of device operating point. The above degradation values were for collector currents between 0.1 and 1.0 milliamps. For collector currents between 5 and 10 milliamps the degradation was a factor of 1.5 to 2.0 less than those above.

Considering the ionization dose estimates given in Table 12-2, it would appear that the surface effects problem could be serious, particularly for the 1000-nautical mile orbit. However, as can be seen from Table 12-2, the ionization dose is primarily due to the electron environment, therefore a good comparative analysis at various altitudes requires a better estimate of the electron decay than that contained above. This is particularly important for the 325-nautical mile and 200 by 25,000-nautical mile orbits. For example, the electron intensity at 325 nautical miles is probably quite reduced, even now, from that shown in Table 12-2. It would be even more so in the 1967 to 1969 time period.

In the extreme case, if one considers the ionization due to the protons alone, the one year doses, for 1.0 gms/cm^2 shielding, range from 10^3 Rads (air) to 3×10^4 Rads (air) for the various orbits. From surface effects experiments on planar devices performed to date, it appears that somewhere between 10^3 and 10^5 Rads is the onset of severe gain degradation in many silicon devices, although this dose range has not been explored in detail. Therefore, surface effects still could be a significant problem just considering the protons alone. This is particularly so at the higher altitudes.

To assess the surface effects in circuits requires detailed knowledge of the circuit, such as gain margin, transistor operating points, junction biases, etc. Such an evaluation is beyond the scope of this study; however, the possible solutions to any surface effects problems appear to be quite limited at the present time. First, surface effects are more severe in high-usage signal devices that operate in low power consumption circuitry. This means that shielding is impractical since large volumes would have to be shielded and from the dose estimates given above, shield thicknesses in excess of 4.0 grams per square centimeter would constitute an extremely large weight penalty. On the other hand, worst case circuit design alone would not be feasible due to the great variability seen in the radiation response

of present state-of-the-art parts. About the only approach available appears to be a combination of worst case circuit design and a parts radiation screening technique that would select only those parts that would not degrade past the margin to which the circuits are designed. Such a program for digital circuitry is currently in progress at the General Electric Missile and Space Division.

On the other hand, shielding of bulk damage effects in power electronics appears to be quite feasible. Surface effects will probably not be a significant problem since these devices operate at high currents. They also are low-usage parts so that shielding of individual transistors would be feasible. Power-weight trade-offs, could be performed to determine the optimum shield thicknesses. The type of shielding to be used; for instance, aluminum versus lead or iridium, for minimum weight would depend upon the volume to be shielded and its geometric shape. For example, to shield an individual transistor, it is better to use a high density material, such as iridium, rather than a low density material such as aluminum. Both the weight and the volume of the shield material would be less for the high density material for the same amount of radiation shielding. As the shielded volume increases in size, however, the minimum weight shield shifts to the lower density materials.

12.2.3 EFFECTS ON SOLAR CELLS

The effects of the environment given above on N/P silicon solar cells for a one year time period is shown in Figures 12-9, 12-10 and 12-11 for altitudes of 325, 1000, and 200 by 25,000 nautical miles, respectively, as a function of cover glass thickness. In the figures, V_{oc}, denotes the cell open-circuit voltage, I_{sc}, is the cell short-circuit current, and P_{max}, is the cell maximum power point. These curves were derived using a computer program that calculates the energy spectrum of the incident radiation as it passes through the various shield thicknesses and then integrates this residual spectrum over the electron and proton damage functions for the cell V_{oc} and I_{sc}. The output is the fraction of original V_{oc} and I_{sc} remaining after the specified flight time. The two outputs are then multiplied together to give the fraction of the maximum power that remains.

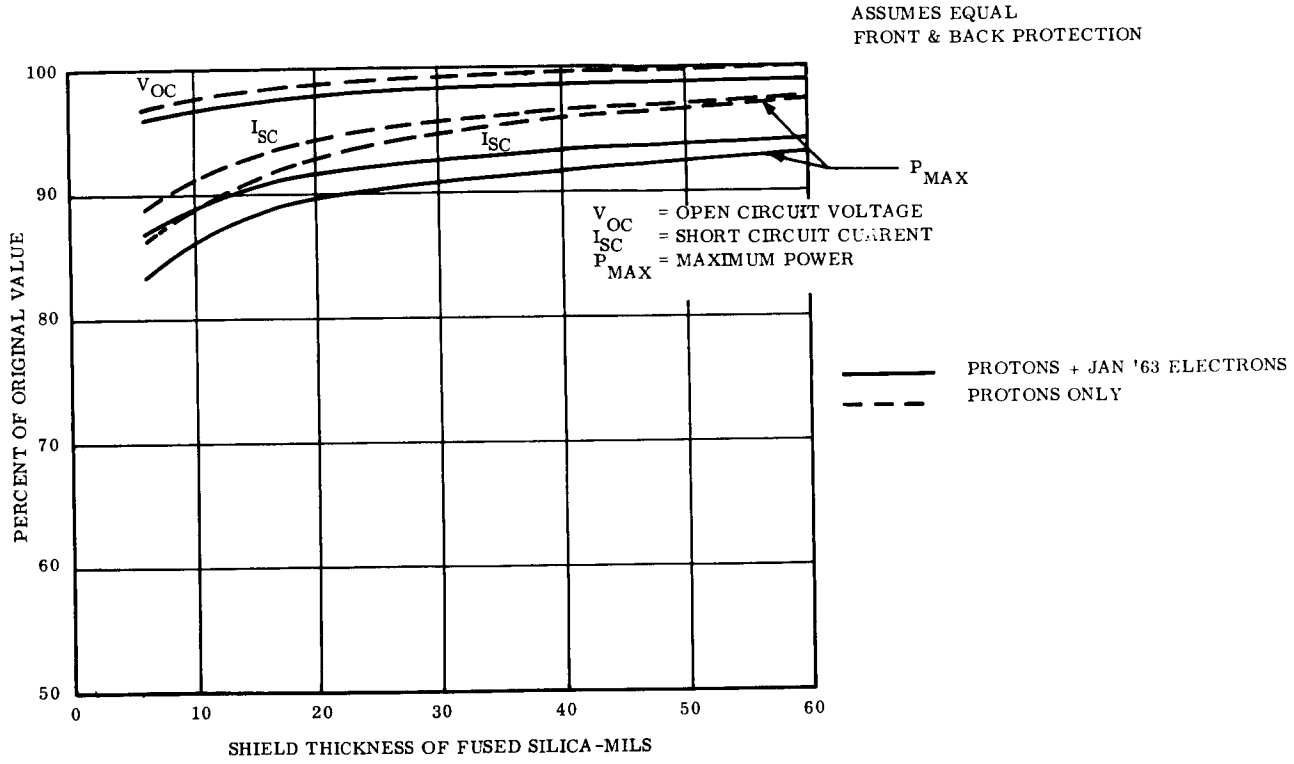

Figure 12-9. N/P Solar Cell Degradation for 325-Nautical Mile, 30-Degree Orbit After One Year

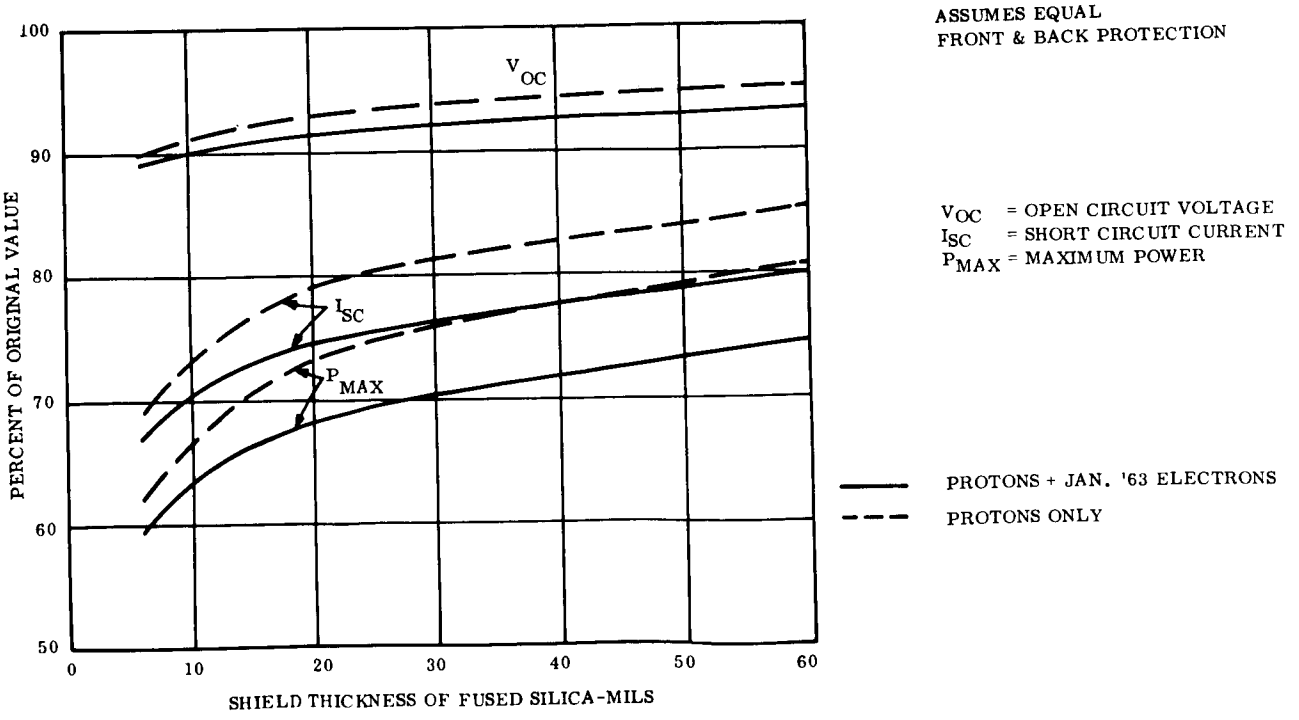

Figure 12-10. N/P Solar Cell Degradation for 1000-Nautical Mile, 101.84-Degree Orbit After One Year

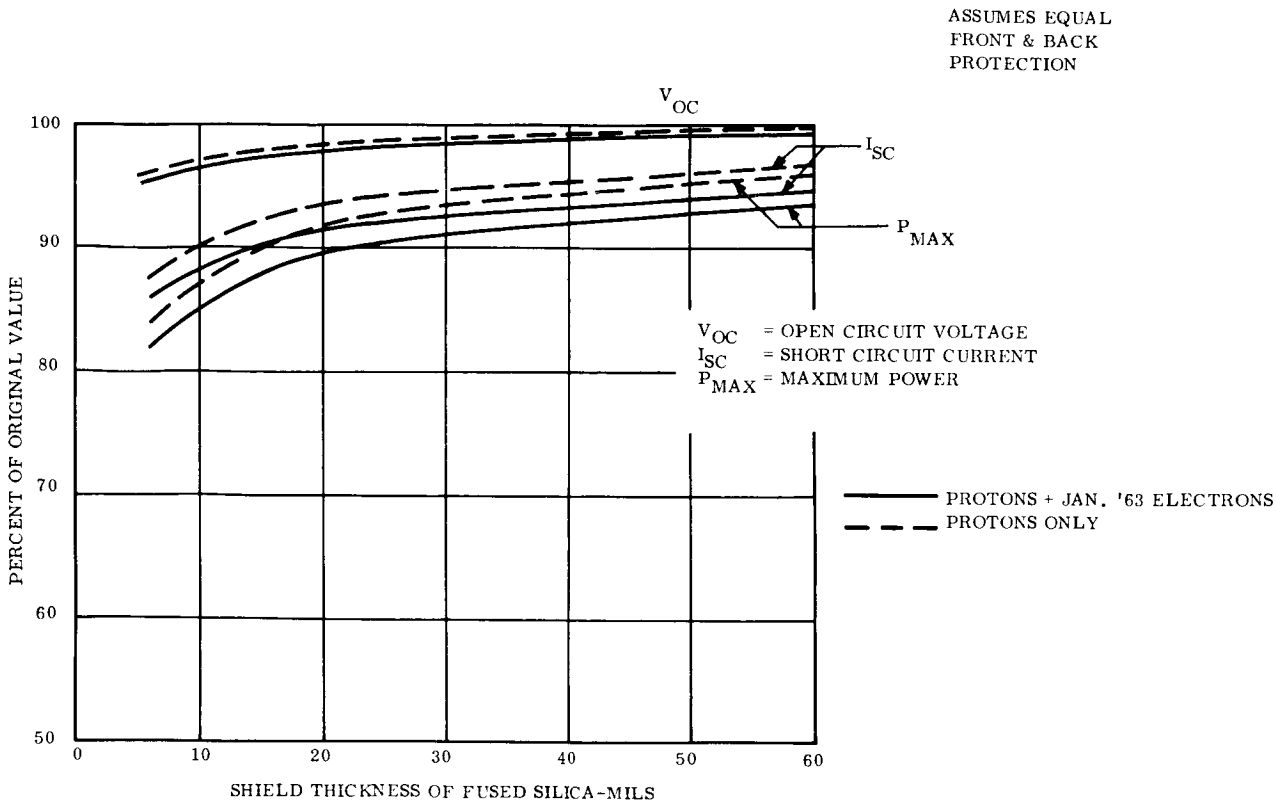

Figure 12-11. N/P Solar Cell Degradation for 200 by 25,000-Nautical Mile, 45-Degree Orbit After One Year

Two sets of curves are plotted in each figure. One represents the effect of the combined environment of protons and electrons as they were in January 1963, that is no electron decay has been assumed since January 1963 (worst case). The other set of curves is for protons alone; assuming all the electrons have decayed. As can be seen from the figures, the difference between these two assumptions is not very great, a variation up to five percent on maximum power for the two altitudes considered. It is not unreasonable to assume that for the 1967 to 1969 time period, the effects for the 325 and 200 by 25,000 nautical mile orbits will be due essentially to protons only. For the elliptical orbit, the damage is due almost entirely to the solar flare protons.

For the 1000-nautical mile orbit, it would appear more realistic at this time to include the full effects of the electrons as shown in Figure 12-10 since the electrons at this altitude are known to be decaying very slowly.

12.2.4 SUMMARY

In summary, it appears that the degradation of solar cells for the 325 and 200 by 25,000-nautical mile orbits will not be severe, approximately 15 percent after a year. The degradation estimate for the elliptical orbit is almost entirely due to solar flare activity. The present estimate is based on data gathered during the last maximum of the solar cycle; how closely this activity will be repeated during the next solar cycle maximum is not known.

Bulk damage to transistors does not appear to be a severe problem, although low frequency power devices may be somewhat effected for the 1000-nautical mile orbit case.

Radiation induced surface effects on transistors and diodes, on the other hand, may impose a severe degradation problem. This is particularly so for the 1000-nautical mile orbit. Since this effect is primarily due to total ionization, rather than atomic displacements as is the case with bulk damage, the overall magnitude of the problem is controlled by the trapped electron environment. Since most of these electrons are believed to be the result of the nuclear test, Starfish, and are known to be decaying, it is difficult to say what this environment will be in the 1967 to 1969 time period. Therefore, a large uncertainty remains as to the magnitude of any radiation induced surface effects in transistors for the orbits of interest.

In formulating the power subsystem design, the radiation degradation effects on solar cells will be considered. The degradation versus shield thickness plots given in Figures 12-9, 12-10 and 12-11 will be used to select the cover glass thickness and size the solar array for the three vehicle designs. Design solutions to the bulk damage and surface effects problems require detailed circuit design so they are beyond the scope of this study. However, these are very important areas which should receive further study when a preliminary design of the spacecraft is undertaken.

12.3 SOLAR CELL PERFORMANCE

The solar cell performance assumed for this study is based on the results of experimental measurements made by the General Electric Spacecraft Department on a group of six

RCA N/P solar cells. N/P solar cells were selected rather than P/N cells because of their superior radiation resistance (N/P solar cells are 10 to 20 times more radiation resistant than P/N cells). The cells were two by two centimeters in size with a silicon base resistivity of one ohm-centimeter, they were highly polished and had alloyed grids. The cells were mounted on pallets with a silicone rubber, in which thermocouples were buried. The pallets were hard-mounted to a temperature-controlled copper heat sink in a small vacuum chamber with a fused silica window. Short-circuit current was determined at various temperatures using a carbon-arc solar simulator. The voltage-current curves were then obtained using a color-temperature controlled tungsten source, using each solar cell as its own illumination transfer standard at each temperature. The resulting V-I curves for one of the cells is shown in Figure 12-12.

The data from these measurements was reduced and is shown in Figures 12-13 and 12-14. Figure 12-13 shows the average efficiency at each temperature and the average slope assumed. The slope results in a relative temperature-efficiency coefficient of $-0.0026/^{o}F$, referred to $85^{o}F$. For this study, this relation was adjusted upwards to correspond to an efficiency of 11 percent at $85^{o}F$. An equation may be written for the relative temperature dependence of efficiency from this data:

$$\eta_T = 2.417 - 0.0026\ T \qquad T = {}^{o}R$$

12.4 SOLAR CELL FILTER CHARACTERISTICS

Interference filters are used to optimize the output of solar cells. The selection of a filter and the resulting characteristics of the filter are considered here.

12.4.1 SOLAR CELL FILTER OPTIMIZATION

Optimization of the solar cell filter is based on considerations for maximum power output of the solar cells as a function of the width of the filter bandpass. The optimum bandpass is primarily influenced by the special response and temperature dependence of the solar cell.

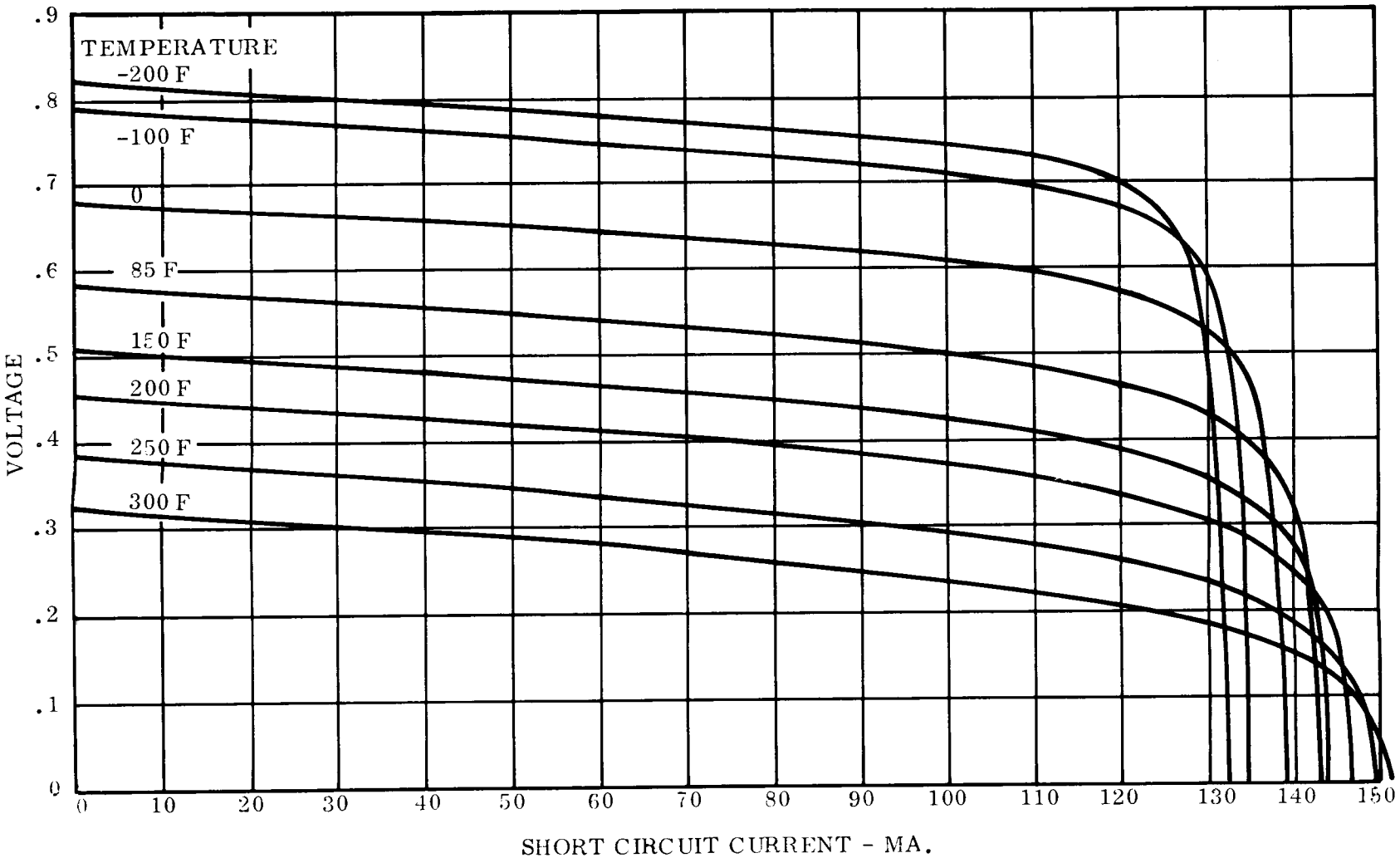

Figure 12-12. Typical V-I Curves for N/P Solar Cell (Two by Two Centimeter Cells)

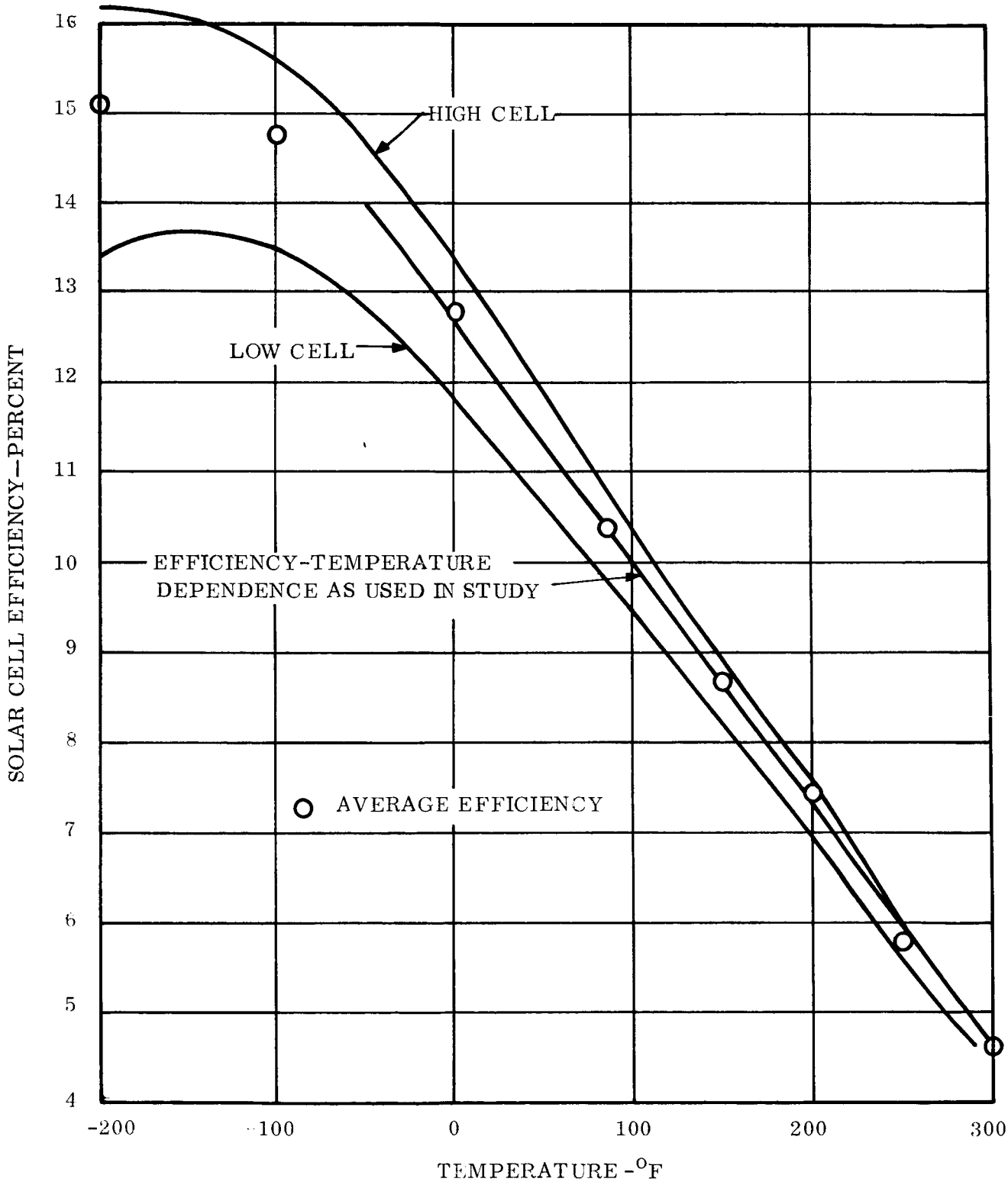

Figure 12-13. Variation of N/P Solar Cell Efficiency With Temperature

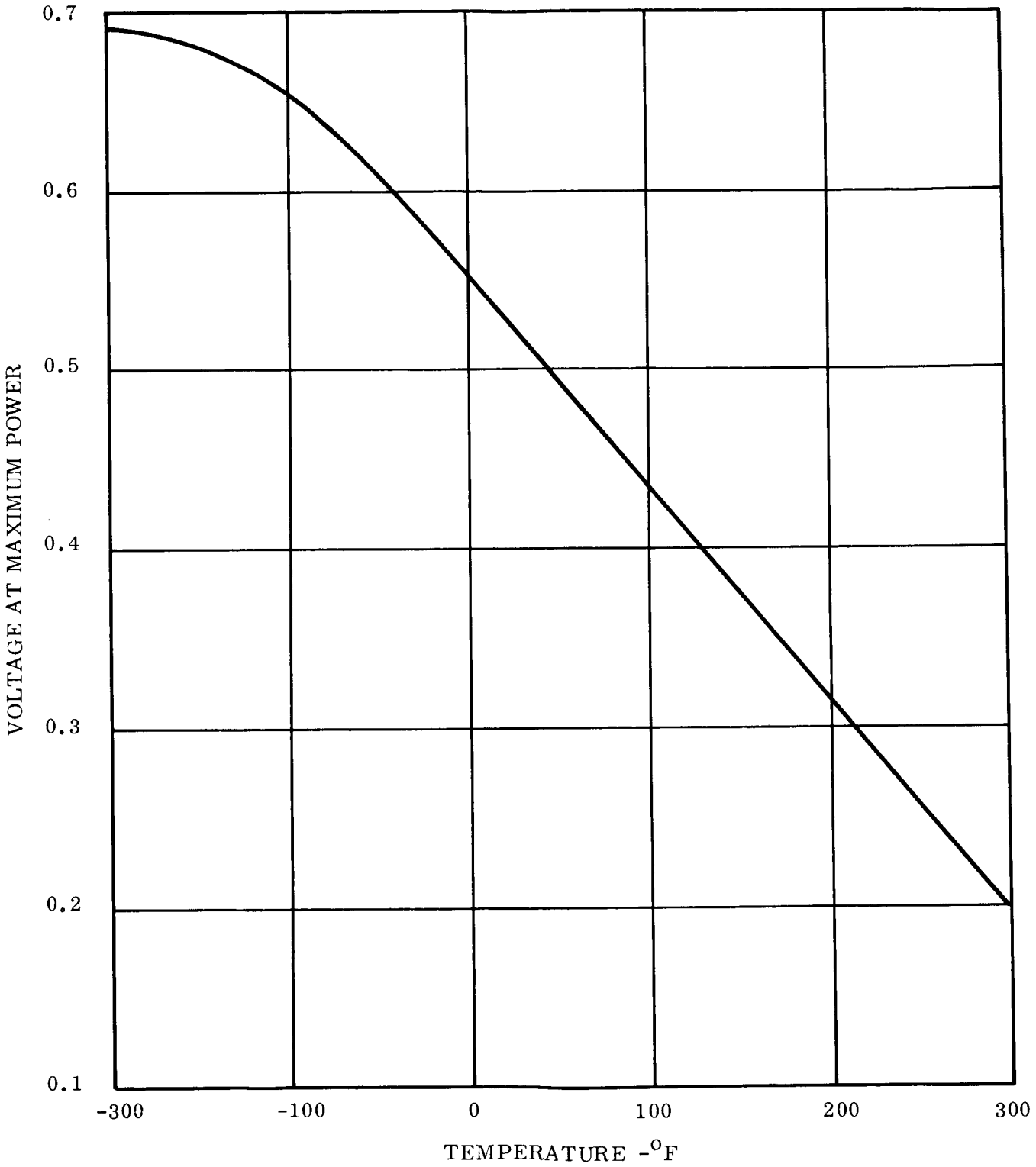

Figure 12-14. Temperature Dependence of Maximum Power Voltage for N/P Solar Cells

Since the filter is an interference type, its transmission characteristic is also a function of the incidence angle of the incoming light. Since the solar panels are sun oriented the array is essentially perpendicular to the solar vector at all times and the incidence angle effects do not influence the selection of the filter.

In selecting the optimum filter, both blue-red and blue filters were considered. The definitions of these filters are based on the wavelength at the 50 percent transmission points:

λ_1 is the short wavelength cut-on for both the blue and the blue-red filter

λ_2 is the cut-off wavelength for the blue-red filter

λ_3 is the long wavelength at which the blue-red filter again transmits.

Typical spectral transmittance of these filters is shown in Figure 12-15. The solar cell spectral response for which the filter was optimized is shown in Figure 12-16.

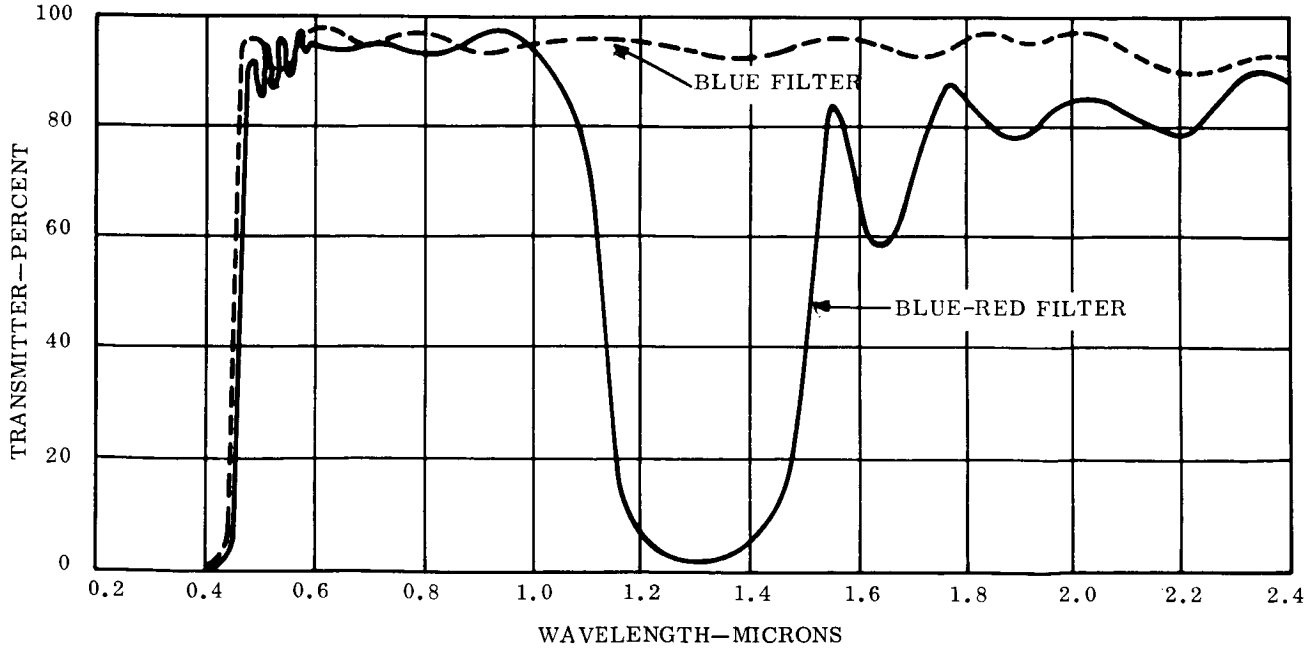

Figure 12-15. Spectral Transmittance of Filters

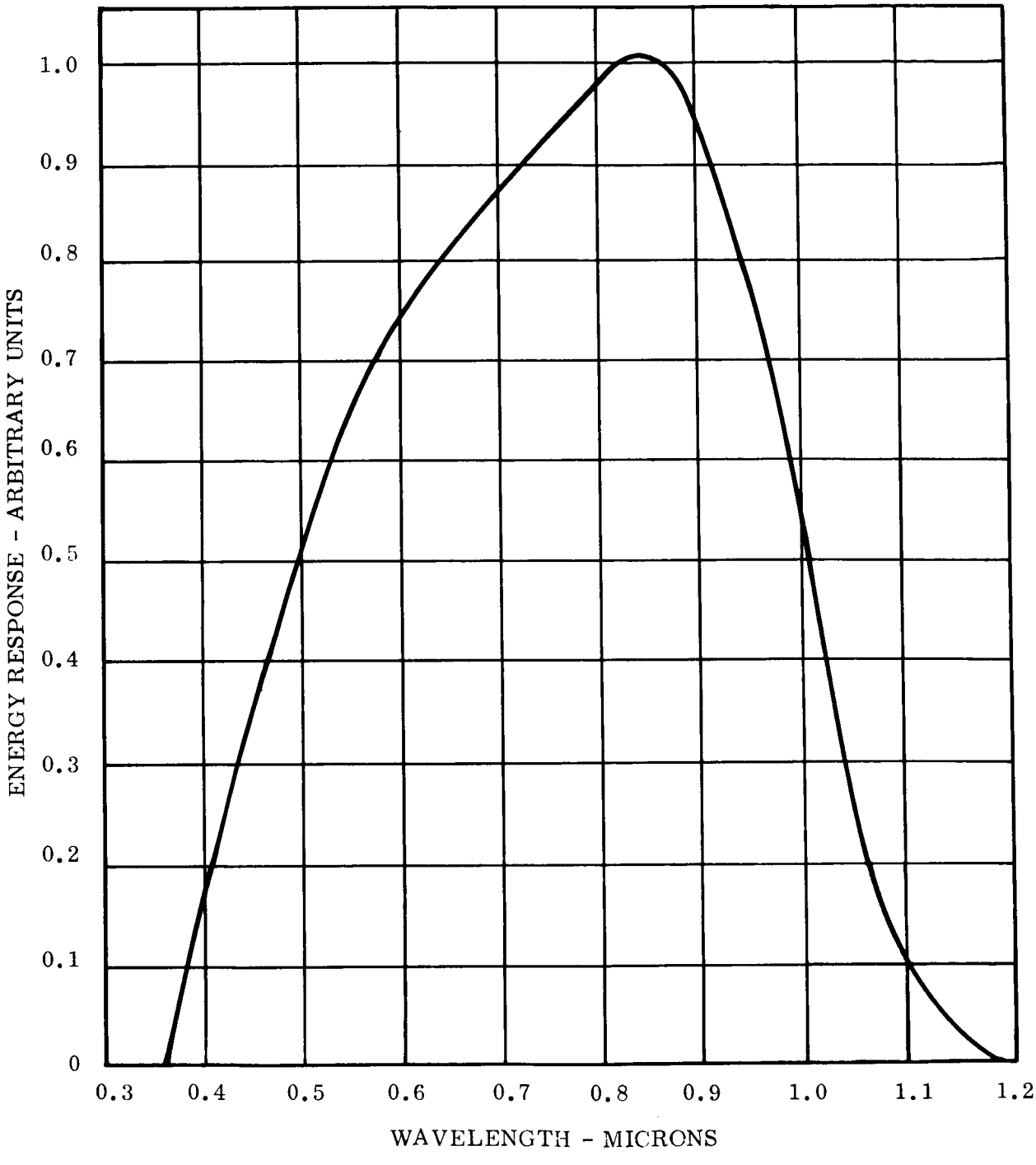

Figure 12-16. Spectral Response of N/P Silicon Solar Cell

Varying the bandpass characteristics of a solar cell filter affects the efficiency of the cell through two mechanisms. Broadening the bandpass increases the actinic transmission (the transmission of light to which the cell responds), directly affecting the cell efficiency. It also increases the amount of energy the cell absorbs and raises its temperature, thus indirectly decreasing the efficiency. The optimum filter occurs at the point where the two effects are equal for a given change in bandpass and the efficiency is maximized.

The filter optimization calculations proceed as follows. For each filter characteristic chosen for study, the average solar absorptance is determined (Section 12.4.2). This value is used to calculate the cell temperature, which in turn is used to calculate the cell efficiency relative to $85^{\circ}F$ by the use of the equation for temperature dependence of cell efficiency as developed in Section 12.3.

The actinic transmittance, η_D, was then determined for this filter by integrating the product of the cell spectral response (Figure 12-16), the filter transmittance, and the solar spectrum. The resultant solar cell efficiency is:

$$\eta = \eta_{SC}\,\eta_D\,\eta_T.$$

For this application, the bare cell efficiency, η_{SC}, will be 11 percent (see Section 12.5.1).

The results of the filter optimization are shown in Figure 12-17. The figure illustrates cell efficiency at end of life as a function of the filter cut-on for both blue and blue-red filters. For each λ_1 for the blue-red filter there is an optimum λ_2, as shown in Figure 12-18. The long wavelength cut-on λ_3 is a function of λ_2, and is shown in Figure 12-19.

As can be seen in Figure 12-17, the maximum efficiency occurs for a λ_1 between 0.40 and 0.43 microns for both the blue and the blue-red filter. Also evident is the relative insensitivity of cell efficiency to the cut-on wavelength in the region near the maximum efficiency point. A change of 40 millimicrons in λ_1 produces a change in efficiency of only one percent.

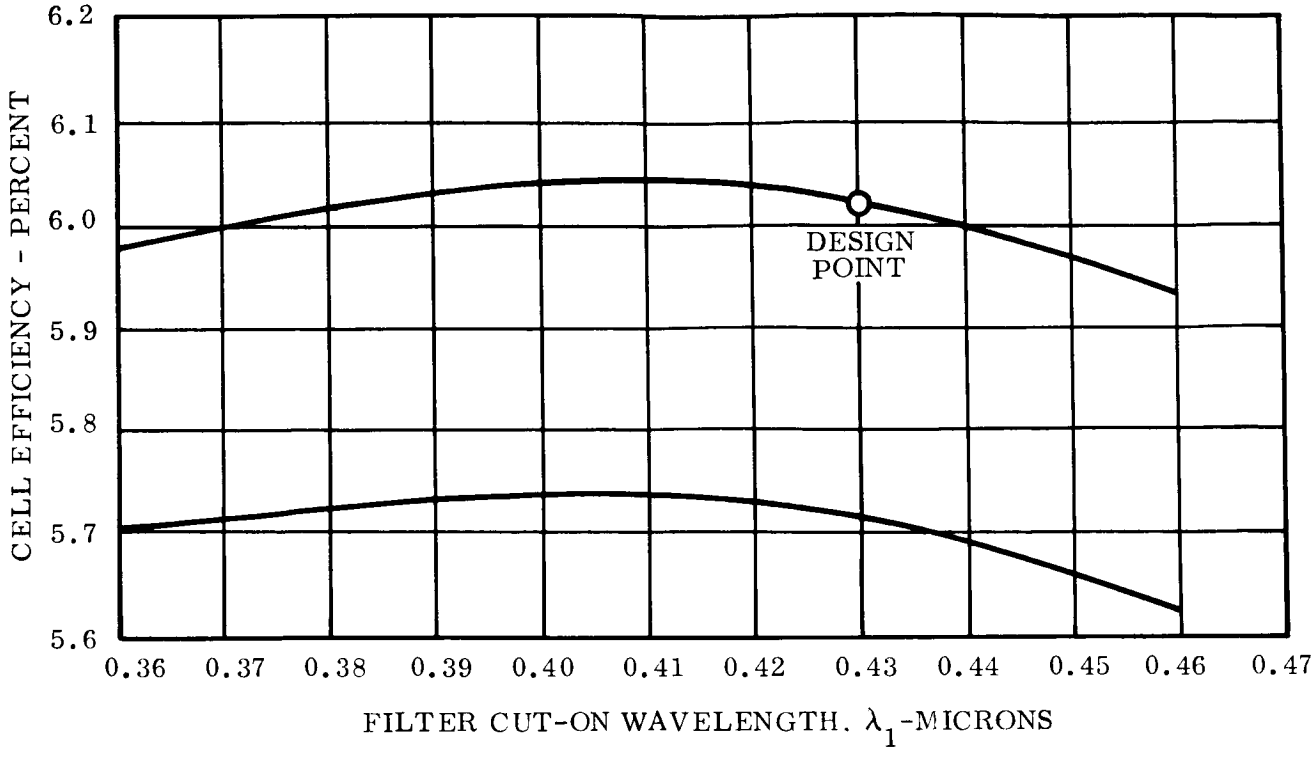

Figure 12-17. Results of Filter Optimization

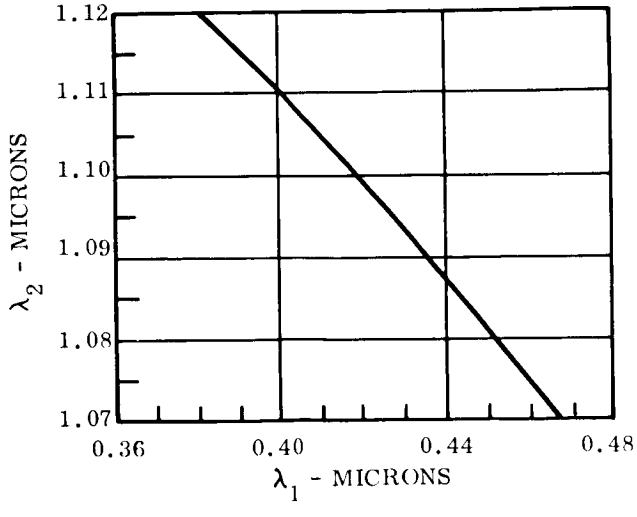

Figure 12-18. Filter Optimization (λ_1 vs. λ_2)

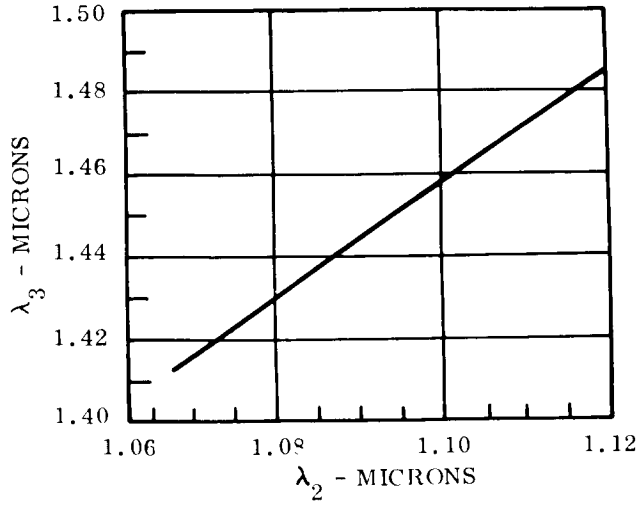

Figure 12-19. Filter Optimization (λ_2 vs. λ_3)

Selecting a filter with the cut-on toward the longer wavelengths offers certain advantages. The panel operated at a lower temperature, thus reducing to some extent the thermal interaction with the vehicle. Any shift of the filter to longer wavelengths by design reduces the ultraviolet leakage of the filter and provides greater protection to the organic cover glass bond.

Because of these considerations, a blue-red filter was selected with the cut-on wavelength shifted to the longer wavelengths as much as possible without seriously compromising the efficiency optimization. The resulting filter has the following characteristics:

λ_1 = 0.43 Microns

λ_2 = 1.09 Microns

λ_3 = 1.43 Microns

η_D = 0.92

α_o = 0.625 (See discussion below).

The solar cell panel does not have zero thickness, and there is a temperature drop through the panel. Approximately one half the heat is conducted through the panel to be radiated from the back side. For a typical panel structure the temperature drop between the front and back faces is 10^{o}F. Thus the solar cells will operate approximately 5^{o}F higher in temperature than the average temperature of the solar array. To account for this increase in temperature, in a convenient manner, the solar absorptance of the filter-cell composite was increased by 0.025, which corresponds to a 5^{o}F temperature increase in solar panel temperature. The resulting filter-cell solar absorptance, α_o, is then 0.65.

12.4.2 MEASUREMENT AND CALCULATION OF SOLAR ABSORPTANCE OF SOLAR CELL FILTER

Solar cell-filter composites were prepared, using several different types of cells and blue-red filters. The total spectral reflectance of these composites was measured in a spectro-

photometer. The solar absorptance was calculated from the absorptance (1.0 - reflectance) weighted with the solar spectrum:

$$\alpha_o = \frac{\int_o^\infty HA\,d\lambda}{\int_o^\infty H\,d\lambda}$$

where: α_o = Solar Absorptance

H = Solar Spectrum

A = Spectral Absorptance of Filter-cell Composite.

The results of these calculations are shown as data points in Figure 12-20. Note that the trend of absorptance versus filter cut-on wavelength for the measured points nearly parallels the theoretical curves. The Texas Instrument's solar cell and RCA solar cell composites have lower absorptance because the surfaces of those cell types are highly polished and are more reflective. This higher reflectance is not immediately obvious on examining the bare cell reflectance curves, which are shown in Figure 12-21, since the reflectance in the spectral region of greater solar intensity (0.4 to 0.6 micron) is greater for the sand-blasted cell than the polished cell. However, the filter also transmits in the infrared, and in that region the increased reflectance of the polished cell has its effect.

The net result is that the reflectance of a solar array made of polished cells will be about 0.08 greater and the temperature will be about 18°F cooler than an array of sandblasted cells. This corresponds to about five percent more power output, and since the initial efficiencies available for the two cell types are about the same, this five percent gain is free.

A comparison was made of the solar absorptance of the various filters and cells and a compromise set of properties was selected for the study. These are marked "Estimated for N/P cells" in Figure 12-20, and were used in the filter optimization procedure outlined in Section 12.4.1.

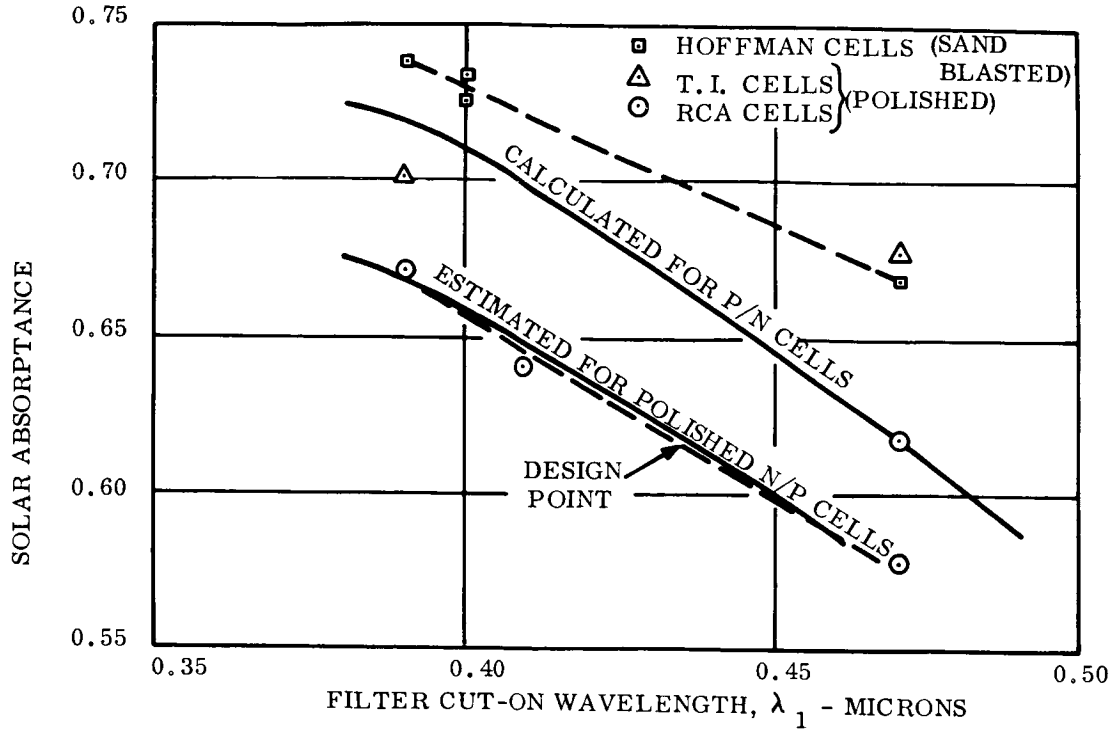

Figure 12-20. Reflectance of Filter - All Composites

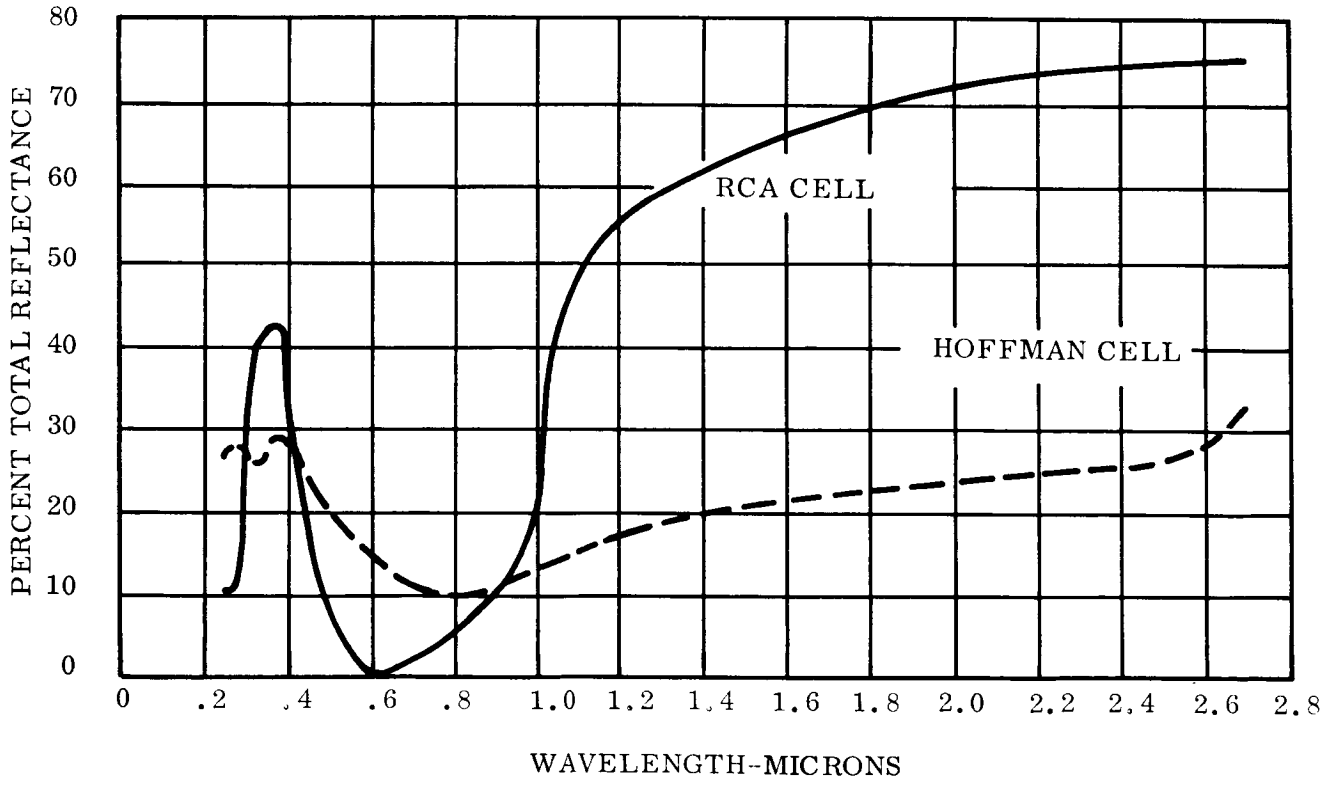

Figure 12-21. Reflectance of Bare Solar Cells

12.4.3 CALCULATION OF TRANSMITTANCE OF SOLAR CELL FILTER

Another parameter used in filter optimization is the transmittance of the solar cell filter to light to which the solar cell responds (the actinic transmittance). This was calculated for filters of various cut-on wavelengths by integrating the product of the solar spectrum, the solar cell spectral response, and the spectral transmittance of the solar cell:

$$\eta_D = \frac{\int_0^\infty HTR\,d\lambda}{\int_0^\infty H\,d\lambda}$$

where η_D = Actinic transmittance

H = Solar spectrum

T = Spectral transmittance

R = Solar cell spectral response.

The results of these calculations are shown in Figure 12-22 as a function of the filter cut-on wavelength.

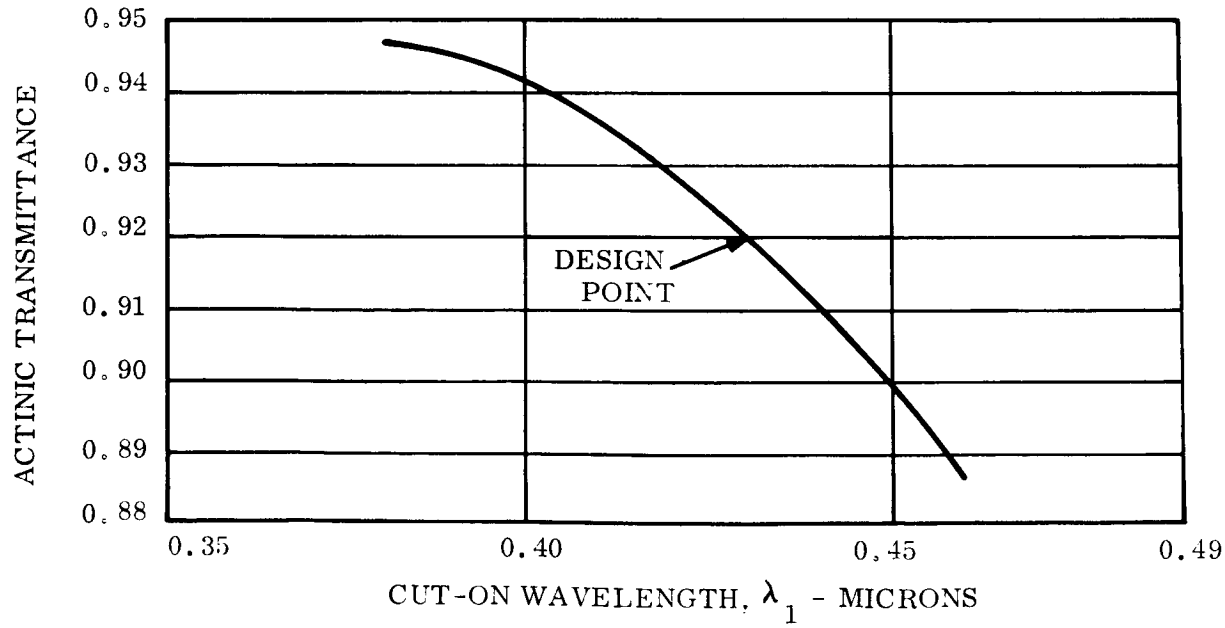

Figure 12-22. Calculated Transmittance of Blue-Red Filter

12.5 SOLAR ARRAY PERFORMANCE

Using the performance parameters established in Sections 12.2, 12.3, and 12.4, the solar array performance is calculated in this section.

12.5.1 GOVERNING EQUATION

The power output per square foot of sun oriented solar array is given by:

$$P = SZ\,\eta_{SC}\,\eta_T\,\eta_D\,\eta_U\,\eta_M\,\eta_{ME}\,\eta_S\,\eta_{RD}\cos\theta$$

where P = Power output, watts/ft^2

S = Solar intensity, watts/ft^2

Z = Solar cell packing factor

η_{SC} = Efficiency of bare cell (free space +85^{o}F)

η_T = Temperature-efficiency dependence of solar cell

η_D = Actinic Transmittance of filter

η_U = Ultraviolet degradation factor

η_M = Manufacturing loss factor

η_{ME} = Micrometeorite loss factor

η_S = Solar constant variation factor

η_{RD} = Radiation degradation factor

θ = Array tilt angle (measured from perpendicular to sun's rays).

Each of these factors is discussed below:

a. Solar Constant (S)

The solar intensity at 1 AU is assumed to be 130 watts per square foot. The solar intensity changes slightly throughout the year as a result of the variation of the earth's distance from the sun. This variation is accounted for by the solar constant variation factor, η_S, discussed below.

b. Packing Factor (Z)

A ratio of active cell area (1.9 square centimeters for a one by two centimeter cell) to panel area of 0.90 was assumed. This has been found to be reasonable based on past experience with manufacturing solar arrays of the type required for this application.

c. Solar Cell Efficiency (η_{SC})

An air mass zero efficiency of 11 percent is assumed for a bare cell at 85^{o}F. The Spacecraft Department has measured the efficiency of several N/P cells from one vendor at 10.5 percent and these cells were mechanical rejects with no particular attention paid to trying to select high efficiency. The same vendor has submitted price and delivery estimates to MSD within the past few months covering a range of air mass zero efficiencies from 9 to 11 percent in quantities up to several hundred thousand. They indicate deliveries in the tens of thousands per month are obtainable for the 11 percent cells beginning about six months after receipt of an order. Therefore, for the relatively low power level involved in this application, no difficulties are anticipated in obtaining the required number of 11 percent cells.

d. Temperature Efficiency Dependence (η_T)

A degradation factor of -0.26 percent per degree temperature rise above $85^{o}F$ is assumed. This is based on measured data on 10.5 percent efficient N/P solar cells (see Section 12.3). Therefore, $\eta_T = 2.417 - 0.0026T$, where T is in ^{o}R.

e. Actinic Transmittance of Filter (η_D)

A value of 0.92 was used for the actinic transmittance of the filter. This value was derived in Section 12.4.1.

f. Ultraviolet Degradation Factor (η_U)

An ultraviolet degradation factor of 0.95 is assumed. This is based on the General Electric Spacecraft Department's experience with the development and testing of solar arrays. This factor covers an observed decrease in output shortly after exposing the cell cover-glass combination to sunlight. This has been attributed to a decrease in the transmission properties of the filter due to exposure to ultraviolet radiation. It has been found that the bulk of this effect occurs during the first 20 hours in sunlight, either in vacuum or in the atmosphere. No significant further deterioration is experienced after this period. Testing has confirmed this conclusion for periods up to a simulated 4.3 years of sunlight exposure. Investigation into the detailed mechanism of this effect indicates there is a possibility of eliminating it by proper treatment of the filter. If this proves to be the case, this loss factor can be eliminated.

g. Manufacturing Loss Factor (η_M)

A manufacturing loss factor of 0.97 percent is assumed. This factor covers losses incurred in soldering, etc., during manufacturing and the value assumed is based on the Spacecraft Department's experience in the manufacture of solar arrays.

h. Micrometeorite Loss Factor (η_{ME})

Measurements made by the Spacecraft Department indicate the maximum degradation from micrometeorites to be five percent. Solar cell filter composites were prepared, their output measured, and then they were thoroughly sandblasted using a fine abrasive. Measured output after sandblasting showed a 4.5 percent reduction in short circuit current and a five percent reduction in current at the maximum power voltage.

i. Solar Constant Variation Factor (η_S)

The orbit of the earth about the sun is elliptical, and the varying earth-sun distance causes a maximum variation in the solar constant of ± 3.4 percent about the mean value of 130 watts per square foot. Therefore, a solar intensity variation of 0.966 was used in sizing the solar array.

j. Radiation Degradation Factor (η_{RD})

This factor accounts for the degradation in solar array output resulting from radiation damage. The radiation degradation factor is defined as the percent of the original power output available at the end of one year. This subject was covered in Section 12.2 and the results are summarized in Table 12-3.

Table 12-3. Radiation Degradation Factors

Orbit Altitude (Nautical Miles)	Radiation Degradation Factor, η_{RD}		
	6 Mils	15 Mils	30 Mils
1000	0.59	0.71	0.76
200 by 25,000	0.84	0.90	0.93
325	0.86	0.91	0.95

k. Array Tilt Angle (θ)

For this application the entire spacecraft will be sun pointing and since the solar thermionic system requires an orientation accuracy of approximately 0.1 degree, there should be no difficulty in mounting the solar panels such that they are oriented to the sun within ± 2 degrees. The cosine of two degrees is 0.99939 so the cosine of θ term in the solar array power output equation is essentially one.

Summarizing the factors to be used yields:

$S = 130 \text{ watts/ft}^2$

$Z = 0.9$

$\eta_{SC} = 0.11$

$\eta_T = 2.417 - 0.0026T$

$\eta_D = 0.92$

$\eta_U = 0.95$

$\eta_M = 0.97$

$\eta_{ME} = 0.95$

$\eta_S = 0.966$

η_{RD} = See Table 12-3

$\cos\theta = 1$

With the exception of temperature, all of the factors are known and the basic equation reduces to

$$P = 10.0\ \eta_T\ \eta_{RD}.$$

The radiation degradation factor, η_{RD}, still appears because the solar cell cover glass thickness has not been selected. This thickness will be determined in a subsequent section and then η_{RD} will be known.

To compute η_T the solar cell operating temperature must be estimated. This is done in Section 12.5.2.

12.5.2 SOLAR ARRAY OPERATING TEMPERATURE

The steady-state thermal balance equation for a solar array panel operating in space is given by

$$\underbrace{S\left[Z\alpha_o + (1-Z)\,\alpha_F\right]\cos\theta}_{\text{SOLAR RADIATION INPUT}} + \underbrace{A\,\alpha_B}_{\text{EARTH ALBEDO INPUT}}$$

$$+ E_B\,\epsilon_B + \underbrace{E_F\,Z\,\epsilon_C + E_F\,(1-Z)\,\epsilon_F}_{\text{EARTH RADIATION INPUT}}$$

$$= \sigma\underbrace{\left[Z\,\epsilon_C + (1-Z)\,\epsilon_F + \epsilon_B\right]T^4}_{\substack{\text{ENERGY RADIATED FROM CELLS, UNCOVERED FRONT AREAS, AND BACK OF PANEL}}} + \underbrace{P}_{\substack{\text{ELECTRICAL POWER OUTPUT OF ARRAY}}}$$

Where the terms which have not been previously introduced are defined below:

α_o = Average absorptance of solar cells

α_F = Absorptance of area between solar cells

α_B = Absorptance of back surface of solar panel

σ = Stefan-Boltzman constant, watts/ft^2-$^oR^4$

ϵ_C = Emittance of solar cells

ϵ_F = Emittance of area between solar cells

ϵ_B = Emittance of back surface of solar panel

A = Earth albedo flux, watt/ft^2

E_B = Earth thermal radiative flux received by the back portion of the solar panel, watts/ft^2

E_F = Earth thermal radiative flux received by the front portion of the solar panel, watts/ft^2

T = Average solar panel temperature, ^oR.

The following values of absorptivity and emissivity will be used in this analysis:

α_o = 0.65 (See Section 12.4.1)

α_F = 0.2 The area between the cells consists of aluminum substrate and solder connections. It was assumed that some of this area would be coated with a high reflectance coating to reduce the solar intake on the panel.

α_B = 0.2 Several high-emittance coatings have been developed which have measured absorptivity values in this range.

ϵ_C = 0.83 This is the measured emittance of fused silica.

ϵ_F = 0.49 As above, some of this area would be covered with a high reflectance-high emittance coating, increasing the emittance over that of bare solder or aluminum.

ϵ_B = 0.90 Several high-emittance coatings have been measured in the past, and the results are in this vicinity.

The earth albedo and radiative flux values can be computed using the following expressions:

$$A = a F_B S$$

$$E_B = \sigma F_B T_e^4$$

$$E_F = \sigma F_F T_e^4$$

where a = The earth albedo factor which varies with position and season from 0.20 to 0.54. An average value of 0.36 was used in these calculations.

T_e = The effective temperature of the earth for space radiation. This value was taken as 450^oR

F_B = View factor between the back face of the solar panel and the earth

F_F = View factor between the front face of the solar panel and the earth.

Obviously the view factors between the solar panel surfaces and the earth vary throughout the orbit. In this analysis the calculations are based on the "worst case" combination of view factors. As a result, the power output values calculated will represent the minimum solar array output and significantly larger power outputs will be generated at other points in the orbit. The worst case view factors for the three orbits of interest were obtained from Reference 12-1 and are presented in Table 12-4 below. These values coupled with the equations presented above were used to calculate the earth albedo and radiative flux values also given in Table 12-4.

Table 12-4. Earth Albedo and Radiative Flux Inputs

ORBIT ALTITUDE (Nautical Miles)	F_B	F_F	A WATTS/FT^2	E_B WATTS/FT^2	E_F WATTS/FT^2
1000 (101.84°)*	0.04	0.04	1.87	0.82	1.87
200 x 25,000 (45°)	0.52	0	24.4	10.65	0
325 (30°)	0.75	0	35.1	15.4	0

Using the expression developed for the electrical power output, P, in Section 12.5.1 and substituting the known values into the thermal balance equation yields:

$$8.5\text{x}10^{-10}T^4 + \eta_{RD}\,(24.17 - 0.026T) = 79.16 \text{ (1000 nm)}$$

$$8.5\text{x}10^{-10}T^4 + \eta_{RD}\,(24.17 - 0.026T) = 91.87 \text{ (200 x 25,000 nm)}$$

$$8.5\text{x}10^{-10}T^4 + \eta_{RD}\,(24.17 - 0.026T) = 98.32 \text{ (325 nm)}$$

*Numbers in parentheses indicate orbit inclinations.

Substituting the radiation degradation factors given in Table 12-3 and solving for the solar array temperature, T, yields the results presented in Table 12-5.

Table 12-5. Solar Panel Temperature

ORBIT ALTITUDE (Nautical Miles)	SOLAR PANEL TEMPERATURE - ^{o}R		
	6 MILS	15 MILS	30 MILS
1000 (101.84^{o})	542	538	537
200 x 25,000 (45^{o})	560	559	558
325 (30^{o})	572	570	569

Several important points should be emphasized regarding the temperatures presented in Table 12-5. First these temperature estimates represent the maximum value the solar panels will reach during the mission life. As indicated previously, they were calculated for the worst case thermal position in the orbit. Therefore, at other points in the daylight segment of the orbit the solar panels will operate at lower temperatures and thus produce more power. These temperatures were also calculated for conditions at the end of one year in orbit. Temperatures are maximum at the end of the mission life because the electrical power produced by the solar cells is reduced due to radiation damage. The small decrease in temperature with increasing cover glass thickness results because the increase in shielding thickness protects the solar cells to a greater extent and the power output is therefore degraded less over the one year period. In the initial phase of the mission, before radiation has affected the solar cell output, the solar panels would operate at the same temperature regardless of cover glass thickness.

12.5.3 POWER OUTPUT PER SQUARE FOOT OF SOLAR ARRAY

Now that the solar array temperatures have been estimated, the power output per square foot of solar array can be calculated using the following expression developed in Section 12.5.1:

$$P = 10.0\ \eta_T \eta_{RD}\ \text{watts/ft}^2.$$

This equation was evaluated for the radiation degradation factors and temperatures given in Tables 12-3 and 12-5 respectively. The resulting power outputs are given in Table 12-6.

Table 12-6. Solar Array Minimum Power Outputs

ORBIT ALTITUDE (Nautical Miles)	POWER OUTPUT - WATTS/FT^2		
	6 MILS	15 MILS	30 MILS
1000 (101.84°)	6.0	7.22	7.77
200 by 25,000 (45°)	8.07	8.65	9.27
325 (30°)	8.0	8.52	8.9

Since maximum temperature values were used, the power output per square foot of solar array figures represent the minimum values corresponding to the worst thermal position in the orbit and operation after one year in space.

For a given cover glass thickness the minimum power output figures are approximately the same for the 325 and 200 by 25,000-nautical mile orbits. However, the power output of the solar array in the 325-nautical mile orbit will not vary greatly from the minimum figures given in the table, while in the 200 by 25,000-nautical mile case, the power output will be substantially higher than the minimum figure throughout most of the orbit period. This occurs in the latter case because the wide altitude extremes encountered in the elliptical orbit result in large variations in the earth radiation and albedo inputs to the solar panels.

In spite of the lower array temperature, the minimum power output for the 1000-nautical mile case is substantially lower (approximately 25 percent) than the array output in the other two orbits. This is due to the higher radiation degradation associated with this orbit.

Also, in the 1000-nautical mile orbit, because of the particular orbit inclination, the solar panel view factor will not change appreciably with orbit position. Therefore, the power output of the solar array will be essentially constant throughout the daylight segment of the orbit.

In each of the three orbits, the power output will be appreciably higher in the initial phases of the mission; this is because the radiation environment will not have degraded the solar cell performance appreciably and the cell operating temperature will be lower.

12.5.4 SELECTION OF COVER GLASS THICKNESS

To this point, the solar array power output calculations have been made as a function of cover glass thickness. The necessary information is now available to select the proper cover glass thickness.

Figure 12-23 shows solar panel specific weight as a function of cover glass thickness. This curve is based on the Spacecraft Department's past experience in the design and development of solar panels of the type and size required for this application. A weight breakdown of the components, excluding the panel structure, used to establish the results given in Figure 12-23 is presented in Table 12-7.

Table 12-7. Solar Panel Weight Breakdown

COMPONENT	WEIGHT LB/FT^2
Cover Glass (Fused Silica 30 Mils)	0.344
Glass-to-Cell Adhesive, Wire and Solder	0.05
Solar Cells	0.28
Cell-to-Substrate Adhesive (10 Mils)	0.075
Electrical Insulation Coating on Substrate (2-Mil)	0.015
Diodes	0.003
Terminals	0.02
TOTAL WEIGHT EXCLUDING STRUCTURE	0.777 Pounds/Square Foot

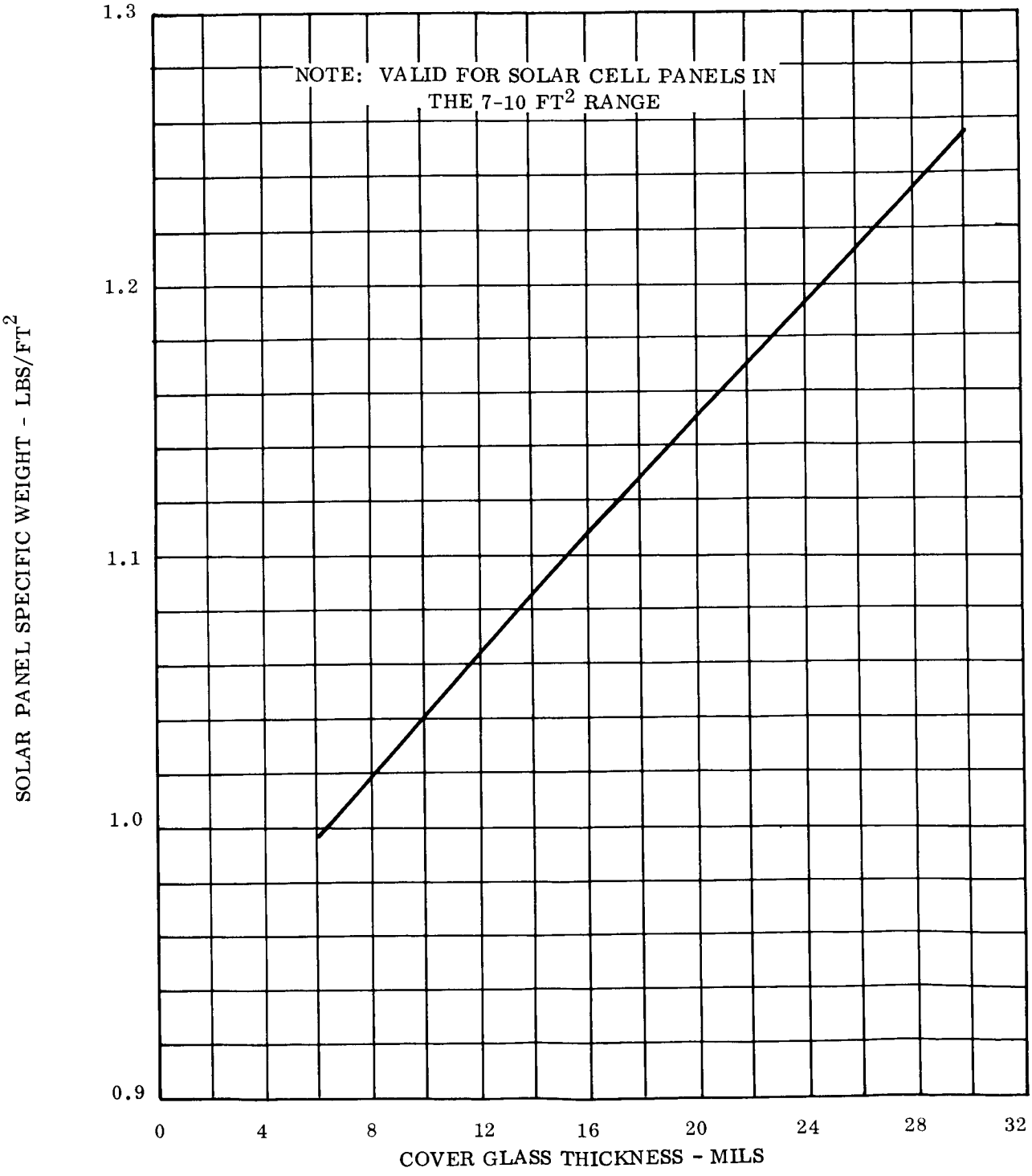

Figure 12-23. Solar Panel Specific Weight

These figures include a cover glass thickness of 30 mils. The unit area weight of other cover glass thicknesses can be found by multiplying the thickness by 0.01145 $lb/ft^2/mil$. The difference between the weight figures presented in Table 12-7 and those given in Figure 12-23 represents the panel structure weight.

Coupling the results given in Table 12-6 and those presented in Figure 12-23, the specific power (watts per pound) of the solar array can be computed as a function of cover glass thickness. This was done and the results are presented in Table 12-8. The unsupported solar panel area was assumed to be six square feet.

Table 12-8. Solar Panel Scientific Power

ORBIT ALTITUDE - (Nautical Miles)	POWER OUTPUT - WATTS/FT^2			SOLAR PANEL SPECIFIC WEIGHT - LB/FT^2			SPECIFIC POWER - WATTS/LB		
	6 Mils	15 Mils	30 Mils	6 Mils	15 Mils	30 Mils	6 Mils	15 Mils	30 Mils
1000	6.0	7.22	7.77	1.00	1.10	1.26	6.00	6.65	6.18
200 by 25,000	8.07	8.65	9.27	1.00	1.10	1.26	8.07	7.86	7.35
325	8.0	8.52	8.9	1.00	1.10	1.26	8.00	7.74	7.07

These results are plotted in Figure 12-24. It is apparent that the cover glass thickness should be kept as small as possible for the 200 by 25,000 and 325-nautical mile orbits. Experience indicates that the minimum useable glass thickness is six mils. Handling smaller thicknesses is difficult and results in a high percentage of breakage. Although for these two orbits it might result in higher specific powers, the cover glass cannot be completely eliminated because the filter is deposited on the under side of the glass. For the 1000-nautical mile orbit, the optimum filter thickness is approximately 15 mils.

The power output figures on which the solar array sizing will be based are summarized in Table 12-9.

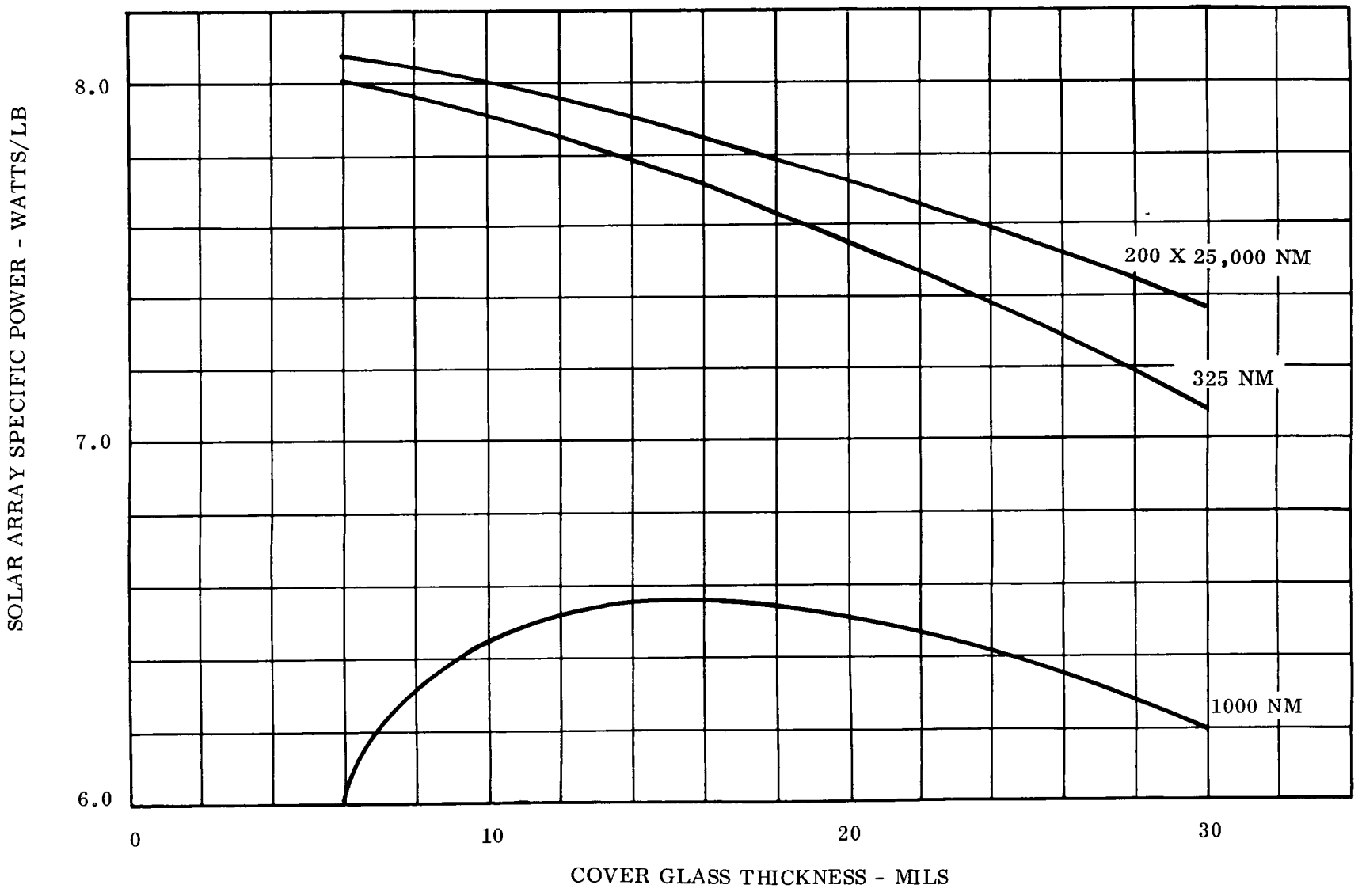

Figure 12-24. Selection of Optimum Cover Glass Thickness

Table 12-9. Solar Array Power Output at Optimum Cover Glass Thickness

ORBIT ALTITUDE (Nautical Miles)	COVER GLASS THICKNESS MILS	SOLAR ARRAY POWER OUTPUT WATTS/FT^2
1000	15	7.22
200 by 25,000	6	8.07
325	6	8.0

12.6 POWER REQUIREMENTS

The power requirements can be considered in two parts: (1) that required during initial stabilization before the spacecraft is capable of generating power, and (2) that needed during normal orbital operation. The expected power requirements for these two conditions are outlined in the following two sections.

12.6.1 POWER REQUIREMENTS DURING INITIAL STABILIZATION

While the spacecraft is on the launch pad the power requirements would be supplied by a ground power supply external to the launch vehicle. At launch this source of power would be disconnected. In the ensuing period from launch until the vehicle is stabilized and the solar panels oriented to the sun, the spacecraft will have no power generating capability and the power requirements will be supplied by batteries located onboard the launch vehicle or within the spacecraft. Of prime interest here is the power needed from the time the spacecraft is separated from the launch vehicle until the solar panels are deployed and oriented to the sun; since these requirements must be supplied by batteries located on the spacecraft.

After the spacecraft separates from the launch vehicle it will take approximately ten minutes (see Section 11) to stabilize, deploy the solar panels, and orient the vehicle to the sun. During this period the spacecraft power requirements will be confined primarily to the attitude control and TT&C subsystems. The attitude control subsystem will be engaged in

stabilizing and sun orienting the spacecraft while the TT&C subsystem is needed to track and command the vehicle, and to handle diagnostic instrumentation.

Table 12-10 outlines the estimated power requirements during the ten-minute stabilization period.

Table 12-10. Power Requirements During Initial Stabilization

	COMPONENTS	POWER WATTS	DURATION MINUTES	ENERGY REQUIREMENTS WATT-MINUTES
ATTITUDE CONTROL SUBSYSTEM	Gyros (3)	35	10	350
	Flywheels (2)	4	10	40
	Control Electronics	9	10	90
	Logic Devices	3	10	30
	Pneumatic Solenoids	80	1	80
	A-C and D-C Power Conditioning (75% Efficiency)	7	10	70
TT&C SUBSYSTEM	Command Receiver (2)	0.4	10	4
	Command Decoder (2)	7	5	35
	Programmer	1	10	10
	PCM Encoder	2	10	20
	Signal Conditioner	1	10	10
	Diagnostic Instrumentation	1	10	10
	Tracking Beacon[a]	2	10	20
	Core Storage[b]	0.2	10	2
TOTAL				771 Watt-Minutes

NOTES:

a. The tracking beacon is replaced by a transponder in the highly elliptical orbit case. The transponder requires 12 watts continuously for the ten-minute period.

b. The core storage is replaced by a tape recorder in the highly elliptical orbit case. The tape recorder requires 10 watts continuously for the ten-minute period.

To allow for contingencies the total energy requirements presented in Table 12-10 are increased (approximately 10 percent) to 850 watt-minutes or 14.2 watt-hours. This figure will be used for the 1000 and 325-nautical mile orbits. The 200 by 25,000-nautical mile orbit requires 969 watt-minutes which increased approximately 10 percent becomes 1065 watt-minutes or 17.8 watt-hours. These requirements will be supplied by primary silver oxide-zinc batteries which are sized in Section 12.7.3.

12.6.2 POWER REQUIREMENTS DURING NORMAL ORBITAL OPERATION

By combining the power requirements for the primary and secondary experiments and the various spacecraft subsystems, power profiles can be developed for each of the three missions. This was done using the power requirements given in Sections 5.4,* 8.6, 10.11 and 11.5 , and the results are presented in Table 12-11. These power requirements are arranged to represent the "worst case" condition that could be encountered. All of these requirements will not occur every orbit and will not always occur in the particular sequence assumed, however, they could occur in the form assumed and if they did they would represent the most severe demand on the power subsystem. The power requirement summarized in Table 12-11 are presented graphically in Figures 12-25, 12-26 and 12-27. These requirements will be supplied by a combination solar cell-nickel cadmium battery power supply which is sized in Section 12.7.3.

12.7 POWER SUBSYSTEM DESIGN

12.7.1 DESCRIPTION OF SUBSYSTEM

A schematic of the power subsystem is presented in Figure 12-28.

The solar array, using N/P silicon solar cells, supplies power to the load and charging power to the batteries when the vehicle is in the daylight portion of the orbit. Rechargeable nickel-cadmium batteries supply the power requirements when the vehicle is in the earth's shadow and short term peaks during the daylight portion of the orbit. The power requirements

*Located in Volume II

Table 12-11. Spacecraft Power Requirements [a]

	Experiment or Subsystem	Power Requirements	Comments
Mission A	A- Thermionic Experiment	4.4 watts continuously during the daylight portion of the orbit. 1.4 watts continuously during the dark segment of the orbit.	1.4 watts continuously for instrumentation. 0.4 watts during daylight for cesium reservoir heaters. 2.6 watts during daylight for reflectometer.
	B- Secondary Experiments	18.1 watts continuously during the daylight portion of the orbit. 7 watts continuously during the dark segment of the orbit. A 22.3 watt spike of 15 minutes duration during the daylight portion of the orbit.	This includes all of the priority A and B experiments listed in Table 5-5 (Volume II) except the earth albedo experiment.
	C- TT&C Subsystem	6 watts continuously throughout the orbit. An 18 watt peak of 12 minutes duration occuring during the dark segment of the orbit.	The 6 watts are for data collecting and 18 watts are required during data transmission.
	D- Attitude Control Subsystem	36 watts continuously throughout the orbit. A 81 watt peak of 3 minutes duration during the dark portion of the orbit. Also a 40 watt peak of 10 minutes duration during the light portion of the orbit.	The 81 watt peak is associated with unloading the flywheels and reorienting the spacecraft when it emerges from the earth's shadow. Both of these functions require firing pneumatic solenoids. The 40 watt peak is associated with the flywheels demand for more power during the reorientation phase after each shadow period.
	E- Critical Spacecraft Component Instrumentation	One watt continuous.	Primarily for temperature measurements using thermistors.
Mission B	A- Thermionic Experiment	4.4 watts continuously during the daylight portion of the orbit. 1.4 watts continuously during the dark segment of the orbit.	1.4 watts continuously for instrumentation. 0.4 watts during daylight for cesium reservoir heaters. 2.6 watts during daylight for reflectometer.
	B- Secondary Experiments	14.1 watts continuously during the daylight portion of the orbit. 6.3 watts continuously during the dark segment of the orbit. A 20.2 watt spike of 15 minutes duration during the daylight portion of the orbit.	This includes all of the priority A and B experiments listed in Table 5-5 (Volume II) except the Radiation Effects on Solar Cells and the Earth Albedo Experiments. The earth sensor portion of the ultraviolet experiment is also eliminated.
	C- TT&C Subsystem	20 watts continuously throughout the orbit. A 40 watt peak of 5 minutes duration and a 34 watt peak of 5 minutes duration both occuring during the dark segment of the orbit. These peaks do not coincide.	The 20 watts are for data collection and 40 watts are required during data transmission. The 34 watt peak is associated with the R&RR tracking phase.
	D- Attitude Control Subsystem	36 watts continuously throughout the orbit. A 81 watt peak of 3 minutes duration during the dark portion of the orbit. Also a 40 watt peak of 10 minutes duration during the light portion of the orbit.	The 81 watt peak is associated with unloading the flywheels and reorienting the spacecraft when it emerges from the earth's shadow. Both of these functions require firing pneumatic solenoids. The 40 watt peak is associated with the flywheels demand for more power during the reorientation phase after each shadow period.
	E- Critical Spacecraft Component Instrumentation	One watt continuous.	Primarily for temperature measurements using thermistors.
Mission C	A- Thermionic Experiment	4.4 watts continuously during the daylight portion of the orbit. 14 watts continously during the dark segment of the orbit.	1.4 watts continuously for instrumentation. 0.4 watts during daylight for cesium reservoir heaters. 2.6 watts during daylight for reflectometer.
	B- Secondary Experiment	23.1 watts continuously during the daylight portion of the orbit. 7 watts continuously during the dark segment of the orbit. A 27.2 watt spike of 15 minutes duration during the daylight portion of the orbit.	This includes all of the priority A and B experiments listed in Table 5-5 (Volume II) except the Radiation Effects on Solar Cell experiment.
	C- TT&C Subsystem	7 watts continuously throughout the orbit. An 18 watt peak of 4 minutes duration occuring during the dark segment of the orbit.	The 7 watts are for data collection and the 18 watts are required during data transmission.
	D- Attitude Control Subsystem	36 watts continuously throughout the orbit. A 81 watt peak of 3 minutes duration during the dark portion of the orbit. Also a 40 watt peak of 10 minutes duration during the light portion of the orbit.	The 81 watt peak is associated with unloading the flywheels and reorienting the spacecraft when it emerges from the earth's shadow. Both of these functions require firing pneumatic solenoids. The 40 watt peak is associated with the flywheels demand for more power during the reorientation phase after each shadow period.
	E- Critical Spacecraft Component Instrumentation	One watt continuous.	Primarily for temperature measurements using thermistors.

Notes

a - These power requirements represent the "worst case" conditions the power subsystem would see during the mission.

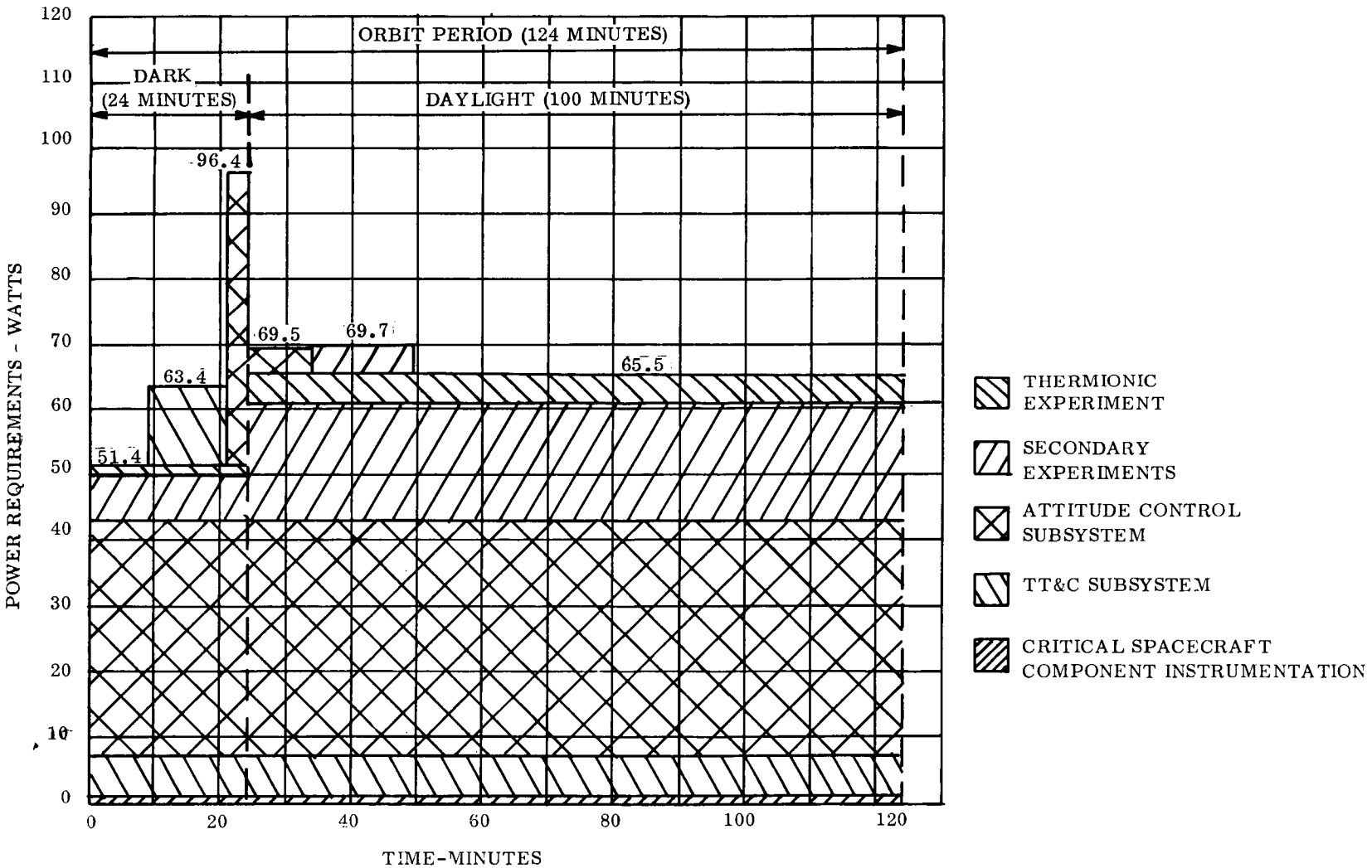

Figure 12-25. Power Requirements for Mission A

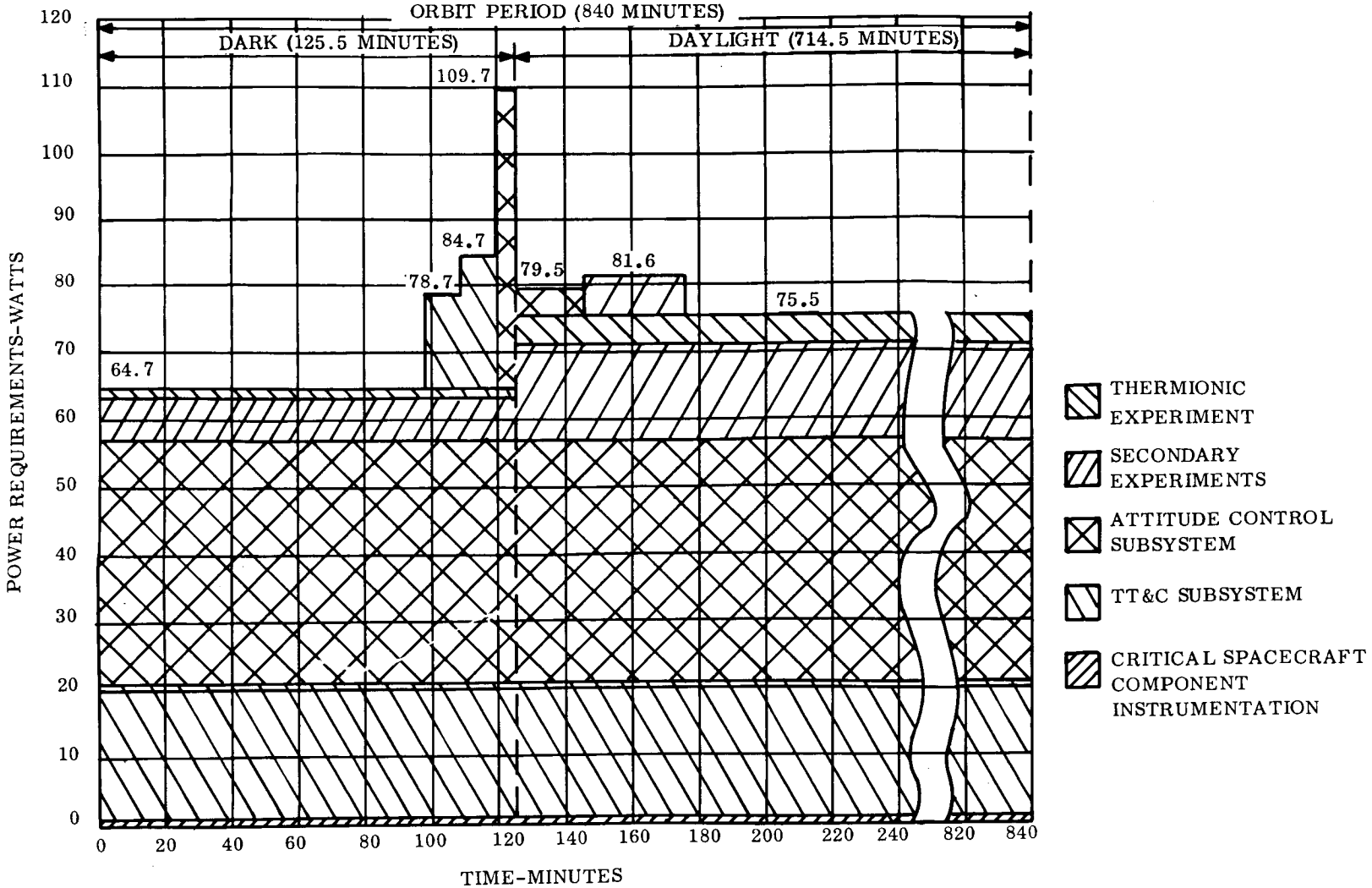

Figure 12-26. Power Requirements for Mission B

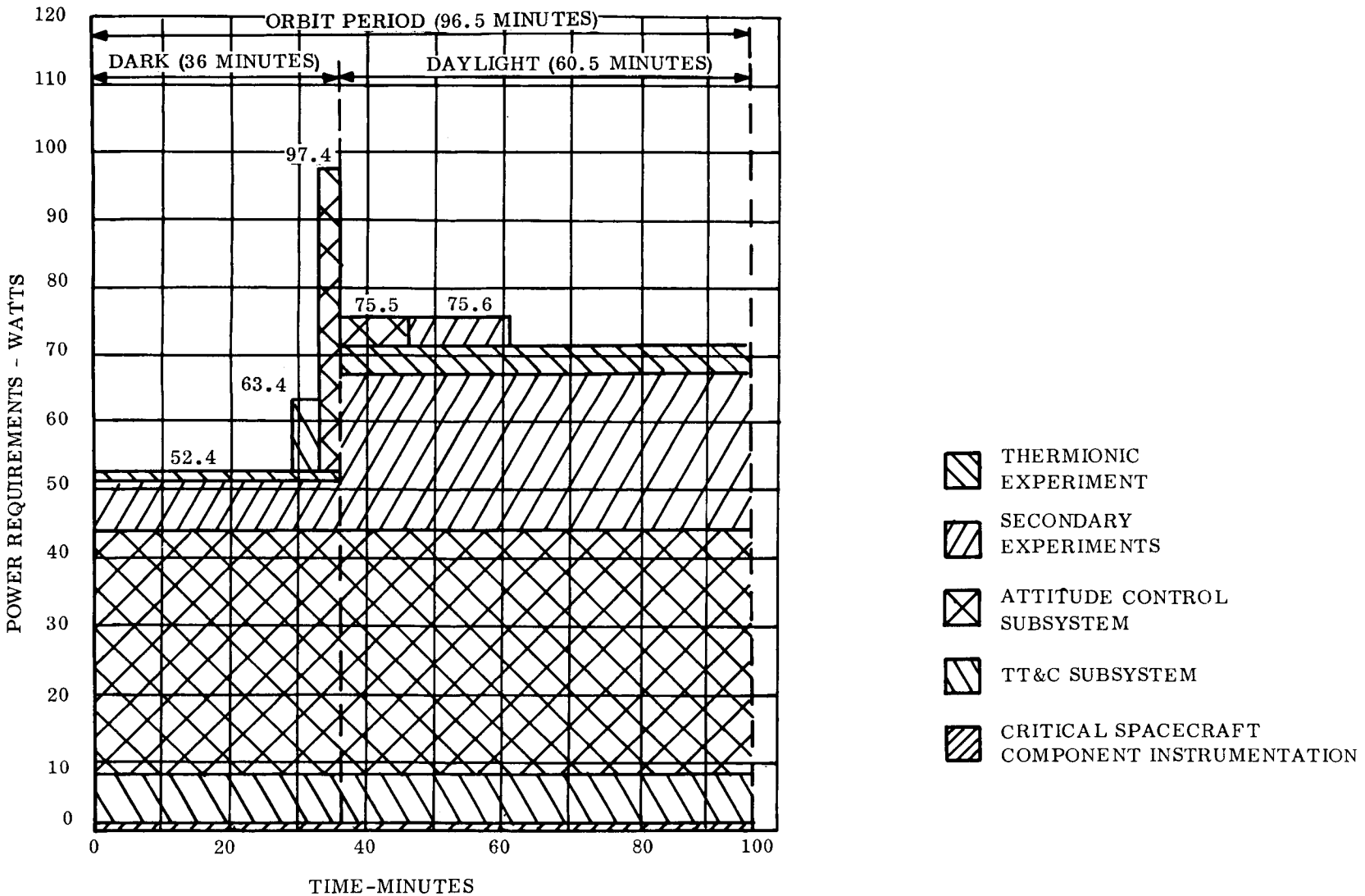

Figure 12-27. Power Requirements for Mission C

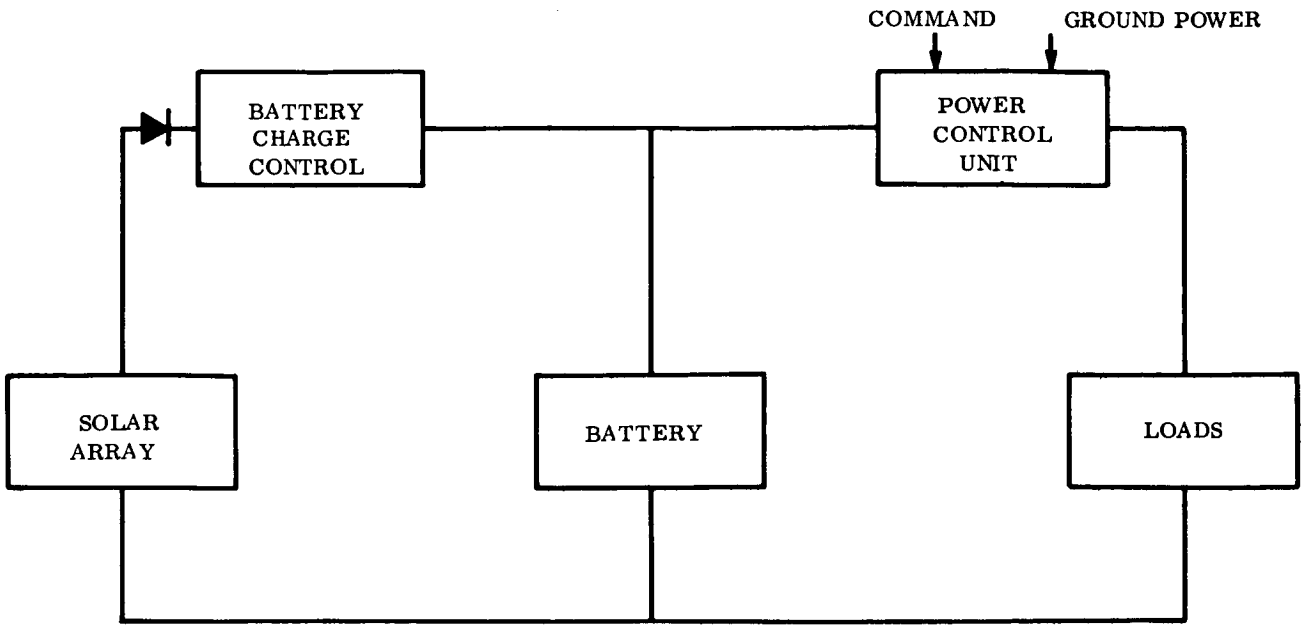

Figure 12-28. Power Supply Schematic

during initial stabilization, before the solar panels are sun oriented, would be supplied by a non-rechargeable (primary) silver oxide-zinc battery.

The battery charge regulator controls the rate at which the battery is charged. It is a switching type unit which maintains the required average battery charging current and operates at a very high efficiency. With this arrangement, the battery also provides coarse voltage regulation on the main bus (the bus voltage varying between battery charge and discharge values) with an expected variation of approximately ± 15 percent. Each load would provide its own voltage level and regulation.

The power control unit provides for switching of various components according to command and/or programmed inputs, contains input connections from ground power, and may also provide some circuit protection.

12.7.2 DESCRIPTION OF COMPONENTS

Since detailed component designs are beyond the scope of this study the exact techniques employed in the component designs are unknown. However, the component descriptions given here assume approaches presently used in the design of similar components.

12.7.2.1 Solar Array

The solar array would consist of one by two-centimeter silicon N/P solar cells of 11 percent efficiency in air mass zero illumination at 85°F. The cells would have grids of alloyed construction; the front cell surface would be polished and would have an anti-reflection coating which is otpimized for 0.6 micron; the base resistivity would be one ohm-centimeter; and the contact strip would be on the short end of the cell, resulting in an active area of 1.9 square centimeters per cell.

The solar cells would be connected in parallel in groups of ten to form submodules, which would then be connected in groups of 36 (typical) to form modules. The cells will be bonded flat to the substrate. Typical module construction is shown in Figure 12-29. The solar array would provide 28 volts ± 15 percent to the bus.

Fused silica cover glasses would be applied to the cells to serve as protection against the ionizing radiation and micrometeorite damage. A separate cover glass would be applied to each cell.

Multi-layer interference reflecting filters would be applied to the cover glass to reflect the ultraviolet and infrared portions of the solar spectrum, to protect the cover glass bond from darkening due to the ultraviolet radiation and to increase the efficiency of the solar cells by lowering their operating temperature. The cut-off wavelengths of this filter would be 0.43 and 1.09 microns.

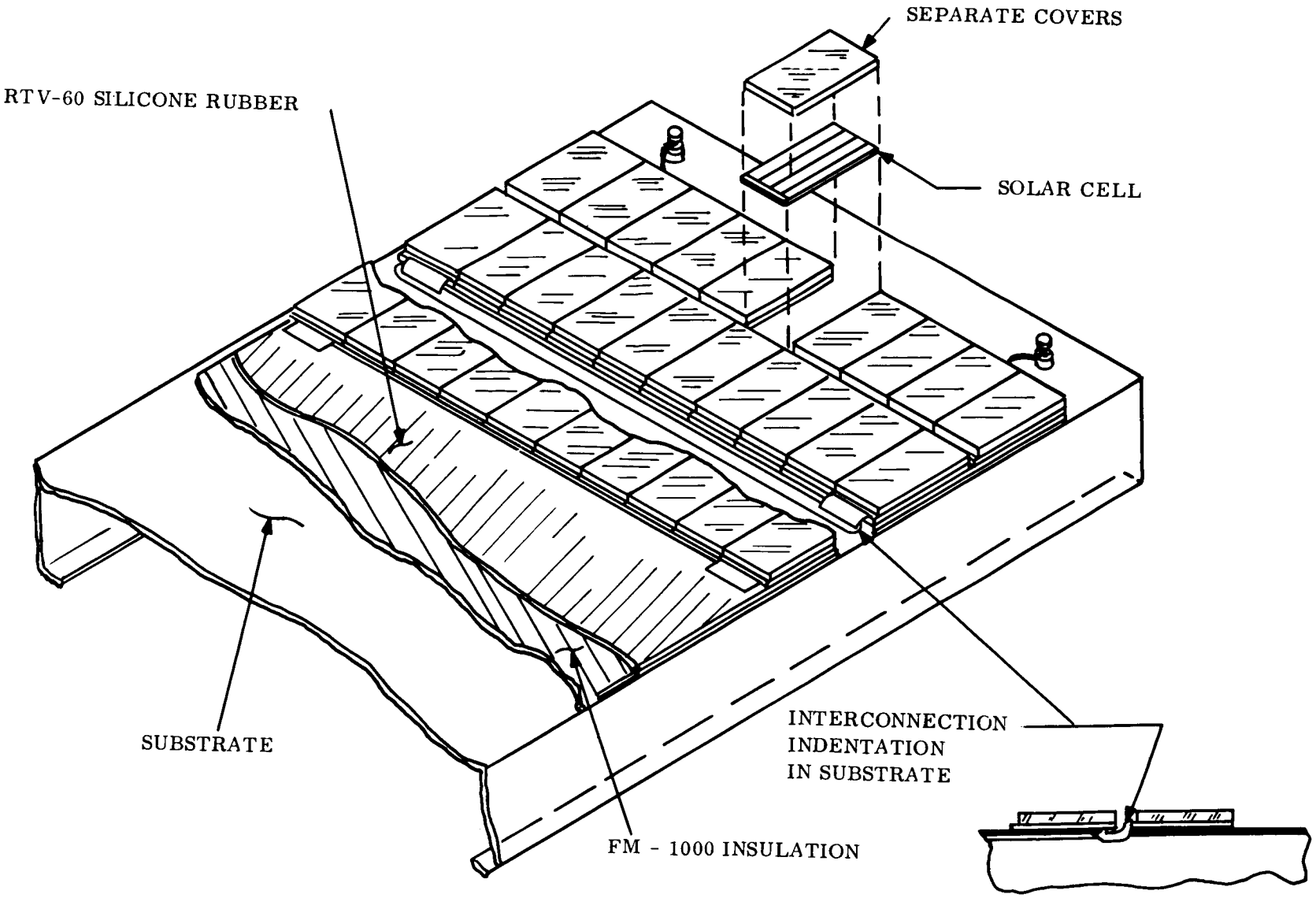

Figure 12-29. Solar Module

Silver strips would be used to connect the solar cells in parallel, and short silver tabs to connect the submodules in series. Thin silver sections of this nature provide high electrical conductivity, are easy to solder, and are light in weight. The cover glass would be bonded to the solar cells using an epoxy resin such as General Electric PD-454. The solar cells would be bonded to the module substrate using a silicon rubber like General Electric RTV-60.

In order to prevent short circuits between the solar cells and the metallic substrate, a thin layer of insulation would be applied directly to the substrate before the cells were bonded. An epoxy adhesive in sheet form such as Bloomingdale FM-1000, would be used for the purpose.

To reduce the temperature drop through the module substrate structure, the substrate would be made of sheet aluminum instead of the traditional aluminum honeycomb. By taking this approach the front-to-back temperature drop is reduced from 30^{o} to 10^{o}F. The modules would be attached to sheet metal supports which would serve as the major structural member.

Diodes would be used in series with each series string. The diodes protect against the eventuality of shorting in the solar array by preventing other parts of the array from discharging into the shorted section.

12.7.2.2 Battery

The battery would consist of sealed nickel-cadmium cells housed in a magnesium of aluminum container. Nickel-cadmium cells are recommended because they have demonstrated long-life capabilities in space under cyclic operating conditions. Silver oxide-zinc cells might also be used depending on developments in the near future. These cells are lighter and smaller than nickel-cadmium cells but as yet have not demonstrated the life and reliability characteristics of nickel-cadmium cells.

Charging of the battery can be accomplished by either the constant current or constant potential methods. A constant-current charge would be maintained at approximately 1.5 amperes and terminated when the battery reached the desired voltage level; the battery would then be floated. A constant potential charge could also be used, but the charge current must be limited in cases where the battery has been deeply discharged. The actual charging scheme is often a combination of the two, with maximum current and voltage limits superimposed. Variable current limits would be used, controlled by the voltage on the battery during charging. The high current rate being used when the battery voltage was low. As the battery voltage increased, the charge current would be reduced until the battery reached its fully charged voltage, by which time the charge would become a constant potential float. The maximum current charge rate limit is imposed to keep the current below the point at which gassing occurs.

The power requirements during initial stabilization of the spacecraft would be supplied by a non-rechargeable silver oxide-zinc battery. This particular type of battery offers a high watt-hours per pound ratio and has demonstrated reliability in space applications.

12.7.2.3 Battery Charge Regulator

The battery charge regulator controls the rate at which the battery is charged. It's primary function is to float the battery at a constant potential when the battery is in a fully charged condition. Following a discharge cycle, the battery charge regulator must maintain the charging current below a prescribed limit until the battery voltage rises to the floating potential. There will be a decrease in the current from the current limit coincident with the increase in battery voltage.

The battery charge regulator would consist of a compound pass transistor to regulate the charge current, a resistance divider sampling circuit in shunt with the battery, a constant voltage diode reference, a single transistor stage comparison circuit and error amplifier, a current limiting emitter resistor, and an over-current sensing transistor to hold the pass transistor at the current limit. A resistor from the main bus in series with the voltage

reference ensures that sufficient current is always supplied to keep the voltage reference diodes in the low impedance breakdown region.

The constant voltage reference would consist of two 6.2-volt temperature compensated, voltage-reference diodes and a conventional silicon diode in series to compensate for the emitter base junction voltage change with temperature of the comparison stage.

12.7.2.4 Power Control Unit

The power control unit would perform power circuit switching to direct power to users as required by the mission and actuate squib firing circuits for separation and deployment. The primary functions would include:

a. Transfer of the load from the auxiliary ground power unit to the vehicle battery during prelaunch checkout

b. Switch power to various parts of the load, such as the attitude control subsystem or transmitter, on signals from the command decoder, programmer, or prelaunch checkout console

c. Switch power to fire separation or deployment squibs

d. Disconnect the main bus power at the end of useful mission life.

Squibs are activated by gating a silicon controlled rectifier to apply power to the squib bridgewire. The power pulse would be drawn from the battery. A thermal fuse element breaks the circuit in the event that a bridgewire shorts, and opens the power drain path from the battery. Series current limiting resistors allow limiting of the total current to the amount necessary to fire, and current division to synchorinize the thermal fuse to allow a minimum time to fire the squib under worst case conditions.

Noise suppression circuits would prevent misfire of the controlled rectifier or transistors by requiring a minimum volt-second pulse necessary to turn on the switch that is significantly greater than any expected noise levels.

The power switching would be accomplished by latching power relays with transistor buffers. The input switching signal would consist of a short medium voltage.

12.7.2.5 Harnesses

Harnesses would be required to conduct power between the components of the power supply subsystem and to the power users. The harness would be divided into two parts. The power harness would conduct power and control signals between the components of the power subsystem. The power distribution harness would conduct power from the power control unit to the user subsystems. The harnesses will be terminated in connectors to provide rapid removal of components.

12.7.3 SIZING OF POWER SUPPLY

In this section the solar array and battery sizes are determined for the power requirements outlined in Section 12.6.

The following nomenclature is employed in this analysis.

P_{sa} = The power output of the solar array measured at the array, watts

P_c = Continuous power requirement during daylight portion of the orbit, watts

E_b = Energy taken from the battery per cycle, watt-hours

C = Nominal capacity of battery, ampere-hours

α = Maximum battery overcharge rate per ampere hour of discharge

β = Minimum battery overcharge required per ampere-hour of discharge

f = Ratio of discharge to charge time

I_L = Average load on the battery, amperes

t_c = Battery charge time, hours

t_d = Battery discharge time, hours

η_b = Battery charge - discharge efficiency

η_d = Diode and harness efficiency

η_{cc} = Battery charge control efficiency

η_{pc} = Power control unit efficiency

η_h = Harness efficiency between the battery and the load.

Based on past hardware design experience representative values for these efficiencies are:

η_b = See Figure 12-30

η_d = 0.96

η_{cc} = 0.94

η_{pc} = 0.97

η_h = 0.98

These values are used in this analysis.

The following design philosophy will be used in sizing the power supply. The power required during the dark portion of the orbit, plus the small peaks that occur during the daylight segment will be supplied by a rechargeable nickel-cadmium battery. The solar array will be sized to provide the constant daylight power requirements plus the energy necessary to charge the battery.

As a sample calculation consider the power requirements for Mission A, given in Figure 12-25.

12.7.3.1 Solar Array

The energy taken from the battery per cycle, E_b, is

$$E_b = \frac{\text{watt-hrs required during dark}}{\eta_{pc}\,\eta_h} + \frac{\text{watt-hrs required during daylight peaks}}{\eta_{pc}\,\eta_h}$$

$$= \frac{51.4 \times 24 + (63.4 - 51.4)\,12 + (96.4-51.4)\,3}{0.97 \times 0.98 \times 60} + \frac{(69.5-65.5)\,10 + (69.7-65.5)\,15}{0.97 \times 0.98 \times 60}$$

= 28.5 watt-hours.

The solar array output must be sufficient to supply the constant portion of the daylight power requirements plus the energy necessary to charge the battery.

Therefore,

$$P_{sa} = \frac{1}{\eta_d\,\eta_{cc}} \left[\frac{E_b}{\eta_b\,t_c} + \frac{P_c}{\eta_{pc}\,\eta_h} \right]$$

$$= \frac{1}{0.96 \times 0.94} \left[\frac{28.5}{0.67 \times 1.67} + \frac{65.5}{0.97 \times 0.98} \right]$$

= 99.5 watts.

In this orbit the solar array power output is 7.22 watts per square foot (see Table 12-9). Therefore, the required solar array area is:

$$\text{Solar Array Area} = \frac{99.5}{7.22} = 13.8 \text{ square feet.}$$

From Table 12-8, the solar array panel will have a specific weight of 1.10 pounds per square foot. Therefore, the solar array weight is:

Solar Array Weight = 13.8 x 1.10 = 15.1 pounds.

12.7.3.2 Secondary Battery

Knowing the energy taken from the battery each cycle allows the battery capacity to be calculated. The following assumptions are made in estimating the performance of sealed, rechargeable nickel-cadmium batteries:

a. Battery capacity, including the case but not including thermal control is assumed to be 9 watt-hours/pound for 100 percent depth of discharge. A volume of 14 cubic inches per pound is assumed.

b. Constant current charging is assumed throughout the charge and overcharge period.

c. The maximum allowable current during the overcharge condition is assumed to be that which will supply 100 percent ampere-hour capacity in a period of six hours. This value is based on past experience. Charging currents in excess of this are considered to run too high a risk of battery failure due to excessive generation of gas and build-up of internal pressure. In addition high charging currents create heating problems.

d. The maximum depth of discharge for repeated cycling is assumed to be 60 percent. For charging times less than 4.5 hours, the maximum allowable current during the overcharge condition as noted in (c) above, will determine battery size, and the depth of discharge will be less than 60 percent, varying linearly with charge time up to 4.5 hours. For charge times greater than 4.5 hours, the charging rate is cut back from the six-hour rate in order to hold depth of discharge at 60 percent.

e. The excess ampere-hours of overcharge required to maintain continuous cycling is assumed to be 25 percent for a six-hour charging rate.

f. For purposes of calculating charging efficiency of the battery, defined as the ratio of the watt-hours delivered during discharge to the watt-hours put back into the battery during the charge plus overcharge period, it is assumed that the average discharge and charge voltages are 1.2 and 1.43 volts per cell respectively. This assumption, together with the assumptions of (e), results in a variation of charging efficiency with actual charging time as indicated in Figure 12-30. Test data indicates that these voltage assumptions are reasonable.

The preceding assumptions are based on the General Electric Spacecraft Department's experience with the use of rechargeable nickel-cadmium batteries for space applications.

Since the time available for recharging the battery is less than 4.5 hours the battery capacity is defined by overcharge limitations rather than depth of discharge limitations (see assumption (d) above). For the overcharge limited case the battery capacity is given by

$$C = \frac{I_L}{\alpha} \left[f (1 + \beta) \right] ,$$

where C = Nominal capacity of battery, ampere-hours

α = Maximum overcharge rate per ampere-hour of capacity

β = Minimum overcharge required per ampere-hour of discharge

f = Ratio of discharge to charge time

I_L = Average load on the battery in amperes.

Based on the power profile given in Figure 12-25 and the assumptions listed previously the governing parameters are:

$$f = \frac{24 \text{ min}}{100 \text{ min}} = 0.24$$

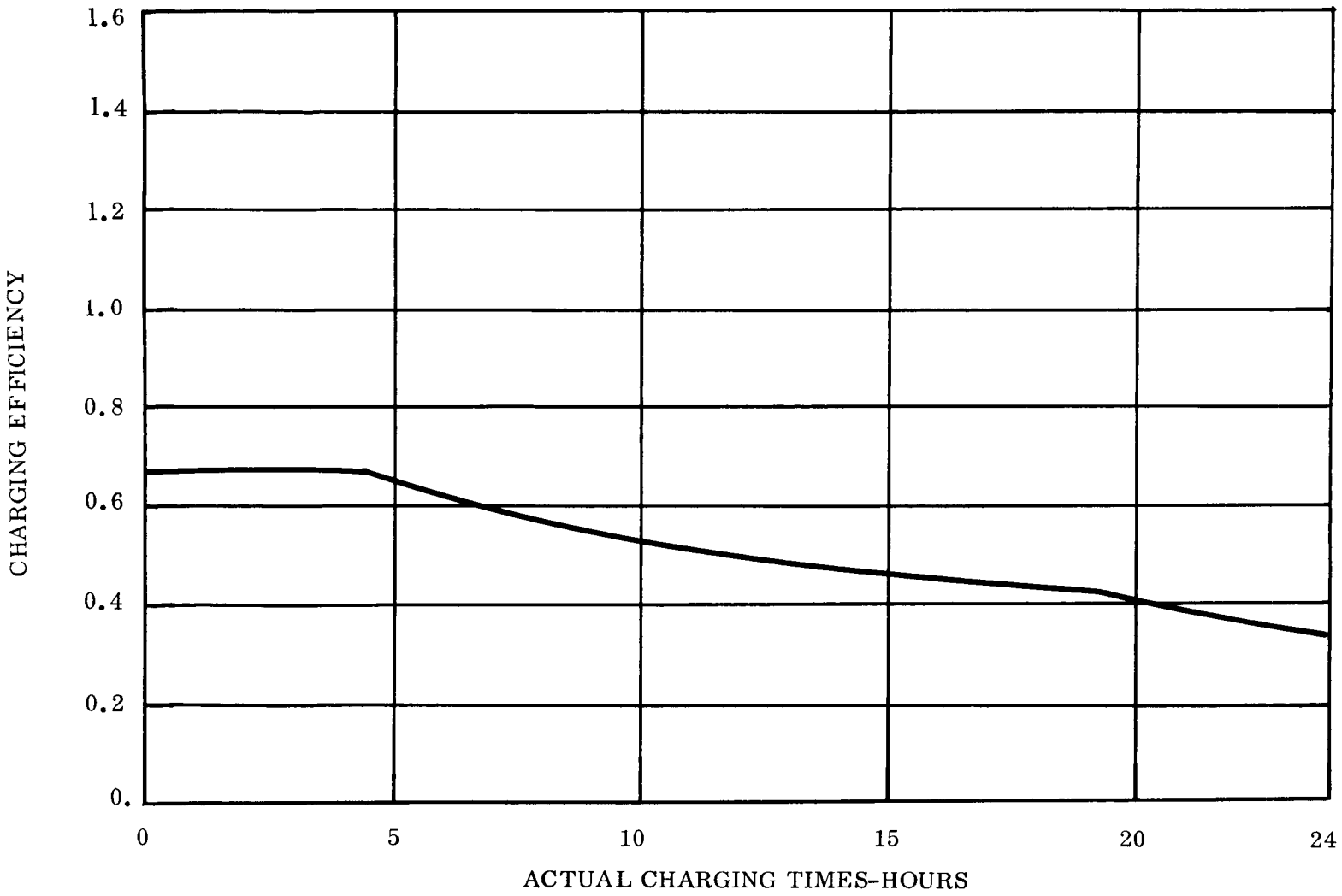

Figure 12-30. Estimated Charging Efficiency of Nickel Cadmium Battery

$$I_L = \frac{63 \text{ watts (avg)}}{28 \text{ volts}} = 2.25 \text{ amperes}$$

α = 1/6 (see assumption c)

β = 0.25 (see assumption d)

Substituting these numerical values yields the required battery capacity.

$$C = 2.25 \times 6 \left[0.24 \, (1 + 0.25) \right]$$

$$= 4.05 \text{ ampere-hours}$$

The maximum battery depth of discharge would be:

$$\text{Secondary battery depth of discharge} = \frac{28.5 \times 100}{4.05 \times 28} .$$

Assuming 9 watts-hours/pound and 14 cubic inches per pound for a 100 percent depth of discharge the battery weight and volume are:

$$\text{Secondary battery weight} = \frac{4.05 \times 28}{9} = 12.6 \text{ pounds.}$$

$$\text{Secondary battery volume} = 12.6 \times 14 = 176.0 \text{ cubic inches.}$$

12.7.3.3 Primary Battery

A non-rechargeable (primary) silver oxide-zinc battery would be used to supply the power required during initial stabilization of the spacecraft. The power required during this period was established in Section 12.6.1 as 14.2 watt-hours.

Flight experience with primary silver oxide-zinc batteries, in this size range, indicates (Reference 12-2) that typical specific weight and volume figures are 20 watt-hours per pound and 25 cubic inches per pound respectively. These figures are for the total battery package including the case.

It is obvious from these figures that the primary battery weight and volume will be very small. Since this is the case the battery capacity will be doubled to allow a large safety factor in case initial stabilization takes longer than estimated. Therefore,

$$\text{primary battery weight} = \frac{14.5 \times 2}{20} = 1.5 \text{ pounds and}$$

$$\text{primary battery volume} = 1.5 \times 25 = 37.5 \text{ cubic inches.}$$

12.7.3.4 Power Conditioning Equipment and Harness

Based on past spacecraft hardware experience, typical specific weight figures (Reference 12-2) for the battery charge regulator, power control unit and solar array harness are 31, 8 and 13 pounds per kilowatt of solar array output respectively. Therefore

$$\text{weight of battery charge regulator} = 31 \times \frac{99.5}{1000}$$

$$\approx 3.1 \text{ pounds,}$$

$$\text{weight of power control unit} = 8 \times \frac{99.5}{1000}$$

$$\approx 0.8 \text{ pounds, and}$$

$$\text{weight of harness} = 13 \times \frac{99.5}{1000}$$

$$\approx 1.3 \text{ pounds.}$$

A typical specific volume figure for power conditioning equipment (including packaging) is 30 cubic inches per pound. Therefore

$$\text{volume of battery charge regulator} = 3.1 \times 30 = 93 \text{ cubic inches, and}$$

$$\text{volume of power control unit} = 0.8 \times 30 = 24 \text{ cubic inches.}$$

12.7.3.5 Summary

The calculations outlined in Sections 12.7.3.1 through 12.7.3.4 were repeated for Missions B and C. The results for all three are summarized in Table 12-13 and 12-14.

12.8 SUMMARY AND CONCLUSIONS

A block diagram of the proposed power subsystem design is given in Figure 12-28. During the initial stabilization period, between the time when the spacecraft is separated from the launch vehicle until the solar panels are deployed and oriented to the sun, the power requirements would be supplied by a primary silver oxide-zinc battery.

After the spacecraft is in normal orbital operation the power required during the dark portion of the orbit, plus the peaks occurring during the daylight period, would be supplied by a rechargeable, sealed nickel-cadmium battery. N on P silicon solar cells would be used to supply the continuous daylight power requirements plus the energy required to recharge the battery.

The proposed spacecraft power supply design is based on components and techniques which are well developed and no technological breakthroughs are required to develop such a system.

The assumed solar cell performance factors are summarized in Table 12-12. A summary of the major subsystem performance parameters are given in Table 12-13 and the subsystem weight and volume estimates are presented in Table 12-14.

The degradation resulting from radiation induced surface effects on transistors and diodes should be investigated further. To do so will require detailed circuit designs which were beyond the scope of this study. It appears that radiation induced surface effects could represent significant spacecraft weight and/or life penalties but no firm conclusions can be drawn until this area is investigated further.

Table 12-12. Solar Cell Performance Factors

Factors	Mission A	Mission B	Mission C
Type of Solar Cell	N/P	N/P	N/P
Efficiency of Bare Cell, % (Free Space, 85°F)	11	11	11
Manufacturing Loss Factor	0.97	0.97	0.97
Ultraviolet Degradation Factor	0.95	0.95	0.95
Micrometeorite Loss Factor	0.95	0.95	0.95
Packing Factor	0.90	0.90	0.90
Temperature-Efficiency Dependence, % per °F	-0.26	-0.26	-0.26
Solar Constant Variation Factor	0.966	0.966	0.966
Filter Transmittance Factor	0.92	0.92	0.92
Radiation Degradation Factor	0.71	0.84	0.86
Cover Glass Thickness, Mils	15	6	6
Filter Type	Blue-Red	Blue-Red	Blue-Red
Filter Cut On Wavelength, Microns	0.43	0.43	0.43
Filter Cut Off Wavelength, Microns	1.09	1.09	1.09
Solar Cell Temperature, °F	78	100	112
Solar Array Specific Power[a], Watts/Square Foot	7.22	8.07	8.0

Note:

a - Minimum output during mission life.

Table 12-13. Summary of Power Subsystem Performance Parameters

Performance Parameters	Mission A	Mission B	Mission C
Solar Array Output, Watts	99.5	115.5	146
Solar Array Area, Ft^2	13.8	14.3	18.3
Secondary Battery Capacity, Watt-Hours	113.5	250	256
Primary Battery Capacity, Watt-Hours	28.4	35.6	28.4

Table 12-14. Spacecraft Power Subsystem Weight

Components	Mission A		Mission B		Mission C	
	Weight (lb)	Volume ($in.^3$)	Weight (lb)	Volume ($in.^3$)	Weight (lb)	Volume ($in.^3$)
Solar Array	15.1	-	14.4	-	18.4	-
Secondary Battery	12.6	176.0 (3.25x5.0x9.0)	27.8	389 (4.5x7.5x11.5)	28.5	399 (4.5x7.5x11.75)
Primary Battery	1.5	37.5 (2x3.4x5.5)	1.8	45 (2.25x3.5x5.75)	1.5	37.5 (2x3.4x5.5)
Battery Charge Regulator	3.1	93 (2x5x9.3)	3.6	108 (3x4x9)	4.5	135 (4x5x6.75)
Power Control Unit	0.8	24 (3x4x2)	0.9	27 (3x4x2.25)	1.2	36 (3x6x2)
Harness	1.3	-	1.3	-	1.5	-
TOTAL	34.4		49.8		55.6	

12.9 REFERENCES

12-1 A.J. Dennison, "The Illumination of a Cell Surface in Space Due to the Sunlight Reflected from the Earth," General Electric, Missile and Space Division, Report No. TIS-61SD101.

12-2 D. Kerr and E. Williams, "Performance Estimates of Recommended Space Power Systems for the 1964-1966 Period," an internal General Electric Spacecraft Department Report, No. PIR 9741-045, March 19, 1963.

SECTION 13

SPACECRAFT CONFIGURATION

PRINCIPAL CONTRIBUTORS:

J. H. Paul
R. E. Biddiscombe
R. L. Ewing

SECTION 13
SPACECRAFT CONFIGURATION

13.1 INTRODUCTION

This section takes the primary experiment, the secondary experiments and the subsystem components defined in the preceding sections and integrates them into a spacecraft configuration. Due to the close similarity between the mode of operation, the components to be included on-board, and the launch vehicles, it was possible to design one basic configuration that would handle all three missions. Some component changes must be made for the different cases but the basic spacecraft structure is the same for Missions A, B and C. This approach offers the advantage of allowing several different missions to be flown with the same basic spacecraft, thus increasing the program flexibility and reducing the cost if more than one of the missions are undertaken.

The constraints imposed on the spacecraft configuration are presented and the various configurations considered in developing the proposed design are discussed. The selected configuration is described in detail and spacecraft weight breakdowns presented for Missions A, B, and C. Calculation of the spacecraft center of pressure, center of gravity and moments of inertia for the Mission A vehicle are presented. These values were considered typical for all three missions and were used in Section 11 to estimate the disturbance torques acting on the spacecraft.

13.2 DESIGN CONSTRAINTS

The design constraints with which the spacecraft configuration must be compatible are discussed in this section.

13.2.1 LAUNCH VEHICLE PAYLOAD-ORBIT CAPABILITY

The launch vehicle and orbits were selected for Missions A, B, and C in the Mission Analysis phase of the study (see Section 6-Volume II). The selections are summarized below.

Mission	Orbit	Launch Vehicle
A	Modified sun-synchronous 1000 nautical mile altitude, 101.84 degrees inclination	IMPROVED DELTA DSV-3E
B	Highly elliptical, 200 nautical mile perigee, 25,000 nautical mile apogee, 45 degree inclination	IMPROVED DELTA DSV-3E
C	Low altitude circular, 325 nautical mile altitude, 30 degree inclination	IMPROVED DELTA DSV-3H

These selections were based on the assumption that the total spacecraft weight would be approximately 350 pounds. Therefore, the chosen spacecraft configuration must be consistent with a total spacecraft weight that the selected launch vehicle can place in the desired orbit.

13.2.2 COMMON SPACECRAFT CONFIGURATION

Because of the close similarity between the mode of operation, the components to be included on board, and the launch vehicles, it was considered desirable and feasible to design one spacecraft configuration that would handle all three missions.

The common spacecraft configuration chosen must be compatible with direct mounting to the IMPROVED DELTA second stage or to the X-258 third stage since both versions are employed in the three missions being considered. This compatibility would be provided by changes in the adapter design. The spacecraft release and separation mechanism would remain the same in each case.

13.2.3 LAUNCH VEHICLE FAIRING

The available IMPROVED DELTA fairing envelopes with and without the X-258 third stage motor are shown in Figure 13-1. The only difference in these fairings is the length of the cylindrical section. The Mission A and B spacecraft must be compatible with the fairing shown on the right of the figure since they use the DSV-3E version of the IMPROVED DELTA. The Mission C spacecraft can use either of the two second stage direct mounting fairings since it uses the DSV-3H launch vehicle which does not employ a third stage. The available length of the fairings does not create any serious spacecraft configuration problems, but the minimum allowable payload diameter of 57 inches represents a significant constraint. If the 50 inch diameter solar concentrator is oriented with its axis in the launch direction very little space is left for mounting the secondary experiments that also require sun orientation. Since the Solar Reflective Surfaces Experiment alone is 24 inches in diameter this approach would necessitate deploying at least some of the secondary experiments.

A possible alternative would be to mount the solar concentrator with its axis normal to the launch axis, and utilize the height of the fairing envelope for mounting the sun-pointing secondary experiments on either side of the solar concentrator. This is considered further in Section 13.3.

13.2.4 SPACECRAFT ORIENTATION

The spacecraft stabilization approach chosen is to mount the solar concentrator and thermionic generator rigidly to the spacecraft body and then point the entire vehicle to the sun (see discussion in Section 11.1). This approach eliminates any requirement for the thermionic system to move with respect to the spacecraft body which simplifies the space-craft structure. It also makes it relatively easy to provide sun-pointing for the solar cell array and secondary experiments that have this requirement. In addition, orientation of the total spacecraft to the sun tends to stabilize the thermal condition of the vehicle during the daylight portion of the orbit.

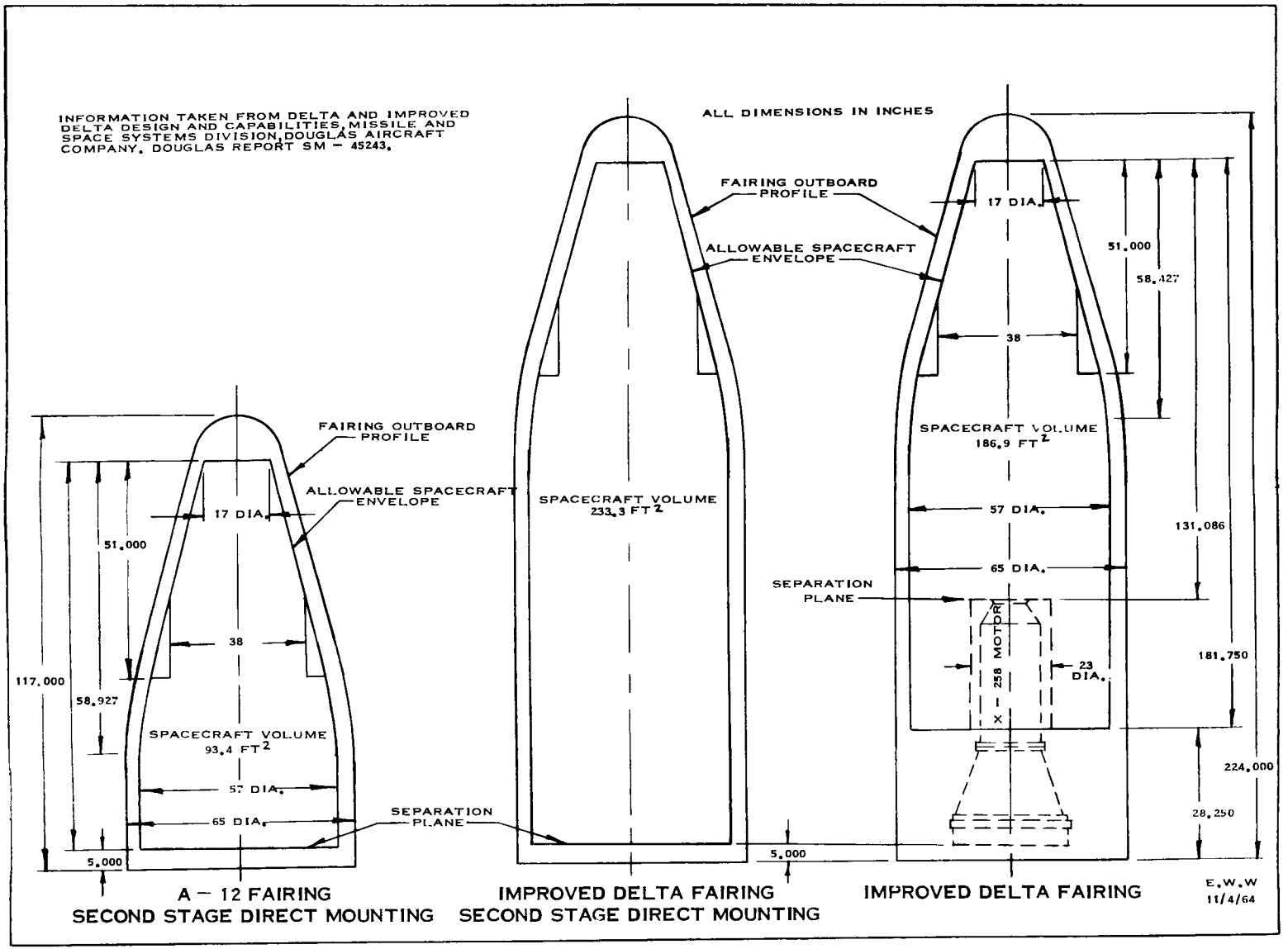

Figure 13-1. Fairings for IMPROVED DELTA Launch Vehicle

13.2.5 CENTER OF PRESSURE/CENTER OF GRAVITY RELATIONSHIP

Because of the necessity to minimize disturbance torques on the spacecraft, it is very desirable that the spacecraft center of pressure be in line with the center of mass when viewed from the sun direction. This condition was easier to achieve with some of the configurations considered than with others, and therefore represented one of the major factors considered in selecting the spacecraft configuration.

13.2.6 INERTIA RATIO

The requirement to minimize disturbance torques on the spacecraft also necessitates keeping the mass moments of inertia about the principal axes as nearly equal as possible in order to minimize the gravity-gradient effects. It is generally not possible to keep the inertias exactly equal but keeping them as close as possible was a consideration in selecting the spacecraft configuration.

13.2.7 SOLAR ARRAY AREA

The required solar array area was sufficient in all three cases to rule out consideration of any approach other than deployable, sun oriented, solar cell panels. Packaging the required solar array area within the fairing constraints did not prove to be a difficult problem. Of greater significance was ensuring that the solar array panels unfolded to a position that resulted in a satisfactory center of pressure/center of gravity relationship, as discussed in Section 13.2.5.

13.2.8 SOLAR THERMIONIC SYSTEM

The restraints imposed by the 50-inch diameter, solar concentrator were discussed in Section 13.2.3. Since it is desirable to minimize blockage of the solar concentrator the minimum number of three struts were used for supporting the thermionic generator from the concentrator torus. For stiffness, and to minimize vibration inputs to the thermionic

system during launch, it was considered desirable to mount the concentrator to the spacecraft at these same three points (i.e. the intersections of the three generator support struts with the concentrator torus). This was therefore a consideration in determining the size and shape of the spacecraft body.

13.2.9 SECONDARY EXPERIMENTS

Consideration was given in selecting the spacecraft configuration, to compatibility with the priority "A" and "B" secondary experiments outlined in Section 5.4.2 of Volume II. It was considered essential that the priority "A" experiments be included on the vehicle as long as they did not compromise the primary experiment. It was also considered very desirable to include as many of the priority "B" experiments as could be integrated into the design within the weight limitations. Since Section 10 established that the telemetry subsystem could handle all thirteen of the priority "A" and "B" experiments the only remaining barrier to their inclusion on the vehicle would be incompatibility with the spacecraft configuration, or weight limitations.

The difficulty of locating the secondary experiments that require sun-pointing was referred to in Section 13.2.3. The largest experiment of this type is the Solar Reflective Surfaces Experiment which is 24 inches in diameter and has an estimated weight for this application of 27 pounds. Locating this experiment and the other sun-pointing experiments in a position where they were sun oriented and still allowed the spacecraft to be well balanced was a difficult constraint to meet.

13.3 SPACECRAFT CONFIGURATIONS CONSIDERED

Several possible spacecraft configurations were considered before the proposed design was selected. Figure 13-2 shows four of the concepts considered. The advantages and disadvantages of each of these are discussed in the following sections.

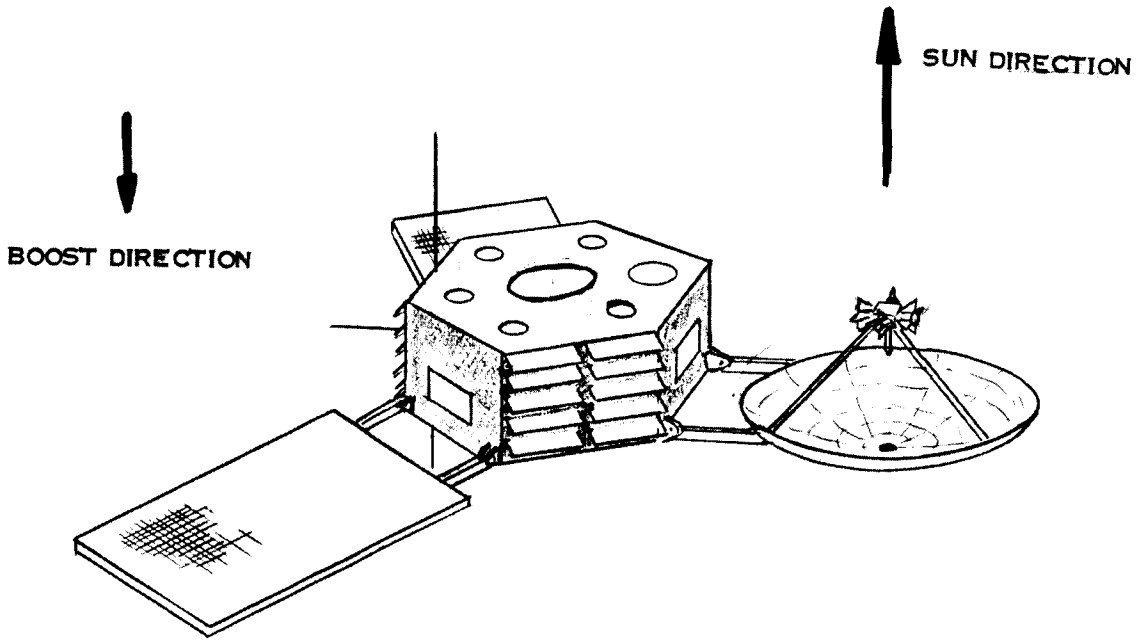

CONFIGURATION B

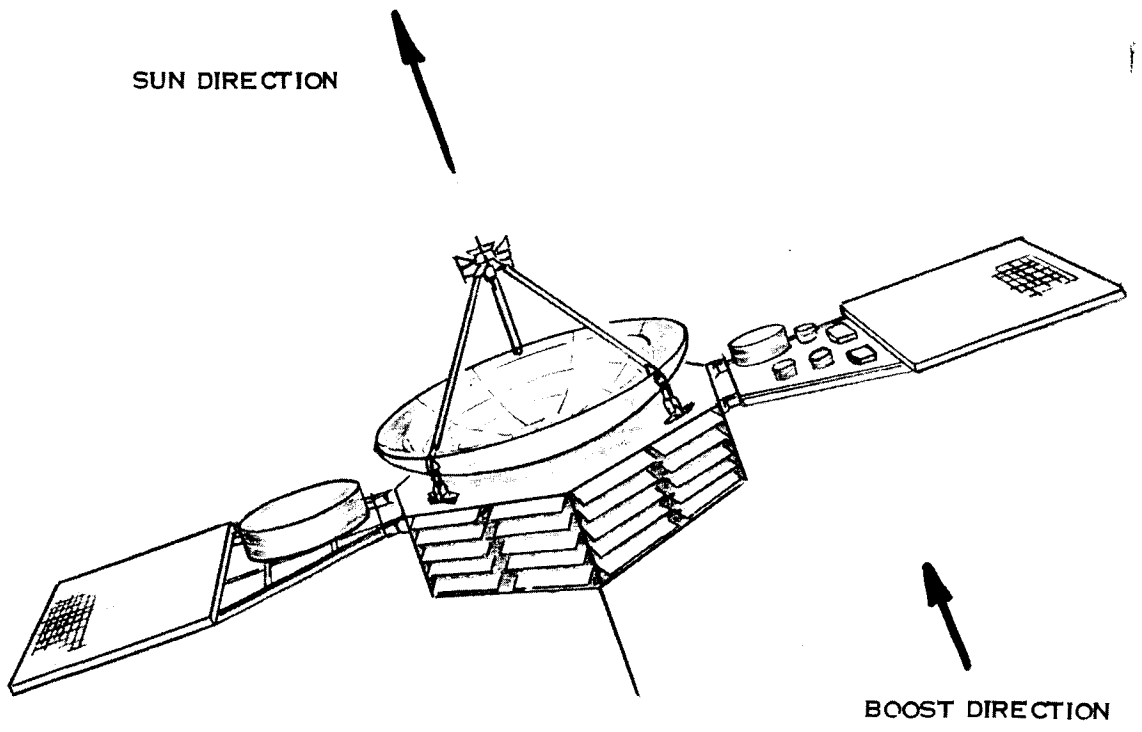

CONFIGURATION A

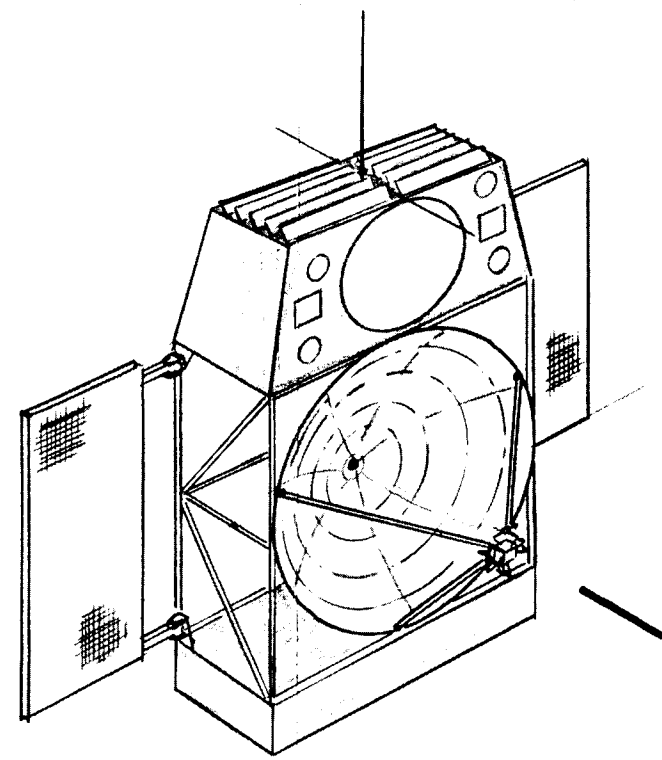

CONFIGURATION C

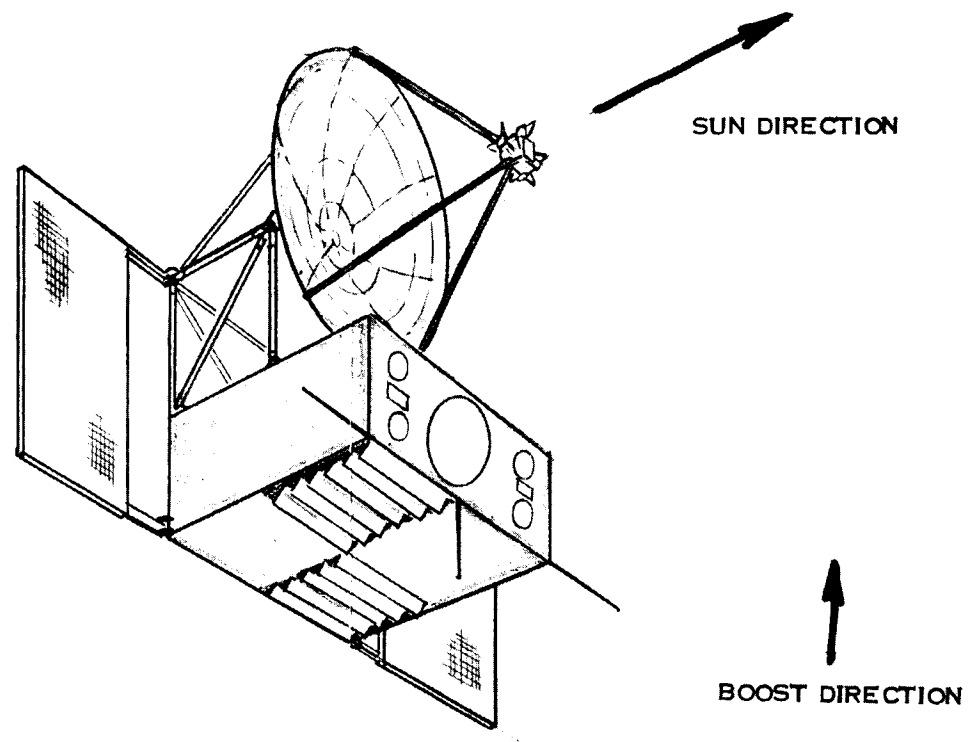

CONFIGURATION D

Figure 13-2. Spacecraft Design Concepts

13.3.1 CONFIGURATION A

This configuration consists of two deployable panels diametrically opposed and attached to a hexagonal spacecraft body. The secondary experiments requiring sun-pointing are mounted on the inboard faces of the panels, and the outboard faces are used for solar cell panels. The thermionic generator is mounted to the spacecraft body with the axis of the solar concentrator oriented in the launch direction and the three mounting points coincident with three corners of the six-cornered spacecraft body.

In the launch configuration, the two panels would be folded upward so that their edges met and latched together with a single pyrotechnically activated pin-puller. The single gas tank is mounted in the center of the vehicle body and the equipment mounted in modular fashion to the sides of the vehicle body.

A six-point tie-down to the adapter would be achieved by a band-clamp running around the six corners of the spacecraft body, and separation achieved by multiple springs.

The principal advantages of this configuration are:

a. The thermionic generator is rigidly supported at three points that transmit load directly through the corners of the vehicle body to the adapter.

b. The solar array and experiment panels form an inherently stiff structure when folded in the launch configuration.

c. The solar and experiment panels can be deployed by a single pyrotechnic device providing high reliability.

d. The simplicity of the structure and mechanisms required for this configuration result in a minimum weight structure.

The principal disadvantage of this configuration is the unbalance of inertias about the pitch and yaw axes which results in unacceptable gravity-gradient disturbance torques. The proposed configuration (see Figure 13-3) reduces this effect considerably and was a direct outgrowth of Configuration A.

13.3.2 CONFIGURATION B

In Configuration B an attempt has been made to expose one face of the spacecraft body to the sun, so that the secondary sun-pointing experiments can be mounted in the vehicle body and do not have to be deployed on panels as in Configuration A. However, this necessitates deploying the thermionic system through 180 degrees after separation from the launch vehicle.

A hexagonal vehicle body, similar to Configuration A, is used in this approach, but the two solar array panels and the thermionic system are located 120 degrees apart around the body to provide a good center of pressure/center of gravity relationship.

The advantages of being able to locate all the secondary experiments in the vehicle body are offset by the following disadvantages:

a. Because of the sensitive nature of the solar concentrator structure and the concentrator-generator alignment it is considered highly undesirable to have to deploy the thermionic system.

b. If this approach were taken a sizable weight penalty would be incurred for the deployment structure associated with the thermionic system.

c. Only three faces of the vehicle body are well suited for active thermal control. This limits the surface area available for mounting equipment that has high heat rejection requirements.

d. The solar array panels would not be as rigidly supported as they were in Configuration A, when folded in the launch configuration.

e. The deployment reliability is less since three and perhaps four pyrotechnic devices must be fired to deploy the solar array panels and the thermionic system.

13.3.3 CONFIGURATION C

Configuration C represents an attempt to provide sufficient surface area for both the solar thermionic system and the secondary experiments, without having to deploy either.

In this approach, the axis of the solar concentrator is oriented at 90 degrees to the longitudinal launch vehicle axis. The spacecraft equipment and secondary experiments are contained in two boxes located on either side of the concentrator. The two equipment boxes are joined by a lightweight truss structure which is also used for mounting the solar concentrator. Two solar array panels are hinged off the truss structure and are folded up in the launch configuration and deployed after orbit injection.

The major advantage of this approach is that both the primary and secondary experiments are fixed and only the solar array panels have to be deployed. However, this advantage is outweighed by the following disadvantages:

a. To produce a sufficiently stiff vehicle(as well as an acceptable vibration environment for the experiments) would require excessive structural weight.

b. The unsymetrical condition created by cantilevering the thermionic generator from the solar concentrator torus, makes the possibility of holding the close alignment requirements between the concentrator and the generator through the launch phase questionable.

c. The shape and nature of the lower equipment box makes the task of mounting this vehicle to the second or third stage of the IMPROVED DELTA a difficult one, resulting in greater structural weight.

d. With no appreciable exchange of heat between the two equipment boxes, thermal balance of this vehicle will be difficult to achieve, even with active temperature control.

13.3.4 CONFIGURATION D

Configuration D was an attempt to improve the structural and thermal characteristics of Configuration C . However, like Configuration C the structural support of the solar concentrator and the thermionic generator during launch is a major problem. This design possesses the (b) and (c) disadvantages given in Section 13.3.3 with the following additional disadvantages.

a. The center of pressure/center of gravity offset of this configuration is considered unacceptable.

b. The location of antenna stubs to achieve an approximately isentropic pattern has not been referred to in Configurations A through C since these designs rate about equal from this standpoint. However, it would be more difficult to achieve the desired antenna pattern with Configuration D than with Configurations A through C.

13.3.5 COMPARISON EVALUATION

The four configurations presented in Figure 13-2 plus the selected configuration given in Figure 13-3 were compared on the basis of ten major design parameters. The five configurations were compared in relation to each parameter and ranked from 1 to 5 in order of preference, with one representing the highest rank. If each of these parameters is considered to be of equal importance then the spacecraft configuration with the lowest total

when all of the ranking factors are added represents the most attractive spacecraft configuration. This procedure was followed and the results are presented in Table 13-1. On this comparison basis the "proposed approach" is the most attractive with Configuration A being a close second.

Since it is doubtful if all of the parameters on which the spacecraft configurations were compared are of equal importance the value of the sum totals at the bottom of the Table 13-1 are debatable, and this was only one of many inputs considered in selecting the final spacecraft configuration. However, the relative ranking of the five configurations on a particular parameter are considered valid and provide insight into the reasoning used in arriving at the proposed configuration.

13.4 PROPOSED SPACECRAFT CONFIGURATION

The proposed spacecraft configuration is shown in Figure 13-3. This design was established as a result of the requirements and concept evaluations outlined in Sections 13.2 and 13.3. However, once it became apparent that the required configuration bore many similarities to the Mariner C vehicle, knowledge of that flight proven design was drawn upon in arriving at some of the design features. This was done deliberately since it was felt that knowledge of flight proven hardware should be made use of wherever possible. The use of existing hardware, which has been flight proven, offers the advantages of higher reliability, shorter development schedules, and lower cost.

13.4.1 SPACECRAFT BODY AND EQUIPMENT PACKAGING

The spacecraft body is an eight-sided prism with flat ends. The components are mounted in modular fashion to the eight side panels (see panel layouts Figure 13-3). As far as possible all of the components comprising a specific subsystem are located on the same panel. This simplifies assembly and checkout of the spacecraft. In order to obtain the desired center of gravity location and balance the moments of inertia it was not possible to follow this rule in all cases. Four of the eight spacecraft sides have active thermal control

Table 13-1. Comparison Evaluation of Spacecraft Configurations

PARAMETER	CONFIGURATION				
	Proposed	A	B	C	D
Rigidity of Thermionic System Support	2	1	3	5	4
Necessity to Deploy Experiments	3	4	5	2	1
Center of Pressure/Center of Gravity Relationship	1	2	3	4	5
Inertia Ratio	1	4	2	3	5
Mechanical Simplicity	4	3	5	1	2
Compatibility with Lightweight Structural Design	2	1	3	5	4
Compatibility with Good Thermal Design	3	4	1	5	2
Compatibility with Launch Vehicle Interface	1	2	3	5	4
Ease of Equipment Packaging	1	2	3	5	4
Ease of Achieving Desired Antenna Pattern	3	1	2	4	5
TOTALS	21	24	30	39	36

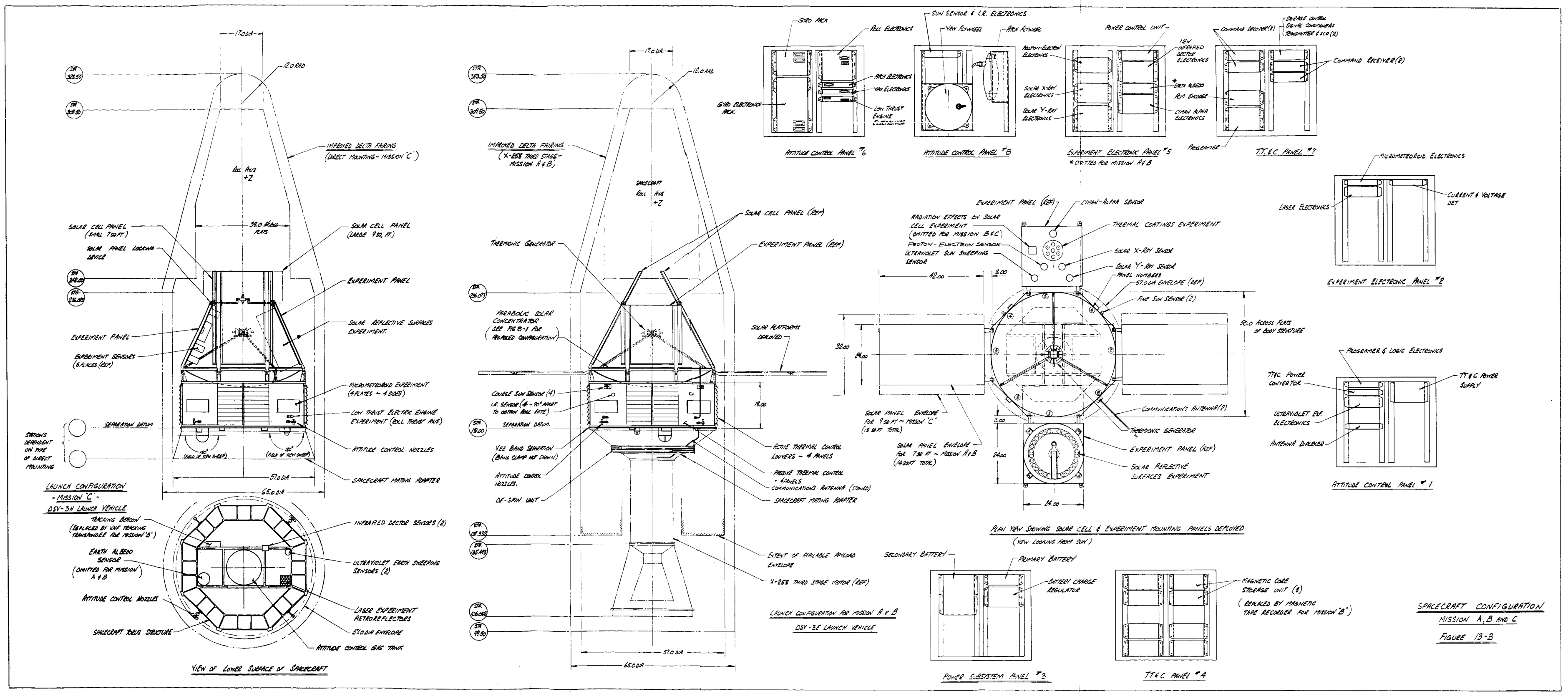

Figure 13-3. Spacecraft Configuration Missions A, B and C

(refer to Section 13.4.5). The remaining four sides are used for mounting the attitude control nozzles, the telemetry antenna, the acoustical sounding plates associated with the micrometeoroid secondary experiment and the engines required for the secondary low thrust electric engine experiment.

The lower octagonal face of the vehicle body is used for mounting the experiments and sensors that must see earth. This end of the spacecraft mates with the truncated conical adapter. The upper octagonal face of the vehicle body is used for mounting the solar thermionic system. Four deployable panels, hinged off this upper face, are used for mounting solar panels and the sun-pointing secondary experiments. The spacecraft body is built from two octagonal machined frames joined by vertical members at the eight corners. Hinge fittings for the four deployable panels and support fittings for the solar thermionic system are bolted to the upper machined frame.

The octagonal ends of the body are partially closed by light honeycomb panels. Four faces of the body have temperature control louvers mounted to their exterior faces. The remaining four faces are covered with a multilayer superinsulation, except for the cut-outs required for sensors, attitude control nozzles, etc.

The attitude control gas tank and associated hardware are mounted on a trusswork in the center of the vehicle body. This location was chosen to minimize the center of gravity shift with gas usage.

All machined parts of the body are magnesium, and all body panels are aluminum. Body panels are generally sized by some dynamic criterion, in which case very little advantage can be shown for the use of magnesium over aluminum.

13.4.2 SOLAR ARRAY PANELS

As shown in Figure 13-3, the solar array consists of two rectangular hinged panels providing approximately 14 square feet of solar array area for Missions A and B and 18 square feet

for Mission C. The solar cells are mounted on aluminum channels, each channel constituting a solar array module (see Figure 12-29 in Section 12.7.2.1). These channel sections are supported and stiffened by two sheet metal members running lengthwise, at 90 degrees to the longitudinal axis the module channels, and terminating in magnesium hinge fittings.

The two solar array panels and the two secondary experiment panels are folded upward and attached to each other to form a rigid structure during the launch phase. By means of a linkage system, only two pyrotechnic devices, one on each solar cell panel, are required to withdraw the four locking pins. The four panels are deployed independently by means of springs at their hinge points and lock positively in place upon reaching the deployed position.

13.4.3 SECONDARY EXPERIMENT PANELS

The smaller secondary experiment panels are constructed in the same manner as the solar array panels. However, in general, heavier gage materials would be used because of the greater weight of the experiments they must support. The experiments could have been mounted directly to a framework and the panel sheet omitted. This approach was not taken because it is desirable for each experiment panel to present the same surface area to the sun in order to minimize the center of pressure/center of gravity offset.

The method of releasing and deploying these panels is described in the preceding section.

13.4.4 THERMIONIC SYSTEM MOUNTING

The proposed method of mounting and aligning the solar concentrator and thermionic generator is described in Section 8.3.3.

13.4.5 THERMAL CONTROL

A detailed thermal analysis of the spacecraft was not conducted in this study but based on past spacecraft design experience it is expected that for the missions considered the spacecraft will require an active thermal control system*. Some of the conditions which are expected to necessitate active thermal control are:

a. The close temperature tolerances that must be maintained on such components as the secondary nickel-cadmium battery ($+50^{o}$ to $+90^{o}$F).

b. Components, such as the secondary nickel-cadmium battery, which have high heat dissipation when being used and are not operated on a continuous basis.

c. The requirement for a long spacecraft life.

d. The long daylight exposure periods associated with Missions A and B.

e. The long shadow periods encountered with Mission B.

f. The frequent thermal cycling associated with Mission C.

The proposed active thermal control system is essentially the same scheme used on the Mariner C spacecraft. The high heat dissipating equipment is mounted on the faces of the spacecraft body that have active thermal control capability and reject their waste heat to space by radiation. The amount of heat rejected is controlled by variable louvers attached to the outside of the panel. Each louvered panel is controlled independently by a bi-metal

*This needs to be investigated in detail. If the required spacecraft thermal environment could be provided by a passive system the spacecraft design could be simplified slightly and the weight probably reduced.

spiral spring that winds up and unwinds according to the temperature it sees, thus opening or closing the louvers. The surface area exposed by opening the louvers is coated with a high emissivity coating to promote radiation heat transfer.

The bi-metal actuator is located in a tunnel insulated on its exterior surfaces with super-insulation. By this means the bi-metal actuator can be mounted so it only receives radiated energy from the panel it is controlling. This method achieves better control of the panel average temperature than if conducted heat were used, since with the latter method the actuator would be more sensitive to local "hot-spots."

In addition to the active thermal control system, the spacecraft thermal balance is maintained by the use of superinsulation and coatings on the other exposed surfaces.

Thermal control of temperature sensitive equipment mounted outside the spacecraft body is achieved passively by the use of thermal coatings and insulation. This problem is simplified somewhat since during the daylight period the direction and magnitude of the solar energy input is constant. However, if a detailed thermal analysis indicates that the temperature of a piece of equipment mounted external to the spacecraft body, falls too low during the dark period, or if the out-of-tolerance performance during the warm-up period is unacceptable, electrical heaters would have to be added. Of course this would increase the spacecraft power requirements.

13.4.6 SPACECRAFT MOUNTING AND SEPARATION

Two different truncated conical adapters are shown in Figure 13-3. Which one of these adapters is used depends on whether the IMPROVED DELTA is used with or without the X-258 third stage. The spacecraft release and separation system is similar for both cases. The lower octagonal frame of the spacecraft body is machined to have a circular flange approximately 55 inches in diameter. This flange forms one half of a marman clamp attachment to a similar ring on the adapter. The two flanges are clamped together by a series of vee-shaped shoes and a band clamp. The band clamp would be split at separation

by a bolt cutter or similar pyrotechnic device, and the spacecraft would separate under the action of four matched springs located at four of the eight corners of the vehicle body.

The adapter for direct mounting to the IMPROVED DELTA second stage is a simple sheet metal truncated cone that grows from the 55-inch diameter at the spacecraft, to the approximately 60-inch diameter that is necessary to mate with the DSV-3H's second stage.

The adapter for the X-258 third stage decreases from the 55-inch diameter at the spacecraft to the 18-inch diameter necessary to mate with the X-258. The yo-yo despin system, required with the solid X-258, is mounted on the adapter. Other equipment, such as the timer, squib battery, terminal boards, and balance weights are also mounted on the adapter. The balance weights are necessary since in this configuration the spacecraft/X-258 assembly must be balanced to achieve the close center of gravity and principal axes alignments required as a result of having to spin-up this assembly on the IMPROVED DELTA second stage.

13.5 SPACECRAFT WEIGHT AND BALANCE CALCULATIONS

This section contains the spacecraft weight estimates for Missions A, B, and C. The required location of the components within the spacecraft body are determined in order to balance the Mission A spacecraft. Also included are the center of gravity, center of pressure and moment of inertia calculations for the Mission A vehicle. The Mission A case is considered typical of the three missions and the center of pressure/center of gravity relationship and inertia imbalance were used in Section 11 to estimate the disturbance torques acting on the vehicle. The magnitude of these disturbance torques sized the attitude control subsystem.

13.5.1 WEIGHT ESTIMATES

Table 13-2 presents a spacecraft weight breakdown for the three missions. The resulting weight totals are:

Spacecraft weight Mission A - 360.1 pounds

Spacecraft weight Mission B - 373.3 pounds

Spacecraft weight Mission C - 404.0 pounds.

These weights do not include the adapter, or in the case of Missions A and B, the yo-yo despin system*. These weights are considered chargeable to the launch vehicle. The launch vehicle performance curves presented in Section 2.4.3, in Volume II, are based on this assumption.

The differences in the total spacecraft weights result primarily from a difference in the attitude control and power subsystem weights. The remaining subsystems and experiments weigh approximately the same for all three missions. The power subsystem weight increases with Missions A through C because the light to shadow ratio becomes progressively worse. The unfavorable light to shadow ratio results in a secondary battery weight which for Missions B and C is more than twice that for Mission A. The attitude control subsystem weight is approximately ten pounds higher for Mission C than for Missions A and B, because of the additional gas required for the pneumatic system. The higher gas requirement occurs because the low altitude of the Mission C orbit results in significantly higher gravity gradient disturbance torques.

13.5.2 SPACECRAFT BALANCE

The component locations shown in Figure 13-3 were selected in order to balance the Mission A spacecraft in the "spin condition" shown in Figure 13-4. Since it is essential that the spacecraft be accurately balanced in the spin condition (see discussion Section 13.6.5) the components were located to provide the required balance and the resulting center of gravity location in the orbit condition (see Figure 13-4) accepted.

*A despin system is not required for Mission C because the DSV-3H launch vehicle does not employ the spin stabilized X-258 third stage motor.

Table 13-2. Spacecraft Weight Breakdown

Subsystem and Component	Mission A Weight (Lb)	Mission B Weight (Lb)	Mission C Weight (Lb)
ATTITUDE CONTROL	(65.9)	(59.2)	(75.5)
Momentum Flywheel (2)	11.0	9.0	17.0
Roll, Pitch, Yaw Gyros and Electronics	11.0	11.0	11.0
Power Supply (AC and DC)	11.5	11.5	11.5
Sun Sensors and Electronics	2.0	2.0	2.0
Programmer and Logic	2.5	2.5	2.5
Attitude Control Electronics (3)	7.0	7.0	7.0
IR Sensors and Electronics	1.0	1.0	1.0
Thermal Sensors	0.2	0.2	0.2
Pneumatic System	19.7	15.0	23.3
Gas (Nitrogen)	3.0	0.9	4.5
Tank	4.1	1.5	6.2
Fill and Check Valves and Filters	2.2	2.2	2.2
Pressure Transducer (2)	0.8	0.8	0.8
Regulator	2.5	2.5	2.5
Solenoids (7)	2.8	2.8	2.8
Nozzles and Orifices (8)	1.0	1.0	1.0
Relief Valve	.8	.8	.8
Lines, Fittings, Clips, Bracketry	2.5	2.5	2.5
POWER SUPPLY	(34.4)	(49.8)	(55.6)
Primary Battery	1.5	1.8	1.5
Secondary Battery	12.6	27.8	28.5
Charge Regulator	3.1	3.6	4.5
Power Control Unit	0.8	0.9	1.2
Solar Array Harness	0.8	0.8	1.0
Inflight Disconnect	0.5	0.5	0.5
Solar Array	15.1	14.4	18.4
Structure and Restraints	6.0	6.2	7.9
Solar Cells	9.1	8.2	10.5

Table 13-2. (Cont.) Spacecraft Weight Breakdown

Subsystem and Components	Mission A Weight (Lb)	Mission B Weight (Lb)	Mission C Weight (Lb)
TELEMETRY, TRACKING AND COMMAND	(43.8)	(46.8)	(48.8)
Antenna and Connectors	1.0	1.0	1.0
Diplexer (Antenna)	1.0	----	1.0
Command Receiver (2)	3.0	3.0	3.0
Command Recoder (2)	5.4	5.4	5.4
Magnetic Core Storage Units (2.5 lb ea.)	20.0	---	25.0
Storage Control Circuitry	1.0	---	1.0
PCM Encoder	3.0	3.0	3.0
TT&C Power Converter	2.0	2.0	2.0
Signal Conditioners	1.0	1.0	1.0
Transmitter and SCO (2)	1.4	1.4	1.4
Tracking Beacon	1.0	---	1.0
Programmer	2.0	2.0	2.0
Multiplexer (Antenna)	---	1.0	---
Magnetic Tape Recorder	---	20.0	---
Tracking Transponder	---	5.0	---
Coax Cabling	2.0	2.0	2.0
SECONDARY EXPERIMENTS	(82.8)	(82.3)	(87.3)
Solar Cell Radiation Effect	0.5	---	---
Thermal Coatings	2.0	2.0	2.0
Solar Concentrator Reflective Surfaces	27.0	27.0	27.0
Infrared Detector	3.0	3.0	3.0
Laser Experiment	10.0	10.0	10.0
Low Thrust Electric Engine	2.3	2.3	2.3
Micrometeoroid Detection	8.0	8.0	8.0
Proton and Electron Spectra and Direction	8.0	8.0	8.0
Solar X-rays	3.0	3.0	3.0
Solar γ Rays	8.0	8.0	8.0
Earth Albedo	---	---	5.0
Ultraviolet Radiation	5.0	5.0	5.0
Lyman-Alpha	6.0	6.0	6.0

Table 13-2. (Cont.) Spacecraft Weight Breakdown

Subsystem and Components	Mission A Weight (Lb)	Mission B Weight (Lb)	Mission C Weight (Lb)
PRIMARY THERMIONIC EXPERIMENT	(38.2)	(38.2)	(38.2)
Generator	5.7	5.7	5.7
Parabolic Concentrator Surface	9.8	9.8	9.8
Generator Mounting Ring	0.3	0.3	0.3
Truss Tubes (3)	0.7	0.7	0.7
Tube Fittings (3)	0.1	0.1	0.1
Support Torus	2.2	2.2	2.2
Support Link (3)	0.1	0.1	0.1
Yoke (Includes Bearings) (3)	0.3	0.3	0.3
Support Fitting (Includes Bearings) (3)	0.3	0.3	0.3
Tie-In Ring	0.2	0.2	0.2
RTV Bond	0.5	0.5	0.5
Control Electronics	6.0	6.0	6.0
Generator Electrical Leads	7.0	7.0	7.0
Reflectometer	5.0	5.0	5.0
DIAGNOSTIC INSTRUMENTATION	(2.8)	(2.8)	(2.8)
Current Detectors	1.1	1.1	1.1
Voltage Detectors	0.5	0.5	0.5
Temperature Sensors	1.2	1.2	1.2
THERMAL CONTROL	(22.0)	(22.0)	(22.0)
Active Thermal Control (12 ft^2)	15.0	15.0	15.0
Insulation (4.7 lb/ft^3 - 1/2 in thick, 0.20 lb/ft^2)	5.4	5.4	5.4
Paint and Grease	0.6	0.6	0.6
Heaters	0.5	0.5	0.5
Misc	0.5	0.5	0.5
HARNESSING	(28.4)	(30.4)	(32.0)

Table 13-2. (Cont.) Spacecraft Weight Breakdown

Subsystem and Components	Mission A Weight (Lb)	Mission B Weight (Lb)	Mission C Weight (Lb)
STRUCTURE	(41.8)	(41.8)	(41.8)
Side Panels (Honeycomb) (8)	9.6	9.6	9.6
Top and Bottom Fill Panels	4.8	4.8	4.8
L's, T's (Framing)	9.2	9.2	9.2
Bulkheads (Internal)	3.7	3.7	3.7
Tank Support Structure and Fittings	1.6	1.6	1.6
Gussets and Misc. Structure	0.3	0.3	0.3
GSE Fittings	0.8	0.8	0.8
Experiment Panels and Hinges (2)	3.3	3.3	3.3
Solar Platform Locks	0.8	0.8	0.8
Separation Ring and Band	3.9	3.9	3.9
Hardware	3.8	3.8	3.8
TOTAL SPACECRAFT WEIGHT	360.1	373.3	404.0

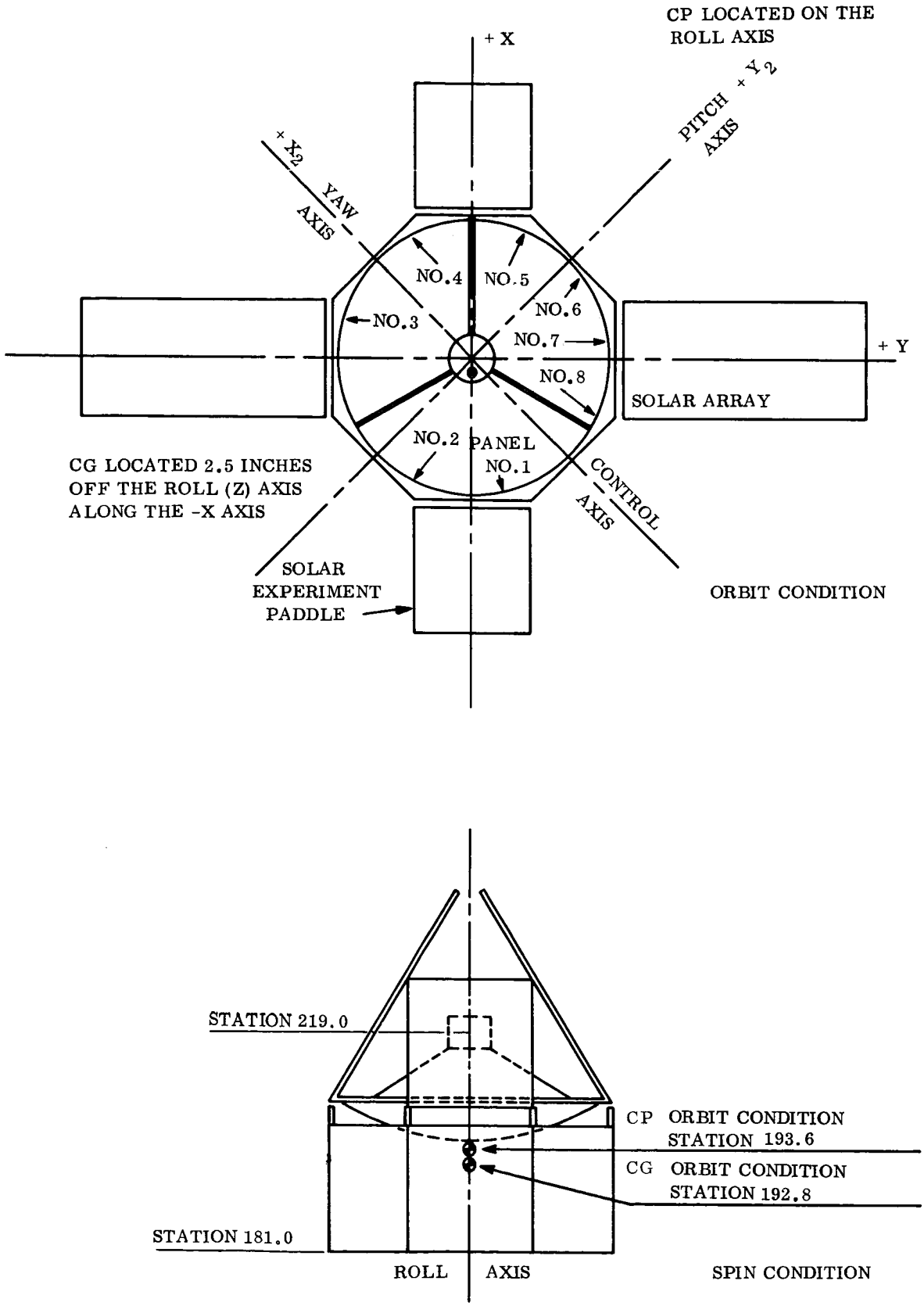

Figure 13-4. Reference Datum for Spacecraft Spin and Orbit Configurations

The equipment located on each of the spacecraft body panels and the total weight of the panels is given in Table 3-3. The panel locations on the spacecraft are shown in Figures 13-3 and 13-4. The Mission A spacecraft balance calculations were performed using the component locations defined by Figure 13-3 and the weights given in Tables 3-2 and 3-3. An outline of these calculations is presented in Table 3-4. These calculations show that the spacecraft center of gravity is on the roll, Z, axis in the spin condition as planned, and is located 2.5 inches off the roll axis at station 192.8 in the orbit condition.

13.5.3 CENTER OF PRESSURE

In order to estimate the disturbance torques acting on the spacecraft it is necessary to know the spacecraft center of pressure in the orbit condition. The center of pressure is defined as the summation of the incremental areas times their distance from the reference axis divided by the total area. This calculation was performed and indicates that the center of pressure for the Mission A* spacecraft is located at station 193.6 on the roll axis. The center of pressure would be expected to fall on the roll axis because of the spacecraft symmetry about that axis.

The important center of pressure/center of gravity relationship is now defined. Looking at the spacecraft in the orbit condition, from the sun direction, the center of pressure is on the roll axis and the center of gravity is 2.5 inches off the roll axis. For the same orbit condition a side view of the spacecraft shows the center of gravity to be 0.8 inch above the center of pressure. These locations are shown in Figure 13-4 and the results are used in Section 11 to compute the spacecraft disturbance torques.

*Since the center of pressure is based on geometry only it would have the same location for the Mission B and C spacecraft as computed for the Mission A case.

Table 13-3. Equipment Panel Arrangement

TT&C PANEL No. 1 (26.45 Pounds)

Structure	1.20
Programmer and Logic	2.50
TT&C Power Converter	2.00
TT&C Power Supply	11.50
Ultraviolet Electronics	4.50
Antenna Diplexer	1.00
Active Thermal Control	3.75

EXPERIMENT PANEL No. 2 (16.95 Pounds)

Structure	1.20
Micrometeoroid Electronics	4.00
Laser Electronics	9.00
Low Thrust Electric Engine	0.15
Current and Voltage Detectors	1.60
Micrometeoroid Sensor	1.00

POWER SYSTEM PANEL No. 3 (22.15 Pounds)

Structure	1.20
Primary Battery	1.50
Secondary Battery	12.60
Charge Regulator	3.10
Active Thermal Control	3.75

TT&C PANEL No. 4 (22.20 Pounds)

Structure	1.20
Magnetic Core Storage	20.00
Micrometeoroid Sensor	1.00

EXPERIMENT PANEL No.5 (30.75 Pounds)

Structure	1.20
Lyman-Alpha Electronics	5.50
Solarγ -Ray Electronics	7.50

EXPERIMENT PANEL No. 5 (Cont)

Solar X-Ray Electronics	2.50
Proton Electron Electronics	7.50
New IR Electronics	2.00
Power Control Unit	0.80
Active Thermal Control	3.75

ATTITUDE CONTROL PANEL No. 6 (22.35 Pounds)

Structure	1.20
Gyro Pack and Electronics	11.00
Roll, Yaw, Pitch Electronics	7.00
Low Thrust Engine Electronics	2.00
Low Thrust Engine	0.15
Micrometeoroid Sensor	1.00

TT&C PANEL No. 7 (21.75 Pounds)

Structure	1.20
Command Receiver (2)	3.00
Command Decoder (2)	5.40
Storage Control	1.00
Signal Conditioner	1.00
Transmitter SCO (2)	1.40
PCM Encoder	3.00
Programmer	2.00
Active Thermal Control	3.75

ATTITUDE CONTROL PANEL No. 8 (16.20 Pounds

Structure	1.20
Yaw Flywheel	5.50
Pitch Flywheel	5.50
Sun Sensor Electronics	2.00
IR Sensor Electronics	1.00
Micrometeoroid Sensor	1.00

Note

Panel Locations shown in Figure 13-4.

Table 13-4. Balance Calculation and Moments of Inertia Summary

	1	2	3	4	5	6	7	8	9	10	11	12	13	14	15	16
ITEM	WEIGHT LB	X-ARM INCHES	X-MOMENT IN.-LB	Z-ARM INCHES	Z-MOMENT IN.-LB	Y-ARM INCHES	Y-MOMENT IN.-LB	WX^2 LB-IN^2	WZ^2 LB-IN^2	WY^2 LB -$IN.^2$	I_{ox} LB -$IN.^2$	I_{oz} LB -$IN.^2$	I_{oy} LB -$IN.^2$	I_x LB -$IN.^2$	I_z LB -$IN.^2$	I_y LB -$IN.^2$
SPIN CONDITION			1 X 2		1 X 4		1 X 6	2 X 3	4 X 5	6 X 7				9+10+11	8+10+12	8+9+13
Panel No. 1	26.45	-22.0	-581.9	190.0	5025.5	0	0	12802	954845	0	1983	749	1305	956828	13551	968952
Panel No. 2	16.95	-17.5	-296.6	190.0	3220.5	-17.5	-296.6	5191	611895	5191	875	875	836	617961	11257	617922
Panel No. 3	22.15	0	0	190.0	4208.5	-22.0	-487.3	0	799615	10721	627	1661	1092	810963	12382	800707
Panel No. 4	22.20	17.5	388.5	190.0	4218.0	-17.5	-388.5	6799	801420	6799	1147	1147	1092	809366	14745	809311
Panel No. 5	30.75	22.0	676.5	190.0	5842.5	0	0	14883	1110075	0	2306	871	1517	1112381	15754	1126475
Panel No. 6	22.35	17.5	391.1	190.0	4246.5	17.5	391.1	6844	806835	6844	1155	1155	1102	814834	14843	814781
Panel No. 7	21.75	0	0	190.0	4132.5	22.0	478.5	0	785175	10527	616	1631	1073	796318	12158	786248
Panel No. 8	16.20	-17.5	-283.5	190.0	3078.5	17.5	283.5	4961	584820	4961	838	838	800	590619	10760	590581
Solar Experiment Panel	28.64	-14.0	-401.0	216.0	6186.2	0	0	5614	1336219	0	2749	1527	1527	1338968	7141	1343360
Solar Experiment Panel	6.19	17.0	105.2	218.0	1349.4	0	0	1788	294169	0	593	330	330	294762	2118	296287
Solar Array	7.95	0	0	225.0	1788.8	-14.0	-111.3	0	402480	1558	1170	384	1549	405208	1942	404029
Solar Array	7.95	0	0	225.0	1788.8	14.0	111.3	0	402480	1558	1170	384	1549	405208	1942	404029
Pneumatic System	19.70	0	0	190.0	3743.0	0	0	0	711170	0	1063	1063	1063	712233	1063	712233
Antenna	1.00	1.7	1.7	181.0	181.0	0	0	3	32761	0	—	—	—	32761	3	32764
Harness and Diagnostic	32.10	0	0	190.0	6099.0	0	0	0	1158810	0	7768	7768	15536	1166578	7763	1174346
Beacon and Sensors	3.70	0	0	181.0	669.7	(5.2)	19.3	0	121216	101	—	—	—	121317	101	121216
Thermionic Generator	5.70	0	0	219.0	1248.3	0	0	0	273378	0	33	33	58	273411	33	273436
Thermionic Support Structure	11.70	0	0	206.0	2410.2	0	0	0	496501	0	3650	3650	7330	500151	3650	503831
Concentrator Surface	9.80	0	0	200.0	1960.0	0	0	0	392000	0	1370	1370	2045	393370	1370	394045
Thermionic Control Elect.	6.00	0	0	191.0	1146.0	0	0	0	218886	0	16	16	16	218902	16	218902
Reflectometer	5.00	0	0	197.0	985.0	0	0	0	194045	0	17	3	17	194062	3	194062
Structure and Thermal	35.90	0	0	186.0	6677.0	0	0	0	1241922	0	11309	11309	20678	1253231	11309	1262600
Total Spin Condition	360.13	0	0	(194.9)	70204.9	0	0	0	13629350	0	190098	143909	220767	13819448	143909	13850117
								Slug-ft^2 about geometric axis			41.0	31.0	47.6			
								Slug-ft^2 about control axis			44.3	31.0	44.3			
ORBIT CONDITION																
REMOVE																
Solar Experiment Panel	28.64	-14.0	-401.0	216.0	6186.2	0	0	5614	1336219	0	2749	1527	1527	1338968	7141	1343360
Solar Experiment Panel	6.19	17.0	105.2	218.0	1349.4	0	0	1788	294169	0	593	330	330	294762	2118	296287
Solar Array	7.95	0	0	225.0	1788.8	-14.0	-111.3	0	402480	1558	1170	384	1549	405208	1942	404029
Solar Array	7.95	0	0	225.0	1788.8	14.0	111.3	0	402480	1558	1170	384	1549	405208	1942	404029
ADD																
Solar Experiment Panel	28.64	-40.0	-1145.6	204.0	5842.6	0	0	45824	1191840	0	1527	2749	1527	1193417	48573	1239241
Solar Experiment Panel	6.19	40.0	247.6	204.0	1262.8	0	0	9904	257611	0	330	593	330	257941	1049	267845
Solar Array	7.95	0	0	204.0	1621.8	-49.0	-389.6	0	330847	19090	1170	1549	384	351107	20639	331231
Solar Array	7.95	0	0	204.0	1621.8	-49.0	389.6	0	330847	19090	1170	1549	384	351107	20639	331231
TOTAL ORBIT CONDITION	360.13	(-2.5)	-898.0	(192.8)	69440.7	0	0	2245	13388167	0	142989	228869	183846	13531156	231114	13574258
								Slug-ft^2 about geometric axis			30.8	49.3	39.6			
								Slug-ft^2 about control axis			35.2	49.3	35.2			

13.5.4 MOMENTS OF INERTIA

Also of importance in computing the spacecraft disturbance torques and sizing the attitude control subsystem are the moments of inertia about the principal axes. These were computed for the Mission A spacecraft in the spin and orbit conditions and the calculations are outlined in Table 13-4. The moments of inertia were computed about the spacecraft geometric axes and then translated to the control axes. The control axes are rotated 45 degrees from the geometric axes (see Figure 13-4). This rotation of the inertia to a new set of axes is accomplished by applying the following equations:

$$I_{x1} = I_x \text{Cos}^2 \theta + I_y \text{Sin}^2 \theta - P_{xy} \text{Sin } 2\theta$$

$$I_{y2} = I_y \text{Cos}^2 \theta + I_x \text{Sin}^2 \theta + P_{xy} \text{Sin } 2\theta$$

Where P_{xy} is the product of inertia term and θ is the angle through which the axis are rotated. Since products of inertia were not computed in this study, the P_{xy} terms were neglected in rotating the axes. It is estimated that neglecting the product of inertia term, resulting from the 2.5 inch center of gravity offset from the roll axis, yields a five percent error in the inertias about the control axes. The resulting inertias about the geometric and control axes are summarized in Table 13-5. These values were used in Section 11 to design the attitude control subsystem.

13.6 SUMMARY AND CONCLUSIONS

The proposed spacecraft configuration is given in Figure 13-3 and the weight breakdown for Missions A, B, and C presented in Table 3-2. The proposed design is representative of the present state of the art in spacecraft construction and involves no unproven techniques or materials.

Table 13-5. Moments of Inertia

Condition	I_{ox}-Yaw Slug-ft^2	I_{oz}-Roll Slug-ft^2	I_{oy}-Pitch Slug-ft^2
1. Spin Condition Paddles Folded Geometric Axis	41.0	31.0	47.6
2. Same As No. 1 except rotated 45 degrees to Control Axis	44.3	31.0	44.3
3. Orbit Condition Paddles Deployed Geometric Axis	30.8	49.3	39.6
4. Same As No. 3 except rotated 45 degrees to Control Axis	35.2	49.3	35.2

Note: Reference Axis Shown in Figure 13-4.

13.6.1 SPACECRAFT WEIGHTS

The total spacecraft weights for Missions A, B, and C are 360, 373, and 404 pounds, respectively. In the mission analysis phase of the study the spacecraft weight was assumed to be 350 pounds and the launch vehicle and orbit selections were made on that basis. In all three cases the spacecraft weight is greater than the assumed 350 pounds which raises the question of the heavier spacecraft weights being compatible with the launch vehicle and orbit selections.

The Mission A spacecraft weight is just slightly over 350 pounds and from Figure 2-42, in Section 2.4.3 of Volume II, it is apparent that the DSV-3E can place up to 500 pounds in a 1000 nautical mile polar orbit if the launch is made from the Western Test Range. The Mission A orbit inclination is 101.84 degrees which will require slightly more launch capability than a polar orbit (90 degrees inclination). However, based on the performance shown in Figure 2-42 the DSV-3E can place the 360 pound Mission A vehicle in the required 1000 nautical mile, modified sun-synchronous orbit, with an inclination of 101.84 degrees. In this case there appears to be a substantial safety factor to work with since the DSV-3E can probably place as much as 450 pounds in the required orbit.

The Mission B case is difficult to evaluate because there are no DSV-3E performance curves available for a 45 degree inclined, 200 by 25,000 nautical mile elliptical orbit. However, Figure 2-30, in Section 2.4.3 of Volume II, provides some feel for this case. The performance estimates presented in this figure are for a 33 degree inclination and a perigee altitude of 100 nautical miles. Based on information presented in this figure it appears that the 25,000 nautical mile apogee altitude could not be obtained with a 373-pound spacecraft using a standard DSV-3E launch vehicle. It appears that the desired orbit altitude could be obtained if N_2O_4/A-50 were used as the second stage propellants or if the first stage was floxed 30 percent. If the standard DSV-3E propellants are used, an apogee altitude on the order of 14,000 to 16,000 nautical miles appears to be the maximum obtainable. This leaves three alternatives:

a. Lower the spacecraft weight

b. Accept a perigee altitude less than 25,000 nautical miles

c. Flox the first stage or use N_2O_4/A-50 as the second stage propellants.

The only way to lower the spacecraft weight would be to reduce the number of secondary experiments included on board. Considering the value of these experiments this approach is not recommended. Accepting a perigee altitude of 14,000 to 16,000 nautical miles instead of 25,000 nautical miles would reduce the daylight period available for evaluating the sun pointing experiments and would mean that proton and electron measurements could not be made across the entire Van Allen radiation belt. Since these factors represent the major advantages of the highly elliptical orbit this approach, although considered acceptable, it is not very attractive. The recommended approach then is to keep the spacecraft design as proposed and use the DSV-3E launch vehicle with the first stage floxed 30 percent.

There are no performance curves available in Section 2.4.3 (Volume II) for the DSV-3H launch vehicle so its ability to place 404 pounds in a 325 nautical mile, circular orbit with a 33 degree inclination, was discussed* with the Delta System Development Office of the Douglas Aircraft Company. Douglas confirmed that the DSV-3H could place 404 pounds, and more, in the desired orbit.

Fortunately, the actual spacecraft weight deviations from the 350 pounds assumed in the Mission Analysis phase of this study do not cause any major problems and the original analysis and conclusions are still valid.

13.6.2 SECONDARY EXPERIMENTS

It was possible to integrate all thirteen of the priority "A" and "B" secondary experiments, defined in Section 5.4.2 of Volume II, into the spacecraft design. This fact adds significantly to the valuable information that would be obtained from the spacecraft and therefore enhances the value of such a program.

*Phone conversation held on March 12, 1965.

A study of Figure 13-3 indicates that there is still space on the sun-pointing experiment panel for additional secondary experiments and the equipment mounting panels in the spacecraft body are not completely filled. This fact suggests that if the launch vehicles chosen can tolerate additional weight, as it appears they can in Missions A and C, the possibility of including additional experiments should be studied.

13.6.3 SPACECRAFT THERMAL CONTROL

A thermal analysis should be conducted to determine if the spacecraft requires active thermal control as assumed or if a completely passive system would be adequate. Such an analysis would require consideration of the spacecraft thermal inputs and the component heat dissipation as a function of time, which was beyond the scope of this study. The active thermal control system proposed, because of its simplicity and the fact that the approach has been flight proven on Mariner C, is considered very reliable. As a result the only major advantage to be derived if it could be eliminated would be a weight saving. The active portion of the thermal control system weighs approximately 15 pounds but if it were eliminated some portion of this weight would undoubtedly be required by the passive system replacing it.

13.6.4 REDESIGN OF REFLECTIVE SURFACES EXPERIMENT

A redesign of the solar reflective surfaces experiment should be undertaken to see if it could be made more compatible with this application. The design employed in this study was developed for a different application (see Section 5.2.6 in Volume II) and only modified for this case. The high concentrated weight (27 pounds over an area 24 inches in diameter) of this experiment makes it very difficult to locate in a position where it can be sun-pointing and not cause a poor center of pressure/center of gravity relationship and a large imbalance in the moments of inertia about the control axes. Integrating this experiment into the spacecraft design proved to be a major problem in developing a satisfactory spacecraft configuration.

13.6.5 SPACECRAFT BALANCE RESTRAINTS

The solid X-258 third stage motor of the IMPROVED DELTA vehicle is spin stabilized before ignition. This requires all third stage components (spacecraft included) to be balanced before flight. The specified requirements as stated in "Delta Spacecraft Design Restraints", Douglas Report SM-42367, are as follows: (1) To be statically balanced, the spacecraft center of gravity shall not be displaced from its centerline by a distance greater than 0.015 inches. The spacecraft centerline is defined as a line perpendicular to the separation face of the spacecraft and passing through the center of the spacecraft adapter fitting. (2) To be dynamically balanced, the spacecraft principal axes of inertia, yaw, pitch, and roll, shall be perpendicular and parallel to the centerline within an angle of 0.002 radians.

Until the spacecraft is defined in greater detail a balance analysis aimed at verifying the vehicles ability to meet these specifications is not warranted. However, it is important that these requirements be recognized since they could place significant restraints on the spacecraft design.